SUPRAMOLECULAR NANOFIBERS

PREPARATION, STRUCTURE-PROPERTY RELATIONS, AND APPLICATIONS

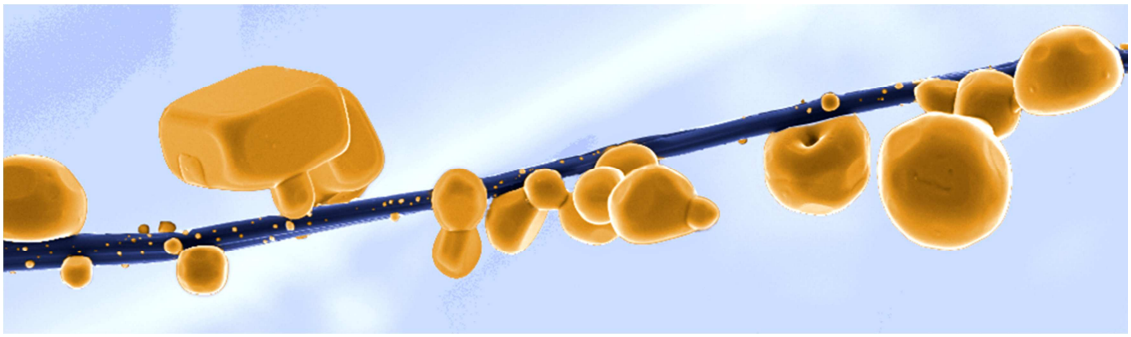

DISSERTATION

zur Erlangung des akademischen Grades
eines Doktors der Naturwissenschaften (Dr. rer. nat.)
im Fach Chemie der Fakultät für
Biologie, Chemie und Geowissenschaften der Universität Bayreuth

vorgelegt von

Holger Misslitz
geboren in Coburg

Bayreuth, 2013

Die vorliegende Arbeit wurde in der Zeit von April 2008 bis Februar 2013 am Lehrstuhl Makromolekulare Chemie I der Universität Bayreuth unter der Betreuung von Herrn Prof. Dr. Hans-Werner Schmidt angefertigt.

Amtierende Dekanin:	Prof. Dr. Beate Lohnert
Tag des Einreichens der Dissertation:	04. Februar 2013
Tag des wissenschaftlichen Kolloquiums:	15. April 2013

Prüfungsausschuss:

Prof. Dr. Hans-Werner Schmidt	(Erstgutachter)
Prof. Dr. Andreas Greiner	(Zweitgutachter)
Prof. Dr. Stephan Förster	(Vorsitzender)
Prof. Dr. Anna Köhler	

Farbgebung des Titelbilds: Alexander Kern

Table of contents

SUMMARY

Conventional polymer nanofibers have gained tremendous interest in the last years in the fields of catalysis as templates, in medicine as tissue engineering, in functional textiles as protective suits, and especially in air filtration as filter media. Generally, nanofibers are prepared by top-down approaches. However, these processes feature several disadvantages. As consequence cost-effective alternative strategies are required. One strategy to this problem is the bottom-up approach – the self-assembly of small molecules. Therefore, this thesis covers different topics with respect to the preparation, structure-property relations, and application of supramolecular nanofibers:

To investigate the impact of the molecular structure on the stacking behavior in the *self-assembly process*, a set of *pyrene-containing model compounds* was synthesized. Here, the focus was set on the influences of sterical demanding side groups as well as hydrogen bonding motifs on the π-stacking of the pyrene units. These influences were, besides others, detected by excimer formation in dilute solution, in the aggregated state and in solid films. It was demonstrated that π-stacking of the pyrene units is the driving force of the self-assembly process in solution in this system. However, hydrogen bonds are required to obtain well-defined supramolecular nanofibers. The influence of the hydrogen bonding motif and the sterical hindrance on the pyrene stacking becomes more and more significant the closer the molecules are forced together. Hence, the columnar stacking is increasingly disturbed in solid films compared to solution.

The class of *1,3,5-benzenetrisamides* is one of the simplest and most-versatile motifs in supramolecular chemistry. Within this thesis, two different *self-assembly processing pathways* of benzenetrisamides from solution; in particular self-assembly upon cooling at constant concentration and self-assembly during solvent evaporation at constant temperature were explored. One factor that determines the actual processing pathway is the solubility of the benzenetrisamide molecule. Exclusive self-assembly upon cooling takes place when the benzenetrisamide is almost completely insoluble in the used solvent at room temperature. The prerequisite for self-assembly during solvent evaporation is certain solubility of the BTAs at room temperature. In addition, these self-assembly pathways were compared with respect to control the supramolecular nanofiber morphology in view of homogeneity, fiber diameter, and fiber diameter distribution. Thereby, influences of external parameters such as temperature, solvent, and concentration were investigated in detail.

Especially in air filtration industry nanofibers are an important tool because of their beneficial effects due to their high surface-to-volume ratio. In industry, electrospinning is the standard technique to post-modify nonwoven filters with conventional polymer nanofibers on the filter surface. However, this process is limited to the surface of the scaffold. In this thesis, the principle utilization of *supramolecular nanofibers in air filtration* is demonstrated for the first time. Here, a solution-based immersion process was developed, which allows a successful *in-situ* formation of supramolecular nanofibers in nonwoven scaffolds. This results in a stable microfiber-nanofiber composite. The main advantage of this process is the effective incorporation of nanofibers in the volume of the nonwoven fabrics. For supramolecular systems, it was claimed that they are too fragile to be competitive with conventional polymers. But the herein prepared supramolecular nanofibers possess enough stability even upon applied airstreams of 3.0 m/s. This stability is by far superior than it is required at standard vacuum cleaners which possess flow velocities of 0.25-0.40 m/s at the filter element. First filtration tests revealed promising filtration efficiencies.

Building on these promising results a *comprehensive study* on *structure-property relations* at the preparation of *microfiber-nanofiber composites* in view of optimized filtration efficiencies was investigated. Depending on the selected benzenetrisamide, solvent, and concentration of the immersion solution, the filtration efficiency of the filters can be adjusted. By varying the thickness of the filters by means of double- and triple-layer filters, for supramolecular modified filters, excellent filtration efficiencies over 90 % were obtained for aerosol particles with the size of 0.2 µm.

To summarize, different issues concerning supramolecular nanofibers were pursued in this thesis spanning from fundamental investigations to utilize the self-assembly process towards forward-looking applications in air filtration.

ZUSAMMENFASSUNG

In den letzten Jahren haben konventionelle, polymere Nanofasern auf den Gebieten der Katalyse (als Template), der Medizin (in der Gewebetechnologie), der Funktionstextilien (Schutzanzüge) und insbesondere in der Luftfiltration als Filtermedium enormes Interesse erlangt. Im Allgemeinen werden polymere Nanofasern mittels Top-Down Prozessen hergestellt, allerdings weisen diese Methoden mehrere Nachteile auf. Daher sind kostengünstige Alternativen zwingend erforderlich. Ein Lösungsansatz ist die Bottom-Up Strategie – die Selbstorganisation von kleinen Molekülen. Aus diesen Gründen beschäftigt sich die vorliegende Arbeit mit verschiedenen Themengebieten hinsichtlich der Präparation, Struktur-Eigenschaftsbeziehungen und der Anwendung von supramolekularen Nanofasern:

Um den Einfluss der molekularen Struktur auf das *Aggregationsverhalten* zu untersuchen, wurden diverse *Pyren-basierte Modellsubstanzen* synthetisiert. Die Einflüsse von sterisch anspruchsvollen Substituenten und Wasserstoffbrücken-bildenden Einheiten auf die π-π Wechselwirkungen der Pyreneinheiten wurden unter anderem durch Excimerbildung in Lösung, im aggregierten Zustand und in Filmen detektiert. Es wurde gezeigt, dass die Triebkraft der supramolekularen Aggregation dieses Systems in Lösung die π-π Wechselwirkung zwischen den Pyreneinheiten ist. Dennoch sind für die Ausbildung wohldefinierter Nanofasern Wasserstoff-brückenbindungen von entscheidender Bedeutung. Je näher die Moleküle zusammenrücken, desto signifikanter werden die Einflüsse von sterisch anspruchsvollen Substituenten und Wasserstoffbrücken-bildenden Einheiten. Daher wird im Vergleich zur Lösung die kolumnare Aggregation der Pyrene in Filmen stärker gestört.

Die Substanzklasse der *1,3,5-Benzoltrisamide* ist eine der einfachsten und vielseitigsten Motive in der supramolekularen Chemie. In dieser Arbeit wurden zwei unterschiedliche *Selbstorganisations-Prozesswege* von Benzoltrisamiden untersucht. Ein Prozessweg umfasst die Selbstorganisation durch Abkühlen bei konstanter Konzentration. Im anderen Prozess wurde die Selbstorganisation durch Verdampfen des Lösungsmittels bei gleichbleibender Temperatur untersucht. Der tatsächlich ablaufende Prozess bei der Selbstorganisation aus Lösung wird unter anderem durch die Löslichkeit der Benzoltrisamidmoleküle bestimmt. Selbstorganisation durch Abkühlen findet statt, wenn die Benzoltrisamide bei Raumtemperatur praktisch unlöslich im verwendeten Lösungsmittel sind. Im Gegensatz dazu wird bei der Selbstorganisation durch Verdampfen des Lösungsmittels eine gewisse Löslichkeit der

Benzoltrisamide bei Raumtemperatur benötigt. Zusätzlich wurde die resultierende Morphologie der supramolekularen Aggregate im Hinblick auf deren Homogenität, Faserdurchmesser und deren Verteilung verglichen. Einflüsse der externen Parameter Temperatur, Lösungsmittel und Konzentration auf die supramolekulare Morphologie wurden detailliert untersucht.

Besonders in der Luftfiltration sind Nanofasern, durch ihr großes Oberflächen-zu-Volumen Verhältnis, ein essentielles Instrument, um die Qualität von Luftfiltern zu verbessern. In der Industrie wird Elektrospinning dazu benutzt, bestehende Vliese auf der Filteroberfläche mit konventionellen Polymernanofasern nachträglich zu modifizieren. Jedoch ist dieser Prozess auf die Oberfläche des Vlieses limitiert. In der vorliegenden Arbeit wird erstmals die Verwendung von *supramolekularen Nanofasern in der Luftfiltration* aufgezeigt. Hierbei wurde ein lösungsbasierter Tauchprozess zur Herstellung von stabilen Mikrofaser-Nanofaser-Kompositfiltern entwickelt. Dieser Prozess ermöglicht eine erfolgreiche *in-situ* Ausbildung supramolekularer Nanofasern innerhalb der Vliese. Der wesentliche Vorteil darin besteht in der effektiven Ausnutzung des gesamten Vlies-Volumens. Es wurde oft behauptet, dass supramolekulare Systeme zu instabil sind, um mit konventionellen Polymeren mithalten zu können. Jedoch besitzen die, in der vorliegenden Arbeit hergestellten supramolekularen Nanofasern hinreichende Beständigkeit. Ihre Stabilität in Luftströmen bis hin zu 3 m/s Anströmgeschwindigkeit ist bei weitem größer, als es zum Beispiel in handelsüblichen Staubsaugern erforderlich ist (0.25 - 0.40 m/s). Zudem zeigen erste Filtertests vielversprechende Abscheidegrade.

Aufbauend auf diesen erfolgsversprechenden Ergebnissen werden an den hergestellten *Mikrofaser-Nanofaser Kompositfiltern* zahlreiche *Struktur-Eigenschafts-beziehungen*, im Hinblick auf eine optimierte Filtereffizienz untersucht. Die Qualität der Filter kann durch die Wahl des Benztoltrisamids, des Lösungsmittels und der Konzentration der Tauchlösung eingestellt werden. Durch die Variation der Filterdicke mittels Verwendung von zwei- bzw. dreilagigen Filtern, wurden (für supramolekulare Systeme) exzellente Abscheidegrade erhalten, die bei der Filtration von 0.2 µm großen Aerosolpartikeln sogar 90 % übersteigen.

Zusammenfassend dargestellt, werden in dieser Arbeit verschiedene Themengebiete rund um die supramolekulare Nanofaser vorgestellt. Diese reichen von fundamentalen Untersuchungen des Selbstorganisationsprozesses bis hin zu zukunftsweisenden Anwendungen in der Luftfiltration.

1. INTRODUCTION

In industrial applications, the progressive miniaturization of devices which is omnipresent in all kinds of industrial sectors in the last decades is not surprising. One of the most conspicuous examples of that trend is the computer industry with its chip-manufacturing. Moreover, miniaturization is expected to pave the way towards more and more efficient devices and nano-materials with novel properties. As consequence, the field of nanoscience and technology is well established.[1]

1.1 Micro- and nanofibers

Among others the field of nanoscience and technology also deals with fibers featuring diameters in the micro- and nanometer range. The main focus is set on the control of shape and dimensionality. In order to fabricate devices or structures in the nanometer range, two opposite concepts can be utilized – a *top-down approach* or a *bottom-up approach*. In Figure 1 both approaches are illustrated in the context of micro- and nanofibers.

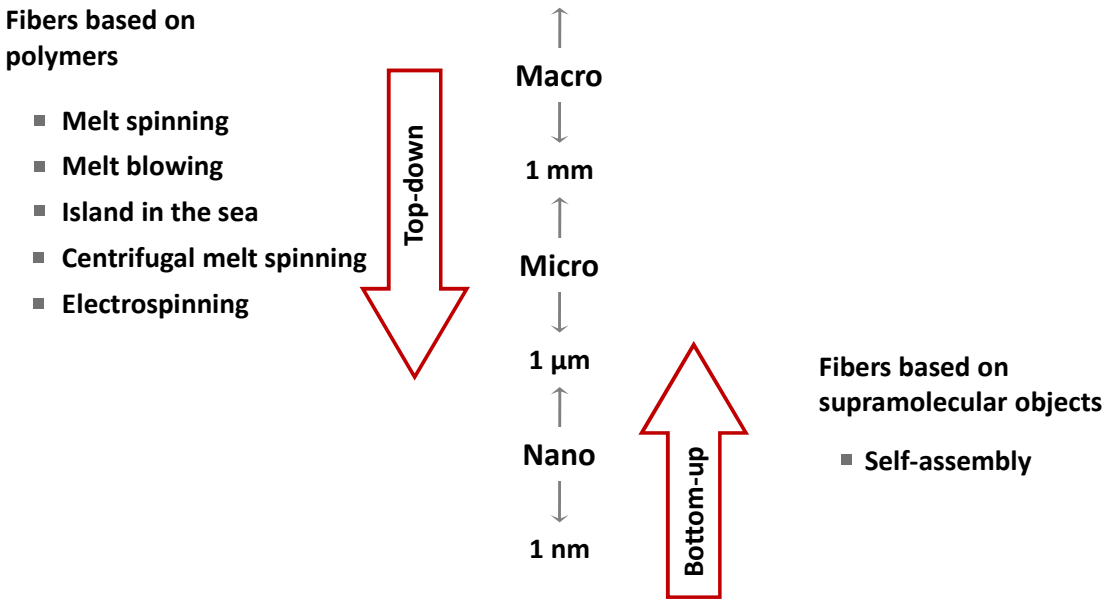

Figure 1. Schematic representation of nano- and microfiber preparation by top-down approaches as well as a bottom-up approach.

Common top-down approaches utilize fiber spinning techniques of synthetic polymers in order to prepare micro- and nanofibers.[2] In filtration industry, for example, those fibers are needed in the production of nonwoven fabrics. Among the spinning

techniques, *melt-spinning*,[3] *melt-blowing*,[4,5] and *electrospinning*[6–8] feature the most prominent processes. However, the limits of these top-down approaches in view of physical capability are almost reached. While conventional melt-spinning is not able to produce directly nanofibers, electrospinning is a relative slow process and cost-intensive. Due to these reasons, in industry, melt-blowing is currently the most efficient process to achieve small fiber diameters.

For classical *melt-spinning* the minimal achievable fiber diameter is about 10 µm.[9] This process, is illustrated in Figure 2. Here, the molten polymer is extruded, forced into a die and drawn down by aerodynamic forces. The polymer melt can be stretched to fibers as long as the temperature is above the glass transition temperature or crystallization occurs. In industrial machines multifilament dies are used to prepare many fibers simultaneously. In the case of nonwoven preparation, these fibers subsequently become entangled to each other by an airstream and are processed further by bonding processes.[10]

In comparison, commercial polymer fibers produced with the *melt-blowing* technique usually exhibit fiber diameters of 2 µm to 1 µm.[11] However, research groups reported from fiber diameters in the nanometer range under specific conditions.[5,12] In this process the molten polymer is also extruded and forced into die assemblies. Directly after the die, a hot airstream (illustrated as primary airstream in Figure 2) converges with the effluent polymer melt to stretch it to thin fibers. To intensify this process a secondary airstream is used after the die. The main difference between melt-spinning and melt-blowing is the setup of the airstreams. In melt-spinning, generally no airstreams are included in the process. One exception is the production of nonwovens. Thereby the airstream is apart from the die and perpendicular to the stretched fibers. In contrast, melt-blowing possess two airstreams; one is located directly at the die orifice and the second stream flows longitudinal to the fibers, resulting in smaller fiber diameters compared to melt-spinning.[10]

By means of a modification of the melt-blown process micro- as well as nanofibers can be produced simultaneously. Thereby, at least two dies with different diameters are used. Irema-Filter GmbH uses this technique to produce filters with mixed fiber sizes. While the coarse fibers ensure the stability of the nonwoven fabrics, the smaller fibers increase the filtration efficiency of small aerosol particles.[13]

In view of small fiber diameters, *electrospinning* is the most effective process. Thereby, fiber diameters of 40 nm can be obtained.[7] Some research groups have even reported, that they achieved fibers with a diameter as low as 2 nm.[14] The first patent how to spin polymers appeared in 1934,[15] while in 1970 the first patent for the preparation of fibers in the sub-micron range was published.[16] However, this technique remained mostly unnoticed outside filter industry until the 1990s.[17] In the electrospinning process, voltages in the range of 5 kV to 30 kV[18] are applied between

a collector and a polymer solution[19] or melt[20] located in a syringe (Figure 3). By forcing the polymer out of the die, the solution evaporates (or the melt solidifies). Directly after the die, the polymer forms one straight jet, which changes due to instabilities into one rapidly bending, whipping strand.[8] The resulting nanofibers are deposited on a grounded collector. The prerequisite for melt electrospun polymers is their non-degradation under the applied conditions which for instance is fulfilled for polyethylene,[21] polypropylene,[22] poly(methyl methacrylate),[23] and several polyamides.[24] In comparison, solution electrospinning gained greater popularity, due to better processability and smaller diameters of the resulting fibers. For solution electrospinning, the polymers have to be soluble in the utilized solvents. Thereby, polymers such as polyamides,[25] polyurethane, polycarbonate,[26] polyethylene oxide,[27] polystyrene,[28] and polyvinylchloride[29] have already been electrospun beside many others.

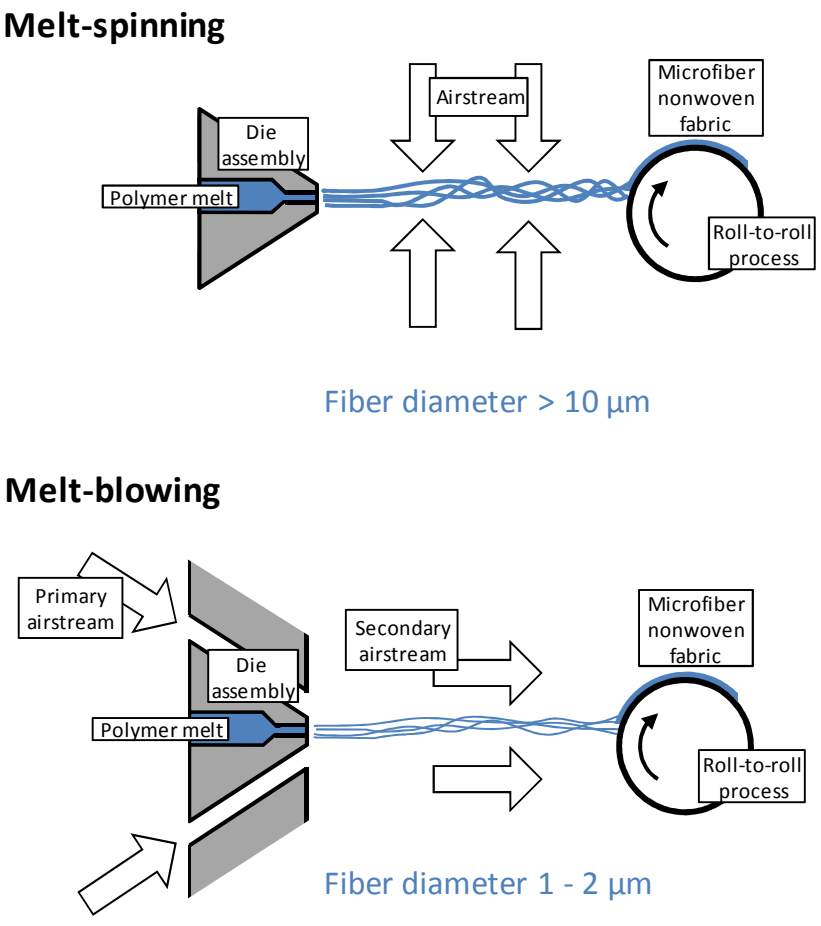

Figure 2. Schematic illustrations of the industrial used processing techniques for nonwoven fabrics.

One application of electrospinning is filtration. Up to now, electrospinning is the only top-down approach to post-modify existing nonwoven fabrics with polymer nanofibers. In this process, the nonwoven fabric moves on the collector at a roll-to-roll process, while nanofibers are spun on top of the surface (Figure 3). Anyhow electrospinning just became a niche process in filtration industry. The reasons are relatively slow spinning velocities of 10-300 mg/die/min, the use of high voltages, and in the case of solution processing the poor solubility of polymers with desirable properties (for instance polyolefines).[30] However, the undoubtedly greatest disadvantage of solution electrospinning is the usage of volatile organic compounds, because of the high inflammability and the explosion hazard. Nevertheless, a lot of research reports on electrospinning are known in fundamental research.[31] Analogous to melt-blowing a simultaneous preparation of heterogeneous fiber diameters (e.g. micro- and nanofibers) is also possible by means of electrospinning. This is called parallel-electospinning.[32]

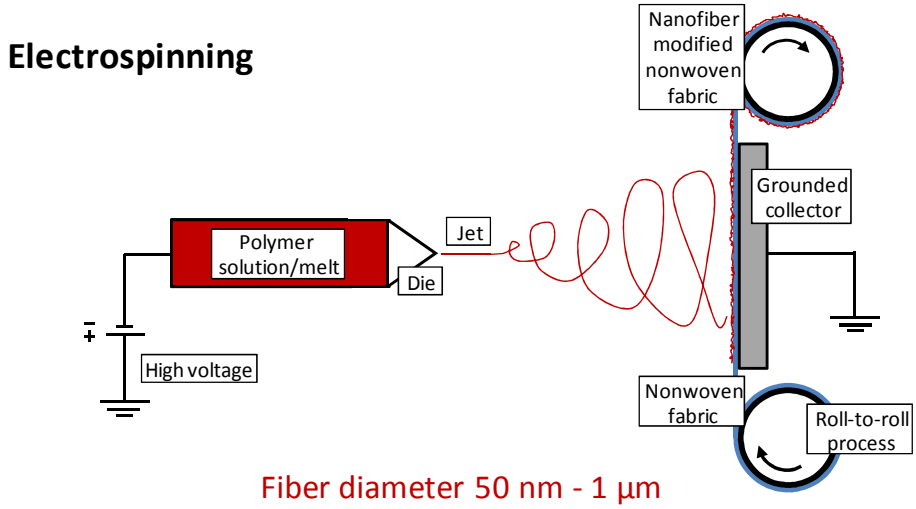

Figure 3. Schematic illustration of the electrospinning process, in which nanofibers are spun on top of a nonwoven fabric.

In contrast, the bottom-up approach starts at the molecular size range generating nano- and micro-objects by self-assembly processes. This is an important domain of the field of supramolecular and macromolecular chemistry. In this thesis, the bottom-up approach – self-assembly of small molecules - is investigated to prepare self-assembled nanofibers and nanofiber webs. Here, structure-property relationships are developed in order to control the fiber morphology also in view of optical and air filtration applications.

1.2 Supramolecular Chemistry

Supramolecular chemistry is an area of chemistry of non-covalent bonds, just as molecular chemistry is based on covalent bonds. Supramolecular chemistry can be seen as the chemistry beyond the molecules and covalent bonds.[33,34]

The synthesis of suitable molecular building blocks is achieved by organic chemistry. Thereby functional moieties capable to form non-covalent bonds are implemented into the molecular structure. In supramolecular chemistry, those bonds are tailored to create controlled self-assembled aggregates. The most important non-covalent interactions, involved in self-assembly processes are hydrogen bonds, π-π stacking, ionic interactions, dipole interactions, and metal coordination.[35] Furthermore, supramolecular chemistry involves the variation of external conditions, most prominently temperature, solvent, and concentration to tailor the self-assembly towards the desired aggregate morphology.[36] Controlling these factors well-defined architectures in the nano- and meso-scale can be realized in liquids and in polymer melts.

In nature, many biomolecules have the extraordinary feature to self-assemble into well-defined and very often one-dimensional structures held together by non-covalent bonds. For instance, those aggregation phenomena can be found in the fauna and flora, in viruses and even in water. In the following, examples are briefly described. Human beings wouldn't be alive without collagen which is the major extracellular structural element of most tissues and organs offering mechanical stability, elasticity and strength. A tissue, build up by collagen, consists of several hierarchical levels. Starting from amino acids polypeptides are formed by covalent bonds. The next hierarchical level consists of three self-assembled polypeptide chains, supercoiled around a central axis to form a triple-helix. This self-assembled structure is defined as collagen. The triple-helices again self-assemble into fibrillar nanofibers, which in turn form collagen microfibers to support cell development and tissue formation.[37] The hierarchical structure of protein materials is exemplarily illustrated in Figure 4 for tendons and bones.

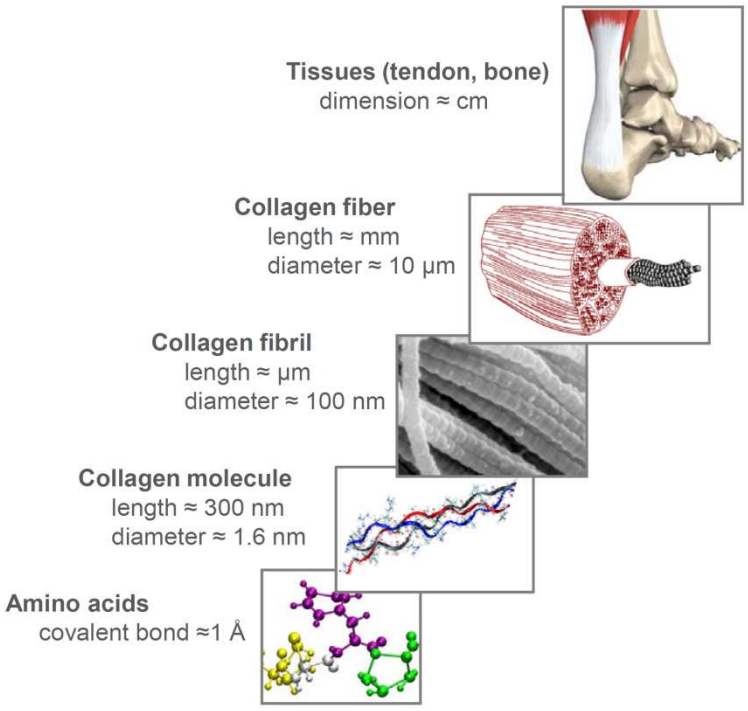

Figure 4. Hierarchical structure of tendons and bones, both are collagen protein materials.[38]

In the flora, the shape of a plant is determined by the position and the growth of cell walls, which can be seen as the "skeleton of plants". The principal component in cell walls is cellulose, which self-assembles by hydrogen bonds into hierarchical structured networks consisting of nanofibers and microfibrils.[39]

Self-assembly is also observed in viruses. The most famous representative is the tobacco mosaic virus. Its commonly known rod-like structure is formed by self-assembled coat proteins located around a single RNA molecule.[40] The exact length of the one-dimensional assembly is determined by the RNA molecule itself.

Another fascinating example of the self-assembly phenomenon in nature is the self-aggregation of water molecules to snow crystals. These single crystals of ice are grown from water vapor and are held together by non-covalent hydrogen bonds. Although this process appears to be very simple and straight forward, the growth of snow crystals still feature a mostly unsolved mystery. Depending on external parameters, such as temperature and supersaturation different morphologies can be observed. Nowadays naturally formed snow crystals are classified into morphological categories such as plates, dendrites, and even one-dimensional columnar assemblies. In the case of the one-dimensional aggregates also tubular structures are known.[41] These entire examples highlight the enormous importance of (one-dimensional) self-assembly, without those, nature wouldn't exist.

Due to the amazing power of supramolecular chemistry in nature, chemists saw much potential in exploiting and imitating intermolecular non-covalent interactions to create materials with novel properties.[42] Besides the interest in ionic and dipole-dipole interactions, van der Waals forces, and metal coordination a lot of effort has been made to investigate systems held together by π-π stacking and hydrogen bonds.[43] Because of the reversibility of their non-covalent bonds supramolecular systems are able to respond to external stimuli.[36,44] The self-assembly as well as the disassembly process can be induced by changing external parameters, such as medium, concentration, temperature, and pH-value.[45] Switching such parameters successively back and forth assembly and disassembly can be indefinitely repeated. Due to this advantage of reversibility over molecular chemistry and the ability to realize almost any desired morphology, supramolecular chemistry is interdisciplinary utilized in the fields of chemistry, physics, biology, and material science.[35,46]

In science supramolecular chemistry is a huge playground for all kind of scientists. Its very first enquiries were made by D. J. Cram, J.-M. Lehn, and C. J. Pedersen who jointly received the Noble Price in Chemistry in 1987 for their development and use of molecules with structure-specific interactions of high selectivity.[33] They were working on the molecular recognition of host-guest systems based on the key-lock concept.[47] Not only in nature, but also in systems which were artificially created, supramolecular nanofibers play an important role. Despite the fact that supramolecular organo-[48] and hydrogelators[49] consist of nanofibers which form a three-dimensional network, a SciFinder® search for the terms “supramolecular nanofibers” and “self-assembled nanofibers” as entered surprisingly results both together in just 140 references. This can be explained by the fact that in the past self-assembled nanofibers were just a means to an end for instance to obtain supramolecular gels. Just recently the supramolecular nanofiber itself became the focus of interest because of a more detailed research with respect to structural as well as to morphological aspects. The majority of those publications dealing with supramolecular nanofibers contain amphiphiles which are self-assembled or even gelled out of aqueous or organic solvents.[50] Because of the possibility to incorporate multiple functions, these nanostructures feature extremely diverse properties, thus, having potential for instance in bio-nanotechnology, such as in vivo imaging,[51] drug delivery,[52] and possessing antimicrobial effects.[53] Furthermore, supramolecular nanofibers can be tuned in view of their mechanical properties by means of a topochemical photopolymerization of diacetylene backbones within the supramolecular nanofibers.[54] The so modified organogelators can for example be utilized as filler materials in polymer nanocomposites for mechanical reinforcement.[55] Supramolecular chemistry itself also provides enough possibilities to adjust the mechanical properties of the self-assembled nano-objects. On the one hand this can

be realized by external factors, such as temperature, concentration, and gel-inducing ions.[56] On the other hand, cooperative as well as competitive combinations of several non-covalent intermolecular interactions result in well-defined assemblies with various stabilities. While a cooperative interplay of non-covalent bonds is able to promote the supramolecular aggregation into nanofibers,[57] competitive forces lead to destabilization. Therefore, it is highly important to investigate the involved non-covalent interactions in detail in order to obtain controlled supramolecular nanofibers.

In all these described examples, *not the molecules themselves but rather their supramolecular assemblies as well as their intermolecular interactions are in focus of the investigations*. Among the non-covalent forces hydrogen bonds and π-π stacking have been identified to be the most important ones in supramolecular chemistry. These two non-covalent interactions are utilized in this thesis to prepare manifold supramolecular nanofibers. Therefore the following sections should give a brief overview of those interactions with exemplary self-assembly motifs.

In the pool of non-covalent interactions, *hydrogen bonds play a superior role* due to their moderate strength, their selectivity, and their high directionality.[45,58] Hydrogen bonds are created between an electron poor hydrogen atom and an electron rich acceptor atom. The overall bond strength is mainly dependent on the quantity of hydrogen bonds. The concept of multiple hydrogen bonds is exploited by various research groups tailoring double, triple or quadruple hydrogen bonding sites in one molecule.[59] Thereby very strong non-covalent interactions are developed to design new supramolecular, polymer-like architectures. One approach to provide quadruple hydrogen bonding sites is based on ureidotriazines.[60] Figure 5 exemplarily shows the aggregation of ureidotriazine based molecules by hydrogen bonds. The bifunctional compounds are able to self-assemble into one-dimensional polymer-like aggregates. In literature those assemblies are also termed “supramolecular polymers”.

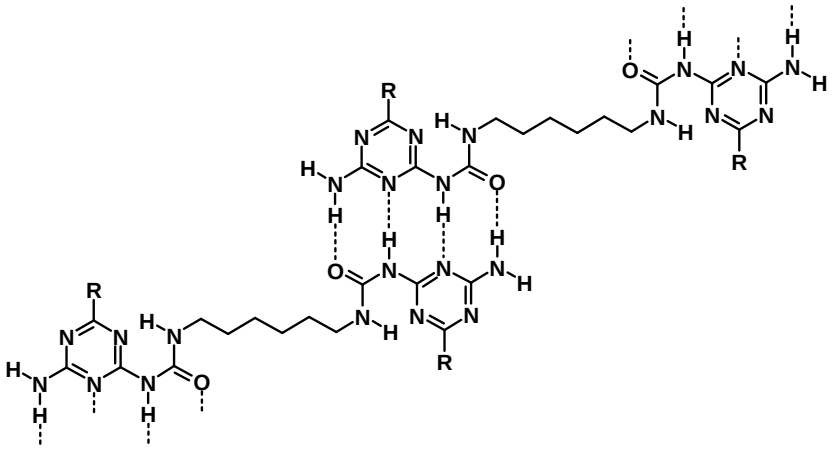

Figure 5. Molecular structure of a “supramolecular polymer” held together by quadruple hydrogen bonding sites. Adopted from reference [60].

Dyes feature extended aromatic π-systems and thus they are suitable for self-assembly by *π-π stacking*. The self-assembly of dyes into wire-like columns, seems to be a promising strategy for charge transport with respect to electronic applications.[61] Well-known arene systems are triphenylenes, perylenes, oligophenylenevinylenes, and pyrenes. Triphenylenes are one of the first investigated molecules that self-assemble by π-π stacking. They generally possess a planar aromatic unit which is capable to create attractive intermolecular interactions, forming rod- or worm-like aggregates. In order to improve solubility for a better handling aliphatic side-chains are often attached at the molecule periphery. Compared to hydrogen bonds, π-π stacking is generally unselective and relatively weak. It was shown that the intercore distances of triphenylarenes in supramolecular aggregates are relatively large compared to other systems indicating the loose and irregular stacking of the aromatic units.[62] Therefore the exclusive use of π-π stacking is in many cases inappropriate to control the morphology of supramolecular aggregates.

The *combination of π-π stacking and other non-covalent interactions such as hydrogen bonds*, however, is a useful tool to provide supramolecular nanofibers.[63] Nevertheless, the combination of non-covalent interactions has to be handled with caution because they can operate in a cooperative as well as in a competitive manner. This results either in an improvement or in a contraction of the stability and directionality of self-assembled aggregates.[64] Therefore detailed fundamental research of the self-assembly process is indispensable.[65] One example of a cooperative combination of π-π stacking and hydrogen-bonds is reported by Sudhölter.[66] They used a molecular motif with a 1,3,5-benzenetricarboxamide central core which is connected via spacers with three triphenylene groups at its periphery (Figure 6). The amide groups form intermolecular hydrogen-bonds stabilizing the columnar self-assembly, while the triphenylenes are able to interact by π-π stacking and therefore facilitating charge transport.

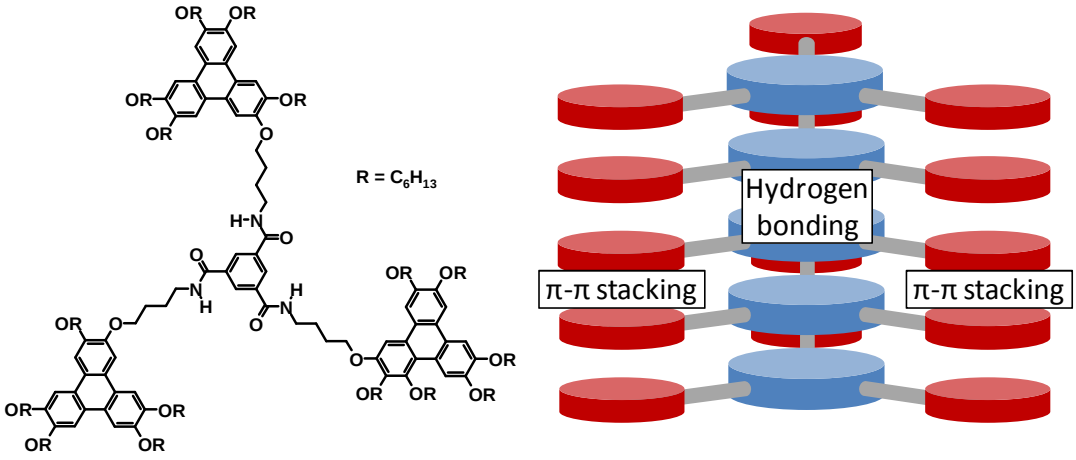

Figure 6. Molecular structure (left) and schematic representation of the columnar assembly (right) of a triphenylene-modified 1,3,5-benzenetricarboxamide. Adopted from reference [66].

E. W. Meijer and co-workers have demonstrated the significance of basic research on non-covalent bonds in self-assembly processes. They intensively investigated one-dimensional fibrillar stacks of 3,3'-diamino-2,2'-bipyridine modified benzenetricarboxamides (Figure 7). In their initial interpretation of experimental results they proposed that the bipyridine units are planar and preorganized by intramolecular hydrogen bonds in the molecular state. During self-assembly it was assumed that the intramolecular hydrogen bonds would change to intermolecular hydrogen bonds, directing the self-assembly into a one-dimensional fibrillar fashion.[67] Further investigations of the non-covalent bonds of this system however showed that the formation of intermolecular hydrogen bonds is very unlikely in the aggregated state due to large intermolecular distances. Therefore the helical aggregates are only held together by π-π stacking (Figure 7).[68]

This example elucidates, that the relevance and strength of all non-covalent interactions – intermolecular as well as intramolecular – must be considered when investigating supramolecular systems because small variations in the molecular structure can extremely influence the supramolecular assembly and therefore affect the aggregate morphology.

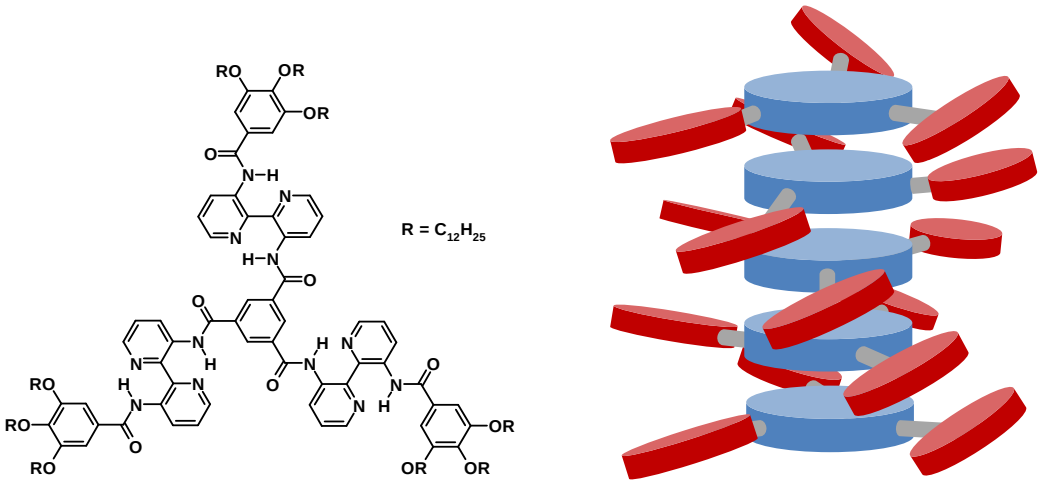

Figure 7. Molecular structure (left) and schematic representation of the columnar assembly (right) of a 3,3'-diamino-2,2'-bipyridine modified C_3-discotic1,3,5-benzenetricarboxamide. Adopted from reference [67].

1.2.1 1,3,5-Benzenetrisamides – a versatile motif in supramolecular chemistry

A comprehensive review about BTAs was previously published by Palmans et al.[69] Besides the structure and the synthesis, also the self-assembly of BTAs in dilute solutions as well as their applications was compiled.

A BTA molecule consists of three different structural units, as indicated in Figure 8. The center is a planar 1,3,5-substituted benzene core, that implements the C_3 symmetry. The amide moieties, the second structural subunit, can be connected to the core at their carbon as well as at their nitrogen atom. In addition, the solubility of these molecules is determined by the peripheral substituents.[70] BTAs are one of the simplest and most versatile motifs in supramolecular chemistry, which self-assemble into one-dimensional supramolecular nano-objects upon certain trigger-mechanisms, such as a shift in temperature,[71] concentration, medium,[72] and pH-value.[73]

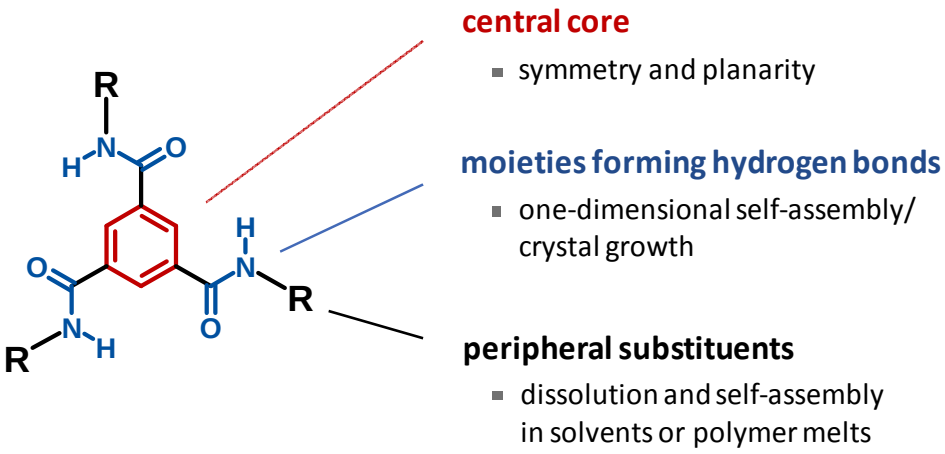

Figure 8. Schematic representation of the molecular structure of 1,3,5-benzenetrisamides (BTAs).

The thermoreversible self-assembly process of the BTAs is displayed in Figure 9. As medium solvents or (in the case of supramolecular polymer additives) polymer melts can be used. Starting with a dissolved BTA system at elevated temperatures, supramolecular one-dimensional aggregation occurs upon cooling. Thereby, the BTA molecules self-assemble by hydrogen bond formation (of the amide groups) and π-π stacking (of the benzene units) into one-dimensional primary aggregates. However, the interactions of the central benzene cores are marginal compared to the strong hydrogen bonds. By further association of the primary aggregates, bundled filaments are formed, which subsequently self-assemble into one-dimensional supramolecular nano-objects in turn. Length and diameter of the supramolecular aggregates depend on the molecular structure and external parameters (self-assembly conditions). Among these, the medium, the BTA concentration, and the temperature profile mainly influence the self-assembly process and the resulting supramolecular morphology.[45,74] In this thesis, these influences are examined in detail on exemplary BTA/solvent

systems. Besides the well-known self-assembly upon cooling (Figure 9), a second self-assembly process which occurs during solvent evaporation is also investigated and characteristic parameters influencing the self-assembly are pointed out.

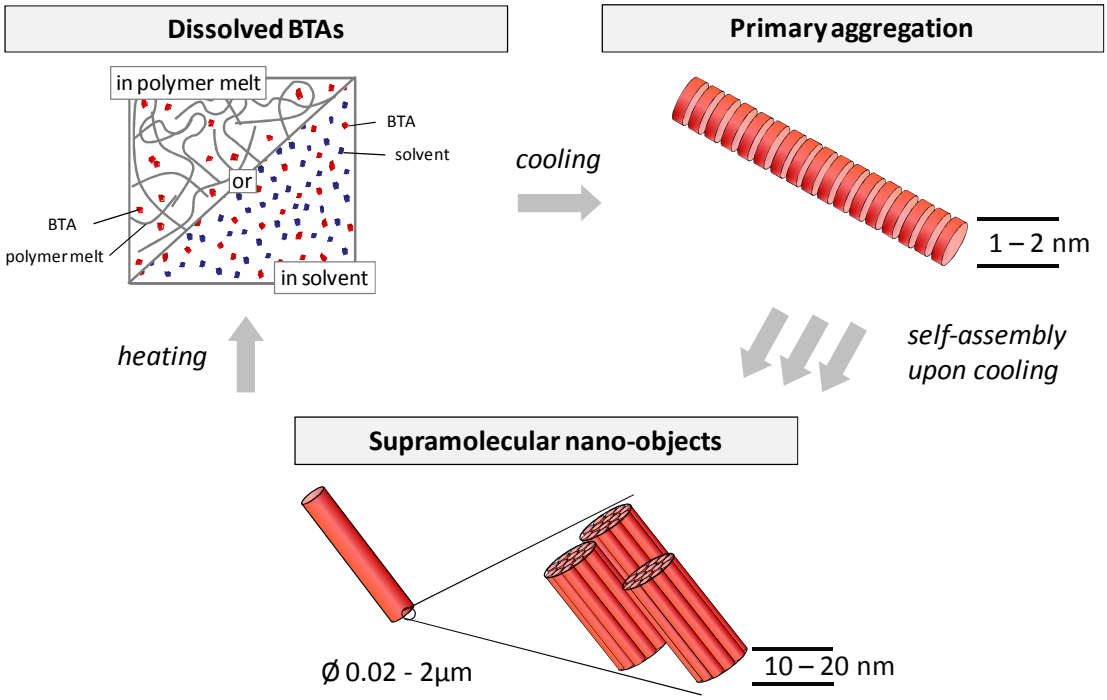

Figure 9. Schematic representation of the thermoreversible self-assembly process of BTAs.

Due to the simplicity of this self-assembly concept behind, 1,3,5-benzenetrisamides gained a lot of interest in academic research.[69]

Semi empirical calculations of supramolecular aggregates of BTAs revealed a staggered orientation of the peripheral substituents. Furthermore, the theoretical calculations showed a macro dipole formation within one supramolecular column when the C=O groups of the amides point into the same direction. A comparison between BTAs with aromatic and aliphatic cores results in differences in the quantity of the macro dipole in the aggregates.[75] Investigations regarding the structural clarification of the aggregates of BTAs were also done by NMR-crystallography combined with ^{13}C isotope marking of the carbonyl groups. The results revealed accordance with the semi empirical calculations of Albuquerque et al. (reference [75]) in view of the dipole moments in one column.[76] Furthermore, it was found, that the crystal structure of the BTAs strongly depends on the peripheral substituents. While methyl- and ethyl-substituents direct the self-assembly into sheet-like aggregates, propyl-rests force the self-assembly into primitive cubic three-dimensional networks.[77] However, BTAs with longer alkyl chains exhibit columnar structures forming hexagonal lattices.[71] In the case of 3-pyridyl substituents, the BTAs form three different crystalline forms from the same solvent system held together by non-covalent bonds (including polymorphic monohydrates).[78]

The class of BTAs is also investigated because of a mesophase behavior of some BTA derivatives. Certain alkyl substituents of the BTAs lead to a thermotropic liquid crystalline behavior in bulk in a broad temperature range. In addition, it was shown, that small columnar aggregates were still existent in the optical isotropic melt.[79] The columnar mesophases are mainly stabilized by the presence of the amide groups yielding strong hydrogen bond formation.[80]

Astonishing applications of BTAs are their usage as polymer additives for nucleation and clarification of polyolefins and semi crystalline polymers. Thereby, BTAs with short, bulky alkyl substituents were used in the case of nucleating isotactic polypropylene.[81] BTAs with a 2,4,6-trimethyl-1,3,5-triamino benzene cores even feature better thermal stability compared to BTAs with unsubstituated cores.[82] Semi crystalline polymers such as polyvinylidenfluoride[83] and polybutylene terephthalate[84] can also be nucleated by BTAs. In polybutylene terephthalate the supramolecular aggregates of the BTA additive could be visualized after alkaline hydrolysis of the polymer matrix. Therefore, it could be demonstrated that the diameter of the supramolecular nano-objects is dependent on the concentration and the cooling rate. Furthermore, not only polymeric bulk materials but also polymer foams can be nucleated by BTAs. The advantage hereby is the fact, that the processing window in injection molding is not affected compared to the neat polymer.[85] In addition, BTAs are also utilized in order to improve the electret performance of polypropylene.[86]

However, BTA nano-objects are not only investigated in polymer matrices. Supramolecular nanofibers of BTAs were further prepared by self-assembly in solution. The mechanical stability of those isolated supramolecular nanofibers is of great interest due to possible future applications. Single fibers, self-assembled from solution were investigated by three-point bending tests by means of an atomic force microscope. Within these investigations, structure-property relations between the molecular structure of the BTA and the mechanical stability of supramolecular BTA nanofibers were determined. In these investigations, E-moduli of 3-5 GPa were detected.[87] In addition, entanglements of supramolecular nanofibers prepared from solution can result in the formation of three-dimensional networks. Hence, this class of molecules can also act as organo-[88] and hydrogelators.[89]

Furthermore, it is possible to obtain supramolecular nanofibers of BTAs by electrospinning from columnar, nematic phases and isotropic melts. The supramolecular morphology of electrospun BTA nanofibers is dependent on the thermal properties of the BTAs, the spinning temperature, and the applied electric field.[90] A comparison between the self-assembled BTA fibers from solution and electrospun fibers showed, that differences in the supramolecular morphology are

existent, however, both sort of fibers feature mechanical stabilities in the same order of magnitude.[91]

1.2.2 Pyrene in supramolecular chemistry

Supramolecular aggregation can be detected with various methods, such as UV-Vis, IR, and photoluminescence spectroscopy. As prerequisite for photoluminescence measurements, the molecular building blocks have to be labeled with photoluminescent units. In this thesis pyrene is used as chromophore, because its optical behavior is well understood.[92] The photoluminescence of pyrene is sensitive to the environment. Monomer fluorescence can be detected at molecular dissolved pyrene molecules. In solution and in condensed matter such as amorphous films and crystals pyrene monomer fluorescence changes into excimer emission under certain circumstances.[93] An excimer may be considered as a pair of molecules that, in the ground state, are far apart from each other, and that absorb light as monomers, but that reorient in the excited state and then fluoresce as dimers.[94] The excimer fluorescence is broad, unstructured and red shifted compared to monomer fluorescence, and the emission again leads to two monomers in the ground state.[95]
Several examples exist in which the excimer emission is indirectly used to detect the aggregation process.[96,97] These characteristic properties have been employed in the investigation of pyrene-based tweezer molecules[98] and multimolecular aggregates of micelles and membranes,[99] the gelation detection of organic low-molecular weight compounds,[100] the inspection of the active sites of enzymes,[101] the molecular recognition process of artificial receptors and DNA sequences[102] and in the detection of nitroaromatic explosives.[103]
In addition to the indirect detection of aggregation processes, pyrene containing molecules themselves are able to self-assemble into supramolecular nanoparticles as well as nanofibers,[97] and are also able to form supramolecular organo- and hydrogels.[104]

1.3 Filtration[10,105,106]

The filtration and separation and, as a result, the isolation of contaminants are omnipresent in all areas of our lives. Filtration technologies are applied in many industrial fields to meet the requirements of the product or to improve worker protection. The most appropriate definition of the term filtration is given by the Association of the Nonwovens Fabrics Industry: "Filtration is a mechanism or device for separating one substance from another. Filtration may be used to separate contaminants from a fluid, or separate value-added materials such as minerals, chemicals, or foodstuffs in a process operation."[107] As fluid, gases as well as liquids are considered.[108] Filtration can be classified into two main segments, the *gas filtration* and the *liquid filtration*.[10] In the field of gas filtration aerosol particles are mainly filtered from air. Additionally, the purification of gaseous fuels such as natural gas and propane embody an application in this sector.[109] Liquid filtration is used in all separation purposes of liquid substances and solvents.

The segments of air filtration and liquid filtration can be divided into subsectors by their applications according to Mayman and Homonoff.[110] The segment of air filtration comprises the *building industry*, the *transportation sector*, *industrial processes*, *personal protection*, *vacuum cleaner bags*, and *special applications*. Filtration in the *building industry* has to ensure the quality of indoor air in households,[111] for instance in air conditioning systems[112] or fume hoods in the kitchen.[113] In the *transportation sector* a significant amount of filters is required in the automotive industry.[114] For instance, in each car more than 20 filters and separators are implemented ranging from diesel soot filters to cabin air filters.[115] In *industrial processes* such as power generation and mining, filters are also crucial.[116] A lot of efforts have been made for *personal protection* filters for instance in breathing protection[117] or protective clothing against contaminants in industrial processes or biological and chemical warfare.[118] The field of v*acuum cleaner bags* is an example for filters in daily life.[119] Furthermore, there are highly *specialized sectors* such as microchip and pharmaceutical industry, which demand for a very low particulate concentration in air. In microchip industry during production of electronic devices particulate matter can cause severe damages or malfunctions of the device. Similarly, in the pharmaceutical sector in which filters are mainly used to reduce germs or bacteria in air.[120]

The liquid filtration segment is divided into the *liquid cartridge*, *transportation*, *machining and metalworking*, and *food* sector.[110] Filter processes in the chemical and pharmaceutical industry are located in the *liquid cartridge* sector.[121] Besides the applications of air filters in the *transportation* sector (automobile industry or in the aviation), the filtration of liquids such as oil, fuel or hydraulic fluids is important to

improve life-time.[122] While m*achining and metal working* processes need particulate-free coolants, also the *food* sector, with the dairy,[123] brewery[124] and nutritional oil industry[125] requires filtration steps for product purification or waste water filtration. The coffee filter is probably the most known example in the food sector.
The broad field of filter applications is expected to grow in the next years because of issues such as fine dust and new tasks in environmental protection. Therefore, new filter media with improved properties are required. In the following general remarks, theoretical considerations concerning air filtration are addressed in detail.

An aerosol is a binary mixture consisting of solid particles or liquid droplets in a gas phase.[126] The suspended particles are called aerosol particles. These aerosol particles can cover all sizes ranging from the nano- to the macro-scale. Figure 10 shows the sizes of the different contaminants in air, categorized in natural and artificial origins. In contrast to natural contaminants, artificial airborne pollutants are created by mankind, especially since industrialization. Artificial pollutants, such as smog, diesel soot, carbon black, and tobacco smoke are predominant in the nanometer scale. Aerosol particles in this size range are called respirable dust and are accumulated in the human lung and are suspected to cause several diseases.[127] Thus, these contaminants represent the most dangerous form of aerosols. The steadily increasing amount of artificial pollutants and demands to clean air is the driving force to develop improved filter media with high filtration efficiency.

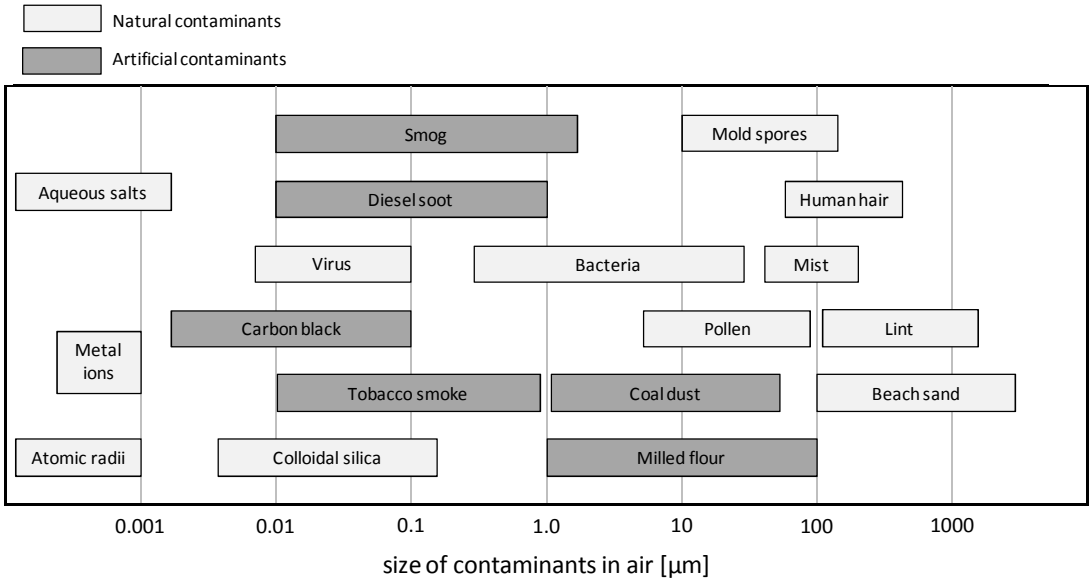

Figure 10. The size range of airborne contaminants. Natural origin contaminants are colored light gray, artificial generated contaminants dark gray. Adopted from reference [10].

1.3.1 Filtration mechanisms and theory

According to Sutherland and Purchas[128] there are four different filtration types: *surface straining*, *depth straining*, *cake filtration* and *depth filtration*. Depending on the filter architecture a mixture of all can be involved in the filtration process. Typically, one of the four types is predominant.

Surface straining is the separation of aerosol particles by size exclusion on the surface of woven meshes with uniform pore size. Only aerosol particles whose dimensions are larger than the pore size are filtered off, particles with smaller sizes penetrate through the filter. Typically, the filters consist of membranes or woven fabrics.[10]

Depth straining exists in filters whose pores are getting progressively smaller from top to bottom. An aerosol particle with particular size is penetrating through the filter as long as its size is smaller compared to the pore size. Within the filter, the pore size is getting smaller than the particle size, thus, the aerosol particle is separated. These two filtration types are based on sieving effects. The filters are based on felts or nonwovens with large fiber diameter compared to the voids. Several definitions are existing, describing the term nonwoven fabric. However, one of the most appropriate definitions has its origin in the Man-Made Fiber and Textile Dictionary,[129] whose authors describe a nonwoven fabric as "an assembly of textile fibers held together by mechanical interlocking in a random web or mat, by fusing of the fibers (in the case of thermoplastic fibers), or by bonding with cementing medium such as […] glue".[10]

In *cake filtration* (or *surface filtration*), the particle separation occurs on or near the surface of the filter. At the beginning of the filtration process a filter cake composed of aerosol particles is developed on top of a filter due to its specific architecture. The filter itself can be regarded as support and the filtration of aerosols is mainly performed by the filter cake. Thus, clogging occurs so that the differential pressure of a filter is progressively increasing. After a certain time interval a threshold value in the throughput is reached and the filter has to be cleaned from the filter cake. Generally, this is achieved by a reverse air pulse.[105] This kind of filter media is typically based on surface modified needle felts.

The fourth filtration type is the *depth filtration*. In contrast to depth straining, aerosols in the depth filtration are also filtered when their particle sizes are smaller than the pores of the filter. The filtration of particles is attributed to three different filtration mechanisms if electrostatic interactions are excluded (Figure 11).

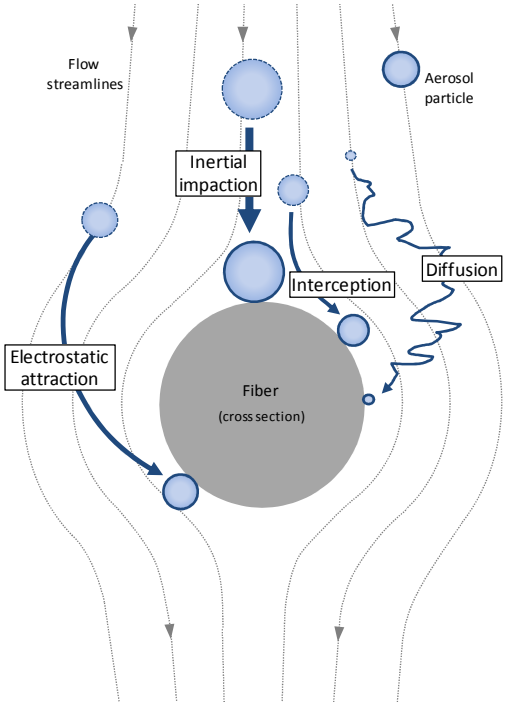

Figure 11. Illustration of depth filtration mechanisms depending on particle sizes and electrostatic effects represented at a fiber cross section with flow streamlines around. Adopted from reference [10].

Depending on their particle size, contaminants can be captured by various mechanisms in depth filtration, namely *inertial impaction*, *interception*, and *diffusion*.[130] Because of their inertia large aerosols are not able to follow the airstream, which flows around the fiber of the filter. Therefore, these particles hit the fiber and thus are deposited on the surface by *inertial impaction*. This filtration mechanism is predominant for aerosol particles of sizes between 0.5 µm and 5 µm. In contrast, *Brownian diffusion* is the predominant filtration mechanism for small aerosol particles (smaller than 0.1 µm[131] or 0.5 µm[10]). Because of this random "zig zag"-motion, the probability of the aerosol particle to contact the fiber and being filtered is drastically increased. Contaminants, which are too small to be filtered by inertia and which are too large to be deposited by the Brownian diffusion follow the air streamlines around a fiber. If the aerosols pass the fiber surface within a distance equal or less of their radii, the particles are captured by the fiber. This mechanism is called *interception*. The probability of particle deposition by interception decreases with decreasing particle diameter. The filtration efficiency of a fibrous material (based on depth filtration) over all particle sizes is the sum of all filtration mechanisms. This is shown in Figure 12 for diffusion and interception as well as inertial impaction. For a typical nonwoven filter the overall filtration efficiency feature a minimum which is located between 0.1 µm to 0.5 µm. This minimum is called most penetrating particle size (MPPS).[132] The location of the MPPS and the amount of particles which penetrate the filter at the MPPS depend on

the nature of the filter, the fiber diameter, the kind of aerosol and the filtration conditions.

Furthermore, a special but efficient mechanism in depth filtration is based on *electrostatic attraction*. Here, the electric or electrostatic charge of the aerosol particles leads to an attraction to the fiber. This mechanism is exploited in electret filters.[8,26]

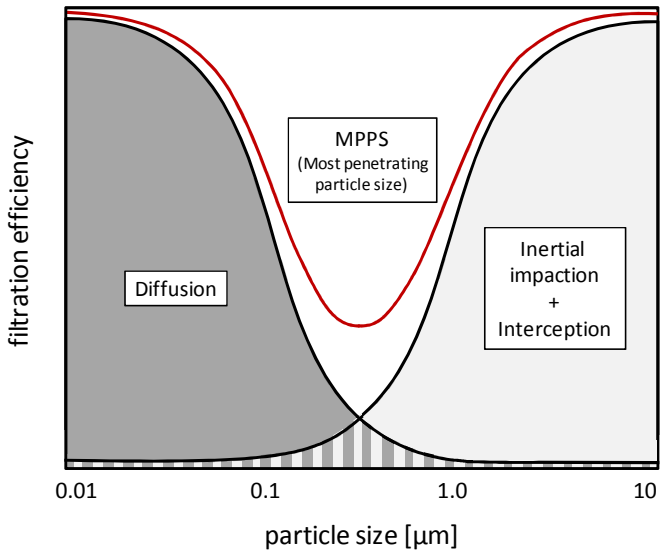

Figure 12. Schematic representation of the filtration efficiency of different filtration mechanisms. The sum of the individual efficiencies yields the overall filtration efficiency of a filter (red). This efficiency typically features a minimum, called most penetrating particle size (MPPS).

To overcome the challenge of low filtration efficiencies for aerosol particles in the range of 0.1 µm – 0.5 µm (MPPS region) many efforts have been made. Nowadays the most promising attempts are filters which are modified with *nanofibers*.[133,134] There are basically two beneficial reasons for nanofiber utilization: a) the *increase of filtration efficiency* and b) the *reduction of the differential pressure*. Theoretical calculations on the benefit of nanofibers in filtration were investigated by Stechina and Pich, who confirmed the expected positive effect.[135]

The first benefit of nanofibers can be explained by their surface-to-volume-ratio. Due to the facts, that the surface area of a fiber scales inversely with its diameter and that the volume of a fiber decreases inversely proportional to the square of the diameter, the resulting surface-to-volume-ratio increases with decreasing fiber diameter. This additional surface area is also available for aerosol particle removal.[11,136] As consequence, the use of nanofibers provides an improvement: shifting the MPPS to smaller particle sizes while simultaneously leading to *enhanced filtration efficiencies* for all particle sizes.[137]

A second effect is the *reduction in differential pressure* if nanofibers are used. This is attributed to the *slip-flow effect* at the fiber surface (Figure 13). In the case of microfibers, the flow velocity on the surface of the fiber is zero (defined as non slip-flow).[138] However, at fibers possessing diameters below 500 nm, this changes to slip flow conditions. Hence, the airstream at the nanofiber surface is non-zero. That means that a larger amount of air penetrates in the same time interval around a nanofiber compared to a microfiber and thus the air drag of a nanofiber is smaller, resulting in a lower differential pressure.[139]

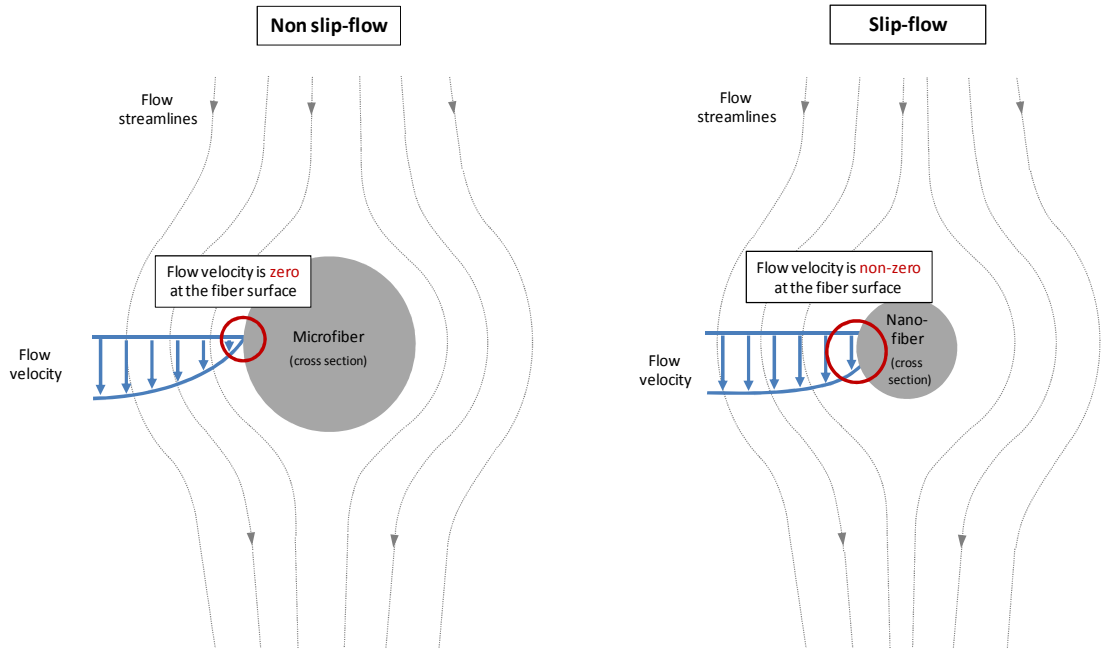

Figure 13. Schematic representation of non slip-flow conditions at a microfiber (left) and slip-flow conditions at a nanofiber (right).

The filtration efficiency and the differential pressure are important parameters particular in view of the quality of a filter. In Figure 14, a typical air filtration procedure is illustrated. In this process, a defined amount of aerosol particles is applied to a filter by an airstream (upstream side). Some of the particles are captured at the filter, others are penetrating through (downstream side).

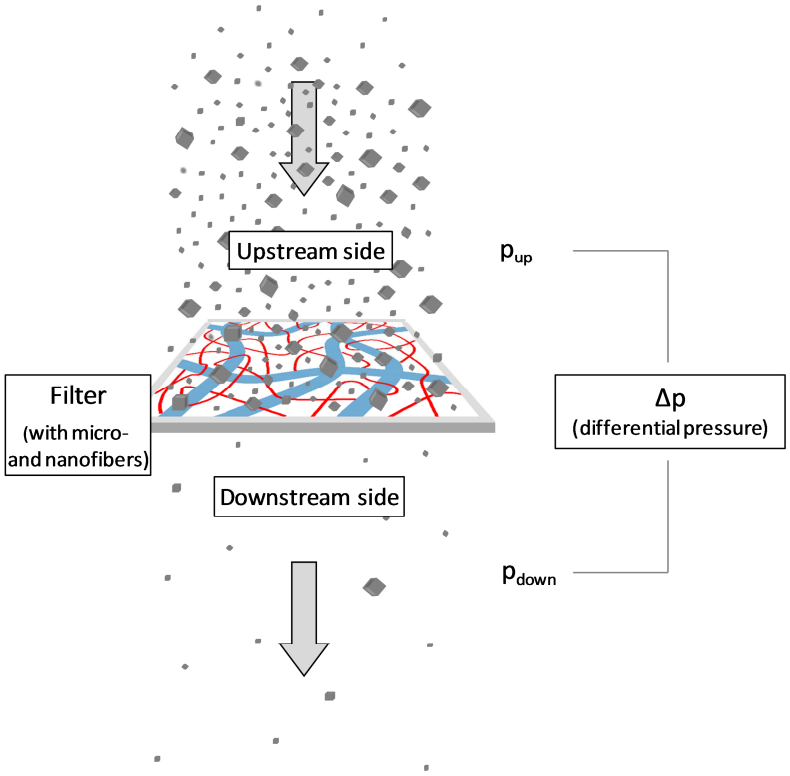

Figure 14. Schematic filtration process of aerosol particles.

In order to quantify the quality of different filters, two parameters have to be measured in those tests, in particularly the *filtration efficiency* and the *differential pressure*.

The filtration efficiency is defined as

$$\mathrm{FE}\ [\%]\ (\mathrm{x}) = \frac{\mathrm{c_{up}(x)} - \mathrm{c_{down}(x)}}{\mathrm{c_{up}(x)}} \cdot 100$$

, with

FE = filtration efficiency,
c_{up} = upstream aerosol particle concentration,
c_{down} = downstream aerosol particle concentration,
x = aerosol particle size.

Because filters separate aerosol particles of various sizes with distinct quality, the filtration efficiency is dependent on the aerosol particle size. A properly designed filter has to assure high efficiency of the removal of aerosol particles of any size.[132]

The differential pressure is defined as

$$\Delta p\ [Pa] = \mathrm{p_{up}} - \mathrm{p_{down}}$$

, with

Δp = differential pressure,
p_{up} = pressure at the upstream side,
p_{down} = pressure at the downstream side of the filter.

The differential pressure originates from the air drag of a filter and implies its throughput quality. The smaller the differential pressure, the lower are the processing and energy costs during the filtration process.

Thus, an "ideal filter" has a filtration efficiency of 100 % for all particle sizes, a differential pressure of 0 Pa, lasts forever, is infinitively small, and doesn't cost anything. In reality this is not realizable. An enhancement in filtration efficiency is typically accompanied by an increase in differential pressure. Therefore, compromises have to be made, which are localized either at the side of high filtration efficiency or at the side of low differential pressure depending on the preference of the application.[10]

The quality of a filter can be determined by means of the quality factor, which is defined as

$$QF = \frac{-\ln(1 - FE)}{\Delta p}$$

, with
QF = quality factor,
FE = filtration efficiency,
Δp = differential pressure.

A filter with enhanced filtration efficiency and/or lower differential pressure possesses a higher quality factor, meaning that the overall quality is improved compared to other filters.[133]

1.3.2 Filter classification and test standards

Depending on their filtration efficiency, commercial air filters are divided into several classes. Filters with very low average efficiency are called *Coarse Filters* and are accordingly divided into the classes G1-G4. Air filters with higher filtration efficiency are defined as *Medium Filters* M5-M6 and *Fine Filters* F7-F9, classified corresponding to their filtration efficiency at 0.4 µm particle size. The most efficient air filters are *HEPA* (High-Efficiency Particulate Air) and *ULPA* (Ultra-Low Penetration Air) filters, which can also be divided into several sub-classes (Table 1). These filters are classified according to their overall average filtration efficiency as well as to their minimum filtration efficiency (MPPS). The particle size range, where the MPPS is located varies for several filters, thus the local filtration efficiency value of each HEPA and ULPA filter is determined at its "personal" minimum.

Originally, HEPA filters were developed for military gas masks to protect mankind from toxic smokes of chemical and biological warfare. The first filters consist of asbestos fibers, developed in Germany. During World War II, the United States developed these filters further. Since then, US military standards were the world wide filter guideline. This changed as HEPA filters found more and more use in non-military applications, such as clean rooms in electronics industry and in hospital operating rooms. Meanwhile, HEPA filters are built of glass microfibers and found their way into "daily life applications" for protection against allergens and harmful microbes in the automobile industry and office buildings. Nowadays, HEPA filters are even implemented in vacuum cleaners.[10]

Table 1. Filter classification of HEPA and ULPA filters. Adopted from reference [10].

Filter class	Overall filtration efficiency [%]	Local filtration efficiency (at MPPS) [%]
H10	85	
H11	95	
H12	99.5	
H13	99.95	99.75
H14	99.995	99.975
U15	99.9995	99.9975
U16	99.99995	99.99975
U17	99.999995	99.999975

Commercial air filters have to be tested subject to different standards. The International Organization for Standardization defines the ISO norms, which are internationally valid. European standards (EN norms) are defined by the European Committee for Standardization and the "Deutsches Institut für Normung" is responsible for German DIN standards. In the United States several organizations define filtration standards. One of them is the ASHRAE (American Society of Heating, Refrigerating and Air-Conditioning Engineers). Among hundreds of different norms, some of the most important air filtration standards are ISO 5011, ISO/TS 11155-1, EN 1822, EN 779, and ASHRAE 52.2, including different fields of industrial applications and their specific test requirements.

The type of *aerosol* is also embedded in the standards, because of the variation of the filtration efficiency depending on the used aerosol. While the test aerosol *Iso fine dust* (Arizona road dust) is used in ISO 5011 (Inlet air cleaning equipment for internal combustion engines and compressors) and ISO/TS 11155-1 (Road vehicles - Air filters for passenger compartments), *DEHS* (diethylhexylsebacate) is taken as aerosol particles in the EN 1822 standard for HEPA and ULPA filters. EN 779 (Particulate air filters for general ventilation) and ASHRAE 52.2 (Method of Testing General Ventilation Air-Cleaning Devices for Removal Efficiency by Particle Size) are the European and American standards for air filters in general ventilation systems, respectively. According to both standards, the tested filter is loaded with *ASHRAE test dust* composed of Iso fine dust, carbon black, and cotton linters. The filtration efficiency of such a loaded filter is afterwards tested with *potassium chloride*.

The downside of these complex standardization systems is that each filter supplier is allowed to test their filters at different standards and therefore the comparability of various filters is getting lost in many cases.[10]

1.3.3 Supramolecular chemistry in combination with a support in view of filtration applications

In contrast to the top-down approaches mentioned above, existing nonwoven fabrics can further be modified with supramolecular nanofibers by a bottom-up approach. However, in literature very less is known about this in view of filtration applications. One of the few research groups, which is working in this research field is using fluorinated urea and amide gelators to modify surfaces of nonwoven polymer fabrics. In the porous supports the organic molecules self-assemble to supramolecular nanofibers to increase the surface roughness as well as to provide improved water- and oil-repellence.[140] Further investigations of this group also disclose the potential usage of these composite materials as filters for gaseous and liquid media. Thereby, the authors mentioned their gelation based preparation, but they do not present any example of filter test according to their stability and filtration efficiency.[141] Another research group shows by means of a three weeks lasting immersion process of aluminium coated meshes in alkylphosphonic acids that self-assembled nanofiber networks which cover pores of 4 µm diameter can be created.[142] Furthermore, in literature it was reported about a supramolecular glycol-lipid hydrogel which is strong enough to entrap polymer nano beads in its three-dimensional nanofiber network.[143] Recently, Krieg et al. reported on a supramolecular organogel, which was deposited on top of a scaffold to obtain an ultrafiltration membrane.[144] Upon the prerequisite of a never dehydrated supramolecular specimen, this kind of filter is suitable to separate gold nanoparticles from an aqueous solution.

However, up to now supramolecular solutions for air filtration applications were not reported. This issue is an objective in this thesis to efficiently modify polymer filters with inexpensive supramolecular nanofibers.

1.4 Objective of this thesis

The objective of this thesis is the investigation of supramolecular nanofibers, particularly their preparation, structure-property relations and applications. Herein, four different issues concerning supramolecular nanofibers are pursued:

The first part of this thesis targets the investigation of the *influence of hydrogen bonding as well as sterical demanding substituents on the π-stacking of pyrene-containing small molecules* in different states of matter. A set of pyrene substituted monoamides and monoesters have to be synthesized and their self-assembly behavior have to be characterized by different methods, such as fluorescence spectroscopy, temperature-dependent FT-IR investigations, dynamic light scattering (DLS) and polarization optical microscopy (POM). In order to get a more detailed insight into the aggregation behavior, further physical investigations and theoretical calculations have to be performed in cooperation with Prof. Dr. Anna Köhler and Prof. Dr. Rodrigo Q. Albuquerque.

The second part of this thesis is concerned with fundamental *investigations of two self-assembly processing pathways*, the self-assembly upon cooling at constant concentration and the self-assembly during solvent evaporation at constant temperature. In order to tailor the supramolecular nanofiber morphology of 1,3,5-benzenetrisamides (BTAs) detailed structure-property relations have to be established. For this purpose, the influence of the molecular structure and of external parameters such as concentration, temperature, and solvent have to be examined and understood.

The third part of this thesis aims for an *application of supramolecular nanofibers in air filtration*. In this field the materials of choice recently changed from micro- to nanofibers because of quality aspects. However, an adequate process how to efficiently incorporate nanofibers inside existing nonwoven filters is not available up to now. Herein, this issue is addressed by means of supramolecular chemistry. A simple, solution-based immersion process in which supramolecular nanofiber webs are formed in-situ in nonwoven scaffolds have to be developed. In order to proof the applicability of supramolecular nanofibers in air filtration processes, first filtration tests have to be performed.

The fourth part of this thesis is based on the promising results of the previous chapter. Here, the focus is set on the establishment of several *structure-property relations in order to optimize the surface area, the mechanical as well as the thermal stability, and the overall filter quality*. For this purpose, variations of the molecular structure, the solvent, the concentration, the kind of aerosol, and the filter setup have to be investigated.

1.5 References

[1] a) J. Ramsden, *Nanotechnology: An introduction*, William Andrew; Elsevier Science, Norwich, N.Y, Oxford **2011**. b) H. S. Nalwa, R. E. Smalley, *Encyclopedia of nanoscience and nanotechnology*, American Scientific Publishers, Stevenson Ranch, California, **2004**. c) C. Milburn, *Nanovision: Engineering the future*, Duke University Press, Durham **2008**. d) E. Regis, *Nano!*, Bantam Books, Toronto **1997**.

[2] J. E. McIntyre, *Synthetic fibres: Nylon, polyester, acrylic, polyolefin*, Woodhead Publishing Limited, Cambridge **2004**.

[3] a) T. Nakajima, K. Kajiwara, J. E. McIntyre, *Advanced fiber spinning technology*, Woodhead, Cambridge, **1994**. b) H. J. Koslowski, *Dictionary of man-made fibers: Terms - figures - statistics*, Dt. Fachverl., Frankfurt, **2010**.

[4] L. S. Pinchuk, *Melt blowing: Equipment, technology, and polymer fibrous materials*, Springer, Berlin; New York **2002**.

[5] Y. Lee, L. C. Wadsworth, *Structure and filtration properties of melt blown polypropylene webs*, *Polym. Eng. Sci.* **1990**, *30*, 1413.

[6] a) J. H. Wendorff, S. Agarwal, A. Greiner, *Electrospinning: Materials, processing, and applications*, John Wiley & Sons, Weinheim; Hoboken, N.J. **2012**. b) Y. Dzenis, *Material Science: Spinning Continuous Fibers for Nanotechnology*, *Science* **2004**, *304*, 1917.

[7] A. Greiner, J. H. Wendorff, *Electrospinning: A Fascinating Method for the Preparation of Ultrathin Fibers*, *Angew. Chem., Int. Ed.* **2007**, *46*, 5670.

[8] C.-S. Wang, *Electrostatic forces in fibrous filters—a review*, *Powder Technology* **2001**, *118*, 166.

[9] T. Grafe, K. Graham, *Polymeric nanofibers and nanofiber webs: a new class of nonwovens*, *Int. Nonwovens J.* **2003**, 51.

[10] I. M. Hutten, *Handbook of nonwoven filter media*, Butterworth-Heinemann, Oxford; Burlington, MA **2007**.

[11] C. J. Ellison, A. Phatak, D. W. Giles, C. W. Macosko, F. S. Bates, *Melt blown nanofibers: Fiber diameter distributions and onset of fiber breakup*, *Polymer* **2007**, *48*, 3306.

[12] V. A. Wente, E. L. F. Boone, *Manufacture of superfine organic fibers*, *Naval Research Laboratory* **1954**, 1.

[13] W. Rupertseder, T. Ertl, *Innovative Filtermedien durch integrierte Nanofasern*, http://www.irema.de/docs/Artikel-Zeitung-deutsch.pdf. Accessed 26 January 2013.

[14] C. Huang, S. Chen, C. Lai, D. H. Reneker, H. Qiu, Y. Ye, H. Hou, *Electrospun polymer nanofibres with small diameters*, *Nanotechnology* **2006**, *17*, 1558.

[15] A. Formhals, *Process and apparatus for preparing artificial threads* US 1975504 **1934**.

[16] W. Simm, K. Gosling, R. Bonhart, B. von Falkai, *Filter made of electrostatically spun fibres* GB 1346231 **1974**.

[17] D. H. Reneker, I. Chun, *Nanometre diameter fibres of polymer, produced by electrospinning*, *Nanotechnology* **1996**, *7*, 216.

[18] T. Subbiah, G. S. Bhat, R. W. Tock, S. Parameswaran, S. S. Ramkumar, *Electrospinning of nanofibers*, *J. Appl. Polym. Sci.* **2005**, *96*, 557.

[19] N. Bhardwaj, S. C. Kundu, *Electrospinning: A fascinating fiber fabrication technique*, *Biotechnol. Adv.* **2010**, *28*, 325.

[20] D. W. Hutmacher, P. D. Dalton, *Melt Electrospinning*, *Chem. - Asian J.* **2011**, *6*, 44.

[21] L. Larrondo, R. St. John Manley, *Electrostatic fiber spinning from polymer melts. I. Experimental observations on fiber formation and properties*, *J. Polym. Sci. Polym. Phys. Ed.* **1981**, *19*, 909.

[22] P. D. Dalton, D. Grafahrend, K. Klinkhammer, D. Klee, M. Möller, *Electrospinning of polymer melts: Phenomenological observations*, *Polymer* **2007**, *48*, 6823.

[23] X. F. Wang, Z.-M. Huang, *Melt-electrospinning of PMMA*, *Chin. J. Polym. Sci.* **2010**, *1*.

[24] S. N. Malakhov, A. Y. Khomenko, S. I. Belousov, A. M. Prazdnichnyi, S. N. Chvalun, A. D. Shepelev, A. K. Budyka, *Method of manufacturing nonwovens by electrospinning from polymer melts*, *Fibre Chem.* **2009**, *41*, 355.

[25] M. G. Hajra, K. Mehta, G. G. Chase, *Effects of humidity, temperature, and nanofibers on drop coalescence in glass fiber media*, *Sep. Purif. Technol.* **2003**, *30*, 79.

[26] P. P. Tsai, H. Schreuder-Gibson, P. Gibson, *Different electrostatic methods for making electret filters*, *Selected Papers from the 28th Annual Conference of the Electrostatics Society of America* **2002**, *54*, 333.

[27] Y. M. Shin, M. M. Hohman, M. P. Brenner, G. C. Rutledge, *Experimental characterization of electrospinning: the electrically forced jet and instabilities*, *Polymer* **2001**, *42*, 9955.

[28] S. Megelski, J. S. Stephens, D. B. Chase, J. F. Rabolt, *Micro- and Nanostructured Surface Morphology on Electrospun Polymer Fibers*, *Macromolecules* **2002**, *35*, 8456.

[29] W.-J. Li, C. T. Laurencin, E. J. Caterson, R. S. Tuan, F. K. Ko, *Electrospun nanofibrous structure: a novel scaffold for tissue engineering*, *J. Biomed. Mater. Res.* **2002**, *60*, 613.

[30] R. S. Barhate, S. Ramakrishna, *Nanofibrous filtering media: Filtration problems and solutions from tiny materials*, *J. Membr. Sci.* **2007**, *296*, 1.

[31] a) W. E. Teo, S. Ramakrishna, *A review on electrospinning design and nanofibre assemblies*, *Nanotechnology* **2006**, *17*, R89. b) S. A. Sell, M. J. McClure, K. Garg, P. S. Wolfe, G. L. Bowlin, *Electrospinning of collagen/biopolymers for regenerative medicine and cardiovascular tissue engineering*, *Nanofibers in Regenerative Medicine and Drug Delivery* **2009**, *61*, 1007. c) M. Bognitzki, W. Czado, T. Frese, A. Schaper, M. Hellwig, M. Steinhart, A. Greiner, J. H. Wendorff, *Nanostructured Fibers via Electrospinning*, *Adv. Mater.* **2001**, *13*, 70. d) S. Agarwal, J. H. Wendorff, A. Greiner, *Progress in the Field of Electrospinning for Tissue Engineering Applications*, *Adv. Mater.* **2009**, *21*, 3343.

[32] A. Holzmeister, M. Rudisile, A. Greiner, J. H. Wendorff, *Structurally and chemically heterogeneous nanofibrous nonwovens via electrospinning*, *Eur. Polym. J.* **2007**, *43*, 4859.

[33] J.-M. Lehn, *Supramolecular Chemistry - Scope and Perspectives Molecules, Supermolecules, and Molecular Devices (Nobel Lecture)*, *Angew. Chem., Int. Ed.* **1988**, *27*, 89.

[34] J. M. Lehn, *Supramolecular chemistry*, *Science* **1993**, *260*, 1762.

[35] J. W. Steed, J. L. Atwood, *Supramolecular chemistry*, Wiley, Chichester, UK **2009**.

[36] T. Fenske, H.-G. Korth, A. Mohr, C. Schmuck, *Advances in Switchable Supramolecular Nanoassemblies*, *Chem. - Eur. J.* **2012**, *18*, 738.

[37] a) D. L. Helseth, A. Veis, *Collagen self-assembly in vitro. Differentiating specific telopeptide-dependent interactions using selective enzyme modification and the addition of free amino telopeptide*, *J. Biol. Chem.* **1981**, *256*, 7118. b) A. Gautieri, S. Vesentini, A. Redaelli, M. J. Buehler, *Hierarchical Structure and Nanomechanics of Collagen Microfibrils from the Atomistic Scale Up*, *Nano Lett.* **2011**, *11*, 757. c) J. Luo, Y. W. Tong, *Self-Assembly of Collagen-Mimetic Peptide Amphiphiles into Biofunctional Nanofiber*, *ACS Nano* **2011**, *5*, 7739.

[38] A. Gautieri, S. Vesentini, A. Redaelli, M. J. Buehler, *Hierarchical nanomechanics of collagen microfibrils*, Nature Proceedings **2010**.

[39] M. C. Jarvis, *Self-assembly of plant cell walls*, *Plant, Cell and Environement* **1992**, 1.

[40] L. C. Palmer, S. I. Stupp, *Molecular Self-Assembly into One-Dimensional Nanostructures*, *Acc. Chem. Res.* **2008**, *41*, 1674.

[41] K. G. Libbrecht, *The physics of snow crystals*, *Rep. Prog. Phys.* **2005**, *68*, 855.

[42] a) J.-M. Lehn, *Supramolecular chemistry: Concepts and perspectives*, VCH, Weinheim; New York **1995**. b) K. E. Geckeler, *Advanced macromolecular and supramolecular materials and processes*, Kluwer Academic/Plenum Publishers, New York **2003**. c) T. Shimizu (Ed.), *Self-Assembled Nanomaterials I*, Springer Berlin Heidelberg **2008**.

[43] J. M. Lehn, *Perspectives in supramolecular chemistry: from molecular recognition to molecular information processing and self organization*, *Angew. Chem.* **1990**, *102*, 1347-62 (See also Angew. Chem., Int. Ed. Engl., 1990, 29(11), 1304-19).

[44] J. F. Folmer-Andersen, J.-M. Lehn, *Thermoresponsive Dynamers: Thermally Induced, Reversible Chain Elongation of Amphiphilic Poly(acylhydrazones)*, *J. Am. Chem. Soc* **2011**, *133*, 10966.

[45] T. F. A. de Greef, M. M. J. Smulders, M. Wolffs, A. P. H. J. Schenning, R. P. Sijbesma, E. W. Meijer, *Supramolecular Polymerization*, *Chem. Rev.* **2009**, *109*, 5687.

[46] G. M. Whitesides, B. Grzybowski, *Self-Assembly at All Scales*, *Science* **2002**, *295*, 2418.

[47] a) J.-M. Lehn, in *Alkali Metal Complexes with Organic Ligands*, Vol. 16, Springer Berlin Heidelberg **1973**, 1-69. b) C. J. Pedersen, H. K. Frensdorff, *Makrocyclische Polyäther und ihre Komplexe*, *Angew. Chem.* **1972**, *84*, 16. c) D. J. Cram, J. M. Cram, *Host-Guest Chemistry: Complexes between organic compounds simulate the substrate selectivity of enzymes*, *Science* **1974**, *183*, 803.

[48] a) N. Mohmeyer, H. W. Schmidt, *A new class of low-molecular-weight amphiphilic gelators*, *Chem. - Eur. J.* **2005**, *11*, 863. b) N. Mohmeyer, H.-W. Schmidt, *Synthesis and Structure–Property Relationships of Amphiphilic Organogelators*, *Chem. - Eur. J.* **2007**, *13*, 4499.

[49] a) Y. Kuang, Y. Gao, J. Shi, H.-C. Lin, B. Xu, *Supramolecular hydrogels based on the epitope of potassium ion channels*, *Chem. Commun.* **2011**, *47*, 8772. b) R. G. Weiss, P. Terech, *Molecular gels: Materials with self-assembled fibrillar networks*, Springer, Dordrecht **2006**.

[50] a) H. Ihara, M. Takafuji, T. Sakurai, *Self-Assembled Nanofibers*, *Encyclopedia of Nanoscience and Nanotechnology* **2004**, *9*, 473. b) N. Kimizuka, in *Self-Assembled Nanomaterials I*, Vol. 219 (Ed.: T. Shimizu), Springer Berlin Heidelberg **2008**, 1-26.

[51] S. R. Bull, M. O. Guler, R. E. Bras, T. J. Meade, S. I. Stupp, *Self-Assembled Peptide Amphiphile Nanofibers Conjugated to MRI Contrast Agents*, *Nano Lett.* **2004**, *5*, 1.

[52] H. Wang, J. Wei, C. Yang, H. Zhao, D. Li, Z. Yin, Z. Yang, *The inhibition of tumor growth and metastasis by self-assembled nanofibers of taxol*, *Biomaterials* **2012**, *33*, 5848.

[53] Y. Wang, L. Cao, S. Guan, G. Shi, Q. Luo, L. Miao, I. Thistlethwaite, Z. Huang, J. Xu, J. Liu, *Silver mineralization on self-assembled peptide nanofibers for long term antimicrobial effect*, *J. Mater. Chem.* **2012**, *22*, 2575.

[54] L. Hsu, G. L. Cvetanovich, S. I. Stupp, *Peptide Amphiphile Nanofibers with Conjugated Polydiacetylene Backbones in Their Core*, *J. Am. Chem. Soc.* **2008**, *130*, 3892.

[55] D. A. Stone, L. Hsu, N. R. Wheeler, E. Wilusz, W. Zukas, G. E. Wnek, L. T. J. Korley, *Mechanical enhancement via self-assembled nanostructures in polymer nanocomposites*, *Soft Matter* **2011**, *7*, 2449.

[56] M. A. Greenfield, J. R. Hoffman, M. de La Olvera Cruz, S. I. Stupp, *Tunable Mechanics of Peptide Nanofiber Gels*, *Langmuir* **2009**, *26*, 3641.

[57] S. Yagai, T. Karatsu, A. Kitamura, *Melamine-Barbiturate/Cyanurate Binary Organogels Possessing Rigid Azobenzene-Tether Moiety*, *Langmuir* **2005**, *21*, 11048.

[58] a) T. Steiner, *The Hydrogen Bond in the Solid State*, *Angew. Chem., Int. Ed.* **2002**, *41*, 48. b) R. P. Sijbesma, F. H. Beijer, L. Brunsveld, B. J. B. Folmer, J. H. K. K. Hirschberg, R. F. M. Lange, J. K. L. Lowe, E. W. Meijer, *Reversible Polymers Formed from Self-Complementary Monomers Using Quadruple Hydrogen Bonding*, *Science* **1997**, *278*, 1601. c) L. J. Prins, D. N. Reinhoudt, P. Timmerman, *Noncovalent Synthesis Using Hydrogen Bonding*, *Angew. Chem., Int. Ed.* **2001**, *40*, 2382.

[59] a) A. Ciesielski, A. R. Stefankiewicz, F. Hanke, M. Persson, J.-M. Lehn, P. Samorì, *Rigid Dimers Formed through Strong Interdigitated H-Bonds Yield Compact 1D Supramolecular Helical Polymers*, *Small* **2011**, *7*, 342. b) F. H. Beijer, H. Kooijman, A. L. Spek, R. P. Sijbesma, E. W. Meijer, *Self-Complementarity Achieved through Quadruple Hydrogen Bonding*, *Angew. Chem., Int. Ed.* **1998**, *37*, 75. c) X. Zhao, Y. L. Chang, F. W. Fowler, J. W. Lauher, *An approach to the design of molecular solids. The ureylene dicarboxylic acids*, *J. Am. Chem. Soc.* **1990**, *112*, 6627.

[60] R. P. Sijbesma, E. W. Meijer, *Quadruple hydrogen bonded systems*, *Chem. Commun.* **2003**, 5.

[61] K. Hunger, *Industrial dyes: chemistry, properties, applications*, Wiley-VCH **2003**.

[62] L. Brunsveld, B. J. B. Folmer, E. W. Meijer, R. P. Sijbesma, *Supramolecular Polymers*, *Chem. Rev.* **2001**, *101*, 4071.

[63] B. Song, H. Wei, Z. Wang, X. Zhang, M. Smet, W. Dehaen, *Supramolecular Nanofibers by Self-Organization of Bola-amphiphiles through a Combination of Hydrogen Bonding and π–π Stacking Interactions*, *Adv. Mater.* **2007**, *19*, 416.

[64] A. Rochefort, É. Bayard, S. Hadj-Messaoud, *Competitive Hydrogen Bonding in π-Stacked Oligomers*, *Adv. Mater.* **2007**, *19*, 1992.

[65] D. González-Rodríguez, A. P. H. J. Schenning, *Hydrogen-bonded Supramolecular π-Functional Materials*, *Chem. Mater.* **2011**, *23*, 310.

[66] I. Paraschiv, M. Giesbers, B. van Lagen, F. C. Grozema, R. D. Abellon, L. D. A. Siebbeles, A. T. M. Marcelis, H. Zuilhof, E. J. R. Sudhölter, *H-Bond-Stabilized Triphenylene-Based Columnar Discotic Liquid Crystals*, *Chem. Mater.* **2006**, *18*, 968.

[67] J. J. van Gorp, J. A. J. M. Vekemans, E. W. Meijer, *C3-Symmetrical Supramolecular Architectures: Fibers and Organic Gels from Discotic Trisamides and Trisureas*, *J. Am. Chem. Soc.* **2002**, *124*, 14759.

[68] T. Metzroth, A. Hoffmann, R. Martín-Rapún, M. M. J. Smulders, K. Pieterse, A. R. A. Palmans, J. A. J. M. Vekemans, E. W. Meijer, H. W. Spiess, J. Gauss, *Unravelling the fine structure of stacked bipyridine diamine-derived C3-discotics as determined by X-ray diffraction, quantum-chemical calculations, Fast-MAS NMR and CD spectroscopy*, *Chem. Sci.* **2010**, *2*, 69.

[69] S. Cantekin, T. F. A. de Greef, A. R. A. Palmans, *Benzene-1,3,5-tricarboxamide: a versatile ordering moiety for supramolecular chemistry*, *Chem. Soc. Rev.* **2012**, *41*, 6125.

[70] M. P. Lightfoot, F. S. Mair, R. G. Pritchard, J. E. Warren, *New supramolecular packing motifs: p-stacked rods encased in triply-helical hydrogen bonded amide strands*, *Chem. Commun.* **1999**, 1945.

[71] M. Kristiansen, P. Smith, H. Chanzy, C. Baerlocher, V. Gramlich, L. McCusker, T. Weber, P. Pattison, M. Blomenhofer, H.-W. Schmidt, *Structural Aspects of 1,3,5-Benzenetrisamides−A New Family of Nucleating Agents*, *Cryst. Growth Des.* **2009**, *9*, 2556.

[72] H. Cao, P. Duan, X. Zhu, J. Jiang, M. Liu, *Self-Assembled Organic Nanotubes through Instant Gelation and Universal Capacity for Guest Molecule Encapsulation*, *Chem. - Eur. J.* **2012**, *18*, 5546.

[73] a) R. C. T. Howe, A. P. Smalley, A. P. M. Guttenplan, M. W. R. Doggett, M. D. Eddleston, J. C. Tan, G. O. Lloyd, *A family of simple benzene 1,3,5-tricarboxamide (BTA) aromatic carboxylic acid hydrogels*, *Chem. Commun.* **2013**, DOI: 10.1039/C2CC37428E. b) A. Bernet, R. Q. Albuquerque, M. Behr, S. T. Hoffmann, H.-W. Schmidt, *Formation of a supramolecular chromophore: a spectroscopic and theoretical study*, *Soft Matter* **2012**, *8*, 66.

[74] A. Sakamoto, D. Ogata, T. Shikata, O. Urakawa, K. Hanabusa, *Large macro-dipoles generated in a supramolecular polymer of N,N′,N″-tris(3,7-dimethyloctyl)benzene-1,3,5-tricarboxamide in n-decane*, *Polymer* **2006**, *47*, 956.

[75] R. Q. Albuquerque, A. Timme, R. Kress, J. Senker, H.-W. Schmidt, *Theoretical Investigation of Macrodipoles in Supramolecular Columnar Stackings*, *Chem. - Eur. J.* **2013**, *19*, 1647.

[76] M. Schmidt, J. J. Wittmann, R. Kress, D. Schneider, S. Steuernagel, H.-W. Schmidt, J. Senker, *Crystal Structure of a Highly Efficient Clarifying Agent for Isotactic Polypropylene*, *Cryst. Growth Des.* **2012**, *12*, 2543.

[77] C. A. Jiménez, J. B. Belmar, L. Ortíz, P. Hidalgo, O. Fabelo, J. Pasán, C. Ruiz-Pérez, *Influence of the Aliphatic Wrapping in the Crystal Structure of Benzene Tricarboxamide Supramolecular Polymers*, *Cryst. Growth Des.* **2009**, *9*, 4987.

[78] L. Rajput, G. Mukherjee, K. Biradha, *Influence of Solvents in Assembling Tris(4-halophenyl)benzene-1,3,5-tricarboxamides: Interplay of N–H···O and Halogen···Halogen Interactions*, *Cryst. Growth Des.* **2012**, *12*, 5773.

[79] a) A. Timme, R. Kress, R. Q. Albuquerque, H.-W. Schmidt, *Phase Behavior and Mesophase Structures of 1,3,5-Benzene- and 1,3,5-Cyclohexanetricarboxamides: Towards an Understanding of the Losing Order at the Transition into the Isotropic Phase*, *Chem. - Eur. J.* **2012**, *18*, 8329. b) Y. Matsunaga, N. Miyajima, Y. Nakayasu, S. Sakai, M. Yonenaga, *Design of novel mesomorphic compounds: N,N',N''-trialkyl-1,3,5-benzenetricarboxamides*, *Bull. Chem. Soc. Jpn.* **1988**, 207. c) Y. Matsunaga, Y. Nakayasu, S. Sakai, M. Yonenaga, *Liquid Crystal Phases Exhibited by N,N',N"-Trialkyl-1,3,5-Benzenetricaboxamides*, *Mol. Cryst. Liq. Cryst.* **1986**, *141*, 327.

[80] P. J. M. Stals, J. F. Haveman, R. Martin-Rapun, C. F. C. Fitie, A. R. A. Palmans, E. W. Meijer, *The influence of oligo(ethylene glycol) side chains on the self-assembly of benzene-1,3,5-tricarboxamides in the solid state and in solution*, *J. Mater. Chem.* **2009**, *19*, 124.

[81] a) M. Blomenhofer, S. Ganzleben, D. Hanft, H.-W. Schmidt, M. Kristiansen, P. Smith, K. Stoll, D. Mader, K. Hoffmann, *"Designer" Nucleating Agents for Polypropylene*, *Macromolecules* **2005**, *38*, 3688. b) F. Abraham, S. Ganzleben, D. Hanft, P. Smith, H.-W. Schmidt, *Synthesis and Structure–Efficiency Relations of 1,3,5-Benzenetrisamides as Nucleating Agents and Clarifiers for Isotactic Poly(propylene)*, *Macromol. Chem. Phys.* **2010**, *211*, 171.

[82] F. Abraham, R. Kress, P. Smith, H.-W. Schmidt, *A New Class of Ultra-Efficient Supramolecular Nucleating Agents for Isotactic Polypropylene*, *Macromol. Chem. Phys.* **2013**, *214*, 17.

[83] F. Abraham, H.-W. Schmidt, *1,3,5-Benzenetrisamide based nucleating agents for poly(vinylidene fluoride)*, *Polymer* **2010**, *51*, 913.

[84] F. Richter, H.-W. Schmidt, *Supramolecular Nucleating Agents for Poly(butylene terephthalate) Based on 1,3,5-Benzenetrisamides*, *Macromol. Mater. Eng.* **2012**, DOI: 10.1002/mame.201200034.

[85] M. Stumpf, A. Spörrer, H.-W. Schmidt, V. Altstädt, *Influence of supramolecular additives on foam morphology of injection-molded iPP*, *J. Cell. Plast.* **2011**, *47*, 519.

[86] a) N. Mohmeyer, N. Behrendt, X. Zhang, P. Smith, V. Altstädt, G. M. Sessler, H.-W. Schmidt, *Additives to improve the electret properties of isotactic polypropylene*, *Polymer* **2007**, *48*, 1612. b) D. P. Erhard, D. Lovera, C. Salis-Soglio, R. Giesa, V. Altstädt, H.-W. Schmidt, in *Complex Macromolecular Systems II*, Vol. 228 (Eds.: A. H. E. Müller, H.-W. Schmidt), Springer Berlin Heidelberg **2010**, 155-207.

[87] a) D. Kluge, F. Abraham, S. Schmidt, H.-W. Schmidt, A. Fery, *Nanomechanical Properties of Supramolecular Self-Assembled Whiskers Determined by AFM Force Mapping*, *Langmuir* **2010**, *26*, 3020. b) D. Kluge, J. C. Singer, J. W. Neubauer, F. Abraham, H.-W. Schmidt, A. Fery, *Influence of the Molecular Structure and Morphology of Self-Assembled 1,3,5-Benzenetrisamide Nanofibers on their Mechanical Properties*, *Small* **2012**, *8*, 2563.

[88] a) Y. Yasuda, E. Iishi, H. Inada, Y. Shirota, *Novel Low-molecular-weight Organic Gels: N,N′,N″-Tristearyltrimesamide/Organic Solvent System*, *Chem. Lett.* **1996**, *25*, 575. b) I. Danila, F. Riobé, J. Puigmartí-Luis, Á. Pérez del Pino, J. D. Wallis, D. B. Amabilino, N. Avarvari, *Supramolecular electroactive organogel and conducting nanofibers with C3-symmetrical architectures*, *J. Mater. Chem.* **2009**, *19*, 4495.

[89] N. E. Shi, H. Dong, G. Yin, Z. Xu, S. H. Li, *A Smart Supramolecular Hydrogel Exhibiting pH-Modulated Viscoelastic Properties*, *Adv. Funct. Mater.* **2007**, *17*, 1837.

[90] J. C. Singer, R. Giesa, H.-W. Schmidt, *Shaping self-assembling small molecules into fibres by melt electrospinning*, *Soft Matter* **2012**, *8*, 9972.

[91] D. Kluge, J. C. Singer, B. R. Neugirg, J. W. Neubauer, H.-W. Schmidt, A. Fery, *Top–down meets bottom–up: A comparison of the mechanical properties of melt electrospun and self-assembled 1,3,5-benzenetrisamide fibers*, *Polymer* **2012**, *53*, 5754.

[92] S. Sankararaman, G. Venkataramana, B. Varghese, *Conformational Isomers from Rotation of Diacetylenic Bond in an Ethynylpyrene-Substituted Molecular Hinge*, *J. Org. Chem.* **2008**, *73*, 2404.

[93] a) M. Schwoerer, H. C. Wolf, *Organic molecular solids*, Wiley-VCH, Weinheim **2007**. b) A. Hayer, V. de Halleux, A. Köhler, A. El-Garoughy, E. W. Meijer, J. Barberá, J. Tant, J. Levin, M. Lehmann, J. Gierschner, J. Cornil, Y. H. Geerts, *Highly Fluorescent Crystalline and Liquid Crystalline Columnar Phases of Pyrene-Based Structures*, *J. Phys. Chem. B* **2006**, *110*, 7653.

[94] F. M. Winnik, *Photophysics of preassociated pyrenes in aqueous polymer solutions and in other organized media*, *Chem. Rev.* **1993**, *93*, 587.

[95] a) J. B. Birks, L. G. Christophorou, *Excimer fluorescence spectra of pyrene derivatives*, *Spectrochimica Acta* **1963**, *19*, 401. b) J. B. Birks, D. J. Dyson, I. H.

Munro, *`Excimer' Fluorescence. II. Lifetime Studies of Pyrene Solutions*, *Proceedings of the Royal Society of London. Series A. Mathematical and Physical Sciences* **1963**, *275*, 575. c) J. B. Birks, A. A. Kazzaz, *Excimer Fluorescence. XII. The Pyrene Crystal Excimer Interaction Potential*, *Proceedings of the Royal Society of London. Series A. Mathematical and Physical Sciences* **1968**, *304*, 291. d) J. B. Birks, M. D. Lumb, I. H. Munro, *'Excimer' Fluorescence. V. Influence of Solvent Viscosity and Temperature*, *Proceedings of the Royal Society of London. Series A. Mathematical and Physical Sciences* **1964**, *280*, 289.

[96] a) L. You, G. W. Gokel, *Fluorescent, Synthetic Amphiphilic Heptapeptide Anion Transporters: Evidence for Self-Assembly and Membrane Localization in Liposomes*, *Chem. - Eur. J.* **2008**, *14*, 5861. b) M. Kimura, N. Miki, D. Suzuki, N. Adachi, Y. Tatewaki, H. Shirai, *Wrapping of Self-Organized Fluorescent Nanofibers with a Silica Wall*, *Langmuir* **2008**, *25*, 776.

[97] J. Xiao, Y. Li, Y. Song, L. Jiang, Y. Li, S. Wang, H. Liu, W. Xu, D. Zhu, *Helical structures architecture of l-{2-(4-hydroxy-phenyl)-1-[(pyren-1-ylmethyl)-carbamoxyl]-ethyl}-carbamic acid tert-butyl ester*, *Tetrahedron Lett.* **2007**, *48*, 7599.

[98] H. M. Colquhoun, Z. Zhu, *Recognition of Polyimide Sequence Information by a Molecular Tweezer*, *Angewandte Chemie International Edition* **2004**, *43*, 5040.

[99] M. S. Becherer, B. Schade, C. Böttcher, A. Hirsch, *Supramolecular Assembly of Self-Labeled Amphicalixarenes*, *Chem. - Eur. J* **2009**, *15*, 1637.

[100] B. Adhikari, J. Nanda, A. Banerjee, *Pyrene-Containing Peptide-Based Fluorescent Organogels: Inclusion of Graphene into the Organogel*, *Chem. - Eur. J.* **2011**, *17*, 11488.

[101] S. T. Caldwell, G. Cooke, S. G. Hewage, S. Mabruk, G. Rabani, V. Rotello, B. O. Smith, C. Subramani, P. Woisel, *Model systems for flavoenzyme activity: intramolecular self-assembly of a flavin derivative via hydrogen bonding and aromatic interactions*, *Chem. Commun.* **2008**, 4126.

[102] R. Varghese, H.-A. Wagenknecht, *DNA as a supramolecular framework for the helical arrangements of chromophores: towards photoactive DNA-based nanomaterials*, *Chem. Commun.* **2009**, 2615.

[103] Y. H. Lee, H. Liu, J. Y. Lee, S. H. Kim, S. K. Kim, J. L. Sessler, Y. Kim, J. S. Kim, *Dipyrenylcalix[4]arene—A Fluorescence-Based Chemosensor for Trinitroaromatic Explosives*, *Chem. - Eur. J.* **2010**, *16*, 5895.

[104] a) U. Maitra, V. K. Potluri, N. M. Sangeetha, P. Babua, Raju A. R., *Helical aggregates from a chiral organogelator*, *Tetrahedron: Asymmetry* **2001**, 477. b) B. Xing, C.-W. Yu, K.-H. Chow, P.-L. Ho, D. Fu, B. Xu, *Hydrophobic Interaction and Hydrogen Bonding Cooperatively Confer a Vancomycin Hydrogel: A Potential Candidate for Biomaterials*, *J. Am. Chem. Soc.* **2002**, *124*, 14846.

[105] K. Sutherland, *Filters and filtration handbook*, Elsevier, Oxford **2008**.

[106] a) A. Rushton, A. S. Ward, R. G. Holdich, *Solid-liquid filtration and separation technology*, Wiley-VCH, Weinheim; New York **2000**. b) R. J. Wakeman, E. S. Tarleton, *Filtration: Equipment selection, modelling and process simulation*, Elsevier Advanced Technology, Oxford, UK, New York **1999**.

[107] I. Butler, *The nonwoven fabrics handbook*, INDA, Association of the Nonwoven Fabrics Industry, Cary, N.C. **1999**.

[108] *The New Encyclopaedia Britannica*, Encyclopaedia Britannica, Chicago **2003**.

[109] A. J. Kidnay, W. R. Parrish, *Fundamentals of natural gas processing*, CRC Press, Boca Raton **2006**.

[110] A. Mayman, E. Homonoff, *The attractiveness of the filter media business: growth and profitability drivers for nonwovens and speciality papers*, *AFSS Adv. Filtr. Sep. Technol.*, *16,* **2002**.

[111] J. L. Sublett, *Effectiveness of Air Filters and Air Cleaners in Allergic Respiratory Diseases: A Review of the Recent Literature*, *Curr. Allergy Asthma Rep.* **2011**, *11*, 395.

[112] J. H. Park, *Filter member manufacturing methods for reducing volume of the filter units and improving the dust collection efficiency and antibacterial property* KR 2005039282 **2005**.

[113] M. H. Langner, *Filtering device for fume hoods, exhaust ventilator hoods, and recirculation hoods* WO 2007147597 **2007**.

[114] M. Adenmark, *Method and system for external indication of regeneration of a particulate filter in vehicle exhaust system* WO 2011087431 **2011**.

[115] M. Durst, *Filtration in Fahrzeugen: Neuentwicklungen - Innovationen - Trends*, Expert-Verl, Renningen **2006**.

[116] A. Farrugia, E. J. Benson, D. I. Holm, *Passive apparatus and method for filtering noxious gases* WO 2007112482 **2007**.

[117] W. W.-F. Leung, *Nanofiber filter face masks and cabin filters* WO 2008131642 **2008**.

[118] a) P. W. Gibson, H. L. Schreuder-Gibson, D. Rivin, *Electrospun fiber mats: Transport properties*, *AIChE J.* **1999**, *45*, 190. b) C. M. Grove, S. E. Chase, *Modular helmet-mask assembly for protection from biological and chemical warfare agents* US 7934497 **2011**.

[119] M. Marchi, *Filter for a vacuum cleaner with self-cleaning system* EP 2335544 **2011**.

[120] P. Neu, B. Ney, K. Thoma, *Gas purification system for medical gases like compressed air* DE 10257629 **2003**.

[121] B. Fernandez Virgel, M. Villoria Cuesta, *Wastewater treatment system for liquid effluents from biological or pharmaceutical processes comprising storage tank,*

sterilizing filter, pump, heat exchanger and automated control ES 2358941 **2011**.

[122] G. C. Kim, H. Y. Lee, *Fuel filter of automobile fuel pump, and manufacturing method thereof* KR 2010016968 **2010**.

[123] M. A. H. Johnston, *Some experience of treating dairy effluent in Northern Ireland*, *Bull. - Int. Dairy Fed.* **1978**, *104*, 177.

[124] J. Pauly, H. Wellhoener, *A new method of treating brewery filter mass*, *Wochenschr. Brau* **1940**, *57*, 266.

[125] P. Hu, G. Chang, Z. Xu, Y. Yu, C. Chen, *Method for solid-liquid separation of vegetable oil or its modified oil* CN 101760297 **2010**.

[126] a) J. Feichter, *Aerosole und das Klimasystem: Atmosphärenforschung*, *Physik in unserer Zeit* **2003**, *34*, 72. b) J. Schnelle-Kreis, M. Sklorz, H. Herrmann, R. Zimmermann, *Atmosphärische Aerosole: Quellen, Vorkommen, Zusammensetzung*, *Chem. Unserer Zeit* **2007**, *41*, 220.

[127] R. Cohen, A. Patel, F. Green, *Lung Disease Caused by Exposure to Coal Mine and Silica Dust*, *Semin. Respir. Crit. Care Med.* **2008**, *29*, 651.

[128] D. B. Purchas, K. Sutherland, *Handbook of filter media*, Elsevier Advanced Technology, Oxford, New York **2002**.

[129] Hoechst Celanese Corporation, *Man-made fiber and textile dictionary*, The Corporation, Charlotte, NC **1988**.

[130] C. Y. Chen, *Filtration of Aerosols By Fibrous Media*, *Chem. Rev.* **1955**, *55*, 595.

[131] D. W. Elliott, W.-X. Zhang, *Field Assessment of Nanoscale Bimetallic Particles for Groundwater Treatment*, *Environ. Sci. Technol.* **2001**, *35*, 4922.

[132] A. Podgórski, A. Bałazy, L. Gradoń, *Application of nanofibers to improve the filtration efficiency of the most penetrating aerosol particles in fibrous filters*, *Chem. Eng. Sci.* **2006**, *61*, 6804.

[133] Y. P. Liu, Y. B. Deng, Z. X. Jiang, *Effect of Nanofiber Diameter on Filtration Efficiency*, *Advanced Materials Research* **2012**, *560-561*, 737.

[134] a) K. Yoon, K. Kim, X. Wang, D. Fang, B. S. Hsiao, B. Chu, *High flux ultrafiltration membranes based on electrospun nanofibrous PAN scaffolds and chitosan coating*, *Single Chain Polymers* **2006**, *47*, 2434. b) T. Grafe, K. Graham, *Polymeric Nanofibers and Nanofiber Webs: A New Class of Nonwovens.* International Nonwovens Technical Conference of the INDA. INDA **2002**. c) R. Mincheva, *Preparation of Polyelectrolyte-Containing Nanofibers by Electrospinning in the Presence of a Non-Ionogenic Water-Soluble Polymer*, *Journal of Bioactive and Compatible Polymers* **2005**, *20*, 419. d) S. B. Squires, M. J. Gardiner, *Cigarette filter incorporating nanofibers* US 20050139223 **2005**.

[135] I. B. Stechkina, A. A. Kirsch, N. A. Fuchs, *Studies on Fibrous Aerosol Filters—IV Calculation of Aerosol Deposition in Model Filters in the Range of Maximum Penetration*, *Ann. Occup. Hyg.* **1969**, *12*, 1.

[136] a) H.-S. Park, Y. Park, *Filtration properties of electrospun ultrafine fiber webs*, *Korean J. Chem. Eng.* **2005**, *22*, 165. b) H.-W. Li, C.-Y. Wu, F. Tepper, J.-H. Lee, C. N. Lee, *Removal and retention of viral aerosols by a novel alumina nanofiber filter*, *J. Aerosol Sci.* **2009**, *40*, 65. c) Y. C. Ahn, S. K. Park, G. T. Kim, Y. J. Hwang, C. G. Lee, H. S. Shin, J. K. Lee, *Development of high efficiency nanofilters made of nanofibers*, *Nano Korea 2004 Symposium on NT Challenge Nano Korea 2004 Symposium on NT Challenge* **2006**, *6*, 1030.

[137] a) T. Grafe, M. Gogins, M. Barris, J. Schaefer, R. Canape, *Nanofibers in filtration applications in transportation.* Filtration 2001 International Conference and Exposition of the INDA. INDA **2001**. b) W. C. Hinds, *Aerosol technology: Properties, behavior and measurement of airborne particles*, John Wiley & Sons, New York **1999**. c) K. Kosmider, J. Scott, *Polymeric nanofibres exhibit an enhanced air filtration performance*, *Filtration and Separation* **2002**, *39*, 20.

[138] R. C. Brown, *Air filtration: An integrated approach to the theory and applications of fibrous filters*, Pergamon Press, Oxford, New York **1993**.

[139] K. Graham, M. Ouyang, T. Raether, T. Grafe, B. McDonald, P. Knauf, *Polymeric nanofibers in air filtration applications.* Fifteenth Annual Technical Conference & Expo of the American Filtration & Separation Society **2002**.

[140] a) A. Raghavanpillai, S. Reinartz, K. W. Hutchenson, *Hydrophobic and oleophobic surface modification using fluorinated bis-urea and bis-amide gelators*, *J. Fluorine Chem.* **2009**, *130*, 410. b) E. J. Acosta, A. Raghavanpillai, S. Peng, S. Reinartz, S. Moudgil, *Partially fluorinated amino acid derivatives as gelling and surface active agents* US 20080113573 **2008**.

[141] J. Ding, Y.-L. Hsiao, C. P. Lenges, Y. Niu, S. Reinartz, C. M. Stancik, J. J. van Gorp, *Nanoweb composite material and gelling method for preparing same* US 20070125700 **2007**.

[142] M. E. Salmon, *The growth and characterization of alkylphosphonic acid self-assembled nanofibers: Dissertation* **2006**.

[143] M. Ikeda, S. Ueno, S. Matsumoto, Y. Shimizu, H. Komatsu, K.-i. Kusumoto, I. Hamachi, *Three-Dimensional Encapsulation of Live Cells by Using a Hybrid Matrix of Nanoparticles in a Supramolecular Hydrogel*, *Chem. - Eur. J.* **2008**, *14*, 10808.

[144] a) E. Krieg, H. Weissman, E. Shirman, E. Shimoni, B. Rybtchinski, *A recyclable supramolecular membrane for size-selective separation of nanoparticles*, *Nat. Nanotechnol.* **2011**, *6*, 141. b) E. Krieg, B. Rybtchinski, *Noncovalent Water-Based Materials: Robust yet Adaptive*, *Chem. - Eur. J.* **2011**, *17*, 9016.

2. SYNOPSIS

The present thesis addresses the preparation and application of supramolecular nanofibers. In a series of four manuscripts different issues concerning supramolecular nanofibers were investigated and detailed structure-property relations established.

The first part of this thesis deals with fundamental questions regarding the aggregation behavior of pyrene-containing small molecules. With a set of four model compounds, the influence of H-bonding and bulky substituents on the π-π-stacking of pyrene was investigated in dilute solution, in the aggregated state, and in solid films. Depending on the state of matter, the impact of H-bonding and bulky substituents on the π-π-stacking of pyrene varies in quantity.

In the second part the focus is set on the preparation of supramolecular nanofibers. In this part, two different self-assembly processing pathways from solution were compared in order to tune the nanofiber morphology with respect to homogeneity, fiber diameter, and fiber diameter distribution. Depending on the solubility of the molecular building blocks different self-assembly pathways can be realized, leading to various supramolecular morphologies. Furthermore, a comprehensive study on structure-property relations with respect to different morphologies of supramolecular (nano-)fibers was conducted. Thereby, parameters such as the molecular structure, the concentration, the solvent, and the cooling rate were varied. The fundamental knowledge obtained from these chapters represents the basis for the more applied developments.

In the third part, we show for the first time, that supramolecular nanofibers can be used in air filtration applications. By a solution-based immersion process supramolecular nanofiber webs were prepared *in-situ* in nonwoven scaffolds resulting in microfiber-nanofiber composites. Furthermore, air filtration tests revealed suitable filtration efficiencies.

Building on these results, the fourth part of this thesis goes one step further investigating detailed structure-property relations in view of the network density, the stability of the nanofiber webs as well as the overall filtration performance of the composite materials. Thereby, variations of the molecular structure, the used solvent, the concentration, the kind of aerosol, and the filter setup were investigated.

In the following, the highlights of each manuscript are presented in a brief summary.

2.1 Controlling the π-stacking behavior of pyrene derivatives: Influence of H-bonding and steric effects in different states of aggregation*

In the first manuscript of this thesis, the influence of the molecular structure on the stacking behavior of pyrene derivatives was investigated. Therefore, a set of well-defined ester derivatives **1a**, **1b** and their corresponding amide compounds **2a**, **2b** were synthesized (Figure 1, A). From the structural point of view, the ester molecules are only able to self-assemble via π-stacking of the pyrene units, while the amides compounds can aggregate by π-stacking combined with hydrogen bonding of the amide groups. In addition, sterical variations were implemented into the molecular structures by means of a non-sterical demanding hydrogen substituent (**1a**, **2a**) and a sterical demanding *tert*-butyl rest (**1b**, **2b**). In this chapter, these molecules were investigated in dilute solution, in the aggregated state as well as in solid films.

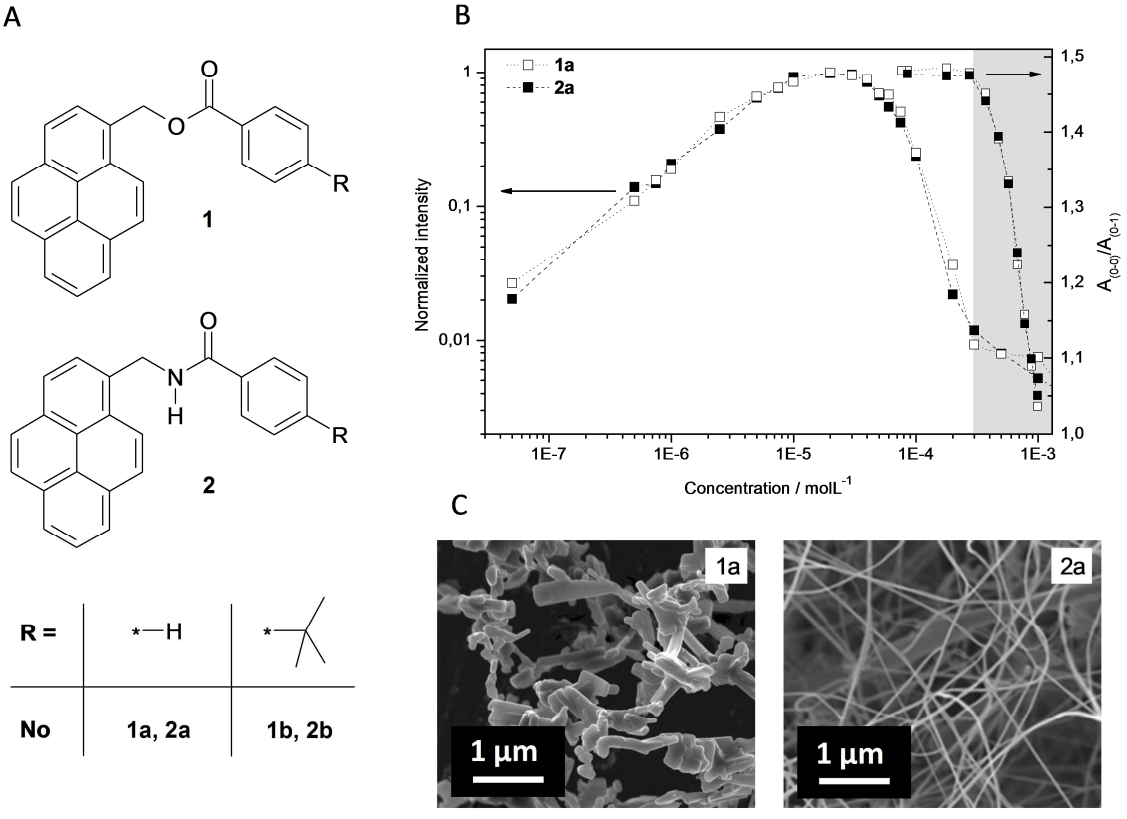

Figure 1. (A) Molecular structures of investigated ester (**1a**, **1b**) and amide (**2a**, **2b**) compounds. (B) Photoluminescence intensities of the monomer peak at 375 nm (left axis) and the absorption ratio of A(0-0)/A(1-0) (right axis) of compounds **1a** and **2a** at different concentrations. The shaded area depicts the concentration range in which the formation of supramolecular aggregates starts to occur. (C) SEM micrographs of freeze-dried supramolecular aggregates of ester **1a** and amide **2a** prepared from dioxane solutions (concentration: $1 \cdot 10^{-2}$ mol/L).

* Manuscript published in: *ChemPhysChem* **2013**, *14*, 1818.
Full manuscript can be found in Chapter 3.2

Concentration-dependent photoluminescence measurements were performed in solution. The emission characteristics of the herein utilized pyrene units are dependent on their environment. Thus, monomer and excimer emission, which differ in energy, can be observed at distinct circumstances. At a minimal threshold concentration of $2 \cdot 10^{-5}$ mol/L monomer emission was quenched for all investigated compounds (Figure 1, B). This result, combined with the fact, that no excimer emission can be observed in this concentration range indicates that a non-emissive intermediate species is formed. Excimer emission can only be observed at concentrations of more than $6 \cdot 10^{-4}$ mol/L. Furthermore, dynamic light scattering (DLS) and UV-Vis experiments revealed supramolecular aggregation in this concentration range for the ester as well as the amide compounds (Figure 1, B). Thus, formation of excimers requires a kind of ground state stabilization that is only available in the environment provided by supramolecular aggregates. A significant influence of the structural variations, namely the linker (ester or amide) and the sterical effect of the substituent (hydrogen or *tert*-butyl substituent) can not be observed. Therefore, we conclude that π-stacking of the pyrene chromophores is the driving force of the aggregation in solution. The rate of excimer formation reveals an influence of the H-bonding and the steric demanding groups. While the excimer formation rate in the ester compound **1a** is comparable to that of unsubstituted pyrene, excimer formation proceeds slower with the amide linker of compound **2a**, and is reduced even more by the bulky substituents of **1b** and **2b**. In order to illustrate the morphology of the supramolecular aggregates, freeze-drying of dioxane solutions of $1 \cdot 10^{-2}$ molL^{-1} was performed. Figure 1, C exemplarily shows the supramolecular morphologies of the aggregates of ester **1a** and amide **2a**. The amides form nanofibers while for the ester compounds rod-like morphologies could be observed. According to FT-IR investigations, the nanofibers of both amides **1a**, **1b** were stabilized by hydrogen bonds in the freeze-dried state.

Furthermore, crystallization of spin-coated films of the ester and amide compounds was evaluated by photoluminescence spectroscopy, FT-IR analysis, and polarized optical microscopy (POM). Each of the freshly prepared films featured exclusively excimer fluorescence (exemplarily shown for amide **2a** in Figure 2, A). Even though optically clear films were observed in POM, the excimer formation was attributed to the existence of supramolecular nano-aggregates. Upon crystallization due to annealing or aging effects excimer formation becomes suppressed while monomer emission can be observed. Here, the mobility of the pyrene units in the crystalline state was restricted and thus the pyrene shift necessary for excimer formation was constrained. In order to elucidate the development of hydrogen bonds during crystallization of the films of both amides, FT-IR analysis was performed featuring a shift of the N-H and the carbonyl stretching vibration to lower wave numbers (exemplarily shown for amide **2a**, Figure 2, B) accompanied by a sharpening of the

peak. However, the sterical demanding *tert*-butyl group of amide **2b** weakened the strength of the hydrogen bonds compared to **2a**.

Crystalline films were investigated at low temperature by photoluminescence spectroscopy. The obtained results were compared with those of computational studies to detect the disturbance of structural variations on the π-stacking of the pyrene units. The compounds **1a**, **2a** and **2b** feature monomer emission at low temperatures. Thus, the structural order in the crystalline state increases the activation energy necessary for excimer formation, which is not available at low temperatures (exemplarily shown for **1a**, Figure 2, C). In contrast, for ester **1b**, excimer emission was observed at all temperatures, indicating the most disordered crystallite structure upon the investigated compounds (Figure 2, D). As result we found, that the columnar stacking is increasingly disturbed by the introduction of the amide and the *tert*-butyl moiety.

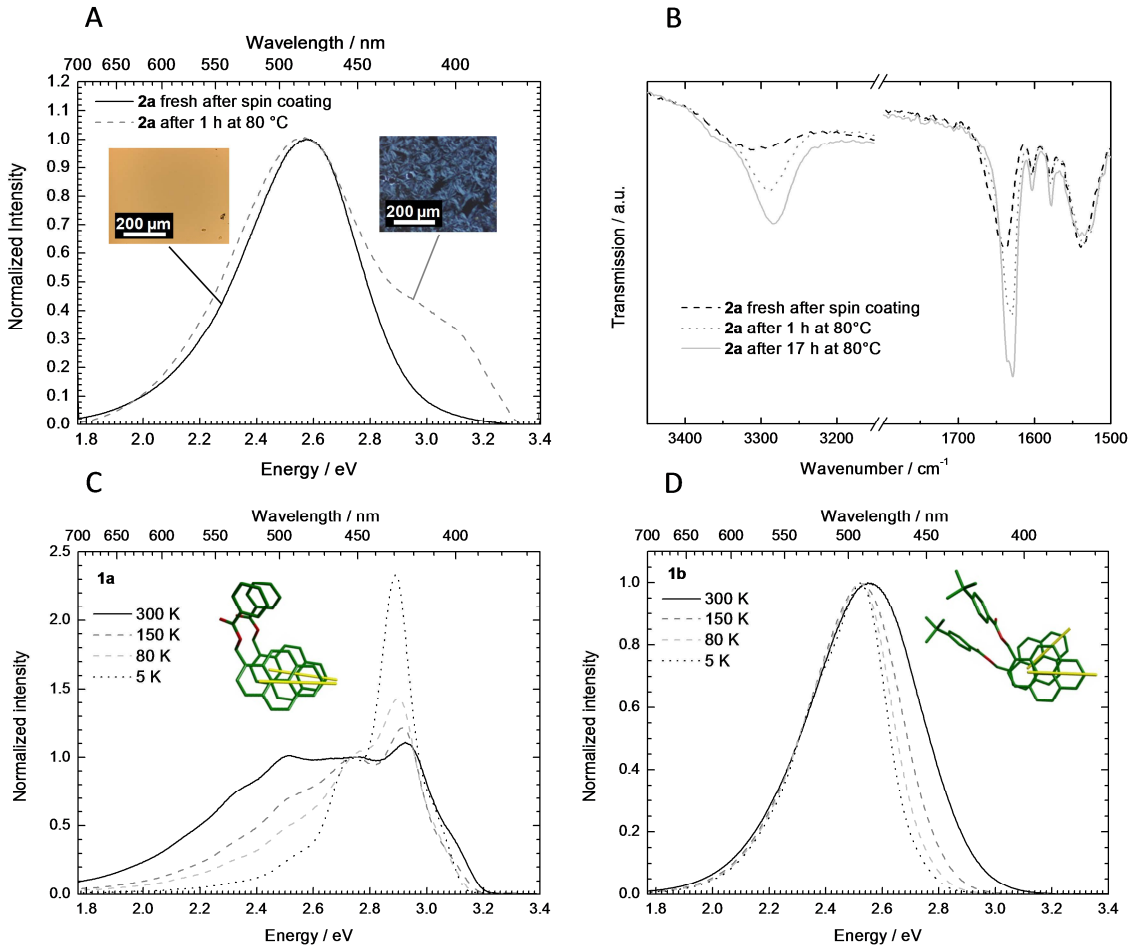

Figure 2. (A) Photoluminescence spectra including corresponding POM images and (B) FT-IR analysis of a spin-coated film of amide **2a** directly after processing and after different time periods. (C+D) Temperature dependent photoluminescence spectra of aged films including geometry optimized dimers of ester **1a** (C) and of ester **1b** (D).

2.2 Supramolecular nanofibers – A study on different processing pathways*

In this chapter, the class of 1,3,5-benzenetrisamides (BTAs) were utilized, whose driving force for their self-assembly are hydrogen bonds. From solution these molecules are able to self-assemble into supramolecular nanofibers. Herein, different self-assembly processing pathways and related structure-property relations were foregrounded. With that knowledge, the supramolecular nanofiber morphology can be controlled with respect to homogeneity, fiber diameter, and fiber diameter distribution.

The first investigated pathway is based on self-assembly upon cooling at a constant concentration and subsequent evaporation of a solvent. Here, we investigated two different BTA/solvent systems: one at room temperature (mainly) insoluble system, which is based on BTA **1** and 2,2,4,4,6,8,8-heptamethylnonane (HMN) (at concentrations ranging from 0.005 wt% - 0.06 wt%) and one more soluble system consisting of BTA **2** and 2-butanone (at a concentration of 1.0 wt%) (Figure 3, A and B). In order to obtain initially optical clear solutions, both BTAs were dissolved at the boiling point of the solvent. Subsequent cooling under controlled conditions leads to supramolecular aggregation in both systems. After solvent evaporation, the supramolecular aggregates were investigated by scanning electron microscopy (SEM). For BTA **1** at a concentration of 0.02 wt%, we obtained supramolecular nanofibers with an homogeneous fiber diameter distribution (Figure 3, A), while for BTA **2** fibers with a bimodal morphology could be observed with average fiber diameters of 0.23 µm and 1.46 µm (Figure 3, B). The distinct supramolecular morphologies can be explained by different solubilities of the BTA/solvent systems after cooling. The residual solubility of BTA **1** in HMN at room temperature is almost zero. Consequently, the self-assembly is completed after cooling and mainly all BTA molecules are aggregated. During solvent evaporation no additional self-assembly occurs anymore. In contrast, the residual solubility of BTA **2** in butanone was determined to 0.6 wt%. Therefore, 0.4 wt% (of the initial concentration of 1.0 wt%) self-assembles upon cooling resulting in the observed microfibers (shaded grey in the histogram in Figure 3, B). During subsequent solvent evaporation the residual dissolved BTA **2** molecules (0.6 wt%) self-assemble to supramolecular nanofibers.

Furthermore, the lateral dimensions of the supramolecular aggregates can be influenced by the choice of self-assembly conditions. Utilizing this self-assembly pathway, the influence of the BTA concentration and the influence of the cooling rate on the resulting supramolecular morphology were investigated. The lower the concentration of the initial solution and the faster the cooling rate, the smaller are the

* Manuscript draft intended for submission to Journal of Supramolecular Chemistry
Full manuscript can be found in Chapter 3.3

diameters of the nanofibers, ranging from 2.19 µm to 190 nm. The power of self-assembly by the triple hydrogen bonding motif is emphasized by quenching experiments in liquid nitrogen. Also at this high cooling rate defined one-dimensional nanofibers were obtained, pointing out a very fast self-assembly.

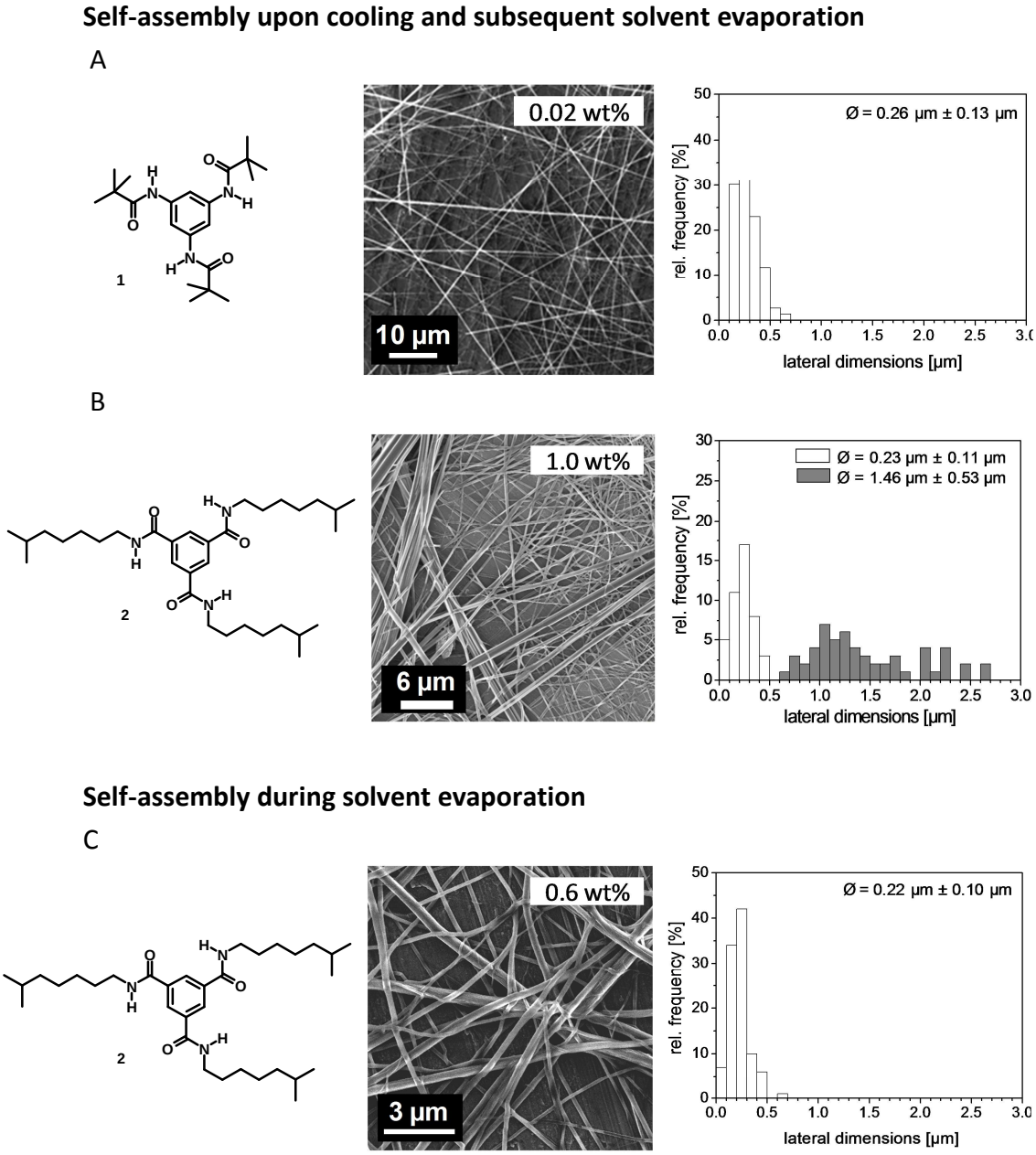

Figure 3. (A) Molecular structure of 1,3,5-benzenetrisamide (BTA) **1** and the SEM micrograph as well as the corresponding histogram of the supramolecular nanofibers of BTA **1** obtained from self-assembly upon cooling and subsequent solvent evaporation (solvent: HMN, concentration: 0.02 wt%, cooling rate: 60 °C/min). (B) Molecular structure of BTA **2** and the SEM micrograph as well as the corresponding histogram of supramolecular aggregates of BTA **2** obtained from self-assembly upon cooling and subsequent solvent evaporation (solvent: butanone, concentration: 1.0 wt%). (C) Molecular structure of BTA **2** and the SEM micrograph as well as the corresponding histogram of supramolecular aggregates of BTA **2** obtained from self-assembly during solvent evaporation (solvent: butanone, concentration: 0.6 wt%).

The second investigated self-assembly pathway is the self-assembly during solvent evaporation. As shown, BTA **2** is soluble in butanone at room temperature up to a threshold concentration of 0.6 wt%. Due to this fact, a BTA **2**/butanone system with a concentration of 0.6 wt% is able to aggregate into supramolecular nanofibers by self-assembly during solvent evaporation (Figure 3, C). Thereby, solvent evaporation leads to oversaturation effects, which induces the self-assembly. The obtained supramolecular nanofibers feature an average fiber diameter of 0.22 µm. These results are in agreement with the findings on higher concentrated BTA-solutions, where a very similar morphology was formed. Furthermore, at the self-assembly during solvent evaporation, structure-property relations regarding the influences of the solvent as well as the molecular structure on the resulting supramolecular morphologies were investigated.

In summary, we found, that the solubility of the utilized BTA/solvent system is the key factor which determines the self-assembly processing pathway.

2.3 Supramolecular nanofiber webs in nonwoven scaffolds as potential filter media*

In this part of the thesis a solution-based method to prepare polymer-microfiber/supramolecular-nanofiber composites was developed. Supramolecular nanofibers of BTA **1** (molecular structure shown in Figure 4, A) were formed *in-situ* in viscose/polyester nonwoven fabrics, which were used as scaffolds to ensure mechanical stability. The fabrics were dipped into BTA/butanone solutions with concentrations of 0.4-1.0 wt% of BTA **1** at elevated temperatures. At solvent evaporation, the molecules self-assemble to supramolecular nanofibers in the openings and voids of the polymer nonwoven scaffold to yield the composites, consisting of supramolecular nanofibers and polymer microfibers (Figure 4, B). Depending on the concentration of BTA **1** in the starting immersion solution, the fraction of filled openings in the fabric as well as the nanofiber density within the supramolecular fiber webs can be adjusted. However, the influence on the morphology of the supramolecular webs, the nanofiber diameter, and the distribution thereof is marginal.

In Figure 4, C and Figure 4, D the resulting microfiber-nanofiber composites prepared from a 0.4 wt% and a 1.0 wt% BTA/butanone solution are shown exemplarily. Starting from a 0.4 wt% butanone solution a nanofiber content of 2.8 wt% was obtained in the composite, while a BTA/butanone solution of 1.0 wt% resulted in a content of 7.0 wt%. The specimen with a content of supramolecular nanofibers of 2.8 wt% reveals an uneven filling of the openings by the self-assembled nanofibers, which are rather located in individual voids, instead of homogeneously distributed all over the fabric. It is remarkable that the supramolecular nanofibers have the tendency to strongly adhere to and even wind around the polymer microfibers. The composite with 7.0 wt% nanofibers exhibit a much denser nanofiber web compared to the ones with lower nanofiber contents. In addition, most of the openings of the nonwoven are filled with nanofibers. With increasing amount of supramolecular nanofibers in the scaffolds, the surface of the microfiber-nanofiber composites was increased as proven by BET measurements of all investigated specimens. In comparison to the blank nonwoven fabric, the surface of the composite with a nanofiber content of 7.0 wt% was increased fourfold.

* Published in: *Small* **2013**, *9*, 2053.
Full publication can be found in Chapter 3.4

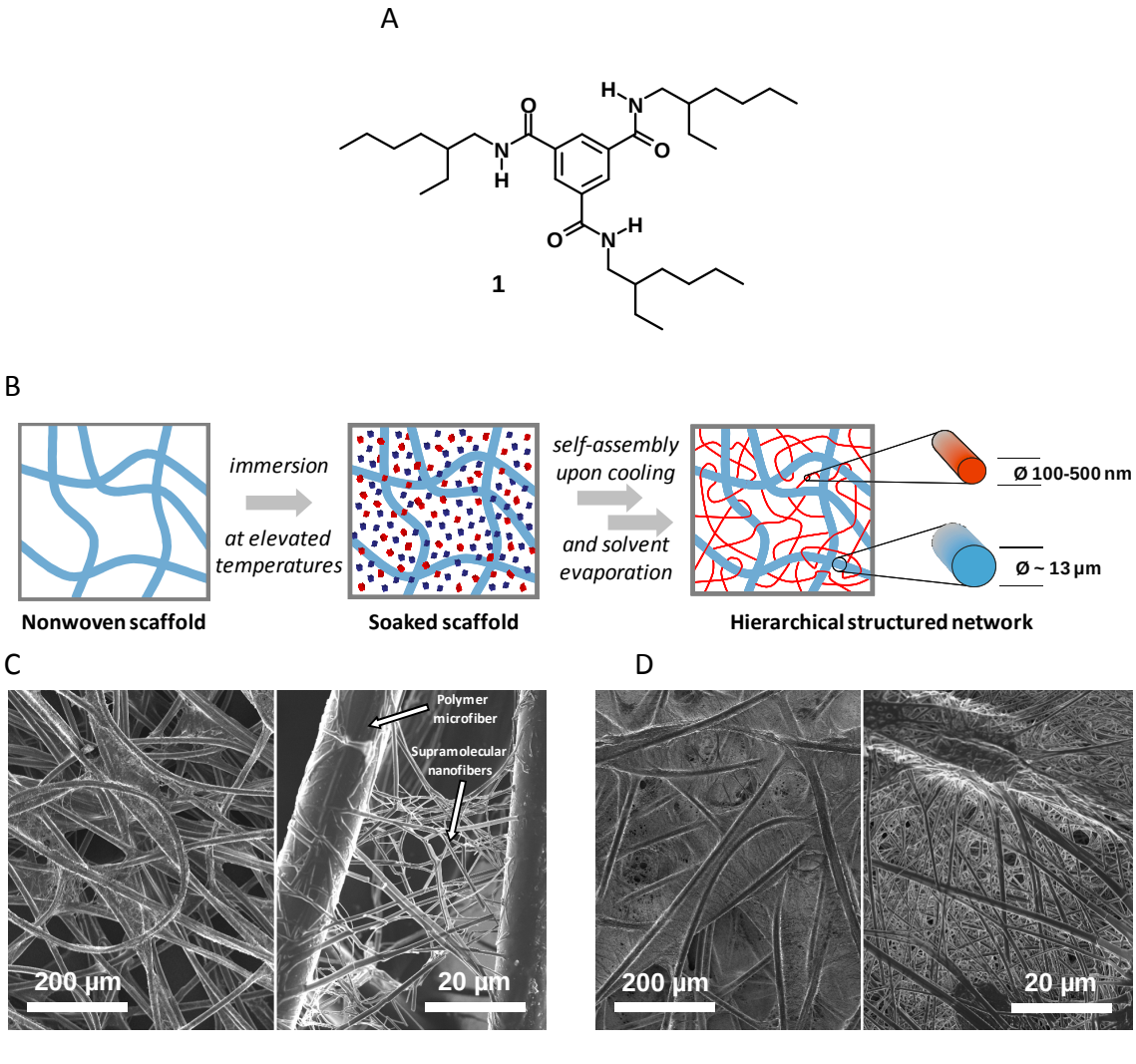

Figure 4. (A) Molecular structure of BTA **1** utilized to prepare the microfiber-nanofiber composites. (B) Schematic representation of the *in situ* formation process of supramolecular nanofibers via self-assembly resulting in microfiber-nanofiber composites. Blue fibers: nonwoven scaffold; red dots: dissolved supramolecular building units; blue dots: solvent; red fibers: supramolecular nanofibers. (C+D) SEM micrograph of the microfiber-nanofiber composites obtained from a 0.4 wt% (C) and a 1.0 wt% (D) concentrated BTA/butanone solution.

The mechanical stability of the supramolecular nanofibers is an important question, especially in view of their use as potential filter media. Therefore, different stability experiments were conducted at a filter test rig. Hereby, an airstream with a flow velocity of 3.0 m/s was applied to the composites and the nanofiber stability was determined on the one hand by continuous differential pressure measurements and on the other hand by a particle analyzer localized after the filter media to detect fiber fragments which might originate from the specimen. In addition, SEM micrographs were recorded before and after the test to investigate possible changes in morphology microscopically. It was found that all investigated microfiber-nanofiber composites were stable at the applied conditions. For supramolecular systems, their stability upon an airstream of 3.0 m/s is immense, especially when compared to standard flow velocities of vacuum cleaners of 0.25-0.40 m/s at the filter element.

A first proof of concept in view of air filtration capability was investigated. Thereby, test aerosol particles were applied onto the microfiber-nanofiber composites and the filtration efficiency was investigated. While the blank polymer microfiber fabric does only separate aerosol particles of 0.2-1.0 µm size to 5 %, the composites feature improved filtration efficiencies. The higher the mass fraction of supramolecular nanofibers in the investigated concentration regime, the better is the filtration efficiency of the specimens. As consequence, filtration efficiencies of up to 85 % for 1.0 µm sized aerosol particles were achieved with the microfiber-nanofiber composite with a content of supramolecular nanofibers of 7.0 wt%.

To conclude, the *in-situ* preparation of microfiber-nanofiber composites is a beneficial alternative compared to established top-down processes (for instance electrospinning) to prepare nanofiber-modified filters. The most eminent advantage of the herein developed preparation process is the post hoc incorporation of nanofibers in the volume of nonwoven fabrics. Further benefits of this process are its simplicity and its variability.

2.4 Structure-property relations of supramolecular nanofibers in nonwoven scaffolds as media for air filtration applications*

The development of improved air filters with supramolecular nanofibers is pushed forward in the last part of this thesis. Thereby, nonwoven fabrics were modified with several BTAs (Figure 5) under different conditions by means of the immersion process which was investigated in the previous manuscript. In this chapter, the focus is set on structure-property relations, in particular between the nanofiber morphology and the filtration efficiencies. Here, the influence of different concentrations, chemical structures, solvents, and different filter setups on the nanofiber web morphology, the filtration quality as well as the temperature stability was investigated. Depending on the chemical structure of the BTA the nanofiber diameter as well as the density and the porosity of the supramolecular networks differ, which in turn affects the filtration efficiency and the differential pressure of the filters. The microfiber-nanofiber composite with nanofibers of BTA **1** separates aerosol particles most efficiently, while the filtration efficiency is reduced to BTA **2** and further to BTA **3**. However, the filter with BTA **1** nanofibers possesses a relatively high differential pressure and thus the following investigations were conducted with BTA **2**.

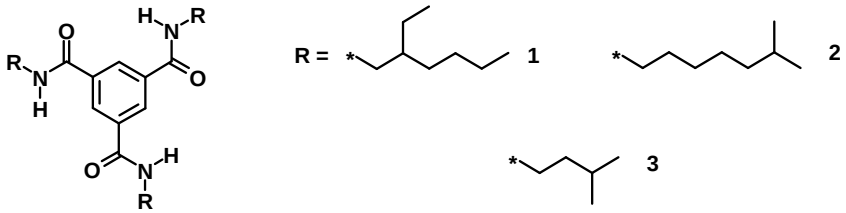

Figure 5. Chemical structures of BTAs **1**-**3** used to prepare supramolecular nanofiber-modified filters.

Among other structure-property relations, the influence of solvent is discussed here for filters modified with BTA **2** nanofibers in detail (Figure 6). The filter prepared from ethanol possesses supramolecular fibers with diameters in the micrometer range. Furthermore, the voids of the scaffold were filled insufficiently (Figure 6, A). This leads to poor filtration efficiency (Figure 6, C). In contrast, homogeneous and fine-pored supramolecular nanofiber webs were obtained for the filter prepared from a butanone solution (Figure 6, B). As a consequence, this filter features improved filtration efficiency, namely almost 80 % for 1 µm-sized aerosol particles. Taking into account that the filter thickness is 0.15 mm, the filtration efficiency of the filter prepared from butanone is very promising.

* Manuscript draft intended for submission to Journal of Materials Chemistry
Full manuscript can be found in Chapter 3.5

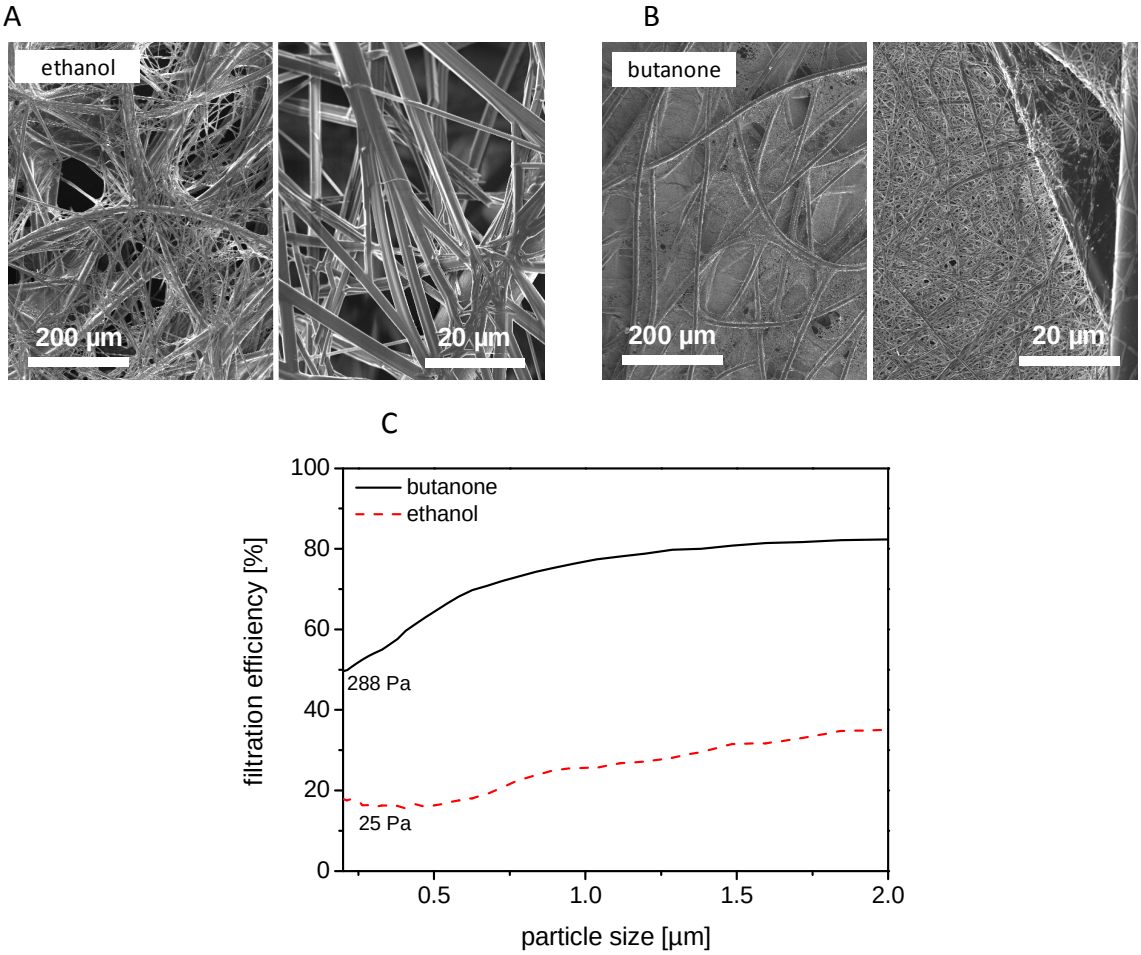

Figure 6. Top: SEM micrographs of the filters with BTA **2** nanofibers prepared from a butanone (A) and an ethanol (B) solution with concentrations of 1.0 wt%, respectively. (C) Filtration efficiencies and pressure drops of the prepared filters shown in (A) and (B). Parameters in the filter tests: filter area: 28.3 cm^2; flow velocity: 25 cm/s; test aerosol: Iso fine dust (aerosol concentration: about 6000 particles/cm^3); testing time: 30 s.

Further, it was demonstrated that the filtration efficiency of the supramolecular modified filters could be optimized with increasing filter thickness. Therefore, triple-layer specimens, which are comprised of three single filters stacked upon each other, were investigated (Figure 7, A). SEM micrographs from the top surface of each layer of a dust-loaded triple-layer filter (nanofiber content in each layer: 7.6 wt%) are shown in Figure 7, B. The micrographs show that coarse dust is separated mainly on the top layer of the filter while at the center and bottom layer only fine dust particles can be observed. For this triple-layer filter the filtration efficiency was determined to 90 % for 0.2 µm sized aerosol particles and even 99.4 % for 1.0 µm sized aerosol particles with a differential pressure of 894 Pa (Figure 7, C). By decreasing the nanofiber content in each layer of the triple-layer filter from 7.6 wt% to 5.8 wt% and further to 4.4 wt%, the differential pressure is successively reduced about 90 %. The filtration efficiency, however, is just declined about 28 %.

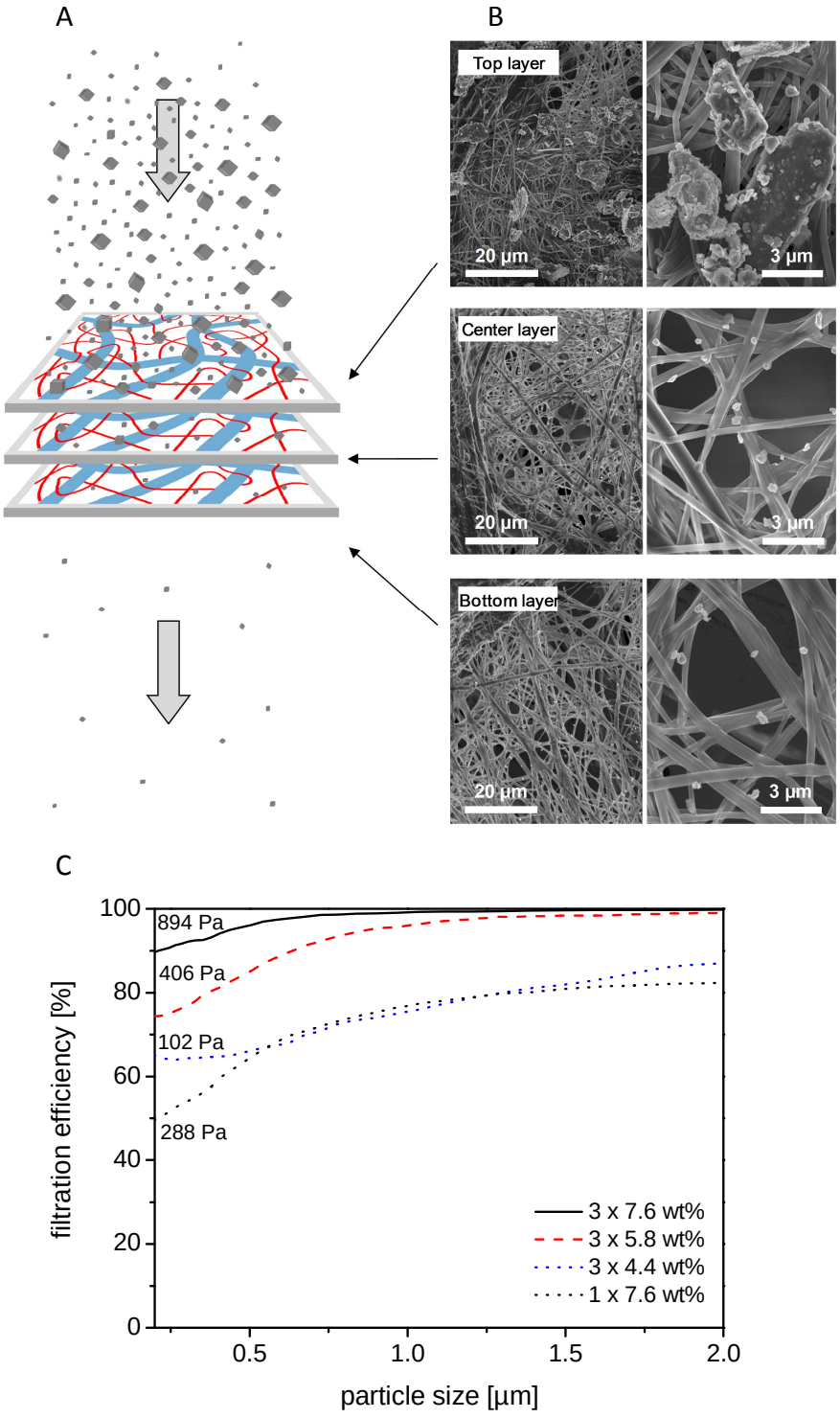

Figure 7. (A) Schematic representation of a triple-layer filter in the filter test and (B) SEM micrographs taken at the top surface of each layer. The SEM micrographs exemplarily show the dust-loaded surface of each layer of the triple-layer filter with mass fractions of supramolecular nanofibers of BTA **2** of 7.6 wt%, respectively. (C) Filtration efficiencies and pressure drops of the triple-layer filters with mass fractions of supramolecular nanofibers of BTA **2** of 7.6 wt%, 5.8 wt%, and 4.4 wt% in each layer. As reference, the single-layer filter with a mass fraction of supramolecular nanofibers of BTA **2** of 7.6 wt% is shown. Parameters in the filter tests: filter area: 28.3 cm^2; flow velocity: 25 cm/s; test aerosol: Iso fine dust (aerosol concentration: about 6000 particles/cm^3); testing time: 30 s.

In comparison to the single-layer filter with 7.6 wt% nanofibers of BTA **2**, the triple-layer filter with a nanofiber content of 4.4 wt% in each layer possesses similar filtration efficiency. But the differential pressure of the triple-layer filter is one third less compared to the single-layer filter. Therefore, higher throughputs could be obtained with the triple-layer filter resulting in a much less cost-intensive filtration process.

In summary, the filtration efficiency was successfully optimized by means of a comprehensive study on structure property relations. Upon the investigated filters, the triple-layer filter with the best filtration efficiency even reaches values of HEPA filters. By further optimization, supramolecular nanofiber modified filters could be serious competitors to conventional prepared filters in industrial air filtration applications.

3. PUBLICATIONS AND MANUSCRIPTS

3.1 Individual contributions

The work presented in this thesis was carried out at the chair of Macromolecular Chemistry I of the University of Bayreuth under the supervision of Prof. Dr. Hans-Werner Schmidt. In the following, the individual contributions to the publications and manuscripts of this thesis are presented.

Controlling the π-stacking behavior of pyrene derivatives: Influence of H-bonding and steric effects in different states of aggregation

Andreas T. Haedler, Holger Misslitz, Christian Buehlmeyer, Rodrigo Q. Albuquerque, Anna Köhler, and Hans-Werner Schmidt

ChemPhysChem **2013**, *14*, 1818.

The work behind this manuscript was carried out in close cooperation with Christian Buehlmeyer and Prof. Dr. Anna Köhler (University of Bayreuth, Experimental Physics II) and Prof. Dr. Rodrigo Albuquerque (University of Bayreuth, Experimental Physics IV). The synthesis of the model compounds was performed by myself with assistance of Doris Hanft and Irene Bauer (technical assistants at the University of Bayreuth). Andreas Haedler performed the UV-Vis measurements in solution. The FT-IR measurements and the optical microscopy investigations were jointly done with Christian Buehlmeyer (EP II) in the framework of his diploma thesis. The time correlated single photon counting (TCSPC) measurements and the absorption as well as the photoluminescence experiments on the solid films were done by Christian Buehlmeyer. Prof. Dr. Rodrigo Albuquerque conducted the simulations. All other experimental work (characterization of the compounds, investigation of the thermal properties, concentration dependent photoluminescence measurements in solution, and SEM investigations of supramolecular aggregates) was performed by myself. The draft of the manuscript was equally written by Andreas Haedler and myself. Prof. Anna Köhler and Prof. Dr. Hans-Werner Schmidt were involved in interpretations, discussions and the finalization of this manuscript.

Supramolecular nanofibers - A study on different processing pathways

Holger Misslitz, Frank Abraham, Klaus Kreger, and Hans-Werner Schmidt

Manuscript draft intended for submission to Journal of Supramolecular Chemistry

The experimental work presented in this manuscript was performed by Frank Abraham (Macromolecular Chemistry I) and myself. Frank Abraham investigated the influences of the concentration and the cooling rate on the self-assembly upon cooling. All other experiments were conducted by myself, with the exception of the focused ion beam experiments, which were performed as service by Werner Reichstein (Bayreuth Institute of Macromolecular Research). The interpretations were performed by myself. It was also me who wrote the first draft of this manuscript. Dr. Klaus Kreger and Prof. Dr. Hans-Werner Schmidt were involved in discussions and the finalization of this manuscript in the present form.

Supramolecular nanofiber webs in nonwoven scaffolds as potential filter media

Holger Misslitz, Klaus Kreger, and Hans-Werner Schmidt

Small **2013**, *9*, 2053.

The experimental work and the first interpretation of the data in this manuscript were performed by myself with the exception of the BET measurements, which were done by Lena Geiling (University of Bayreuth, Inorganic Chemistry I). The first draft of the manuscript was written by myself and jointly finalized with Dr. Klaus Kreger and Prof. Dr. Hans-Werner Schmidt.

Structure-property relations of supramolecular nanofibers in nonwoven scaffolds as media for air filtration applications

Holger Misslitz, Klaus Kreger, and Hans-Werner Schmidt

Manuscript draft intended for submission to Journal of Materials Chemistry

The experiments as well as the evaluation of the acquired data were carried out by myself. The manuscript was also written by myself. Dr. Klaus Kreger and Prof. Dr. Hans-Werner Schmidt were involved in discussions and the finalization of this manuscript in the present form.

3.2 Controlling the π-stacking behavior of pyrene derivatives: Influence of H-bonding and steric effects in different states of aggregation

Andreas T. Haedler,[a]# Holger Misslitz,[a]# Christian Buehlmeyer,[b] Rodrigo Q. Albuquerque,[c] Anna Köhler,[b] and Hans-Werner Schmidt[a]*

[#] both authors contributed equally to this contribution

[a] Macromolecular Chemistry I, Bayreuther Institut für Makromolekülforschung (BIMF), University of Bayreuth, 95440 Bayreuth, Germany

[b] Institute of Experimental Physics II, Bayreuther Institut für Makromolekülforschung (BIMF), University of Bayreuth, 95440 Bayreuth (Germany)

[c] Theoretical Physics IV, University of Bayreuth, 95440 Bayreuth (Germany)
Current address: Institute of Chemistry of São Carlos, University of São Paulo (Brazil)

CHEMPHYSCHEM **2013**, *14*, 1818.

Abstract: The performance of opto-electronic devices built from low molecular weight dye molecules depends crucially on the stacking properties and the resulting coupling of the chromophoric systems. In this paper we investigate the influence of H-bonding amide and bulky substituents on the π-stacking of pyrene-containing small molecules in dilute solution, as supramolecular aggregates, and in the solid state. A set of four pyrene derivatives was synthesized in which benzene or 4-*tert*-butyl benzene was linked to the pyrene unit either via an ester or an amide. All four molecules form supramolecular H-aggregates in THF solution at concentrations above $1 \cdot 10^{-4}$ molL^{-1}. These aggregates were transferred on a solid support and crystallized. We investigate: the excimer formation rates within supramolecular aggregates; the formation of H-bonds as well as the optical changes during the transition from the amorphous to the crystalline state and; the excimer to monomer fluorescence ratio in crystalline films at low temperatures. We reveal that in solution supramolecular aggregation depends predominantly on the pyrene chromophores. In the crystalline state, however, the pyrene stacking can be controlled gradually by H-bonding and steric effects. These results are further confirmed by molecular modeling. This work bears fundamental information for tailoring the solid state of functional optoelectronic materials.

Keywords: self-assembly • kinetics • chromophores • fluorescence • molecular modeling

Introduction

Supramolecular chromophoric or multichromophoric systems are envisioned to serve as active materials in opto-electronic devices, in particular for organic photovoltaics (OPVs).[1] For those applications π-conjugated aromatic systems are promising candidates. They can transfer charge and energy, and their absorption and photoluminescence wavelength can be tuned comparatively easily.[2] Transport as well as the optical properties and thus the device performance depend largely on the electronic coupling of the π-conjugated systems.[3] Therefore, the distance between and the relative orientation of the chromophores are crucial and need to be adjusted thoroughly by fine-tuning the molecular structure.[4] To solve this difficult task, tools and concepts of supramolecular chemistry are utilized. However, a good understanding of the interplay of non-covalent intermolecular interactions like ionic-, dipole- or Van-der-Waals interactions and combinations thereof is needed.[5] Especially H-bonding, hydrophilic-hydrophobic interactions, and steric repulsion are widely used in this context.[6] Furthermore, the influence of those intermolecular interactions on the π-π stacking of the active chromophoric system depends also on the state of matter and aggregation.

A well-established chromophore is needed to investigate the complex relationship between the molecular structure, the relative orientation of the π-conjugated systems and the resulting optic and electronic properties. Pyrene is a suitable candidate as its optical behavior is well understood in solution, the aggregated and the solid state.[7] Förster assigned the quenching of fluorescence in pyrenes to the formation of excimers already in 1955, and Birks later investigated this excimer formation in detail.[8] An excimer may be considered as a pair of molecules that, in the ground state, are bound together only weakly (e.g. in the solid) or not at all (e.g. in solution), and that absorb light as monomers, but that reorient in the excited state and then fluoresce as dimers. [9,10] The excited dimer (= excimer) fluorescence is broad, unstructured and bathochromically shifted from the monomer fluorescence, and it leads to the two monomers in their ground state.[11–13] The strong tendency of pyrene to form excimers prevails both in solution and in condensed matter such as amorphous films, liquid crystals and crystals.[9,14] Note that in the condensed phase, the pyrene chromophores are usually already in close proximity and often, e.g. in the crystal, arranged in sandwich-type pairs. However, for the excimer formation, a displacement leading to closer and/or differently oriented arrangement is still needed. This excimer emission can also be indirectly used to detect the aggregation process of pyrene derivatives.[10,15,16] These characteristic properties have been employed in the investigation of pyrene-based tweezer molecules[17] and multimolecular aggregates of micelles and membranes[18], the gelation detection of organic low-molecular-weight

compounds[19], the inspection of the active sites of enzymes[20], the molecular recognition process of artificial receptors[21] and DNA sequences,[22] and in the detection of nitroaromatic explosives.[23]

Herein, we use pyrene derivatives to study the influence of H-bonding and steric effects on the coupling behavior of the chromophores in different phases. For that purpose a set of four compounds was synthesized comprising of a benzene or a 4-*tert*-butyl benzene group connected to the pyrene via a methylene-ester or -amide linker (Figure 1). The methylene group breaks the conjugation between the dye and the rest of the molecule, hence, the optical properties of the pyrene is not directly influenced by the linker and the benzene substituent. However, indirect influence is possible due to the potential formation of H-bonds in the case of the amide compounds and due to steric effects arising from the additional *tert*-butyl group.

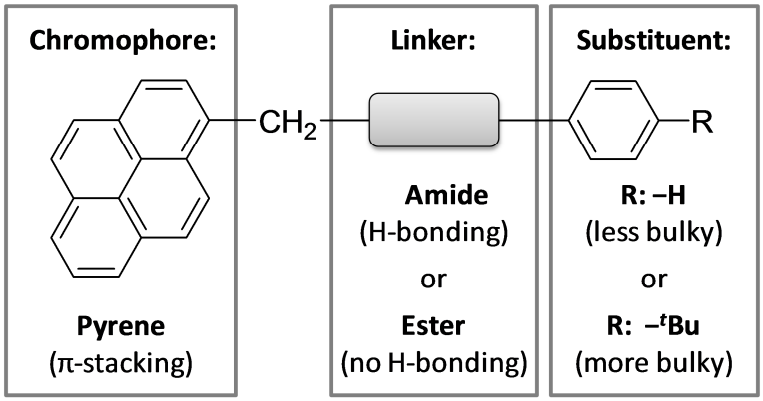

Figure 1. Pyrene derivatives consisting of different linker and substituents separated by a methylene group from the chromophore.

Results and Discussion

Synthesis and thermal properties

The synthetic routes to pyrene-based ester derivatives **1a-b** and their corresponding amide derivatives **2a-b** are shown in Scheme 1. (1-Pyrenyl) methanol was reacted with benzoic acid chloride or *p*-(*tert*-butyl) benzoic acid chloride in chloroform and triethylamine as base to obtain the two ester compounds **1a-b**. For the amide compounds **2a-b** the same acid chlorides were reacted with (1-pyrenyl) methylamine in dry *N*-methyl-2-pyrrolidone (NMP) and pyridine as base. All products are insoluble in apolar solvents and show moderate solubility in THF, chloroform, dioxane and DMSO.

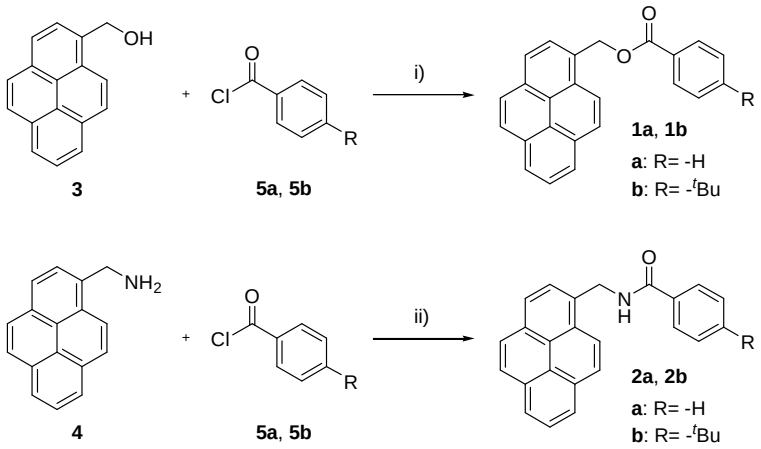

Scheme 1. Synthesis of pyrene derivatives with ester linker **1a-b** and amide linker **2a-b**. i) chloroform, triethylamine, DMAP, 60 °C; ii) NMP, pyridine, 80 °C.

The thermal properties of compounds **1a-b** and **2a-b** were determined by differential scanning calorimetry (DSC). Upon first heating, the ester compounds **1a** and **1b** exhibit melting points (T_m) at 133°C and 140°C, respectively. Both compounds do not crystallize upon cooling forming a vitrified supercooled liquid. Consequently, upon second heating **1a** and **1b** feature glass transitions with temperatures (T_g) at 4°C and 23°C. On further heating, only **1a** recrystallizes at 70°C and subsequently melts at 130°C. As expected, the glass transition temperature is shifted to higher temperatures for compound **1b** due to the bulky *tert*-butyl-group. In contrast, the amide compounds **2a** and **2b** possess a more pronounced crystalline behavior. Upon first heating the melting points were detected at 199°C and 248°C, respectively; while upon cooling both compounds crystallize at 123°C and 178°C. Upon second heating **2a** features a glass transition at 54°C and recrystallize at 114°C indicating incomplete crystallization upon cooling. In contrast, compound **2b** exhibits complete crystallization upon cooling. Hence, to determine its glass transition temperature, an amorphous sample was prepared by rapid quenching from the molten state. The first heating curve reveals the T_g at 77°C. Similar to the ester compounds, the T_g and the T_m increase with the introduction of the *tert*-butyl-group. A significant difference between the ester and the amide compounds are higher T_m (70°C to 100°C) and T_g (50°C) values for the latter. This result is a consequence of the formation of intermolecular H-bonds by the amide units. A similar shift of T_g and T_m to higher temperatures by substituting ester with amide linkages was recently also reported for trisazobenzene derivatives.[24]

Table 1. Thermal properties of amide and ester compounds determined from DSC measurements (Heating and cooling rate: 20 °Cmin^{-1} under N_2)

	T_m / °C (first/second heating)	T_{cryst} / °C (cooling)	$T_{recryst}$ / °C (second heating)	T_g / °C (on heating)
1a	133/130	-	70	4[a]
1b	140/ -	-	-	23[a]
2a	199/196	123	114	54[a]
2b	248/245	178	-	77[b]

[a] Determined from second heating.
[b] Determined upon first heating of a previously quenched sample.

Structural influences on the pyrene interaction in diluted to concentrated THF solution

In this section we first focus on discussing the photophysical properties inherent to all four pyrene-derivative before then considering the differences resulting from the substitutents. *The UV-Vis absorption spectra* were recorded at different concentrations in THF solution and are shown in Fig. 2 exemplary for **1a** and for all compounds in the supporting information Figure S1. For all absorption measurements 1 mm cuvettes were used to account for the high concentrations at which the measurements were performed keeping the maximum OD values below 3. All four compounds show almost identical absorption characteristics (**1a-b**, **2a-b**), which proves the electronic decoupling of the chromophore from the substituent by the methylene spacer. The absorption closely resembles that of pyrene. It shows a very weak feature at about 375 nm and two intense bands, one in the 350-300 nm range and one from 280-240 nm. By comparison with the pyrene spectrum these features can be readily assigned. The weak 375nm feature is the symmetry-forbidden $S_0 \rightarrow S_1$ transition in pyrene, the first intense band with a (0-0) peak at 344 nm and vibronic replicas at 326 nm, 313 nm and 301 nm corresponds to the pyrene $S_0 \rightarrow S_2$ transition and the peak at 278 nm is due to the pyrene $S_0 \rightarrow S_3$ (0-0) transition, with vibronic replicas at shorter wavelength.[25] Those characteristics are likewise reported in literature for similar pyrene derivatives.[15]

An interesting detail concerns the relative intensities of the vibrational peaks at different concentrations. The curves in Figure 2 are normalized to the peak maximum of the (0-1) transition of S_2 at 326 nm, which enables a comparison of the absorption intensities originating from the different vibrational transitions $A_{(0-0)}$, $A_{(0-1)}$, $A_{(0-2)}$, and so forth. With increasing concentration, $A_{(0-0)}/A_{(0-1)}$ decreases while the ratio of the (0-1) transition to higher transitions is almost identical. A similar behavior is also seen for the vibrational structure of the third electronic excitation. This is unusual. A relative reduction of the 0-0 peak intensity compared to the 0-1 has been reported for the S_1 state of perylene bisimide dyes and of the polymer P3HT. In both cases, it has been taken as indication for the formation of weakly interacting H-aggregates.[26,27] Higher electronic excitations have not been considered explicitly so far in this framework. For the best of our knowledge, this is the first experimental report explicitly describing such behavior in the excitation of two higher electronic states. We note, though, that Winnik, in a review article, also noticed a reduction in relative 0-0 peak height with increasing degree of pyrene association.[10] Winnik assessed this by considering the 0-0 peak height and comparing it to the intensity of the minimum between the 0-0 and the 0-1 vibrational peak. In view of todays knowledge on electronic interactions between molecules,[26,28] we consider that the reduction of the 0-0 peak in S_2 and S_3 in the pyrene derivatives may be taken to indicate the formation of such a weakly interacting H-aggregate, i.e. associations of pyrene molecules that electronically interact already in the ground state.

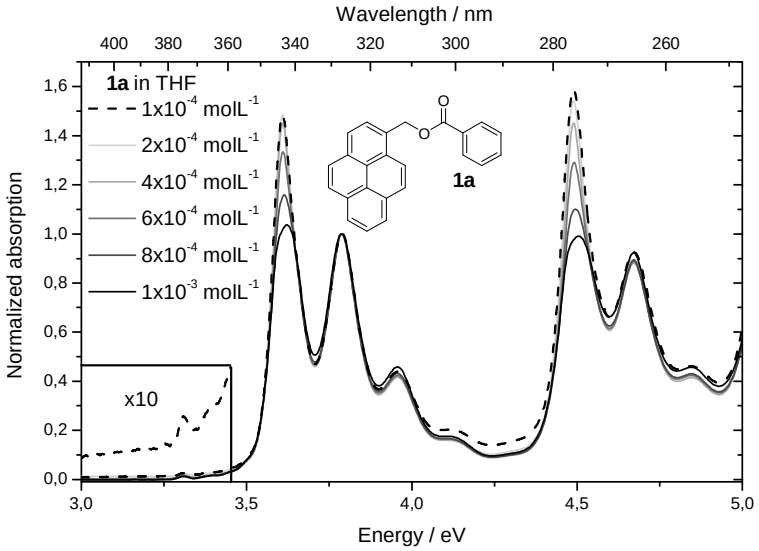

Figure 2. UV-Vis absorption spectra of compound **1a** at different concentrations from $1 \cdot 10^{-4}$ to $1 \cdot 10^{-3}$ molL^{-1} in THF normalized to the (0-1) transition at 326 nm; the enlargement shows the 10 times magnified transition to the first electronically excited state for the concentration of $1 \cdot 10^{-4}$ molL^{-1}.

In the same concentration range ($1\cdot10^{-4}$ molL^{-1} - $1\cdot10^{-3}$ molL^{-1}), *dynamic light scattering (DLS) measurement*s were conducted to obtain an indication for the size of the aggregates. We used a laser beam of 632.8 nm wavelength to avoid the excitation of the pyrene units during the measurements. For all compounds (**1a-b**, **2a-b**) the obtained scattering signal implies that at a concentration of $1\cdot10^{-4}$ molL^{-1} in THF, the size of any supramolecular aggregates is below the detection threshold, whereas particles of at least a few tens of nm in size are detected at concentrations above $1\cdot10^{-3}$ molL^{-1}. From the DLS measurements we cannot give a reliable size-distribution of the particles as the supramolecular aggregates are non-spherical in all cases. The morphology of the supramolecular aggregates at concentrations of $1\cdot10^{-2}$ molL^{-1} was visualized by (SEM) using freeze-dried samples from dioxane (Figure S2.1 and S2.2).

The steady state photoluminescence (PL) spectra of the compounds in THF were investigated at different concentrations ranging from $6\cdot10^{-6}$ to $6\cdot10^{-2}$ molL^{-1}. The spectra are displayed in Figure 3. The evolution of the monomer fluorescence intensity and the relative $A_{(0\text{-}0)}/A_{(0\text{-}1)}$ absorption peak height with concentration is shown in Figure 4. All compounds (**1a-b**, **2a-b**) show the same concentration-dependent PL properties. At low concentrations, the PL spectrum shows a vibrational structure that is characteristic for the $S_1 \rightarrow S_0$ fluorescence of molecularly dissolved pyrenes.[29] With increasing concentration, a broad unstructured emission appears, centered at around 470 nm, that is typical for the excimer fluorescence of pyrene. All four compounds (**1a-b**, **2a-b**) show an identical excimer fluorescence at a concentration of $6\cdot10^{-2}$ molL^{-1}, which confirms the formation of the same excimer species in all cases (Figure S3). This excimer fluorescence is first barely discernible at a concentration of $6\cdot10^{-4}$ molL^{-1} (and more clearly visible at $1\cdot10^{-3}$ molL^{-1}) and then increases in intensity with concentration. In contrast, when considering the intensity of the monomer fluorescence, the intensity increases with concentration until, at $2\cdot10^{-5}$ molL^{-1}, it reaches its maximum and then reduces drastically. The ratio of $A_{(0\text{-}0)}/A_{(0\text{-}1)}$ in absorption remains constant up to a concentration of $3\cdot10^{-4}$ molL^{-1} and then drops steeply.

For the interpretation of this data it is important to recall that the three spectroscopic signatures, i.e. the monomer fluorescence, the excimer fluorescence and the $A_{(0\text{-}0)}/A_{(0\text{-}1)}$ absorption peak height indicate distinct photophysical processes. (i) The sudden decrease of the $A_{(0\text{-}0)}/A_{(0\text{-}1)}$ ratio in absorption gives the concentration at which ground state association begins to occur. In Fig. 4, this is highlighted by a grey shading. In contrast, (ii) the fluorescence quenching at a much lower concentration marks the regime where some interaction takes place in the excited state of the molecule, leading to a non-emissive species. This species cannot be the sandwich-type pyrene excimer identified by Birks[11] for the following reason. The quantum yield of emission of the pyrene monomer and the pyrene excimer observed by Birks are comparable, e.g. in cyclohexane solution being 0.65 for the monomer and 0.75 for the excimer and

in toluene solution being 0.52 and 0.55, respectively.[25] If the excited monomer were to result in an excimer, according to the reaction M+M*→E* (E* denotes the excimer (M+M)*), the reduction of monomer fluorescence should be accompanied by a concomitant growth of excimer fluorescence. In the experiment, this is, however, not the case. We therefore come to the conclusion that the quenching of monomer fluorescence in the intermediate concentration regime ($1\cdot10^{-5}$ molL^{-1}-$3\cdot10^{-4}$ molL^{-1}) indicates the formation of a non-emissive precursor-type species. At this stage, we can only speculate on the nature of this species. It is conceivable that the molecular approach and orientation required for the formation of an emissive excimer is impeded in compounds **1** and **2** by the substituents, so that only a non-emissive precursor can be formed. (iii) We now focus our attention on the experimental observation that excimer fluorescence is only observable at concentrations in excess of $6\cdot10^{-4}$ molL^{-1}, yet not at lower concentration. From the $A_{(0\text{-}0)}/A_{(0\text{-}1)}$ ratio we know that ground-state associates prevail in this regime, and the DSL measurements tell us these evolve into supramolecular aggregates of a few tens of nm for concentrations above $1\cdot10^{-4}$ molL^{-1}. This implies that for the pyrene-derivatives **1** and **2**, the formation of emissive excimers requires a kind of ground state stabilization that is only available in the environment provided by supramolecular aggregates.

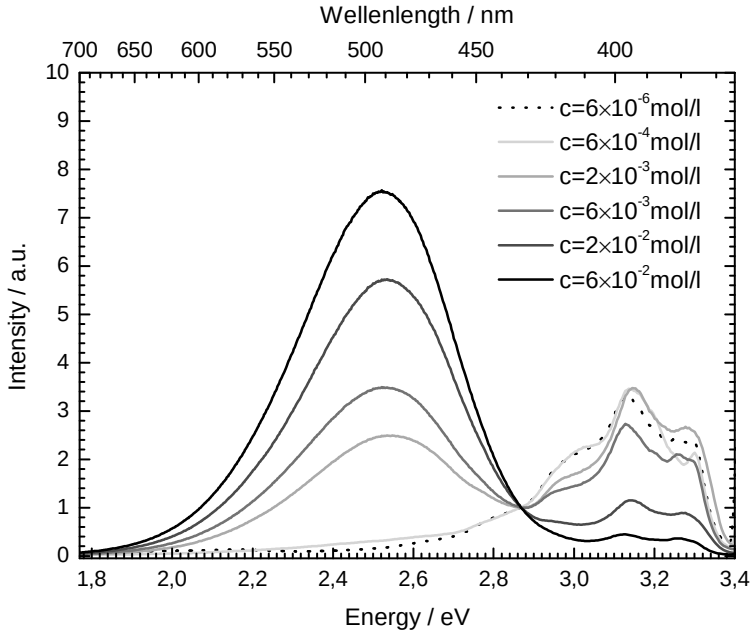

Figure 3. Photoluminescence spectra of compound **2b** at different concentrations from $6\cdot10^{-6}$ to $6\cdot10^{-2}$ molL^{-1} normalized at 434 nm.

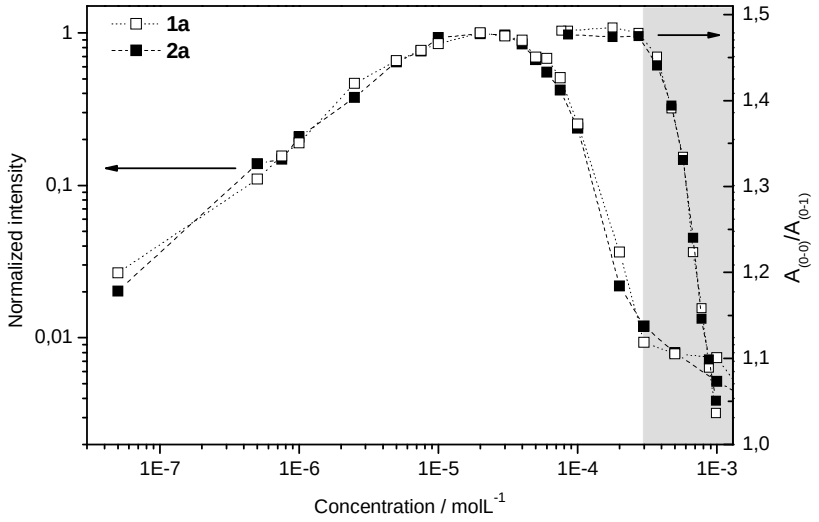

Figure 4. Photoluminescence intensities of the (0-0) transition at 375 nm (left) and the ratio of $A_{(0-0)}/A_{(1-0)}$ (right) of compounds **1a** and **2a** at different concentrations. The shaded area depicts the concentration range in which the formation of starts to occur.

While the decay of the monomer fluorescence with increasing concentration is almost identical for all compounds, a small variation in the ratio of monomer to excimer fluorescence intensity can be observed for the different substituents. In order to evaluate how the excimer formation is affected by chemical modification, we have determined the excimer formation rates using *time-resolved photoluminescence* measurements and analyzing the associated rate equations analogous to the approach taken by Birks et al. in 1963. Birks and coworkers described excimer formation as a process of the type M+M*⇌E* that takes place with a concentration-dependent rate $k_{FM}[M]$ for the forward reaction (excimer formation) and a concentration-independent rate k_{ME} for the back reaction (excimer dissociation).[12] Here, [M] is the concentration of monomers. In addition, the deactivation processes M*→M and E*→M+M are considered with rates k_M and k_E, respectively. After pulsed excitation, the decay of M* and E* is then described by the rate equations $d[M^*]/dt=-(k_M+k_{EM}[M])[M^*]+k_{ME}[E^*]$ and $d[E^*]/dt=-(k_E+k_{ME})[E^*]+k_{EM}[M^*]$. These two coupled differential equations can be solved to give two concentration-dependent decay constants λ_1 and λ_2 from which the excimer formation rate k_{EM} can be extracted by a linear fit to the concentration-dependence since $\lambda_1+\lambda_2=k_M+k_E+k_{ME}+k_{EM}[M]$.[12]

For the pyrene derivatives investigated here, we need to consider that the excimer is evidently not formed by the association of two monomers but that it is preceded by the formation of ground-state associates. As we have no experimental information on the number of electronically interacting molecules in these associates, we take the heuristic approach of considering dimers. The excimer formation is then described as D+D*⇌E*+D with $k_{ED}[D]$ and k_{DE} being the forward and back reaction rate. The

deactivation processes are D*→D and (E*+D)→(D+D) with rates k_D and k_E, respectively. The decay rates can be formulated and analyzed analogously to the Birks-1963 model, $d[D^*]/dt=-(k_D+k_{ED}[D])[D^*]+k_E[(E^*+D)]$ and $d[(E^*+D)]/dt=-(k_E+k_{DE})[(E^*+D)]+k_E[D^*]$. The signals to monitor as function of concentration are then the fluorescence of the (dimer stabilized) excimer (E*+D) at 470 nm and the fluorescence of the excited dimer D*. What is the spectral signature of the dimer fluorescence? Since the dimer is of a weakly interacting H-aggregate type, as suggested by the absorption spectra, the emission is at the same spectral position than the monomer emission, albeit of a different, i.e. weaker oscillator strength. The signal to monitor is therefore the emission at 400 nm.

We have thus measured the photoluminescence decay of the compounds in THF at different concentrations ranging from $2\cdot10^{-4}$ molL^{-1} to $6\cdot10^{-2}$ molL^{-1} using a time-correlated single photon counting (TCSPC) set up. The chromophores were excited with a 375 nm laser and the time-dependent spectra were recorded at 400 nm and at 485 nm. The typical change in the fluorescence decays with increasing concentration is shown in Figures 5 for compound **2a**, along with the concentration-dependence obtained for the decay constants λ_1 and λ_2. The decay curves show a build-up of the excimer emission (grey curve) at short times, e.g. below 50 ns at $5.7\cdot10^{-4}$ molL^{-1} and below 10 ns at $6\cdot10^{-2}$ molL^{-1}, followed by a mono-exponential decay. The dimer emission at 400 nm (black curve) also decays mono-exponentially. The decay of the dimer fluorescence (black curve) becomes faster with increasing concentration as the formation of excimers gets more likely. The excimer fluorescence (grey curve) increases in the beginning due to the time-delayed formation of the excimer species after the initial excitation of the monomer. The excimer fluorescence reaches, as expected, its maximum faster with increasing concentration. From those curves, the decay constants λ_1 and λ_2 can be determined and can be plotted against the concentration of monomers (= twice the dimer concentration) (Figure 5). The dependence of their sum on the concentration agrees well with the linear relationship suggested by the kinetic model and gives, a posteriori, further support to the heuristic approach taken. Fitting the data with the equations from Birks et al. yields the relevant values of k_{ED} (Table 2). The entire approach is portrayed in more detail in the supporting information (Figure S4, S5).[12]

The excimer formation rates (k_{ED}) found in this way for all four compounds (**1a-b**, **2a-b**) for the formation of excimers from pre-existing dimers are between $6.9\cdot10^9$ and $3.9\cdot10^9$ Ls^{-1}mol^{-1}. This agrees well with the value of $6.7\cdot10^9$ Ls^{-1}mol^{-1} determined by Birks et al. for the formation of excimers from individual monomers in the unaltered pyrene[12]. Within the four compounds the ones with the bulky *tert*-butyl group **1b** and **2b** show the lowest excimer formation rates of approximately $3.9\cdot10^9$ Ls^{-1}mol^{-1}. We attribute this to sterical hindrance. For both, the –H and –^{t}Bu substituted compounds

the one with the ester linker **1a** and **1b** show higher excimer formation rates than the corresponding amide compound **2a** or **2b**. Hence, the amide linker does not favor the formation of an excimer but hinders it.

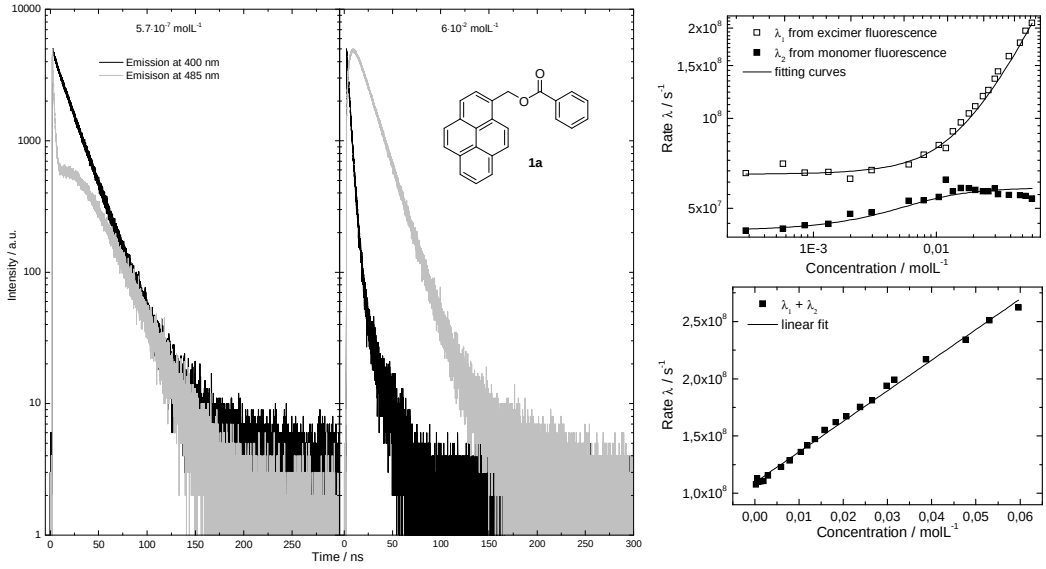

Figure 5. Time resolved photoluminescence transients of compound **1a** at $5.7 \cdot 10^{-4}$ molL^{-1} (left) and $6 \cdot 10^{-2}$ molL^{-1} (middle) showing the fall-off of the emission at 400 nm (black) and at 485 nm (grey). Right top: Fall-off rates λ_1 and λ_2 of the emission at 485 nm (□) and at 400 nm (■) at different concentrations for compound **1a** fitted according to Birks. Right bottom: Sum of λ_1 and λ_2 plotted against the concentration yielding the expected linear dependency.

Table 2. The excimer formation rates for pyrene and the four compounds **1a-b** and **2a-b** determined from the TCSPC measurements.

	Pyrene[a]	**1a**	**2a**	**1b**	**2b**
k_{ED} [$10^9 \cdot$ Ls^{-1}mol^{-1}]	**6,7**	6,88	5,34	3,96	3,96

[a] Value was determined by Birks et al.[12]

We now summarize the insight gained from the spectroscopic investigations in solution. At low concentrations, i.e. below $1 \cdot 10^{-5}$ molL^{-1}, the four compounds (**1a-b**, **2a-b**) are molecularly dissolved in THF. In an intermediate concentration range (about $1 \cdot 10^{-5}$ molL^{-1}- $3 \cdot 10^{-4}$ molL^{-1}), non-emissive intermediate species are formed. They quench the monomer fluorescence yet do not impinge on the absorption spectra, implying that they may be viewed as a non-emissive precursor to an excimer state. At increased concentrations, i.e. above $3 \cdot 10^{-4}$ molL^{-1} weakly interacting ground state H-aggregates are formed. In contrast to unaltered pyrene, in the compounds (**1a-b**, **2a-b**)

with the comparatively large side chains, the formation of emissive excimers requires a stabilization evidently provided by the aggregate. A significant influence of the structural variations, namely the linker moiety (ester or amide) and the sterical hindrance of the substituted benzene unit on the optical and aggregation properties in THF cannot be observed. Therefore, we conclude that the pyrene chromophores, which are coherently present in all compounds, are the crucial and determining part of the compounds in this concentration regime. Only a closer look at the excimer fluorescence and the excimer formation rates reveal the influence of the variable substitutions on the pyrene chromophore. The ester compound **1a** is most feasible to form excimers. The introduction of the *tert*-butyl group strongly hinders the excimer formation. The same effect is observed much weaker when the ester group is replaced with an amide linker. The influence of the linker and the bulky *tert*-butyl group on the pyrene chromophore is just secondary and only observable at concentrations where supramolecular aggregates are present.

Structural influences on the pyrene interaction in thin films

Thin films were prepared as detailed below and investigated in two morphologies, an optically isotropic one and a crystalline one, by using *polarized optical microscopy* (POM), *absorption and fluorescence spectroscopy*, and in the case of the amide compounds also by *FT-IR spectroscopy*. The POM images of the crystalline films are presented in the supporting information (Figure S7).

Optically isotropic films: All compounds (**1a**-**b, 2a**-**b**) were spin coated from THF solution at a concentration of $5 \cdot 10^{-2}$ molL^{-1}. At this concentration supramolecular aggregates are present in solution as previously demonstrated in DLS experiments. The fresh films were optically transparent and no crystalline structure could be observed by POM. The absorption spectra are similar for all compounds (Figure S6) and closely resemble that observed in concentrated solution, except for a slight red-shift. Interestingly, the $A_{(0\text{-}0)}/A_{(0\text{-}1)}$ ratio is slightly lower in concentrated solution (about 1.0 for concentrations of $1 \cdot 10^{-3}$ molL^{-1} and above) than in the thin film (about 1.1). This implies that electronic coupling within aggregates is slightly stronger in solution than in the film, presumably because the local geometry can be optimized more in solution as compared to film. The room-temperature photoluminescence spectra of the fresh films of all investigated compounds do not show any monomer fluorescence. Instead, they show only the same excimer fluorescence that was already observed in concentrated solution, except that the center wavelength shifts from 470 nm in solution to 500 nm in the film due to the different dielectric constant (Figure S8).

From the solution measurements we know that, in contrast to unsubstituted pyrene,

the substituted derivatives (**1a**-**b, 2a**-**b**) only show excimer emission when the excimer geometry is stabilized within a ground state associate. Thus we can interpret the thin film PL data such as to indicate the presence of aggregates in the film. This is not surprising. For example, for the polymers poly(9,9'-dioctyl-fluorene) (PFO) and poly(3-hexylthiophene) (P3HT), it is well known that aggregate formation is enhanced in thin films upon spin-coating when aggregates already existed in the solution used. [30] The absence of any monomer fluorescence suggests that either no monomers are present, or, any excited monomer state is quenched by energy transfer either to non-emissive states such as the states observed in solution at intermediate concentration or to emissive excimers.

Crystalline films: The PL spectra are different when the films are processed such as to obtain a crystalline structure. To induce crystallization, the fresh films of amide **2a** and amide **2b** were annealed above T_g at 80°C and 130°C. The observation of light transmission under crossed polarizers in an optical microscope confirms the presence of crystalline structures in the film (Figure S7). To obtain further insight into the structural changes associated with the crystallization process, FT-IR studies were performed on the films of the amide compounds (**2a**-**b**) in the isotropic and crystalline state. For both compounds, a shift of the N-H and the carbonyl stretching vibration to lower wave numbers as well as an increase in the IR absorption intensity is observed during the crystallization process. Both changes in the FT-IR spectra strongly indicate the formation of strong hydrogen-bonds.[31] The shift of the N-H and carbonyl stretching vibration from 3312 cm^{-1} to 3281 cm^{-1} and from 1637 cm^{-1} to 1629 cm^{-1}, respectively, is shown exemplarily for compound **2a** in Figure 6. Amide **2b** exhibits the same trend but much less pronounced. This indicates weaker hydrogen-bonds due to the steric hindrance of the *tert*-butyl group (Figure S10).

For the ester compounds, a different approach needed to be taken to obtain crystalline films. Unlike the amide compounds, the fresh films of the ester compounds exhibited dewetting at elevated temperatures. Therefore, they were aged at room temperature in the dark for several months to induce crystallization, as confirmed by POM. Hence, in all cases we were able to convert the optically isotropic fresh film into one containing crystallites. The aging and annealing processes were conducted until a stable state was achieved and no further changes could be observed in the POM, FT-IR and photoluminescence spectra at room temperature.

For all compounds except **1b**, the photoluminescence spectra change upon crystallization. During this process, the excimer emission is reduced and simultaneously a structured higher-energy emission rises. This is exemplarily shown in Figure 7 for ester **1a**.

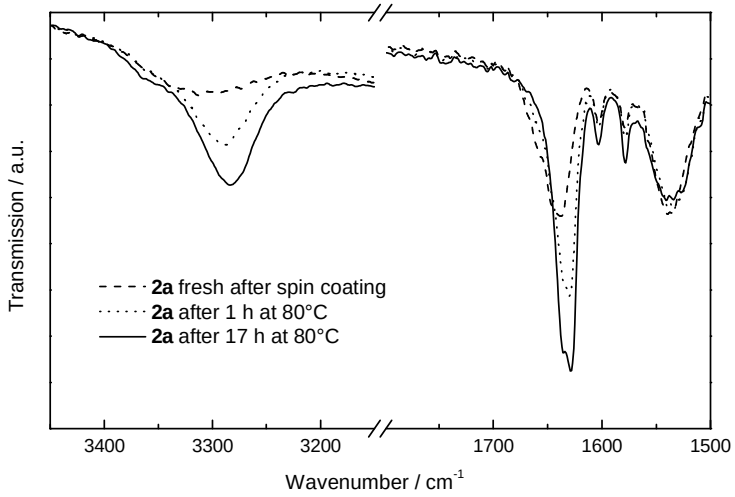

Figure 6. Enlargements of the relevant parts of the FT-IR spectra of a thin film of compound **2a** during the aging process resembling different degrees of crystallization; the N-H stretching vibration (left: around 3300 cm^{-1}) and the carbonyl stretching vibration (right: around 1630 cm^{-1}) are represented.

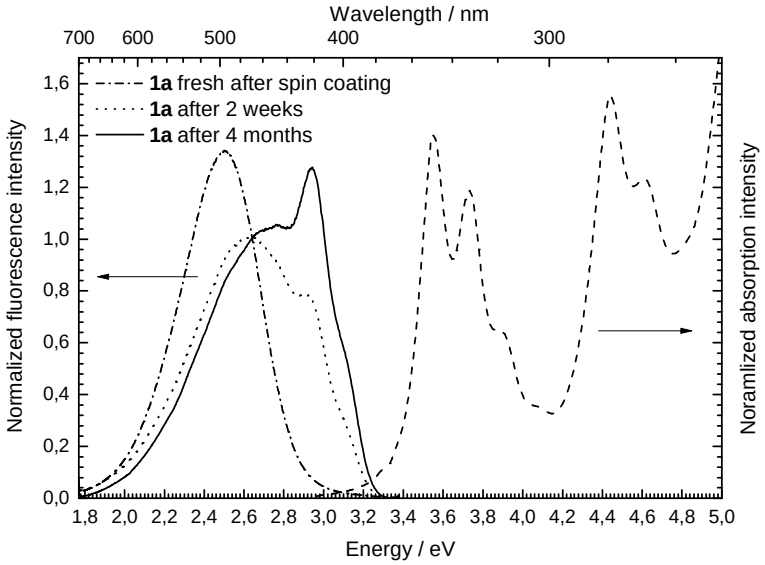

Figure 7. Absorption (right) of a amorphous thin film of compound **1a** directly after spin coating and photoluminescence spectra (left) of a thin film of compound **1a** during the aging process resembling different degrees of crystallization.

For a clearer understanding of the molecular behavior in the crystalline state, the thin film photoluminescence was investigated as a function of temperature upon heating from 5 K to 295 K. The spectra at selected temperatures are shown in Figure 8. For all compounds except **1b**, the excimer fluorescence vanishes gradually upon decreasing the temperature, while simultaneously the structured higher energy fluorescence intensity rises. At 5 K, only the structured higher energy emission prevails. In contrast, compound **1b** shows exclusively excimer fluorescence even at 5 K. In general, the

relative fraction of excimer emission compared to the higher energy emission is higher in compounds **1b** and **2b** containing the sterically demanding *tert*-butyl group compared to compounds **1a** and **2a**, that only contain a –H atom instead. The relative amount of excimer emission is also higher in the ester-containing compounds (**1a** and **1b**) compared to the amide-containing compounds (**2a** and **2b**).

To understand the changes that take place in the electronic structure upon crystallization, let us first recall that compound **2a** allows for the most ordered structure due to the effect of the H-bonding amide moieties. On the other hand, the sterically demanding *tert*-butyl group and the absence of the stabilizing amide group implies that compound **1b** is likely to have the least ordered structure. This correlates with the fact that compound **2a** shows the lowest relative amount of excimer emission while **1b** exhibits purely excimer emission. Evidently, excimer formation is prevented upon crystallization, while it is promoted by aggregates. This is different to the situation in unsubstituted pyrene, where excimers are formed in the crystalline state. In fact, in pyrene crystals, the basis of the unit cell is formed by sandwich-type dimer pairs of pyrene-molecules that slip horizontally upon photoexcitation to form an excimer.[9,25]

How can we understand the absence of excimer emission in crystallites of the substituted pyrene-derivatives? The aggregates prevailing in the optically isotropic film and the crystallites in the films evidenced by the POM patterns differ in the degree of structural order. We propose that the aggregates that are formed in solution or in the non-equilibrium structure of a spin-cast film will be subject to a certain amount of structural variation with regard to molecular orientation or distance. Further, intermolecular distance between two pyrenes may vary at the interface between the ends of two aggregates. Some of these local geometries may be suitable for excimer formation after photoexcitation. As mentioned above, the fact that in freshly spun films only excimer fluorescence is observed implies that there is an excimer-site within the exciton diffusion range of any photoexcited chromophore. In contrast, the structure within the crystallites is, by definition, more regular and, as experiment tells us, of a kind that does not allow for excimer formation. It seems that the horizontal slip movement that results in excimers in unsubstituted crystalline pyrene is impeded by the large sidechain in substituted crystallized pyrene. Thus, upon crystallization, the number of sites that allow for excimer formation therefore reduces, as manifested in Figure 7.

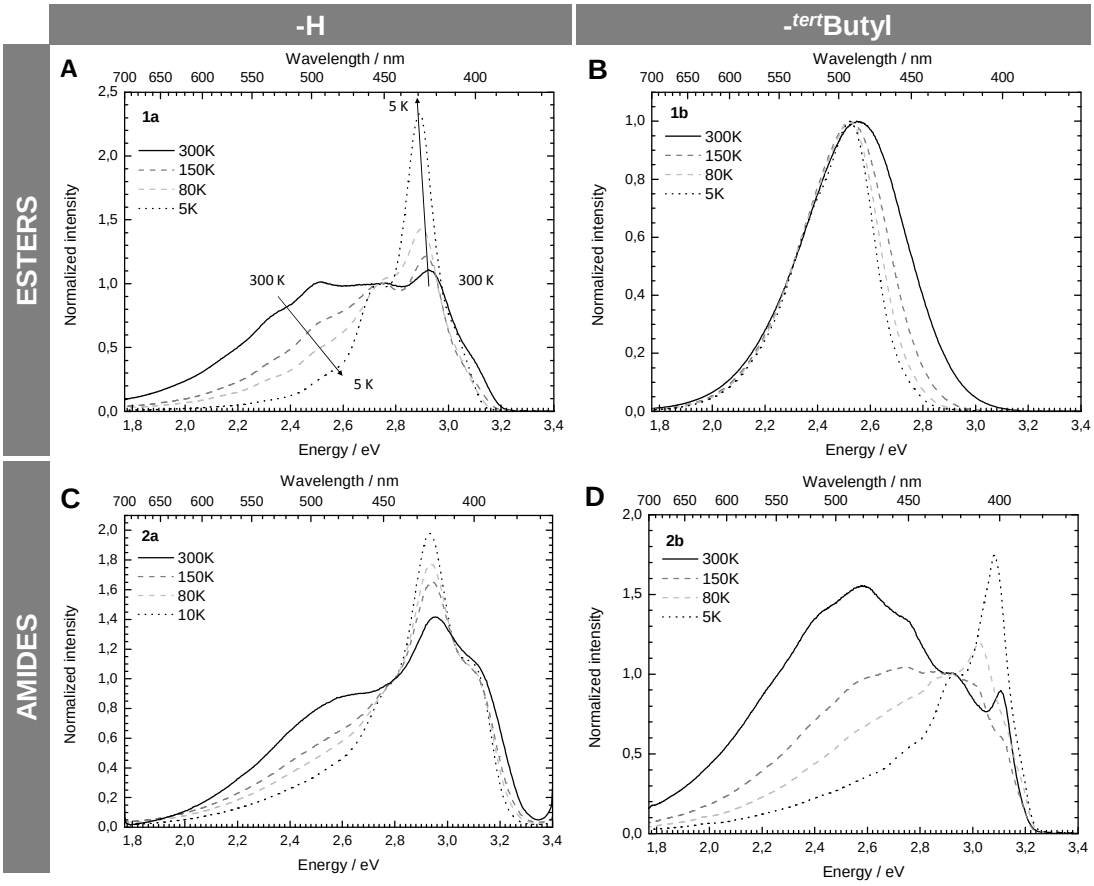

Figure 8. Photoluminescence spectra at different temperatures from room temperature to 5 K of the four compounds **1a** (A), **1b,** (B), **2a** (C) and, **2b** (D) in crystallized thin films. For a comprehensive representation, graph A was normalized at 2.73 eV, graph B at the maximum intensity, graph C at 2.78 eV and, graph D at 2.93 eV. For compound **1a** the decrease of the excimer fluorescence and the increase in monomer fluorescence with reduced temperature are indicated with arrows. This is also commonly observed for compounds **2a** and **2b**.

In this framework, we can interpret the results of Figure 8. For compound **1b**, which is structurally most disordered, excimer emission is observed at all temperatures even when the light transmission in the POM indicates that crystallites have been formed. This leads to two conclusions. First, in this compound, the remaining structural inhomogeneity is sufficient to result in sites for excimer formation and / or monomer quenching within the exciton diffusion range of each chromophore. Second, since excimer emission occurs at 5 K, it does not require any activation energy. This confirms that sites with molecules already in the excimer geometries must be pre-existing. In passing we point out that the increasing blue-shift of the high-energy emission tail with increasing temperature is an exceptionally nice example for the increase in thermal equilibrium energy in a Gaussian density of states.[32] We now turn to compounds **1a**, **2a** and **2b**. At 5 K, these compounds show a structured emission with a 0-0 peak at 400 nm and a 0-1 peak at about 425 nm. The relative intensity of the vibrational peaks varies between the compounds. This emission can be attributed to the pyrene

monomer unit, possibly slightly modified by weak H-type interaction. (Since the $S_1 \rightarrow S_0$ transition in pyrene is symmetry-forbidden, one cannot distinguish whether the 0-0 peak height is modified due to symmetry-selection rules or due to weak H-type interaction). At 5 K, spectral diffusion of singlet excitons is reduced. Evidently, structural order in the crystalline compounds **1a**, **2a** and **2b** is increased such that there are no sites with excimer geometry within reach at 5 K. At elevated temperatures, the exciton diffusion range increases so that some excimer sites can be populated and a spectrum showing both, monomer and excimer fluorescence results.

Structural influences on the pyrene interaction – Molecular Modeling

The conclusions drawn so far on the basis of spectroscopic data are well supported by molecular modeling of the crystallite structure. In order to assess, how the molecules pack, the geometry of the monomers of the esters **1a, 1b** and the amides **2a, 2b** were optimized using the B3LYP functional and basis set 6-31G. The optimized structures, together with the predicted partial charges, were used to build and optimize the structure of the aggregates by means of Molecular Mechanics (MM), from which qualitative results could be obtained (Figure 9).

As expected, the π-π stacking of the pyrene moieties is the dominant driving force towards self-aggregation. This can be seen from the almost parallel orientation of the chromophores in all cases. The distance between the pyrene units is approximately 3.50 Å in the calculated hexamer aggregates, which is in good agreement with crystal structure data of stacked pyrenes featuring a distance of 3.53 Å.[29] In the case of the amide compounds **2a** and **2b** additional H-bonds are observed in the MM calculations with O-H distances of 1.92 Å and 2.17 Å, respectively. The longer O-H distance of compound **2b** indicates weaker H-bonds than in the case of compound **2a** which can be attributed to the additional bulky *tert*-butyl group. This is in perfect agreement with the previous results from the FT-IR measurements. Furthermore, the sterically demanding *tert*-butyl group of compound **2b** enforces a slight twist in the molecular structure within the calculated hexamer aggregate.

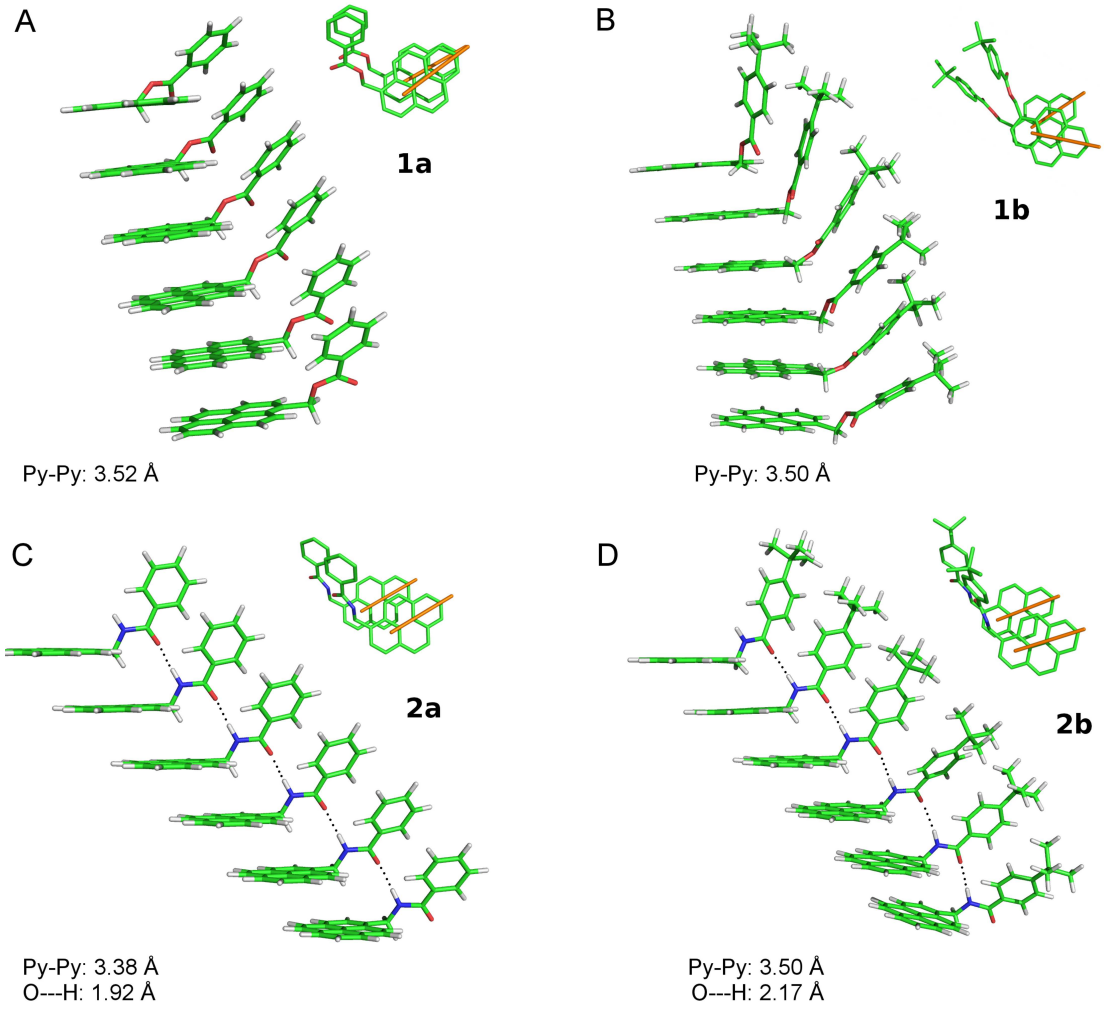

Figure 9. Molecular mechanics geometry optimization of hexamer aggregates of the esters **1a** (A) and **1b** (B) and the amides **2a** (C) and **2b** (D) with the corresponding top views of two stacked molecules. The two orange lines represent the twist of two adjacent pyrene chromophores. Additionally, the distance between two pyrene chromophores and in the case of the amide compounds **2a-b** the O-H distance of the H-bonding amide moieties are stated. The geometry of the monomers was optimized with DFT.

Although in general π-π stacking of the pyrene moieties is present in all calculated hexamer aggregates, slight differences can be observed in the relative orientation of the chromophores. While ester compound **1a** features an almost perfect π-π stacking of the pyrene units an increasing parallel offset is observed for compound **2a** and **2b**. Additionally, in the hexamer aggregate of compound **1b** a rotational twist of adjacent pyrene units is present (orange lines Figure 9). In compound **1a** the π-π stacking of the pyrene chromophores is the only intermolecular interaction. The columnar stacking is increasingly disturbed by the introduction of the amide and the *tert*-butyl moiety. The results from the molecular modeling calculations are in good agreement with the previous discussion on thin film properties, whereas the solution properties differ. In the film the steric demand and disorder introduced by the *tert*-butyl group (Figure 9B,D) correlates well with the enhanced propensity to form excimers which

was already observed in the low temperature photoluminescence measurements (Figure 8B,D). Compound **1b**, which has, as already assumed previously, the least ordered structure is unique in two ways - it exhibits a strong rotational twist of adjacent pyrene chromophores and shows exclusively excimer fluorescence even after crystallization and at very low temperatures. On the other hand, H-bonding amide groups as well as the lack of the sterically demanding *tert*-butyl group promote a more ordered structure reducing the propensity to form excimers in the crystalline state. Note that in the crystalline state, unlike the unchanged pyrene, the investigated molecules (**1a-b**, **2a-b**) do not arrange in a sandwich-type structure but seem to exhibit equidistance.

Conclusion

In conclusion, we were able to understand the influence of H-bonding amide linkers and sterically demanding *tert*-butyl groups on the π-stacking of pyrene chromophores in different states of matter. This was achieved by carefully studying a set of four pyrene derivatives exhibiting either an ester or amide linker and with or without a bulky *tert*-butyl substituent. The four compounds were investigated from molecularly dissolved solutions up to concentrations where supramolecular aggregates are formed, as well as in spin-cast films in a virgin and in a crystallized state.

The influence of the linker and the steric hindrance on the pyrene stacking gets more significant the closer the molecules are forced together. In dilute solution up to the threshold concentration for the formation of aggregates the molecular behavior is independent of the variable groups, as all four compounds show identical spectra and behavior. The four compounds differ, however, from unsubstituted pyrene. Whereas unsubstituted pyrene readily forms excimers in solution from monomers, in the substituted derivatives excimer formation requires additional stabilization within aggregates. The rate of excimer formation depends on the nature of the sidechain. While the excimer formation rate in the ester compound **1a** is comparable to that of unsubstituted pyrene, excimer formation proceeds slower with the amide linker of compound **2a**, and is reduced even more by the bulky substituents of **1b** and **2b**.

In thin films we find that excimers are readily formed within the supramolecular aggregates present in freshly spin-cast films, yet that excimer formation becomes suppressed by crystallization. Such crystallization can be induced by heating the amide-containing compounds, which develop intermolecular H-bonds, as well as by aging at room temperature in the case of the ester compounds. The amount of structural order in the crystalline state is strongly dependent on the variable groups. H-bonding amide groups in contrast to ester groups promote a more ordered structure, while the sterically demanding *tert*-butyl substituent hinders a highly ordered packing of the

molecules. In the case of compound **1b** this leads to a strong rotational twist of adjacent pyrene moieties and an enhanced propensity to form excimers in the crystalline structure. Compound **2a** on the other hand favors a highly ordered packing resulting in the least amount of excimer fluorescence of all compounds.

With this variety of experiments we were able to understand the molecular behavior and the influence of the variable groups on the pyrene stacking in different states of matter in great detail. This study clearly points out how crucially the molecular design can affect the performance of chromophoric systems.

Experimental Section

Materials and methods:

Solvents were distilled and when necessary dried according to standard procedures. All starting materials were obtained from Aldrich, Alfa Aesar, Fluka or Riedel-de Haën and used without further purification. ^{1}H-NMR spectra were recorded on a Bruker Avance 300 spectrometer. Mass spectra were recorded on a Finnigan MAT 8500 apparatus (EI, 70 eV) using direct injection mode. Elemental analysis (C, H, N) was carried out with an EA 3000 instrument (HEKAtech).

*General synthetic route to pyrenyl substituted esters **1a-b**:*

1-Pyrenyl-methanol (2.5 g, 10.8 mmol) were dissolved in chloroform in a schlenk tube under inert gas. Triethylamine (1.8 mL) and 4-dimethylaminopyridine (DMAP) (50 mg) were added. The solution was cooled to 0°C and benzoic acid chloride (12.0 mmol) was added dropwise. The reaction mixture was boiled for 15 h. After cooling to room temperature, the yellow mixture was filtered (Alox N) and washed with chloroform. The solvent was evaporated and the raw product was dissolved in dichloromethane and extracted subsequently with aqueous HCl (2N), aqueous $NaHCO_3$ (5 %) and water. The solution was dried over Na_2SO_4 and the solvent was evaporated in vacuum.

1a: Yield 2.9 g of a yellow powder (92 %, 8.9 mmol); Rf=0.76 (Hexane/THF 2:1); m.p. 133°C; 1H NMR (300 MHz, [D_6]DMSO, 25°C, TMS): δ=6.11 (s, 2H), 7.50 (m, 1H), 7.64 (m, 1H), 7.98 (m, 1H), 8.08-8.49 ppm (m, 9H); IR: ν˜=1709 cm^{-1} (C=O); UV/Vis (THF): λ_{max} (ε)=344 nm (31924 $mol^{-1}dm^3cm^{-1}$); elemental analysis calcd (%) for $C_{24}H_{16}O_2$ C 85.69, H 4.79, O 9.51; found: C 85.55, H 5.07, O 9.17.

1b: Compound **1b** was recrystallized from toluene. Yield 1.8 g of a yellowish powder (43 %, 4.6 mmol); Rf=0.83 (Hexane/THF 2:1); m.p. 140°C; 1H NMR (300 MHz, [D_6]DMSO, 25°C, TMS): δ=1.52 (s, 9H), 6.09 (s, 2H), 7.50 (d, J=8.4 Hz, 1H), 7.90 (d, J=8.4 Hz, 1H), 8.08-8.46 ppm (m, 9H); IR: ν˜=1717 cm^{-1} (C=O); UV/Vis (THF):

λ_{max} (ε)=344 nm (32819 $mol^{-1}dm^3cm^{-1}$); elemental analysis calc (%) for $C_{28}H_{24}O_2$: C 85.68, H 6.16, O 8.15; found: C 85.66, H 5.95, O 8.39.

*General synthetic procedure to pyrenyl substituted amides **2a-b**:*

1-Pyrenyl-methyl-amine-hydrochloride (2.5 g, 9.4 mmol) was suspended in *N*-methyl-2-pyrrolidone (NMP) in a schlenk tube under inert gas. Dry pyridine (20 mL) and LiCl (0.05 g) was added and the mixture was stirred for 30 min. The solution was cooled to 0°C and benzoic acid chloride (9.4 mmol) was added dropwise and the reaction mixture was stirred for 2 h at 70 °C to yield a yellowish solution. After cooling to room temperature, the mixture was precipitated in ice water (600 mL). The mixtures were filtered to retrieve the solid, which was washed with water and dried under vacuum at 80°C.

2a: Compound **2a** was recrystallized from ethyl acetate/hexane mixture (1:1). Yield 3.1 g of a white powder (98 %, 9.2 mmol); Rf=0.22 (THF/Toluene 1:20); m.p. 199°C; 1H NMR (300 MHz, [D_6]DMSO, 25°C, TMS): δ=5.24 (d, J=5.6 Hz, 2H), 7.45-7.54 (m, 3H), 7.93-7.96 (m, 2H), 8.04-8.54 (m, 9H), 9.25 ppm (t, J=5.6Hz, 1H); IR: ν˜=1625 (C=O), 3266 cm^{-1} (N-H); UV/Vis (THF): λ_{max} (ε)=344 nm (29098 $mol^{-1}dm^3cm^{-1}$); elemental analysis calcd (%) for $C_{24}H_{17}NO$: C 85.95, H 5.18, N 4.18, O 4.77; found: C 85.91, H 5.07, N 3.79, O 5.04.

2b: Compound **2b** was recrystallized from toluene. Yield 2.6 g of a white powder (71 %, 6.6 mmol); Rf=0.31 (THF/Toluene 1:20); m.p. 248°C; 1H NMR (300 MHz, [D_6]DMSO, 25°C, TMS): δ=1.29 (s, 9H), 5.24 (d, J=5.7 Hz, 2H), 7.49 (d, J=8.2 Hz, 2H), 7.89 (d, J=8.2 Hz, 2H), 8.06-8.53 (m, 9H), 9.18 ppm (t, J=5.7 Hz, 1H); IR: ν˜=1633 (C=O), 3311 cm^{-1} (N-H); UV/Vis (THF): λ_{max} (ε)=344 nm (31324 $mol^{-1}dm^3cm^{-1}$); elemental analysis calcd (%) for $C_{28}H_{25}NO$: C 85.90, H 6.44, N 3.58, O 4.09; found: C 85.51, H 6.07, N 3.70, O 4.76.

Differential Scanning Calorimetry (DSC):

The thermal properties were investigated by DSC measurements with a PERKIN-ELMER DSC7 (standard heating rate: 20 K/min) utilizing 10 mg of the compounds.

Dynamic Light Scattering (DLS):

DLS was performed on an ALV DLS/SLS-SP 5022F compact goniometer system with an ALV 5000/E cross-correlator and a He-Ne laser (632.8 nm). All measurements were performed at concentrations of $1\cdot10^{-4}$ $molL^{-1}$, $1\cdot10^{-3}$ $molL^{-1}$, and $1\cdot10^{-2}$ $molL^{-1}$ of the four compounds **1a-b** and **2a-b** in THF.

Thin film preparation:

THF solutions (concentration: $5\cdot10^{-2}$ $molL^{-1}$) of the four compounds were spin coated on spectrosil or silicon wafer substrates (30 s, 1020 rpm).

UV-Vis spectroscopy:

UV-Vis spectra on solution and thin film samples were recorded on a JASCO V-670 spectrophotometer. For the measurements in THF the path length of the cuvettes was 1 mm. The extinction coefficient of the 0-0 transition to the S_2 state was for all compounds about $5 \cdot 10^4$ $Lmol^{-1}cm^{-1}$ in the molecularly dissolved state at $1 \cdot 10^{-4}$ $molL^{-1}$ which results in an OD of 0.5. The further increase of the concentration aggregation occurs and the extinction coefficient is substantially reduced so that the OD values are still below 3. Note also that only the extinction coefficients of the two 0-0 transitions to the S_2 and S_3 states are reduced due to aggregation at higher concentrations, while the others remain unchanged.

Photoluminescence spectroscopy in solution:

For the photoluminescence study THF solutions of the compounds were prepared and investigated with a FluoroMax 3 spectrometer at an excitation wavelength of 344 nm.

Photoluminescence spectroscopy on thin films:

The photoluminescence measurements of the thin films were performed on a home-built setup. An argon laser (Coherent Innova 300C) with wavelengths of 354 nm and 361 nm was used for the excitation and a CCD-camera (Andor iDus DU420) was used as detector.

Time-correlated single photon counting (TCSPC) measurements:

The TCSPC measurements were conducted on a FluoTime 200 setup from PicoQuant. The samples were excited with 375 nm laser pulses and the resulting fluorescence was detected with a MCP-PMT detector from Hamamatsu.

Optical microscopy:

The spin coated thin films were investigated between crossed polarizers on an optical microscope (Leica DMRX) equipped with a hot-stage (Mettler, model FP82TM).

Preparation of freeze dried samples:

Supramolecular aggregates of the four compounds were prepared in dioxane (concentration: $1 \cdot 10^{-2}$ $molL^{-1}$) by heating to dissolution and subsequent cooling to room temperature. One drop of the mixture was given on a DSC pan, frozen in liquid nitrogen/pentane mixture and subsequently dried at high vacuum (0.007 mbar).

Scanning electron microscopy (SEM):

The samples were coated using platinum (about 1.4 nm) in a Cressington sputter coater 208HR. The SEM micrographs were recorded on a LEO 1530 FE-SEM (Zeiss, Jena) with Schottky-field-emission cathode and an in-lens detector.

FT-IR spectroscopy:

The infrared measurements were performed on a Perkin Elmer FT-IR Spectrum 100 spectrometer. The solution measurements were conducted in THF solutions at $1 \cdot 10^{-2}$ $molL^{-1}$ using a NaCl cell of 0.5 mm diameter. For the measurements on thin films, the films had to be spin coated on silica wavers (30 s, 1020 rpm). The resulting films were measured at the ATR unit of the spectrometer.

Modeling:

Initially a conformational search was carried out to know the most probable conformation of the molecules **1a**, **1b**, **2a** and **2b**. DFT calculations were carried out for those compounds using the functional B3LYP and basis set 6-31G for all atoms and the program Gaussian03 was used. No constraints in the geometry optimizations were applied. The optimized geometries were checked by calculation of the vibrational spectra, where no negative frequencies were found. The optimized geometries and the partial charges obtained from the DFT calculations were used in order to build aggregates containing 6 monomers each. The geometries of the aggregates were then optimized using the Molecular Mechanics and considering explicitly the atomic charges (MM+ force field, Hyperchem 7.5 program).

Acknowledgements

We gratefully acknowledge financial support by the Deutsche Forschungsgemeinschaft within the DFG Research Training Group (GRK 1640) "*Photophysics of Synthetic and Biological Multichromophoric Systems*". ATH and HM would also like to thank the elite study program "Macromolecular Science" at the University of Bayreuth. "Elite Netzwerk Bayern" is acknowledged for a fellowship for ATH. We are indebted to Doris Hanft and Irene Bauer for synthetic support and Dr. Klaus Kreger for many fruitful discussions.

References

[1] a) T. Aida, E. W. Meijer, S. I. Stupp, *Science* **2012**, *335*, 813–817. b) V. Percec, M. Glodde, T. K. Bera, Y. Miura, I. Shiyanovskaya, K.D. Singer, V.S.K. Balagurusamy, P.A. Heiney, I. Schnell, A. Rapp, H.-W. Spiess, S. D. Hudson, H. Duan, *Nature* **2002**, *419*, 384-387. c) F. Würthner, K. Meerholz, *Chem. Eur. J.* **2010**, *16*, 9366–9373. d) B. Bodenant, F. Fages, M.-H. Delville, *J. Am. Chem. Soc.* **1998**, *120*, 7511–7519. e) Y. Sun, G. C. Welch, W. L. Leong, C. J. Takacs, G. C. Bazan, A. J. Heeger, *Nat. Mater.* **2011**, *11*, 44–48.

[2] a) K. R. Leight, B. E. Esarey, A. E. Murray, J. J. Reczek, *Chem. Mater.* **2012**, *24*, 3318–3328. b) L. F. Dössel, V. Kamm, I. A. Howard, F. Laquai, W. Pisula, X. Feng, C. Li, M. Takase, T. Kudernac, S. de Feyter et al., *J. Am. Chem. Soc.* **2012**, *134*, 5876–5886. c) Z. Chen, A. Lohr, C. R. Saha-Möller, F. Würthner, *Chem. Soc. Rev.* **2009**, *38*, 564-584.

[3] a) L. van Dijk, P. A. Bobbert, F. C. Spano, *J. Phys. Chem. B* **2009**, *113*, 9708–9717. b) L. van Dijk, F. C. Spano, P. A. Bobbert, *Chemical Physics Letters* **2012**, *529*, 69–73. c) A. A. Voityuk, *Phys. Chem. Chem. Phys.* **2012**, *14*, 13789-13793.

[4] a) M. R. Molla, S. Ghosh, *Chem. Mater.* **2011**, *23*, 95–105. b) F. Würthner, *Chem. Commun.* **2004**, 1564-1579.

[5] a) A. Ajayaghosh, S. J. George, A. P. Schenning in *Topics in Current Chemistry* (Ed.: F. Würthner), Springer-Verlag, Berlin/Heidelberg, **2005**. b) T. Metzroth, A. Hoffmann, R. Martín-Rapún, M. M. J. Smulders, K. Pieterse, A. R. A. Palmans, J. A. J. M. Vekemans, E. W. Meijer, H. W. Spiess, J. Gauss, *Chem. Sci.* **2010**, *2*, 69-76.

[6] a) D. González-Rodríguez, A. P. H. J. Schenning, *Chem. Mater.* **2011**, *23*, 310–325. b) T. Shu, J. Wu, M. Lu, L. Chen, T. Yi, F. Li, C. Huang, *J. Mater. Chem.* **2008**, *18*, 886-893. c) M. Blomenhofer, S. Ganzleben, D. Hanft, H.-W. Schmidt, M. Kristiansen, P. Smith, K. Stoll, D. Mäder, K. Hoffmann, *Macromolecules* **2005**, *38*, 3688–3695. d) J. B. Bodapati, H. Icil, *Photochem. Photobiol. Sci.* **2011**, *10*, 1283-1293.

[7] a) S. Sankararaman, G. Venkataramana, B. Varghese, *J. Org. Chem.* **2008**, *73*, 2404–2407. b) X. Zhang, S. Rehm, M. M. Safont-Sempere, F. Würthner, *Nature Chem* **2009**, *1*, 623–629.

[8] T. Förster, K. Kasper, *Zeitschrift für Elektrochemie Berichte der Bunsengesellschaft für physikalische Chemie*, **1955**, *59*, 976–980,. can be found under http://onlinelibrary.wiley.com/doi/10.1002/bbpc.v59:10/issuetoc.

[9] M. Schwoerer, H. C. Wolf, *Organic molecular solids*, Wiley-VCH, Weinheim, **2007**.

[10] F. M. Winnik, *Chem. Rev.* **1993**, *93*,587-614.

[11] J. B. Birks, L. G. Christophorou, *Spectrochimica Acta*, **1963**, *19*, 401-410.

[12] J. B. Birks, D. J. Dyson, I. H. Munro, Proceedings of the Royal Society A: Mathematical, Physical and Engineering Sciences **1963**, 275, 575–588.

[13] a) J. B. Birks, M. D. Lumb, I. H. Munro, *Proceedings of the Royal Society A: Mathematical, Physical and Engineering Sciences* **1964**, *280*, 289–297. b) J. B. Birks, A. A. Kazzaz, T. A. King, *Proceedings of the Royal Society A: Mathematical, Physical and Engineering Sciences* **1966**, *291*, 556–569. c) J. B. Birks, A. A. Kazzaz, *Proceedings of the Royal Society A: Mathematical, Physical and Engineering Sciences* **1968**, *304*, 291–301.

[14] A. Hayer, V. de Halleux, A. Köhler, A. El-Garoughy, E. W. Meijer, J. Barberá, J. Tant, J. Levin, M. Lehmann, J. Gierschner et al., *J. Phys. Chem. B* **2006**, *110*, 7653–7659.

[15] J. Xiao, Y. Li, Y. Song, L. Jiang, Y. Li, S. Wang, H. Liu, W. Xu, D. Zhu, *Tetrahedron Letters* **2007**, *48*, 7599–7604.

[16] a) L. You, G. W. Gokel, *Chem. Eur. J.* **2008**, *14*, 5861–5870. b) F. D. Lewis, J.-S. Yang, C. L. Stern, *J. Am. Chem. Soc.*, **1996**, *118*, 12029-12037. c) M. Kimura, N. Miki, D. Suzuki, N. Adachi, Y. Tatewaki, H. Shirai, *Langmuir* **2009**, *25*, 776–780.

[17] a) H. M. Colquhoun, Z. Zhu, *Angew. Chem. Int. Ed.* **2004**, *43*, 5040–5045. b) B. W. Greenland, S. Burattini, W. Hayes, H. M. Colquhoun, *Tetrahedron* **2008**, *64*, 8346–8354.

[18] M. S. Becherer, B. Schade, C. Böttcher, A. Hirsch, *Chem. Eur. J.* **2009**, *15*, 1637–1648.

[19] B. Adhikari, J. Nanda, A. Banerjee, *Chem. Eur. J.* **2011**, *17*, 11488–11496.

[20] S. T. Caldwell, G. Cooke, S. G. Hewage, S. Mabruk, G. Rabani, V. Rotello, B. O. Smith, C. Subramani, P. Woisel, *Chem. Commun.* **2008**, 4126-4128.

[21] H. M. Colquhoun, Z. Zhu, D. J. Williams, M. G. B. Drew, C. J. Cardin, Y. Gan, A. G. Crawford, T. B. Marder, *Chem. Eur. J.* **2010**, 16, 907-918.

[22] a) L. Hernandez-Folgado, D. Baretić, I. Piantanida, M. Marjanović, M. Kralj, T. Rehm, C. Schmuck, *Chem. Eur. J.* **2010**, *16*, 3036–3056. b) R. Häner, F. Samain, V. L. Malinovskii, *Chem. Eur. J.* **2009**, *15*, 5701–5708. c) R. Varghese, H.-A. Wagenknecht, *Chem. Commun.* **2009**, 2615-2624.

[23] a) Y. H. Lee, H. Liu, J. Y. Lee, S. H. Kim, S. K. Kim, J. L. Sessler, Y. Kim, J. S. Kim, *Chem. Eur. J.* **2010**, *16*, 5895-5901. b) A. D. Hughes, I. C. Glenn, A. D. Patrick, A. Ellington, E. V. Anslyn, *Chem. Eur. J.* **2008**, *14*, 1822–1827.

[24] K. Kreger, P. Wolfer, H. Audorff, L. Kador, N. Stingelin-Stutzmann, P. Smith, H.-W. Schmidt, *J. Am. Chem. Soc.* **2010**, *132*, 509–516.

[25] J. B. Birks, *Photophysics of aromatic molecules*, Wiley-Interscience, London, New York, **1970**.

[26] D. Görl, X. Zhang, F. Würthner, *Angew. Chem. Int. Ed.* **2012**, *51*, 6328–6348.

[27] J. Clark, J.-F. Chang, F. C. Spano, R. H. Friend, C. Silva, *Appl. Phys. Lett.* **2009**, *94*, 163306.

[28] a) F. C. Spano, *Chemical Physics* **2006**, *325*, 22–35. b) S. Ghosh, X.-Q. Li, V. Stepanenko, F. Würthner, *Chem. Eur. J.* **2008**, *14*, 11343–11357.

[29] J. B. Birks, *Rep. Prog. Phys.* **1975**, *38*, 903–974.

[30] a) A. L. T. Khan, P. Sreearunothai, L. M. Herz, M. J. Banach, A. Köhler, *Phys. Rev. B* **2004**, *69*, 085201. b) C. Scharsich, R. H. Lohwasser, M. Sommer, U. Asawapirom, U. Scherf, M. Thelakkat, D. Neher, A. Köhler, *J. Polym. Sci. B Polym. Phys.* **2012**, *50*, 442–453.

[31] a) D. J. Skrovanek, S. E. Howe, P. C. Painter, M. M. Coleman, *Macromolecules* **1985**, *18*, 1676–1683. b) T. Mes, M. M. J. Smulders, A. R. A. Palmans, E. W. Meijer, *Macromolecules* **2010**, *43*, 1981–1991.

[32] H. Bässler, *phys. stat. sol. (b)* **1993**, *175*, 15–56.

Supporting Information to

Controlling the π-stacking behavior of pyrene derivatives: Influence of H-bonding and steric effects in different states of aggregation

Andreas T. Haedler,[a]# Holger Misslitz,[a]# Christian Buehlmeyer,[b] Rodrigo Q. Albuquerque,[c] Anna Köhler,[b] and Hans-Werner Schmidt[a]*

[#] both authors contributed equally to this contribution

[a] Macromolecular Chemistry I and
Bayreuther Institut für Makromolekülforschung (BIMF)
University of Bayreuth, 95447 Bayreuth (Germany)

[b] Institute of Experimental Physics II and
Bayreuther Institut für Makromolekülforschung (BIMF)
University of Bayreuth, 95447 Bayreuth (Germany)

[c] Institute of Chemistry of São Carlos
University of São Paulo (USP)
13560-970 São Carlos-SP (Brazil)

Table of contents:

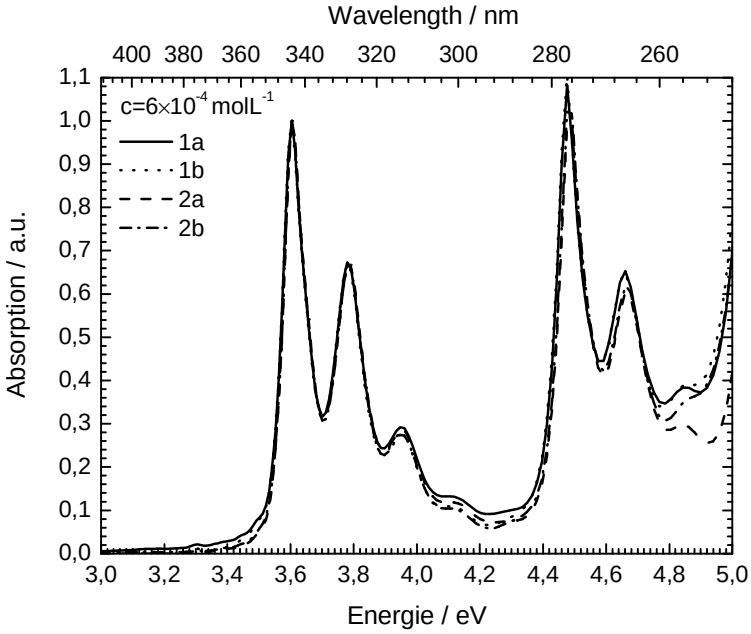

Figure S1. Absorption spectra of the four pyrene derivatives **1a-b** and **2a-b** in THF at $6 \cdot 10^{-4}$ molL^{-1} exhibiting the excitation from the electronic ground state to the 1st and 2nd excited state with respective vibrational fission.

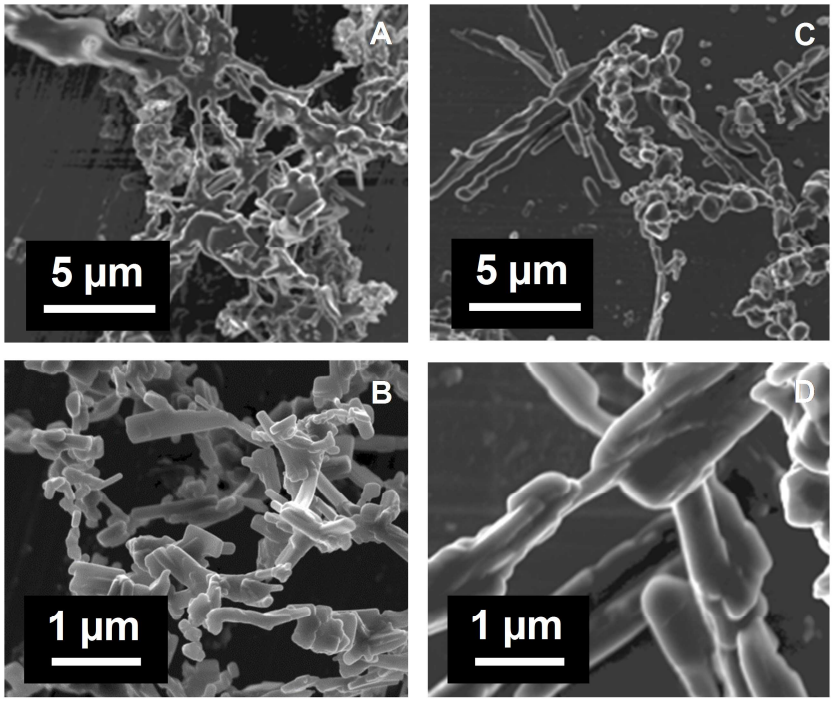

Figure S2.1. Scanning electron microscopy images of supramolecular structures from dioxane solutions after freeze-drying (concentration: $1 \cdot 10^{-2}$ molL^{-1}) of the esters **1a** (left: A, B) and **1b** (right: C, D); the bottom micrographs show a fivefold higher magnification.

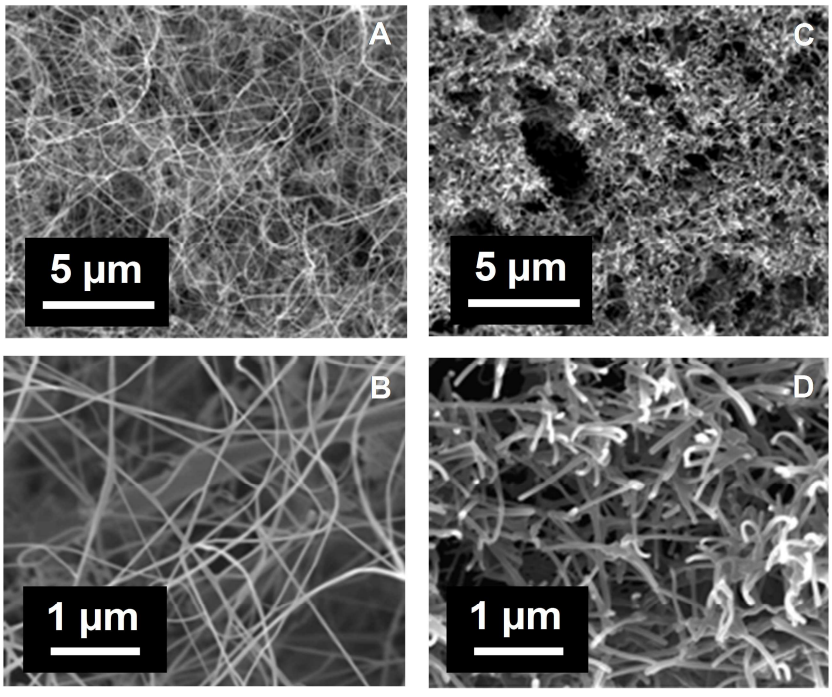

Figure S2.2. Scanning electron microscopy images of supramolecular structures of dioxane solutions after freeze-drying (concentration: $1 \cdot 10^{-2}$ molL^{-1}) of the amides **2a** (left: A, B) and **2b** (right: C, D); the bottom micrographs show a fivefold higher magnification.

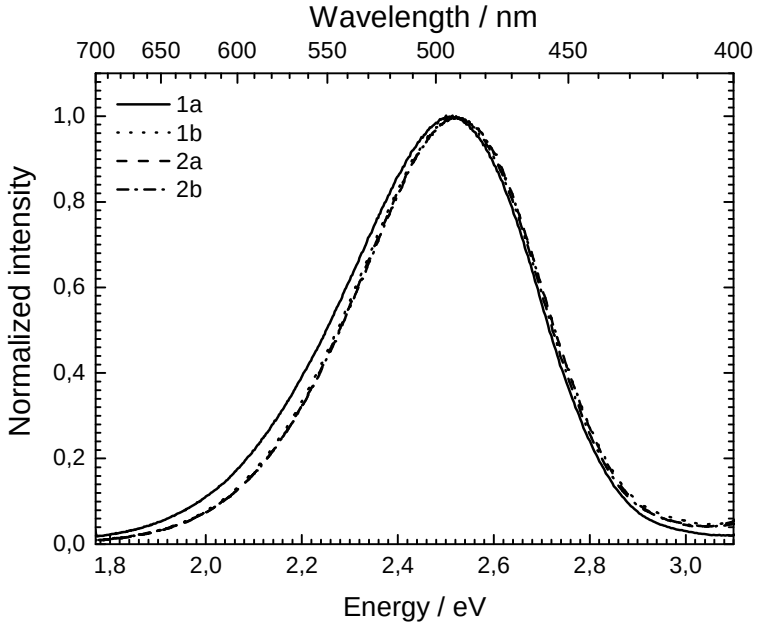

Figure S3. Excimer fluorescence spectra of the four compounds **1a-b** and **2a-b** at $6 \cdot 10^{-2}$ $molL^{-1}$ in THF.

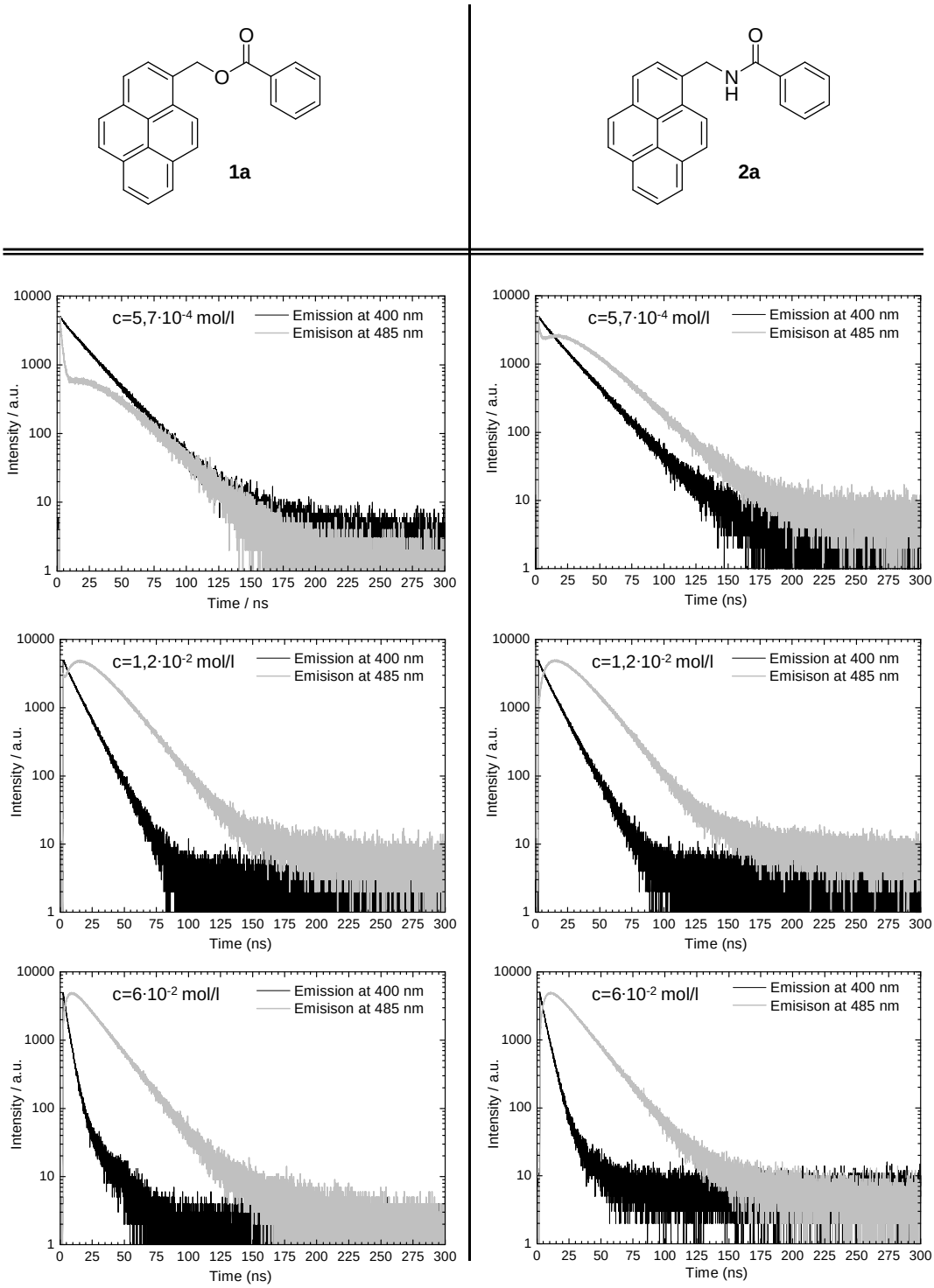

Figure S4. Time resolved photoluminescence spectra of compound **1a** (left) and **2a** (right) at different concentrations $5.7 \cdot 10^{-4}$ molL^{-1} (top), $1.2 \cdot 10^{-2}$ molL^{-1} (middle) and, $6 \cdot 10^{-2}$ molL^{-1} (bottom) shown for the monomer (black) and the excimer fluorescence (grey). For compound 2a the fits are shown from which λ_1 and λ_2 are derived.

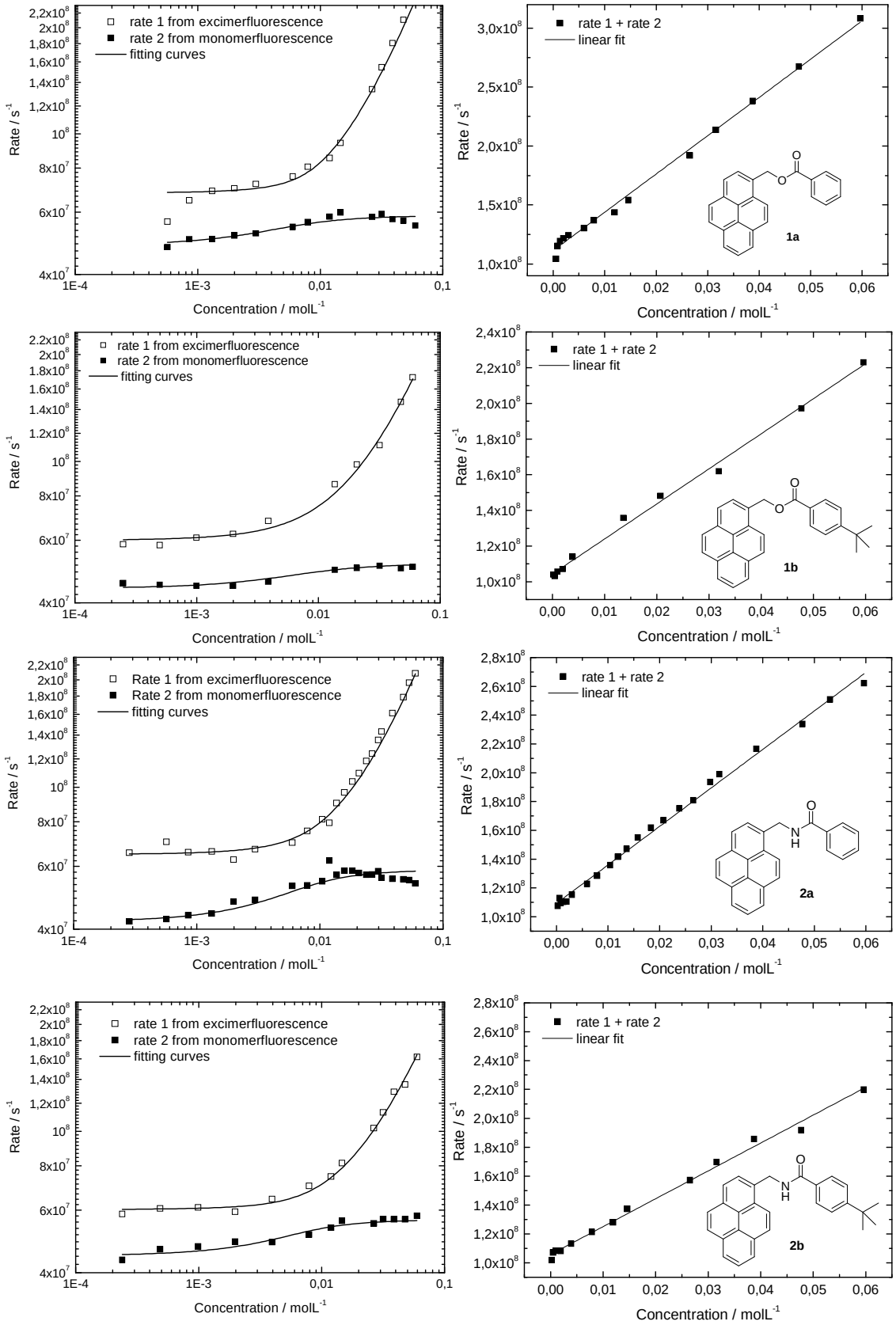

Figure S5. Left: Excimer (□) and monomer (■) fluorescence fall-off rates at different concentrations for compound **1a-b** and **2a-b** (from top to bottom) fitted according to Birks. Right: Sum of the two fall-off rates plotted against the concentration yielding the expected linear dependence.

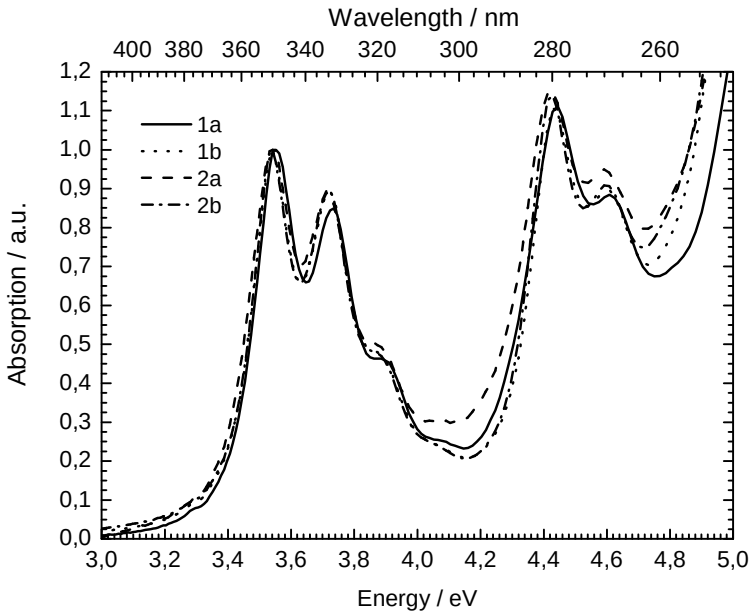

Figure S6. Absorption spectra of the four compounds **1a-b** and **2a-b** in optically transparent thin films.

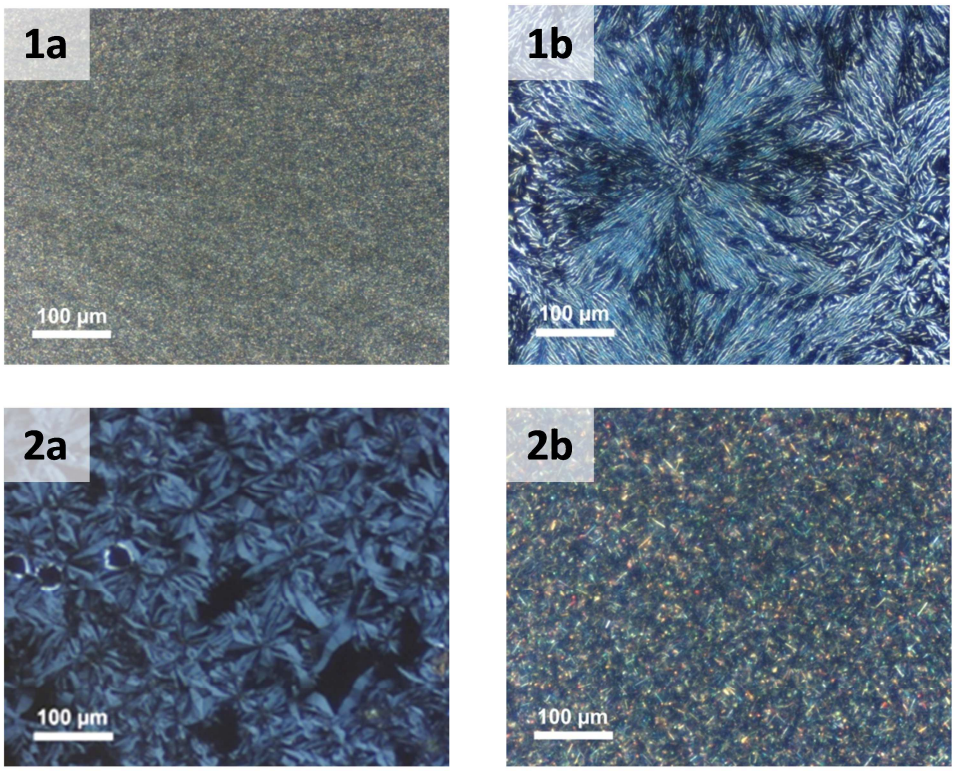

Figure S7. Optical micrographs taken between two crossed polarizers of the ester compounds **1a** and **1b** after aging at room temperature for two months (top) and the amide compounds **2a** and **2b** after annealing at 80°C and 130°C (bottom).

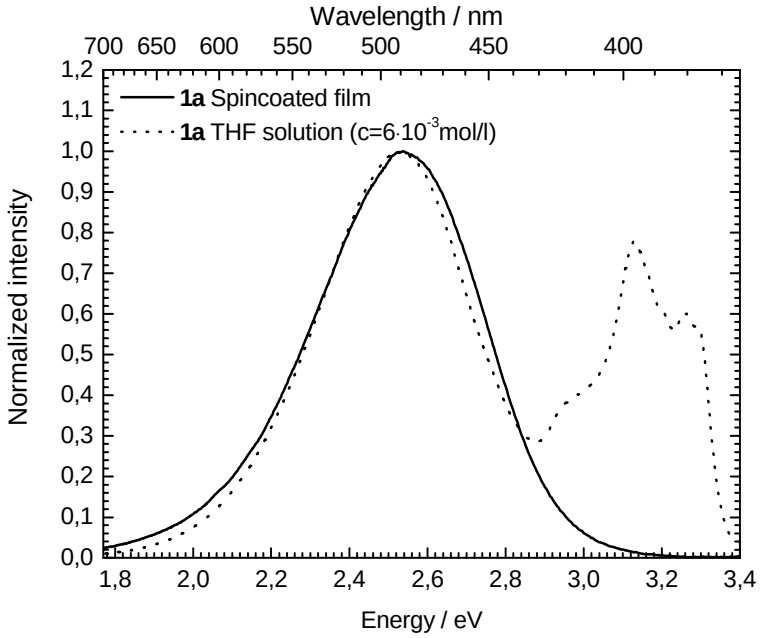

Figure S8. Excimer fluorescence of the fresh prepared thin films exemplarily shown for compound **1a** (—) compared with the corresponding fluorescence spectrum in THF at $6 \cdot 10^{-3}$ $molL^{-1}$ (·····).

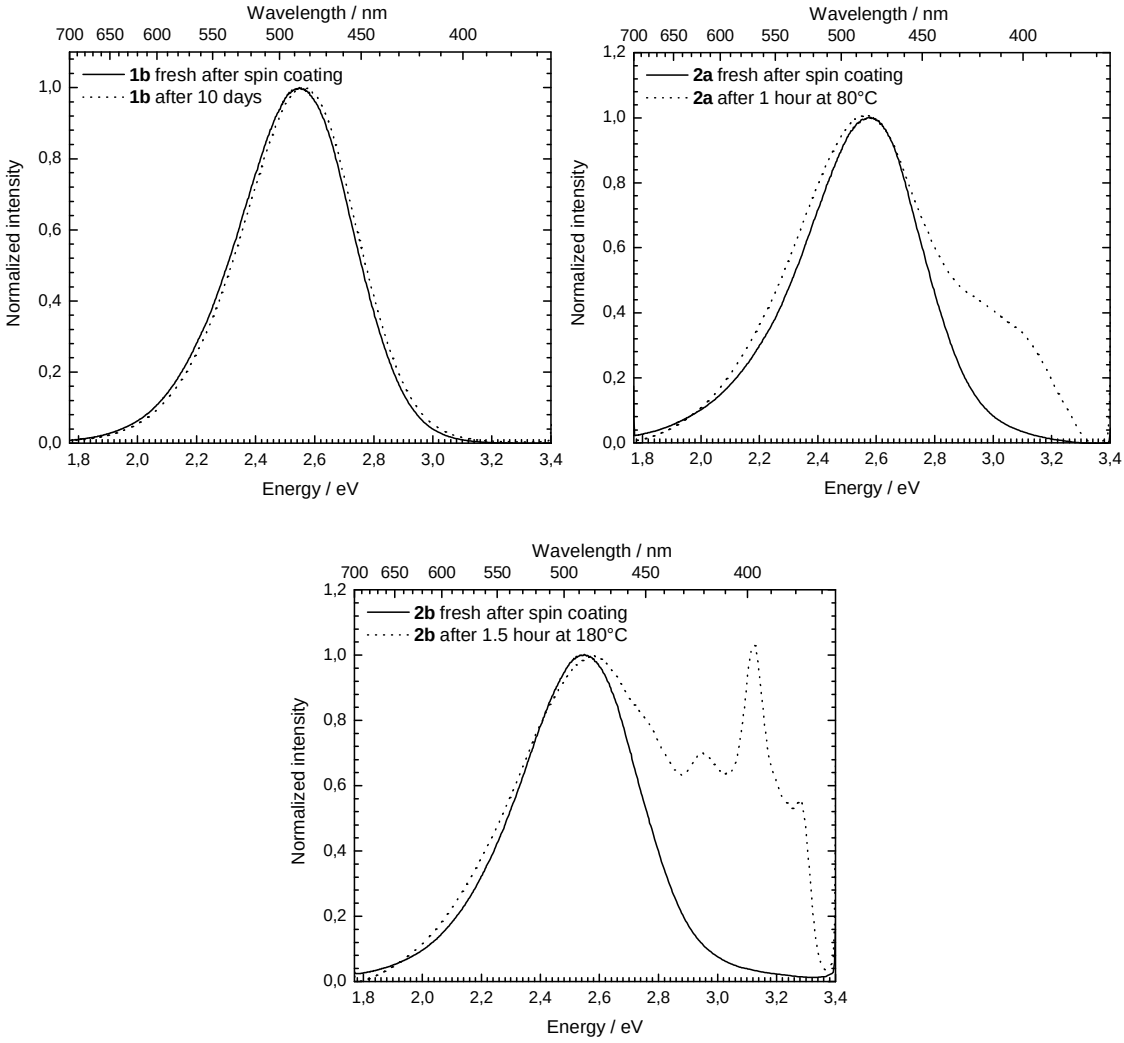

Figure S9. Photoluminescence spectra of thin films of compound **1b** directly after processing and after 10 days at room temperature (top left), of compound **2a** directly after processing and after 1 h at 80°C (top right), and of compound **2b** directly after processing and after 1.5 h at 180°C (bottom).

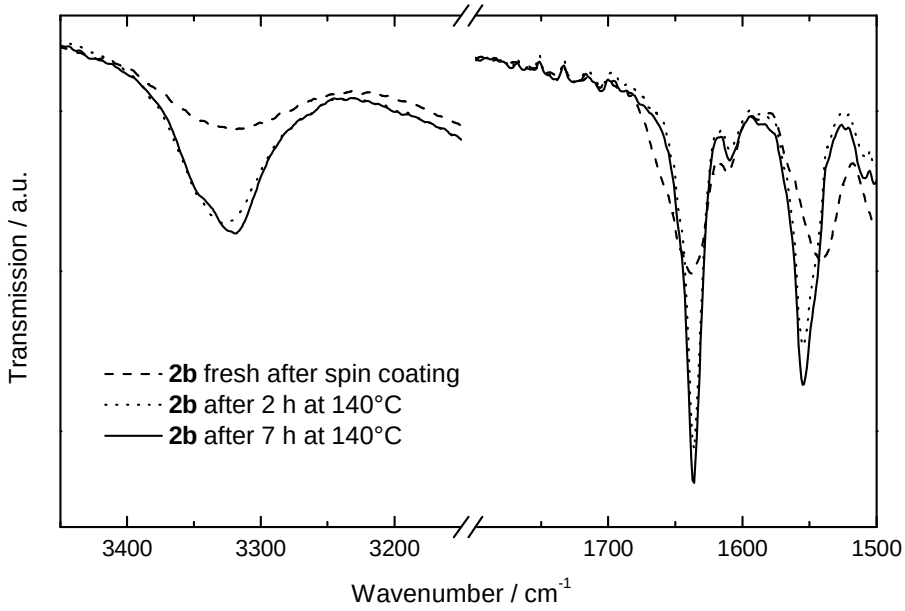

Figure S10. Enlargements of the relevant parts of the FT-IR spectra of a thin film of compound **2b** during the aging process directly after processing, after 2 h and, after 7 h at 140°C resembling different degrees of crystallization; the N-H stretching vibration (left: around 3300 cm^{-1}) and the carbonyl stretching vibration (right: around 1630 cm^{-1}) are represented.

3.3 Supramolecular nanofibers – A study on different processing pathways

*Holger Misslitz, Frank Abraham, Klaus Kreger, and Hans-Werner Schmidt**

Macromolecular Chemistry I, Bayreuther Institut für Makromolekülforschung (BIMF), Bayreuther Zentrum für Kolloide und Grenzflächen (BZKG), University of Bayreuth, 95440 Bayreuth, Germany

INTENDED FOR SUBMISSION TO **JOURNAL OF SUPRAMOLECULAR CHEMISTRY**

Abstract: 1,3,5-Benzenetrisamides (BTAs) are one of the simplest and well investigated motifs in supramolecular chemistry. It is known that the resulting supramolecular morphologies can be varied by several self-assembly conditions. However, detailed studies how to control the self-assembly of BTAs towards desired morphologies are rarely investigated. In order to control the nanofiber morphology of BTAs, herein, we compare two different self-assembly processing pathways from solution. *Self-assembly upon cooling at a constant concentration and subsequent solvent evaporation* represents the first pathway. In this part, two BTA/solvent systems, which differ in solubility, were compared. The second pathway is the *self-assembly during solvent evaporation at constant temperature*. We found out, that the key factor which mainly determines the occurring self-assembly is the solubility of the BTA/solvent system. Furthermore, a comprehensive study on structure-property relations with respect to different morphologies of supramolecular (nano-)fibers was conducted. Thereby, parameters such as the molecular structure, the concentration, the solvent, and the cooling rate were varied. The fundamental knowledge obtained in this work represents the indispensable basis for further applications in which self-assembly of BTAs is involved.

Keywords: supramolecular chemistry • self-assembly • nanofibers • structure-property relations

Introduction

In the last years, the class of 1,3,5-benzenetrisamides (BTAs) gained huge interest in many research fields.[1] Besides others, the reasons for this deep interest are that BTAs are one of the simplest motifs in supramolecular chemistry and their synthesis is quite straight forward. BTAs are able to self-assemble into supramolecular aggregates.[2] The self-assembly of BTAs is achieved under certain conditions, which can be induced by several triggers mechanisms, such as a shift in temperature,[3] concentration, medium,[4] and pH-value.[5] The driving force for supramolecular aggregation of BTAs is hydrogen bond formation between the amide groups of the single molecules.[6] Because of the directionality of the hydrogen bonds, the self-assembly of BTAs can be utilized to prepare supramolecular nanofibers.[7] It is known, that within one supramolecular column a macro dipole is formed[8] and due to this reason BTA aggregates can be aligned in electric fields.[9] However, the overall macro dipole of the supramolecular structure is compensated by neighboring columns, whose macro dipoles are aligned anti parallel.[10] Furthermore, it was found, that the crystal structure of the BTAs strongly depends on the peripheral substituents. While methyl- and ethyl-substituents direct the self-assembly into sheet-like aggregates, propyl-rests force the self-assembly into three-dimensional networks with a primitive cubic crystal lattice.[11] BTAs with longer alkyl chains exhibit columnar structures forming hexagonal lattices. In the case of 3-pyridyl substituents, the BTAs form three different crystalline forms from the same solvent system held together by non-covalent bonds (including polymorphic monohydrates).[12] The class of BTAs is also investigated because of their complex mesophase behavior.[13] As the supramolecular aggregates, also the columnar mesophases are mainly stabilized by strong hydrogen bond formation.[14] Depending on the alkyl substituents, certain BTAs exhibit a thermotropic liquid crystalline behavior in bulk in a broad temperature range. In addition, it was shown, that small columnar aggregates were still existent in the optical isotropic melt.[15]

Astonishing applications of BTAs are their usage as polymer additives for nucleation and clarification of polyolefins and semi crystalline polymers. Thereby, BTAs with short, bulky alkyl substituents were used in the case of nucleating isotactic polypropylene.[16] BTAs with 2,4,6-trimethyl-1,3,5-triamino benzene cores even feature better thermal stability compared to BTAs with unsubstituted ones.[17] Semi crystalline polymers such as polyvinylidenfluoride[18] and polybutylene terephthalate[19] can also be nucleated by BTAs. In polybutylene terephthalate the supramolecular aggregates of the BTA additive could be visualized after alkaline hydrolysis of the polymer matrix. As consequence, it could be demonstrated that the diameter of the supramolecular nano-objects is dependent on the concentration and the cooling rate. In addition, BTAs are also utilized in order to improve the electret performance of polypropylene.[20]

However, BTA nano-objects are not only investigated in polymer matrices. Supramolecular nanofibers of BTAs were further prepared by self-assembly in solution. The mechanical stability of those isolated supramolecular nanofibers is of great interest due to possible future applications. Single fibers, self-assembled from solution were investigated by three-point bending tests by means of an atomic force microscope. Within these investigations, structure-property relations between the molecular structure of the BTA and the mechanic stability of self-assembled BTA nanofibers were determined. Hereby, E-moduli of 3-5 GPa were detected.[21] Furthermore, entanglements of supramolecular nanofibers prepared from solution can result in the formation of three-dimensional networks. Hence, this class of molecules can also act as organo-[22] and hydrogelators.[23]

In addition, it is possible to obtain supramolecular nanofibers of BTAs by electrospinning from the isotropic melt and the columnar, hexagonal phase. Besides the thermal properties of the BTAs, the supramolecular morphology of the nanofibers is also dependent on the spinning temperature and the applied electric field.[24] A comparison between the self-assembled BTA fibers from solution and electrospun fibers showed, that differences in the supramolecular morphology are existent, however, both sort of fibers feature mechanical stabilities in the same order of magnitude.[25]

Furthermore, it has to be noted, that the self-assembly of BTAs in all the above described applications is dependent on several factors. The supramolecular morphology can be influenced by the molecular structure of the BTAs as well as the external parameters used at the self-assembly process, such as the medium, the cooling window and rate, the evaporation window, and the concentration.[12] By changing these conditions, the supramolecular morphology can be highly controlled (**Scheme 1**).

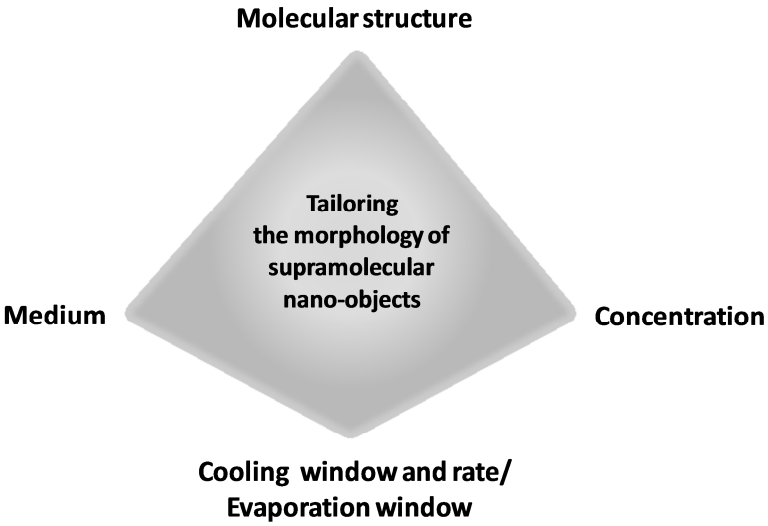

Scheme 1. Influences by which the morphology of supramolecular aggregates can be controlled.

The paper compares two self-assembly processing pathways of BTAs from solution in order to control the nanofiber morphology with respect to homogeneity, fiber diameter, and fiber diameter distribution. The first pathway is based on self-assembly upon cooling at a constant concentration and subsequent evaporation of a solvent. For this, two BTAs with different solubility will be compared. The second self-assembly pathway is the direct evaporation at constant temperature. Furthermore, for both self-assembly processing pathways structure-property relations with respect to the supramolecular morphology were investigated.

Results and Discussion

The first self-assembly pathway combines *self-assembly upon cooling at a constant concentration and subsequent evaporation* of the solvent at room temperature. In this part, we compare two different BTA/solvent systems (**Figure 1**). The first system consists of BTA **1**, which is based on a triaminobenzene core and bulky t-butyl substituents and 2,2,4,4,6,8,8-heptamethylnonane (HMN) as solvent. HMN is a non-polar, high-boiling solvent, in which in general the dissolution concentration of BTAs with short aliphatic substituents is fairly below 1 wt% near the boiling point of 240 °C. In the system **1** and HMN, the upper dissolution concentration at 240 °C is in the range of 0.06 wt%, whereas solubility at room temperature of **1** is almost negligible. The second system consists of BTA **2** and the more polar solvent 2-butanone. **2** is based on a trimesic acid core and features longer aliphatic substituents. Both, the larger substituent and the more polar solvent increase the solubility of BTAs significantly. Obviously, the substituents have also an influence on the thermal properties. **1** is a crystalline compound with an orthorhombic metric, in which the molecules feature a pseudohexagonal rod packing. **1** sublimes at 374 °C. **2** with longer aliphatic side chains

possess a columnar hexagonal plastic mesophase at room temperature, a columnar hexagonal ordered phase at 240 °C and become isotropic at 291 °C.

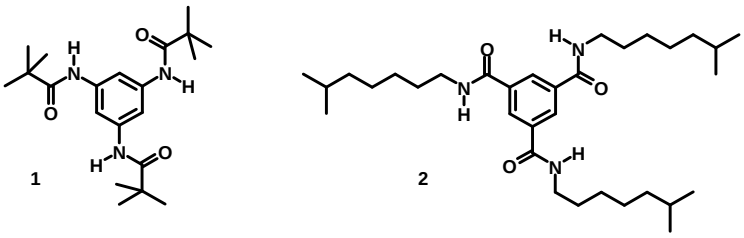

Figure 1. Chemical structures of *N*,*N*',*N*''-1,3,5-Benzenetriyltris[2,2-dimethyl-propanamide] (**1**) and N^1,N^3,N^5-Tris(6-methylheptyl)- 1,3,5-benzenetricarboxamide (**2**) utilized to investigate the first self-assembly pathway.

In **Scheme 2** the self-assembly pathway for BTA/solvent systems with low BTA solubility, i.e. **1** in HMN is illustrated. In the first step the BTA was dissolved at high temperatures. Upon cooling the solution the BTA self-assembles into one-dimensional supramolecular aggregates. At room temperature, the residual solubility of **1** in HMN is almost zero, hence, the self-assembly is completed and mainly all BTA molecules are aggregated. Subsequently, the solvent is evaporated and finally we obtain the dried supramolecular aggregates. In this drying step, no additional self-assembly occurs anymore.

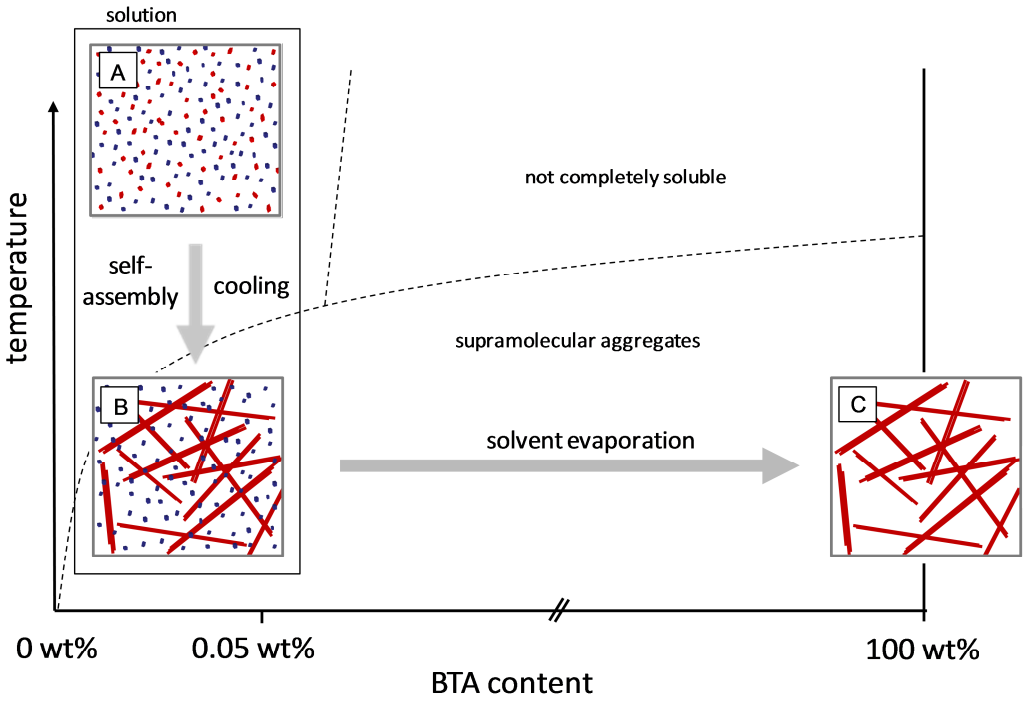

Scheme 2. Schematic representation of the self-assembly process upon cooling in a simplified temperature/composition diagram. Three stages (A-C) are schematically depicted in the diagram. (A): BTA solution with blue dots representing solvent molecules and red dots the BTA molecules. (B) self-assembled BTA aggregates in suspension. (C): supramolecular aggregates.

The morphology of supramolecular aggregates is highly influenced by several factors. For this BTA/solvent system, the influence of the cooling rate and the influence of the concentration are exemplarily discussed in the following. In **Figure 2** the structure-property relation between the cooling rate and the resulting supramolecular morphology of **1** is shown. As concentration 0.06 wt% was chosen. For all samples, all processing parameters were set constant except the cooling rate. Two BTA/HMN samples were cooled at defined cooling rates of 10 °C/min and 60 °C/min, respectively. A third specimen was quenched in liquid nitrogen, in order to obtain an extraordinary high cooling rate. In each case very homogeneous supramolecular fibers with huge aspect ratios were obtained, which are exemplarily illustrated by the scanning electron microscopy (SEM) micrographs in Figure 2. As can be seen in the micrographs the fiber diameter decreases from low to high cooling rates. At a cooling rate of 10 °C/min the lateral dimensions of the aggregates exhibit a large average diameter of 2.19 µm and a broad fiber diameter distribution. By increasing the cooling rate to 60 °C/min, the average fiber diameter (1.11 µm) as well as the width of the distribution of the resulting lateral dimensions is reduced. An even faster cooling rate is reached by quenching the specimen in liquid nitrogen. Thereby, the thinnest supramolecular fibers were obtained with an average fiber diameter of 0.40 µm. In this case, the fiber diameter distribution is significantly narrower compared to higher cooling rates. It is remarkable, that such fast cooling does not prohibit the self-assembly process. As consequence, the intermolecular hydrogen bonds have to be developed very rapidly, enabling the accurate one-dimensional self-assembly.

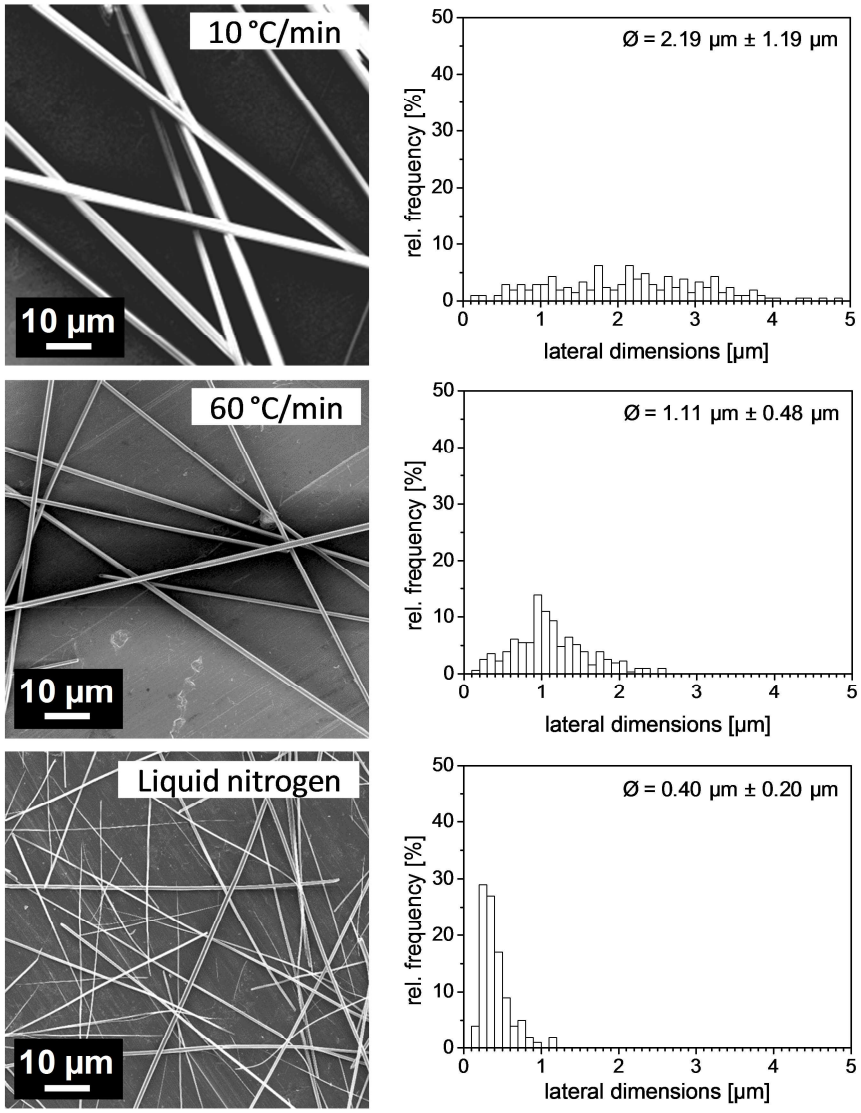

Figure 2. SEM micrographs and the corresponding histograms of self-assembled nanofibers of **1** prepared by applying different cooling rates (HMN, 0.06 wt%).

In addition, the structure-property relation between the starting concentration of the BTA/HMN solution and the resulting supramolecular morphology was investigated (**Figure 3**). Because of low solubility of **1**, we used concentrations between 0.005 wt% and 0.06 wt%. As cooling rate 60 °C/min was chosen. As can be seen in the micrographs, nanofibers with huge aspect ratios were again obtained in each case. Depending on the concentration, the diameter of the nanofibers differs. The higher the concentrations of the starting solutions, the thicker are the supramolecular fibers. At a concentration of 0.06 wt% the average fiber diameter is located at 1.11 µm and a broad diameter distribution is obtained. By decreasing the concentration to 0.03 wt% and further to 0.02 wt%, the average fiber diameter is reduced to 0.48 µm and 0.26 µm, respectively. Also the fiber diameter distributions are getting narrower compared to higher concentration. At the lowest investigated solution concentration

of 0.005 wt% supramolecular nanofibers with the lowest average fiber diameter of 0.19 µm are obtained. Also the corresponding fiber diameter distribution exhibits the narrowest distribution of the investigated samples.

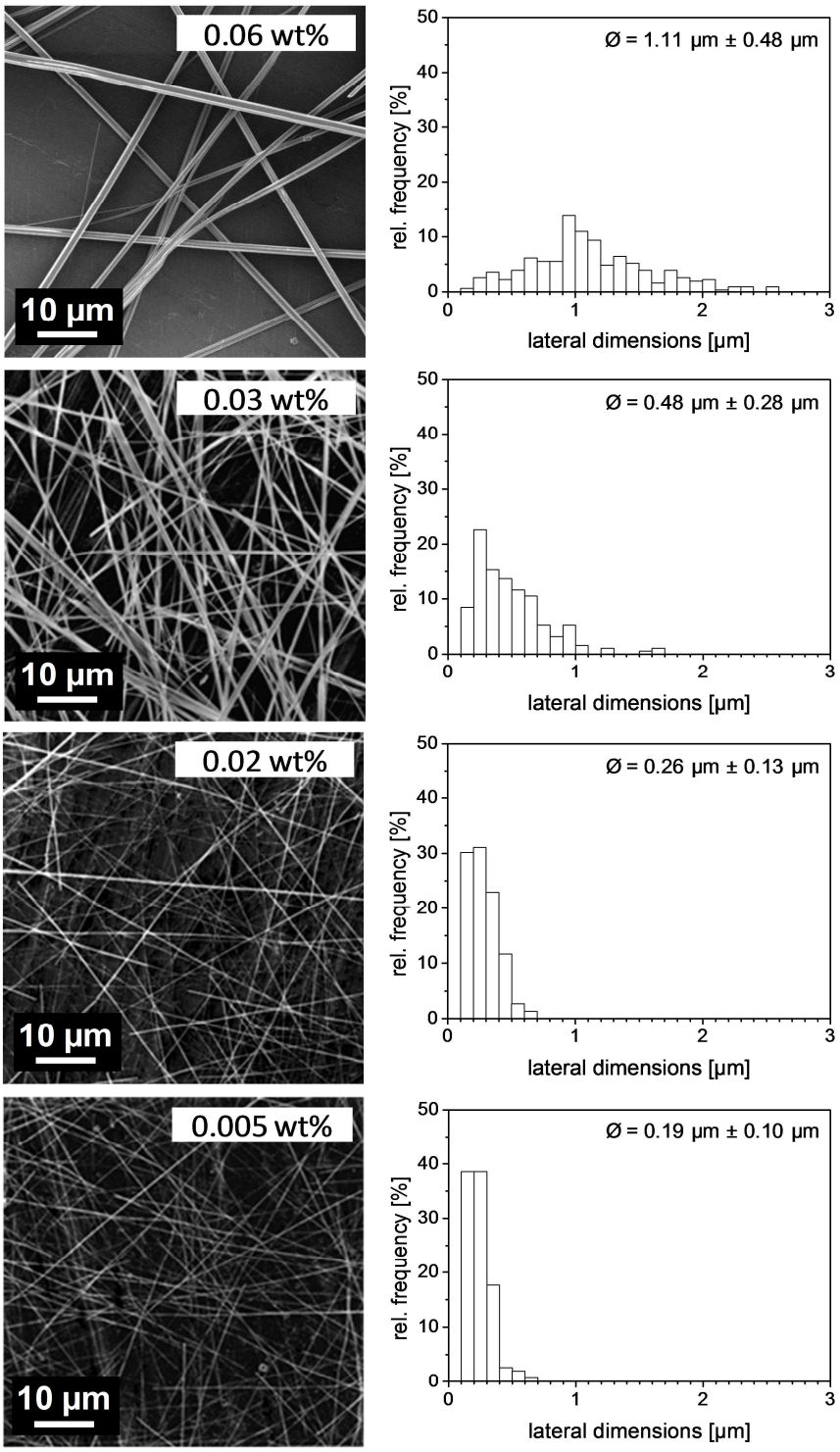

Figure 3. SEM micrographs and the corresponding histograms of self-assembled nanofibers of **1**, prepared from different concentrations (HMN solution, cooling rate 60 °C/min).

In addition, we studied the inner morphology of the supramolecular fibers. In order to get access to the fiber cross-sections focused ion beam (FIB) cutting was done. This was possible, because the fibers of **1** are stable up to high temperatures. Two different supramolecular fibers of **1** with diameters of 120 nm and 1.2 µm were cut perpendicular to their longitudinal axis. The resulting cross sections are represented in **Figure 4**. As can be seen in the micrograph, the supramolecular aggregates of **1** with small diameters feature solid cores. However, it has to be mentioned, that the ion beam could modify the morphology of the aggregates. Thus possible holes could be molten down. In the case of aggregates with larger diameters hexagonal cross sections featuring a hollow core were observed. In the tubular assembly, the walls are 300-400 nm thick, while the hole possesses a diameter of about 500-600 nm. A surface structure can be observed at the inner side of the walls indicating that they consist of several smaller fibrillar aggregates attached parallel to each other.

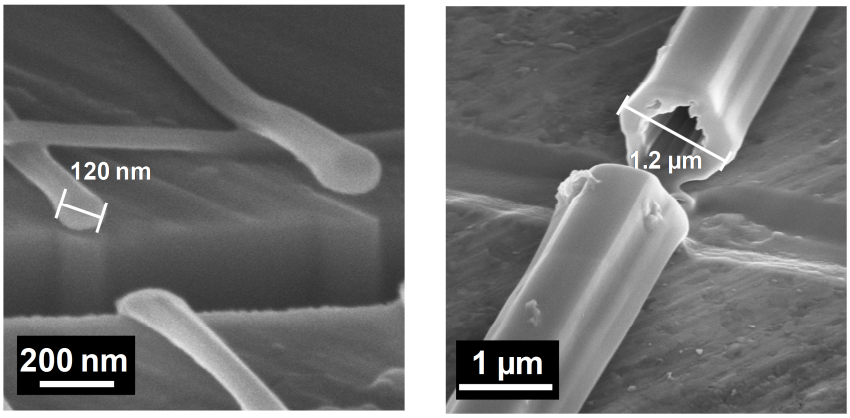

Figure 4. SEM micrographs of the cross sections of focused ion beam cut fibers of **1** prepared from HMN solutions. Left: 0.01 wt% starting concentration, right: 0.06 wt% starting concentration.

In order to investigate the self-assembly upon cooling by means of a higher soluble BTA/solvent system, **2** was used in butanone. Due to the fact of better solubility of **2**, much higher concentrations can be realized (up to 2.0 wt%). Herein, we focused on a concentration of 1.0 wt%. For the self-assembly, the samples were prepared the same way as the BTA/solvent system **1**/HMN (heating, cooling, and drying). The resulting supramolecular aggregates of **2** are represented in **Figure 5**. Surprisingly, we do not observe fibers with homogenous fiber diameters in the micrograph. Instead a combination of thick and thin fibers was obtained. The corresponding histogram reveals a bimodal fiber distribution with average diameters of 0.23 µm and 1.46 µm, respectively. While the diameters of the nanofibers feature a narrow distribution, the lateral dimensions of the thicker fibers are broadly distributed. One possible explanation for the bimodal fiber diameter is a high residual solubility of **2** in butanone after cooling.

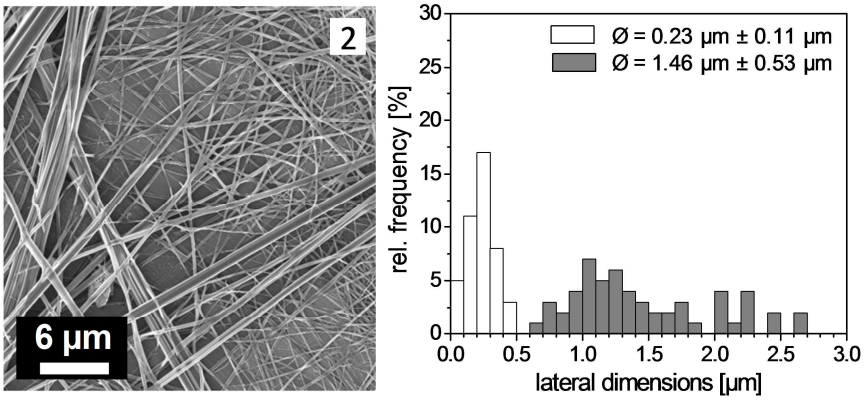

Figure 5. SEM micrograph and the corresponding histogram of supramolecular fibers of **2** prepared out of a butanone solution (initial concentration: 1.0 wt%).

In order to reveal the reason for a bimodal fiber diameter distribution we further conducted the following experiments (**Figure 6**): **2** was dissolved in butanone with an initial concentration of 1.0 wt% at elevated temperature. Cooling leads to the development of supramolecular assemblies. These aggregates are separated with a syringe filter (0.2 µm) and are subsequently analyzed by SEM. Supramolecular fibers with an average diameter of 1.00 µm and a broad fiber distribution are obtained (see Figure 6). Subsequently, the BTA/butanone solution remaining after the filtration step (filtrate) is left at ambient conditions to evaporate the solvent. The thereby resulting supramolecular aggregates are also visualized by SEM whereby supramolecular nanofibers featuring an average fiber diameter of 0.25 µm with a small diameter distribution are observed. Evidently, the thicker fibers originate from self-assembly upon cooling while the thinner nanofibers arise from self-assembly during solvent evaporation due to high residual solubility of **2** in butanone after cooling. In addition, the amount of nanofibers self-assembled during solvent evaporation is determined gravimetrically. The result corresponds to a solution concentration of 0.6 wt%. Taking the initial BTA concentration of 1.0 wt% into account, the amount of fibers self-assembled upon cooling has to be the remaining 0.4 wt%. As consequence, for this BTA/solvent system (**2**/butanone) an exclusive self-assembly during solvent evaporation should be achievable up to a threshold concentration of 0.6 wt% under the applied conditions. Above this value, always combinations of self-assembly during solvent evaporation and self-assembly upon cooling are obtained.

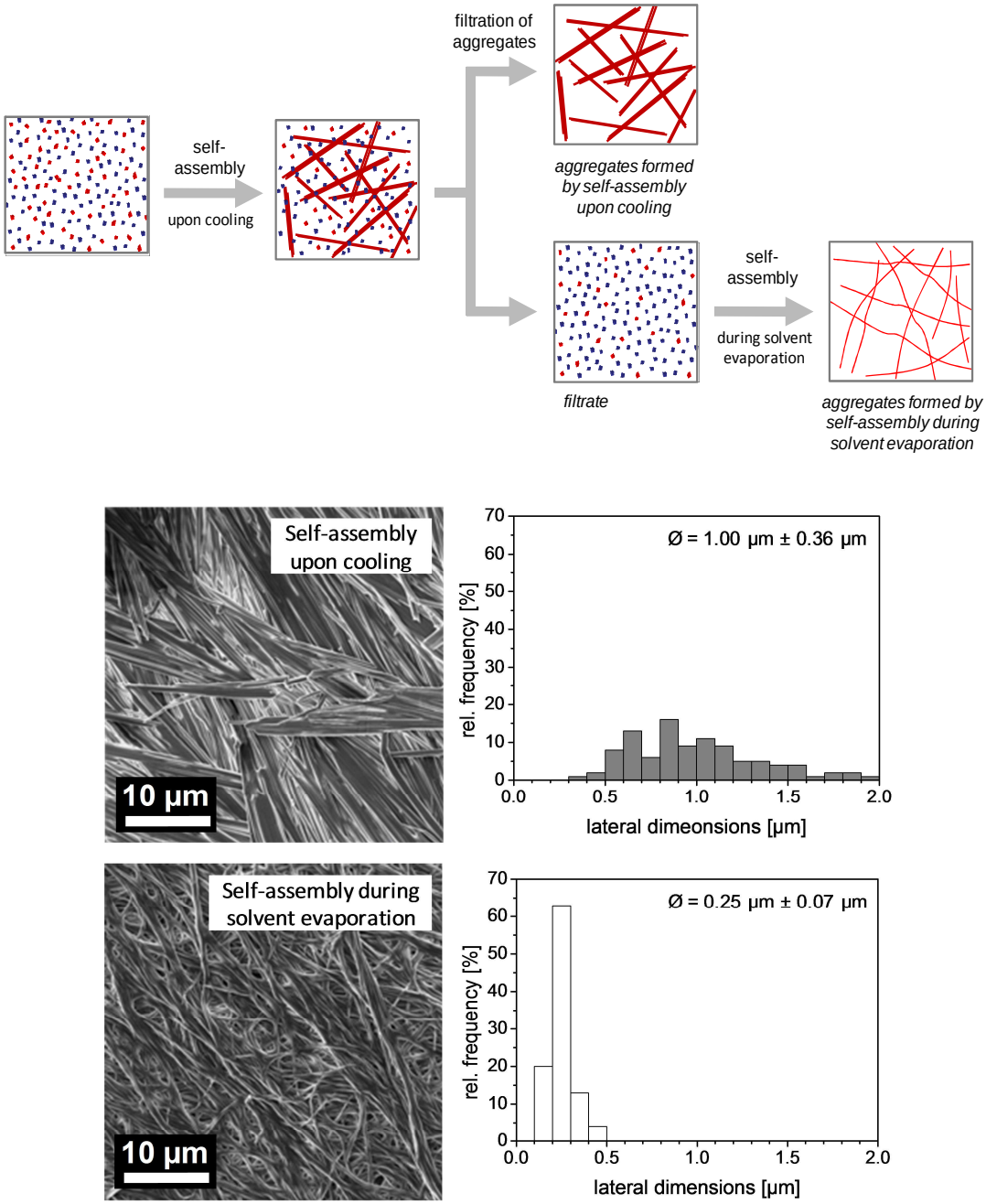

Figure 6. Top: Schematic representation of the separation process of the self-assembled aggregates derived upon cooling and during solvent evaporation. Bottom: SEM micrographs and the corresponding histograms of supramolecular fibers of **2**. The fibers were prepared out of a butanone solution with an initial concentration of 1.0 wt%.

In addition, the crystal structures of the supramolecular aggregates were determined by XRD measurements. **Figure 7** shows the XRD diffractograms of the supramolecular aggregates obtained from self-assembly upon cooling and from self-assembly during solvent evaporation. Both diffractograms feature comparable peaks indicating the same crystal structure of both assemblies. The first four peaks located in the small-angle region feature spacings in the reciprocal ratio of 1:√3:2:√7 indicating a columnar

hexagonal packing. The intercolumnar distances are determined by means of the Bragg's law. In both cases the intercolumnar distances feature about 1.7 nm. The large quantity of peaks in the spectra points to a three-dimensional order, which is realized in a crystalline phase. However, we observe a waxy behavior in bulk, which indicates a plastic phase. Therefore both sort of fibers assemble in a columnar hexagonal plastic mesophase. Detailed investigations on the phase behavior of the BTA molecules are previously published by our group.[15]

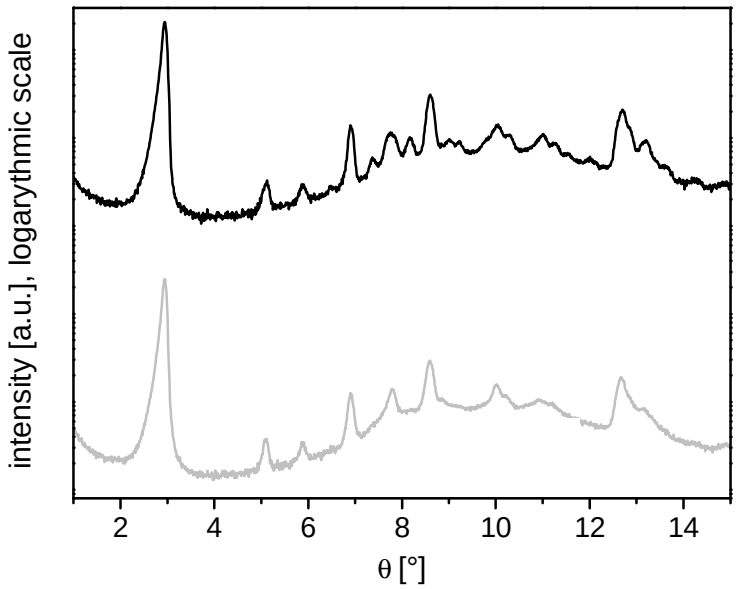

Figure 7. XRD diffraction patterns of supramolecular nanofibers of **2** self-assembled upon cooling (top, black) and during solvent evaporation (bottom, grey), respectively.

Now we further want to proof our assumption made above, that supramolecular nanofibers of **2** in butanone can be achieved up to a threshold concentration of 0.6 wt% by exclusive *self-assembly during solvent evaporation at constant temperature*. The utilized self-assembly processing pathway is shown in a temperature/composition diagram in **Scheme 3**. The starting prerequisite of complete solubility of the BTA/solvent system at room temperature is ensured by the long peripheral alkyl substituents of BTA **2** in combination with an appropriate concentration (≤ 0.6 wt%) in a polar solvent (butanone) (A). During solvent evaporation this pre-adjusted BTA concentration increases. By traversing the "phase boundary" an oversaturation is reached and the excessive BTAs self-assemble into supramolecular nanofibers (B). This is continued until all solvent is evaporated and only supramolecular BTA fibers are left (C).

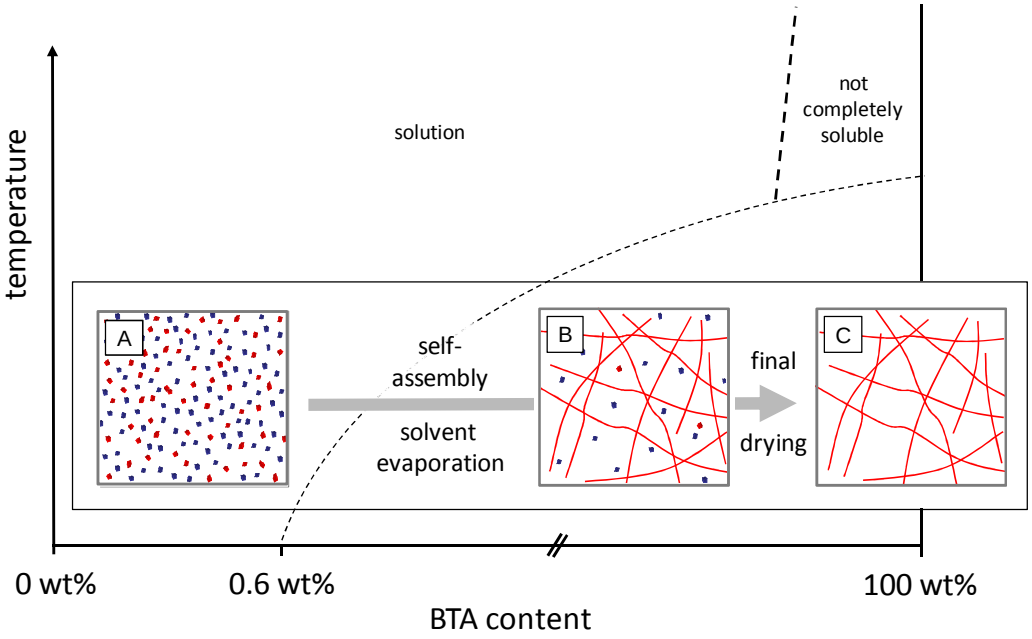

Scheme 3. Schematic representation of the self-assembly process during solvent evaporation in form of a temperature/composition diagram. (A): dissolved BTA molecules in polar solvents, blue dots: solvent molecules, red dots: dissolved BTA molecules. (B) self-assembled BTA aggregates in suspension; (C): dried supramolecular aggregates.

In the following, structure property relations between the resulting supramolecular morphology and the used solvent as well as the molecular structure are pointed out. Due to the concentration increase during solvent evaporation in the actual self-assembly process, the investigation of the influence of different concentrations is redundant. In order to study the influence of solvent, **2**/butanone and **2**/ethanol solutions with concentrations of 0.6 wt% were prepared. Besides the different solvents, all processing parameters at the preparation were set constant. At first view, the morphologies of the aggregates self-assembled in butanone and in ethanol are quite similar (**Figure 8**). However, the fibers prepared in butanone are very thin, which can be also seen in the corresponding histogram. Some of the fibers even have diameters less than 100 nm. The mean fiber diameter is determined to 0.22 µm, which is in good agreement with the average fiber diameter of the nanofibers obtained from exclusive self-assembly during solvent evaporation in the combined self-assembly process represented in Figure 5 and Figure 6. In contrast, the BTA fibers prepared in ethanol are thicker, featuring an average fiber diameter of 0.53 µm. Even though both solvents have almost the same boiling point, they possess different vapor pressures (butanone: 105 hPa; ethanol: 58 hPa). Because of this, butanone evaporates faster. Hence, the various supramolecular morphologies could origin from different self-assembly velocities.

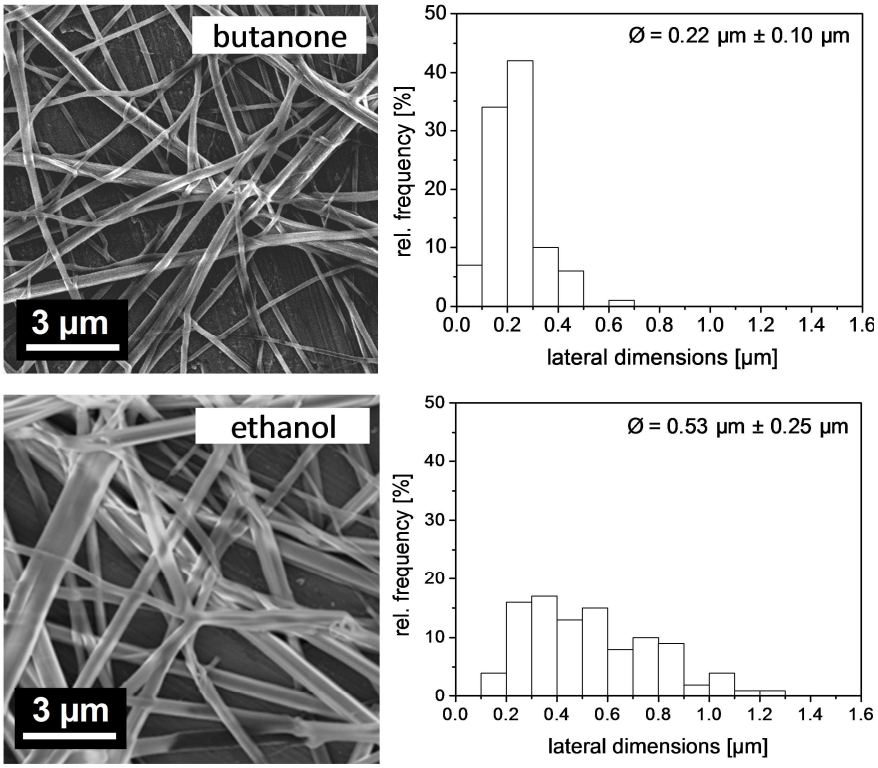

Figure 8. SEM micrographs and the corresponding histograms of self-assembled nanofibers of **2** prepared from a butanone and an ethanol solution with an initial concentration of 0.6 wt%, respectively.

The resulting supramolecular aggregates, self-assembled during solvent evaporation from butanone and ethanol, respectively, possess further differences in view of their cross sections. Under the applied conditions, we always observed solid cores of the supramolecular fibers prepared from butanone solution. In contrast, fibers prepared from ethanol both solid as well as hollow fibers could be obtained under distinct conditions. For fibers with diameters in the nanometer range, only solid cores were observed. However, with increasing diameter more and more hollow fibers emerge. Exemplarily, for supramolecular fibers of **2** prepared in ethanol, a solid nanofiber end as well as a hollow microfiber which was broken during sample preparation is shown in **Figure 9**. The cross sections of both fibers feature hexagonal dimensions. The hole of the tubular assembly is about 1 µm in diameter while its walls are 400-600 nm thick. Due to the structuring at the walls of the hollow fiber, it can be assumed, that the walls consist of several smaller aggregates which are parallel aligned along their longitudinal axis.

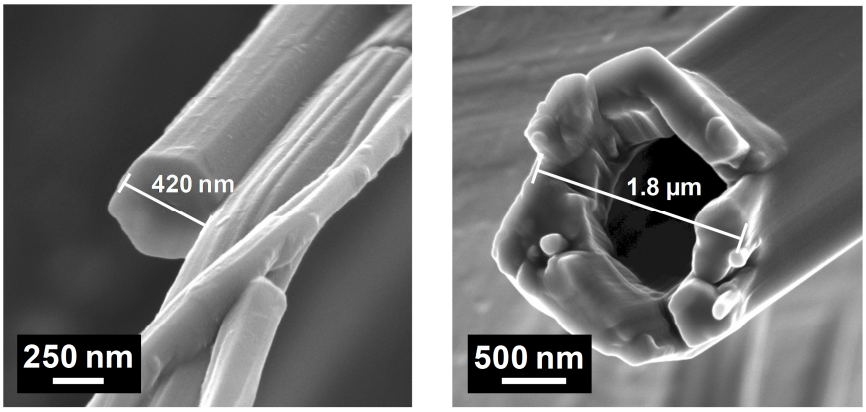

Figure 9. SEM micrographs of the cross sections of a self-assembled solid nanofiber (left) and a hollow microfiber (right), prepared from an ethanol solution of **2**.

Since the peripheral alkyl substituents of the BTAs are responsible for solubility properties, the self-assembly can also be influenced by the molecular structure. To identify this structure-property relation, BTA-dependent self-assembly studies were performed (**Figure 10**). The molecular structures of **2** and **3** do not vary dramatically. As only difference, the methyl groups are located at the C-6 positions at compound **2**, while at **3** they are located at the C-1 positions. As can be seen in the SEM micrographs, the supramolecular fibers of **2** are lying randomly on top of each other, while the fibers of **3** seem to be connected at nodal points forming a three-dimensional network. In the corresponding histograms, diverse widths of the diameter distributions as well as different average fiber diameters of 0.22 µm (**2**) and 0.45 µm (**3**) are obtained. Evidently, subtle changes in the molecular structure influence the supramolecular morphology.

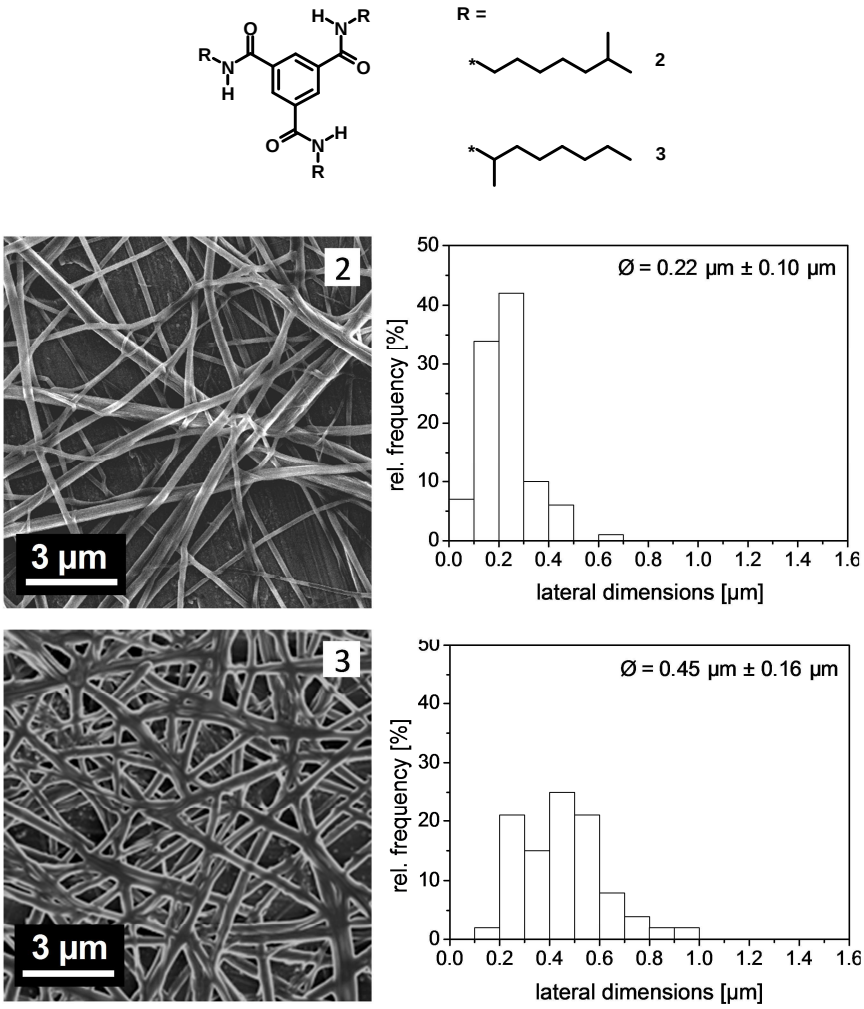

Figure 10. SEM micrographs and the corresponding histograms of self-assembled nanofibers of **2** and **3** (N^1,N^3,N^5-Tris(1-methylheptyl)-1,3,5-benzenetricarboxamide) prepared from butanone solutions (initial concentration: 0.6 wt%).

Conclusion

In summary, we investigated different self-assembly pathways for various BTA/solvent systems. We found, that the solubility of the utilized BTA/solvent system is the key factor which determines the occurring self-assembly processing pathway. Thereby, we distinguish between two different BTA/solvent systems: I.) BTAs with short substituents in combination with apolar solvents, which result in (mainly) insoluble systems at room temperature. II.) BTAs with long alkyl chains as substituents combined with polar solvents, such as ethanol or butanone which possess complete solubility at room temperature in a certain concentration range. While the insoluble systems self-assemble exclusively upon cooling, highly soluble systems at room temperature assemble during solvent evaporation. As consequence, BTA/solvent systems which are

just partially soluble at room temperature assemble in a combination of self-assembly upon cooling and self-assembly during solvent evaporation resulting in a bimodal fiber morphology. By means of separating both sort of supramolecular aggregates, we were able to determine their origins in view of the self-assembly processing pathways. Despite their different origins, XRD measurements reveal the same crystal structure for both sort of supramolecular fibers. Furthermore, we demonstrated a comprehensive study of structure-property relations by means of variations in the molecular structure as well as external parameters such as medium (solvent), concentration, and cooling rate in order to control the supramolecular nanofiber morphology.

Acknowledgements

We gratefully acknowledge financial support by the Deutsche Forschungsgemeinschaft within the collaborative research centre SFB 840 (Project B8). The authors are indebted to W. Reichstein (Bayreuth Institute of Macromolecular Research) and A. Timme (Macromolecular Chemistry I, University of Bayreuth) for conducting focused ion beam experiments and XRD measurements, respectively. H.M. acknowledges support by the Elite Study Program - *Macromolecular Science* (Elite Network of Bavaria).

Experimental Section

Materials:

Tris(2,2-dimethylpropionylamino)-1,3,5-benzene **1** was synthesized according to standard procedures.[26] The synthesis and characterization of N,N',N''-Tris(6-methylheptyl)-1,3,5-benzenetricarboxamide **2** and N,N',N''-Tris(2-methylheptyl)-1,3,5-benzenetricarboxamide **3** were previously described by us.[15]

All solvents were purchased from Aldrich. 2,2,4,4,6,8,8-heptamethylnonane was freshly distilled under reduced pressure (15 mbar) prior to use. All other solvents were used as received.

Sample preparation for aggregates obtained from self-assembly upon cooling:

Four suspensions with different concentrations (0.06, 0.03, 0.02, and 0.005 wt%) were prepared by adding **1** to 6 g of HMN. For further homogenization these suspensions were heated to reflux (240 °C) and subsequently stirred under argon for 15 min to dissolve the BTA. Cooling to room temperature while stirring gave slightly turbid suspensions. About 0.5 ml of these suspensions were filled into home-made high

pressure pans, transferred in the Dropping Point Cell FP83HT from Mettler Toledo (controlled with the Mettler Toledo Central Processor FP90), heated to 240 °C, and subsequently cooled to room temperature with defined cooling rates of 60 °C/min and 10 °C/min, respectively. In case of liquid nitrogen cooling, the filled high pressure pan was removed out of the dropping point apparatus at 240 °C, immediately put into liquid nitrogen for 15 min, and equilibrated at room temperature. About 10 µl of each suspension was transferred onto an aluminum disk, the HMN was evaporated under high vacuum at room temperature, and the samples were examined by SEM.

Sample preparation for aggregates obtained from self-assembly during solvent evaporation:
The samples were prepared by adding **2** and **3** to 20 ml of the solvent butanone or ethanol, respectively, resulting in clear solutions at concentrations of 0.6 wt%. About 10 µl of each solution was then transferred onto an aluminum disk and the solvent was removed at ambient conditions. Final drying was done under high vacuum for 15 min. Subsequently, the samples were examined by SEM.

Sample preparation for aggregates obtained from a combination of self-assembly upon cooling and self-assembly during solvent evaporation:
The samples were prepared by adding **2** to 20 ml of butanone, resulting in a mixture with a total amount of 1.0 wt% of **2**. For homogenization these suspensions were heated to reflux until clear solutions were obtained, and the samples were subsequently cooled to room temperature. About 0.5 ml of these suspensions was filled into home-made high pressure pans. In the Dropping Point Cell FP83HT from Mettler Toledo the different samples were heated to 75 °C and afterwards cooled to room temperature with a defined cooling rate (10 °C/min). About 10 µl of the sample was then transferred onto an aluminum disk and the solvent was removed at ambient conditions. Final drying was done under high vacuum for 15 min. Subsequently, the samples were examined by SEM.

Scanning electron microscopy (SEM):
For SEM investigations, samples were fixed via a double-sided adhesive conductive carbon tape on a SEM sample holder. Subsequently, the samples were sputtered with platinum (1.5 nm) by a Cressington Sputter Coater 208HR. SEM micrographs were recorded using a Zeiss 1530 FESEM equipped with an In-lens detector. Focused ion beam experiments were carried out on a Zeiss 1540 EsB CrossBeam.

Fiber diameter histograms:

In each analyzed SEM micrograph, fiber diameters of 100 different positions were determined utilizing measureIT software from Olympus. The histograms were prepared with intervals of 100 nm steps. In case of micrographs with less than 100 objects several SEM micrographs were used to determine the lateral dimensions.

Gravimetrical detection of the concentration of the BTA responsible for self-assembly upon cooling and self-assembly during solvent evaporation:

10 ml of five butanone suspensions (initial concentration: 1.0 wt%) of **2** were prepared in vials. The samples were heated to reflux until optically clear solutions were obtained and cooled to room temperature. After 12 h the formed aggregates were filtered with a commercial syringe filter (PTFE, 0.2 µm). The syringe filters were opened and the filter with the supramolecular aggregates on top were fixed on a SEM sample holder and analyzed by SEM. The remaining filtrates were dried at ambient conditions. The amount of the resulting dry nanofibers remaining in the vials was determined gravimetrically for each vial and an average value was calculated. The obtained nanofibers were fixed on a SEM sample holder to be investigated by SEM.

XRD analysis:

The XRD-measurements in the angle range of $\theta = 0.5° - 15°$ were carried out on a Huber Guinier diffractometer 600 equipped with a Huber germanium monochromator 611 to get Cu $K_{\alpha 1}$ radiation ($\lambda = 154.051$ pm). An extra slit diaphragm reduces the broadening of the primary beam due to scattering in air. The obtained dry nanofibers were prepared in soda mark tubes (2 mm diameter).

References

[1] S. Cantekin, T. F. A. de Greef, A. R. A. Palmans, *Chem. Soc. Rev* **2012**, *41*, 6125.

[2] a) L. Brunsveld, A. Schenning, M. Broeren, H. Janssen, J. Vekemans, E. Meijer, *Chem. Lett.* **2000**, 292. b) M. Wegner, D. Dudenko, D. Sebastiani, A. R. A. Palmans, T. F. A. de Greef, R. Graf, H. W. Spiess, *Chem. Sci.* **2011**, *2*, 2040.

[3] M. Kristiansen, P. Smith, H. Chanzy, C. Baerlocher, V. Gramlich, L. McCusker, T. Weber, P. Pattison, M. Blomenhofer, H.-W. Schmidt, *Crystal Growth & Design* **2009**, *9*, 2556.

[4] H. Cao, P. Duan, X. Zhu, J. Jiang, M. Liu, *Chem. Eur. J.* **2012**, *18*, 5546.

[5] a) R. C. T. Howe, A. P. Smalley, A. P. M. Guttenplan, M. W. R. Doggett, M. D. Eddleston, J. C. Tan, G. O. Lloyd, *Chem. Commun.* **2013**, DOI: 10.1039/c2cc37428e b) A. Bernet, R. Q. Albuquerque, M. Behr, S. T. Hoffmann, H.-W. Schmidt, *Soft Matter* **2011**, *8*, 66.

[6] M. P. Lightfoot, F. S. Mair, R. G. Pritchard, J. E. Warren, *Chem. Commun.* **1999**, 1945.

[7] a) S. Lee, J.-S. Lee, C. H. Lee, Y.-S. Jung, J.-M. Kim, *Langmuir* **2010**, *27*, 1560. b) P. P. Bose, M. G. B. Drew, A. K. Das, A. Banerjee, *Chem. Commun.* **2006**, 3196. c) B. Narayan, C. Kulkarni, S. J. George, *J. Mater. Chem.* **2013**, *1*, 626.

[8] R. Q. Albuquerque, A. Timme, R. Kress, J. Senker, H.-W. Schmidt, *Chem. Eur. J.* **2013**, *19*, 1647.

[9] a) L. Sardone, V. Palermo, E. Devaux, D. Credgington, M. de Loos, G. Marletta, F. Cacialli, J. van Esch, P. Samorì, *Adv. Mater.* **2006**, *18*, 1276. b) C. F. C. Fitie, W. S. C. Roelofs, P. C. M. M. Magusin, M. Wubbenhorst, M. Kemerink, R. P. Sijbesma, *J. Phys. Chem. B* **2012**, *116*, 3928.

[10] M. Schmidt, J. J. Wittmann, R. Kress, D. Schneider, S. Steuernagel, H.-W. Schmidt, J. Senker, *Crystal Growth & Design.* **2012**, *12*, 2543.

[11] C. A. Jiménez, J. B. Belmar, L. Ortíz, P. Hidalgo, O. Fabelo, J. Pasán, C. Ruiz-Pérez, *Crystal Growth & Design* **2009**, *9*, 4987.

[12] L. Rajput, G. Mukherjee, K. Biradha, *Crystal Growth & Design* **2012**, *12*, 5773.

[13] a) I. Tomatsu, C. F. C. Fitié, D. Byelov, W. H. de Jeu, P. C. M. M. Magusin, M. Wübbenhorst, R. P. Sijbesma, *J. Phys. Chem. B* **2009**, *113*, 14158. b) Y. Matsunaga, Y. Nakayasu, S. Sakai, M. Yonenaga, *Molecular Crystals and Liquid Crystals* **1986**, *141*, 327. c) Y. Matsunaga, N. Miyajima, Y. Nakayasu, S. Sakai, M. Yonenaga, *Bull. Chem. Soc. Jpn.* **1988**, *61*, 207.

[14] a) P. J. M. Stals, J. F. Haveman, R. Martin-Rapun, C. F. C. Fitie, A. R. A. Palmans, E. W. Meijer, *J. Mater. Chem.* **2009**, *19*, 124. b) P. J. M. Stals, M. M. J. Smulders, R. Martín-Rapún, A. R. A. Palmans, E. W. Meijer, *Chem. Eur. J.* **2009**, *15*, 2071.

[15] A. Timme, R. Kress, R. Q. Albuquerque, H.-W. Schmidt, *Chem. Eur. J.* **2012**, *18*, 8329.

[16] a) M. Blomenhofer, S. Ganzleben, D. Hanft, H.-W. Schmidt, M. Kristiansen, P. Smith, K. Stoll, D. Mäder, K. Hoffmann, *Macromolecules* **2005**, *38*, 3688. b) F. Abraham, S. Ganzleben, D. Hanft, P. Smith, H.-W. Schmidt, *Macromol. Chem. Phys.* **2010**, *211*, 171.

[17] F. Abraham, R. Kress, P. Smith, H.-W. Schmidt, *Macromolecular Chemistry and Physics* **2013**, *214*, 17-24.

[18] F. Abraham, H.-W. Schmidt, *Polymer* **2010**, *51*, 913.

[19] F. Richter, H.-W. Schmidt, *Macromol. Mater. Eng.* **2012**, DOI: 10.1002/mame.201200034.

[20] a) N. Mohmeyer, N. Behrendt, X. Zhang, P. Smith, V. Altstädt, G. M. Sessler, H.-W. Schmidt, *Polymer* **2007**, *48*, 1612. b) D. P. Erhard, D. Lovera, C. Salis-Soglio, R. Giesa, V. Altstädt, H.-W. Schmidt (Eds.: A. H. E. Müller, H.-W. Schmidt), Springer Berlin Heidelberg. Berlin, Heidelberg **2010**, 155.

[21] a) D. Kluge, F. Abraham, S. Schmidt, H.-W. Schmidt, A. Fery, *Langmuir* **2010**, *26*, 3020. b) D. Kluge, J. C. Singer, J. W. Neubauer, F. Abraham, H.-W. Schmidt, A. Fery, *Small* **2012**, *8*, 2563.

[22] a) Y. Yasuda, E. Iishi, H. Inada, Y. Shirota, *Chem. Lett.* **1996**, 575. b) K. Hanabusa, C. Koto, M. Kimura, H. Shirai, A. Kakehi, *Chem. Lett.* **1997**, 429. c) J. J. van Gorp, J. A. J. M. Vekemans, E. W. Meijer, *J. Am. Chem. Soc.* **2002**, *124*, 14759. d) I. Danila, F. Riobe, J. Puigmarti-Luis, A. Perez del Pino, J. D. Wallis, D. B. Amabilino, N. Avarvari, *J. Mater. Chem.* **2009**, *19*, 4495.

[23] N. E. Shi, H. Dong, G. Yin, Z. Xu, S. H. Li, *Adv. Funct. Mater.* **2007**, *17*, 1837.

[24] J. C. Singer, R. Giesa, H.-W. Schmidt, *Soft Matter* **2012**, *8*, 9972.

[25] Daniel Kluge, Julia. C. Singer, Benedikt R. Neugirg, Jens W. Neubauer, Hans-Werner Schmidt, Andreas Fery, *Polymer* **2012**, *53*, 5754.

[26] H.-W. Schmidt, M. Blomenhofer, K. Stoll, H. Meier, **2004**, WO 2004072168.

3.4 Supramolecular nanofiber webs in nonwoven scaffolds as potential filter media

*Holger Misslitz, Klaus Kreger, and Hans-Werner Schmidt**

Macromolecular Chemistry I, Bayreuther Institut für Makromolekülforschung (BIMF), Bayreuther Zentrum für Kolloide und Grenzflächen (BZKG), University of Bayreuth, 95440 Bayreuth, Germany

SMALL **2013**, *9*, 2053.

Microfiber-nanofiber composites are prepared by *in situ* formation of supramolecular nanofiber webs based on 1,3,5-benzenetricarboxamides in polymer nonwoven scaffolds. These composites are sufficiently stable to be suited for air filtration applications. The image shows supramolecular nanofibers strongly fixed to the nonwoven microfibers.

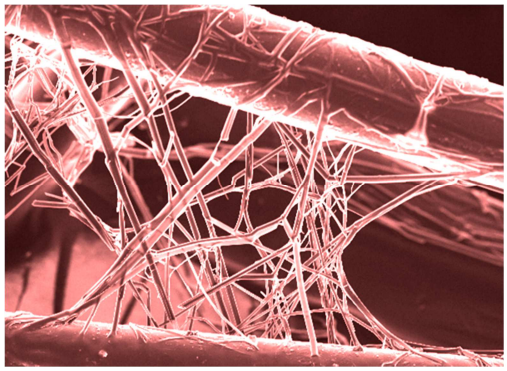

Keywords: Self-assembly, nanofibers, microfiber-nanofiber composites, filters

Self-assembly phenomena and supramolecular concepts are of keen interest in manifold scientific areas.[1–3] For example, self-assembly of small molecules into supramolecular nanofibers in organic liquids or water has been demonstrated and is utilized to efficiently prepare thermoreversible organo-[4–7] and hydrogels.[8–12] However, very little is known about the formation of stable nanofiber webs and the intrinsic stability in the dried state. Both issues are of key relevance for fibrous materials in applications, such as filtration. Only very few publications in this area exist. For instance, Raghavanpillai *et al*. demonstrated the formation of supramolecular nanofiber webs with organogelators in combination with a porous support, but no filter experiments were reported.[13] Krieg *et al*. have shown recently that a deposited supramolecular membrane on top of a supporting syringe filter is suitable to separate gold nanoparticles of different size from solution.[14,15]

Although many examples of compounds are known which are capable of forming supramolecular nanofibers, one of the simplest and well-established structural motif is based on 1,3,5-benzenetrisamides (BTAs).[6,16–19] Self-assembly of BTAs into columnar stacks driven by directed hydrogen bond formation results in a broad variety of morphologies.[20] The formed morphology depends on the molecular structure of the BTA, the solvent, the concentration, and the applied processing conditions. As a consequence of this complexity, BTAs have to be tailored towards specific applications. Successful examples are supramolecular additives for nucleation[21–29] and clarification[21] of thermoplastic semi-crystalline polymers or as additives to improve the electret performance of polypropylene.[30–32]

Recently, we have shown by AFM force mapping methodology that single self-assembled BTA-nanofibers feature a remarkable mechanical stability with Young's moduli in the low GPa range[33,34] demonstrating that supramolecular nanofibers can withstand certain mechanical stress. These findings encouraged us to explore the *in situ* formation of supramolecular nanofiber webs in nonwoven scaffolds with the emphasis to prepare sufficiently stable polymer-microfiber/supramolecular-nanofiber composites, also in view of filter applications.

This communication reports on the feasibility of this approach and demonstrates for the first time the overall stability and principle applicability in air filtration. In nanofiber technology for filter purposes, electrospun polymer nanofibers are generally used in combination with a support.[35] Fiber deposition is conducted typically on top of this support. In contrast, we present here a bottom-up approach in which the formation of supramolecular nanofibers is carried out inside the scaffold. This *in situ* process can be easily accomplished by dipping a nonwoven fabric (physically or chemically connected sheet of fibers with openings and voids) into an immersion solution at elevated temperatures. At this temperature the supramolecular building units are dissolved. The immersion solution penetrates the fabric through the openings and voids. After

removing the soaked scaffold and during solvent evaporation the small molecules self-assemble into supramolecular nanofibers within the nonwoven (**Scheme 1**).

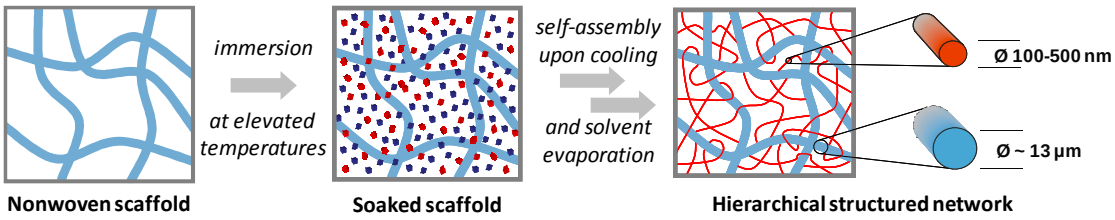

Scheme 1. Schematic representation of the *in situ* formation process of supramolecular nanofibers via self-assembly resulting in microfiber-nanofiber composites. Blue fibers: nonwoven scaffold; red dots: dissolved supramolecular building units; blue dots: solvent; red fibers: supramolecular nanofibers.

As a nonwoven, a commercially available, 0.15 mm thick viscose/polyester fabric with a uniform fiber diameter of 13 µm and a basis weight of 32.2 g/m^2 was used (see supporting information, **Figure S1**). In screening experiments evaluating different BTAs in different solvents, the compound N,N',N''-Tris(2-ethylhexyl)-1,3,5-benzenetricarboxamide **1** in 2-butanone has been proven to be a suitable system. It should be mentioned that BTA **1** is not a gelator for 2-butanone, which is an advantage for the here employed process. Taken into account that the solvent uptake in the nonwoven fabric is approximately the seven to eightfold weight of the fabric, the concentration of **1** in the immersion solution was investigated only up to 1.0 wt% in order to avoid too dense filling of the fabric with supramolecular nanofibers. Screening experiments revealed that the interesting concentration range of the immersion solution is between 0.4 wt% and 1.0 wt%. In order to vary the final amount of the nanofibers in the composite, four concentrations (0.4 wt%, 0.6 wt%, 0.8 wt%, and 1.0 wt%) were used. The influence of the concentration of the immersion solution on the resulting morphology of the nanofiber-microfiber composite and on the nanofiber diameter and distribution is discussed in the following. The content of the supramolecular nanofibers in the nanofiber-microfiber composite was determined by weighing samples with and without supramolecular nanofibers. We found an average nanofiber content in the composites of 2.8 wt%, 4.4 wt%, 6.4 wt%, and 7.0 wt% correlating with the increasing concentration of the immersion solution and solution uptake. The morphology of the microfiber-nanofiber composites was investigated by means of scanning electron microscopy (SEM). **Figure 1** compares SEM pictures in an overview and in a ten times higher magnification of nonwovens with different nanofiber content. The thick fibers correspond to the nonwoven microfibers (see supporting information, Figure S1) and the thin fibers to the self-assembled nanofibers. These nanofibers are located on top and between the microfibers.

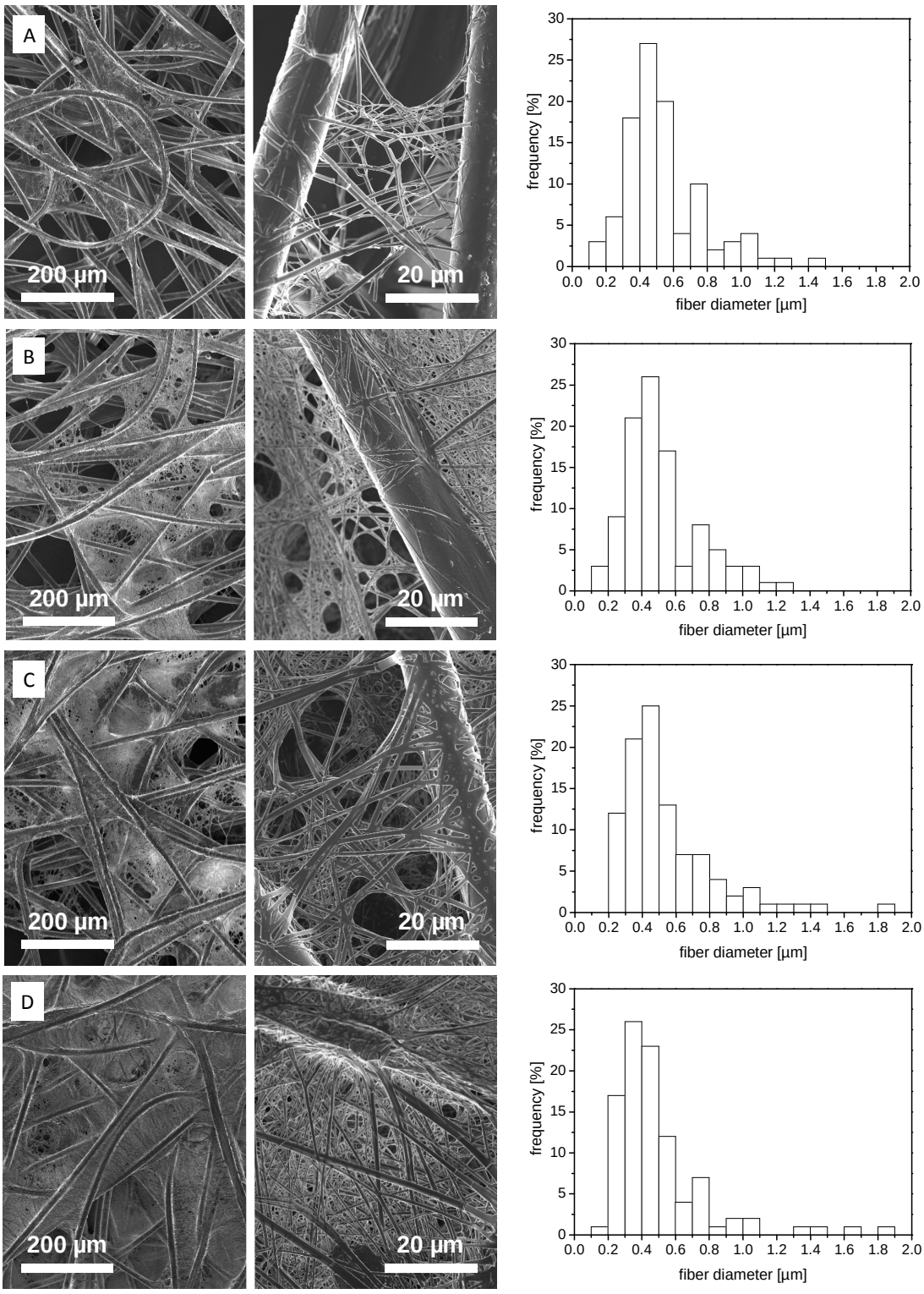

Figure 1. SEM micrographs of the microfiber-nanofiber composites **A-D** with increasing amount of nanofibers (**A**: 2.8 wt%; **B**: 4.4 wt%; **C**: 6.4 wt%, and **D**: 7.0 wt%) prepared from four concentrations of **1** in the immersion solutions (0.4 wt%, 0.6 wt%, 0.8 wt%, and 1.0 wt%). The corresponding histograms (100 nm intervals) of the nanofiber diameters on the basis of more than 90 fibers are shown on the right.

At the lowest investigated concentration of the immersion solution at 0.4 wt% the overview SEM picture (**A**, left) reveals an uneven filling of the openings by the self-assembled nanofibers inside the nonwoven fabric. The supramolecular nanofibers are rather located in individual voids. This phenomenon was generally observed for low concentrations and is attributed to the complex drying process within the nonwoven. It seems that during solvent evaporation at the final stages only some openings are covered. This would not happen if the BTA would form a gel. In such a case an interpenetrating and evenly distributed network structure would be expected. At a higher magnification (**A**, right) the supramolecular nanofiber web is clearly visible. It is remarkable that the supramolecular nanofibers have a strong tendency to self-fixate to the polymer microfibers and even seem to wind around the microfibers. These findings are unexpected and different from known morphologies of xerogels prepared from supramolecular fibrillar gels, where typically homogenous collapsed networks are observed. On the right of Figure 1 the fiber diameter histograms are presented, which are based on evaluating more than 90 fibers from representative sections of a larger area of the sample. For the microfiber-nanofiber composite **A** with a supramolecular fiber amount of 2.8 wt%, about 93% of the fiber diameters are below 1 µm. The average diameter of this fraction of the supramolecular nanofibers is 484 nm ± 177 nm with a minimum of 160 nm. At a higher concentration of the immersion solution (0.6 wt%), resulting in a content of 4.4 wt% of supramolecular nanofibers in the composite **B**, the overview image confirms that more of the openings are closed. The picture at higher magnification shows also much denser nanofiber webs, which are fixed in a similar manner as found above strongly to the polymer microfibers. About 95% of the fibers are below 1 µm. Here the average fiber diameter is 472 nm ± 189 nm with a minimum of 150 nm. In addition, the supramolecular nanofiber web contains a few larger fibers with diameters above 1 µm. Remarkably, the overall thickness and the distribution of the nanofibers is very similar as discussed before. At the next higher concentration of the immersion solution (0.8 wt%), corresponding to a nanofiber content of 6.4 wt% (**C**), more openings are filled and the same morphology of the supramolecular fiber webs is present (average nanofiber diameter: 471 nm ± 180 nm; minimum: 220 nm). At the highest investigated immersion solution concentration (1.0 wt%), resulting in a final supramolecular fiber content of 7.0 wt% in composite **D**, most of the openings of the nonwoven are filled with nanofibers. Again the same morphology of the supramolecular fiber web with about 93% of fiber diameters below 1 µm and some larger fibers is observed (average nanofiber diameter: 426 nm ± 170 nm; minimum: 160 nm). All experiments and investigations were performed several times and proved to be reproducible. These results clearly show that at least for this BTA compound in the investigated concentration range the influence of the concentration on the morphology of the supramolecular fiber web,

nanofiber diameter and distribution thereof is marginal. However, concentration changes strongly influence the fraction of filled openings in the nonwoven. In addition, it determines the nanofiber density within the supramolecular fiber webs.

Nanofibers feature a beneficially high surface area to volume ratio, since the specific surface area scales inversely with the diameter. Hence, nanofibers are very promising for filtration applications, as the probability of a particle deposition on the filter media is increased with increasing specific surface area resulting in improved efficiencies.[36] Therefore, Brunauer-Emmett-Teller (BET) surface area analyses were conducted on microfiber-nanofiber composite **A** - **D** and on the nonwoven as reference (**Figure 2**). The untreated nonwoven exhibits a BET surface area of 0.12 m^2/g, whereas the surface area of the composite materials is increasing up to a value of 0.47 m^2/g.

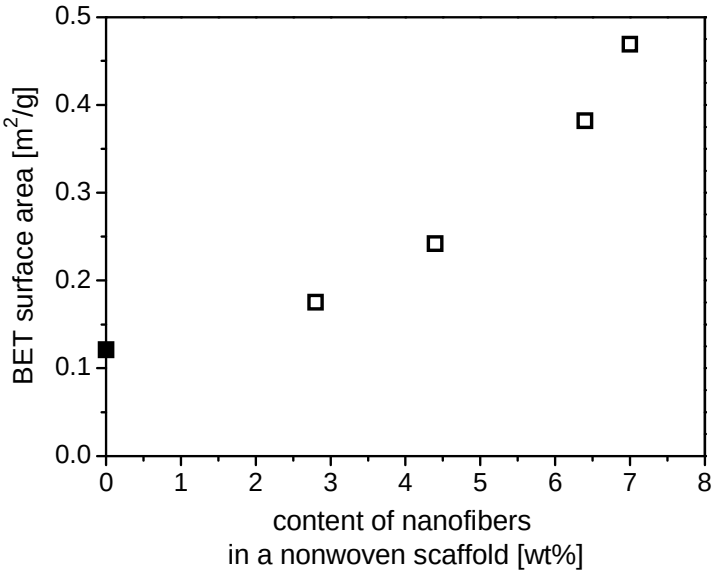

Figure 2. BET surface area of the nonwoven scaffold (solid square) and the microfiber-nanofiber composites **A** - **D** (open squares).

The overall mechanical stability of the supramolecular nanofibers is an important question, particularly in view of their use as potential filter media. We have conducted three experiments to gain more insight into the stability of the nanofiber web within the microfiber-nanofiber composite: (i) monitoring the differential pressure during an airstream test, (ii) monitoring possible fragments originating from the supramolecular nanofibers during the test, and (iii) SEM investigations before and after such an experiment. For these experiments, the microfiber-nanofiber composite **D** with the highest nanofiber content was subjected to an airstream test in a filter test rig at a flow rate of 3 m/s for a time period of 24 h. During these experiments the differential pressure, which is defined as the difference in pressure before and after a filter (see supporting information **Figure S2**), was monitored (**Figure 3**). The microfiber-nanofiber

composite **D** causes a differential pressure of about 1900 Pa. This value is more than a magnitude of order higher than the differential pressure of the microfiber scaffold without supramolecular nanofiber web (156 Pa). This large difference proves that the entire exposed area of 9.4 cm^2 of the microfiber-nanofiber composite **D** is uniformly covered by supramolecular nanofibers and no large pathways, holes or cracks exist. Most important is that during this experiment the pressure drop is constant for 24 h proving that the composite **D** remains intact. The filter test rig also allows the detection of particles in the size range of 0.2 µm to 10 µm by means of a particle size analyzer behind the microfiber-nanofiber composite. Thus, it is possible to detect fragments originating from the supramolecular nanofibers. During the entire 24 h airstream test, no fragments were monitored. This result is of critical importance, as it proves that the supramolecular nanofibers are robust enough and do not break up during such an experiment. The results are confirmed by SEM investigations (**Figure 4**) showing no significant difference of the morphology of the composite before and after the airstream test.

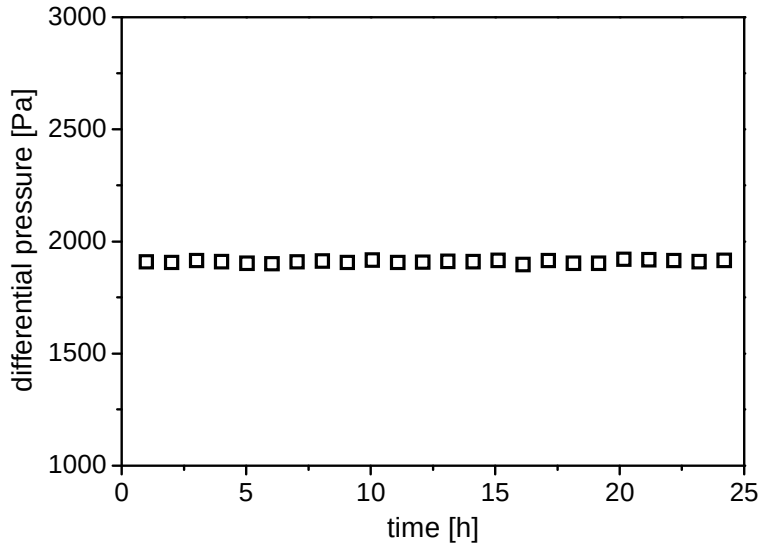

Figure 3. Temporal evolution of the differential pressure during an airstream test with microfiber-nanofiber composite **D** at a flow rate of 3.0 m/s. The exposed area was 9.4 cm^2. Measurements were taken in one hour steps.

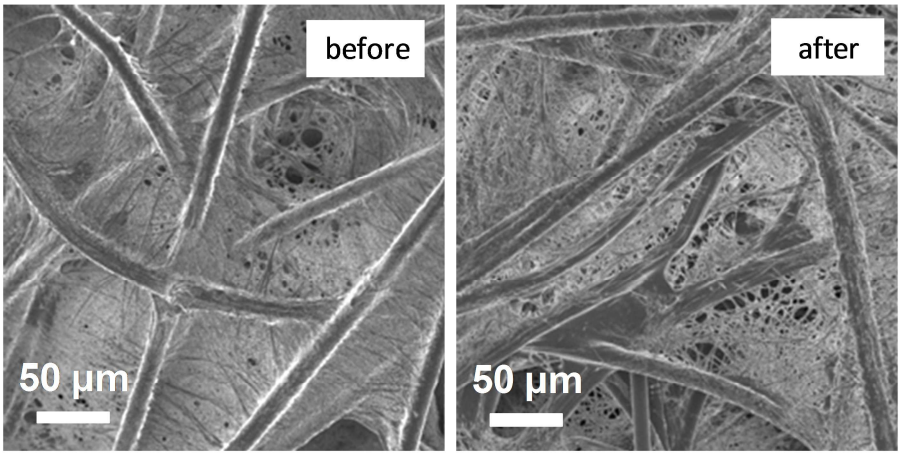

Figure 4. SEM micrographs of the microfiber-nanofiber composite **D** (containing 7.0 wt% of nanofibers) before and after the airstream test.

To validate the applicability of supramolecular nanofiber webs in the nonwoven scaffold as filtration medium, filtration tests were performed with ISO fine test dust, a fine particulate matter. The particle size distribution in the range of 0.2 µm to 1.0 µm is shown in the supporting information, Figure S2. The filtration efficiency is defined as the percentage of the particles removed by the filter medium and depends on the size of the particulate matter (Figure S2). The filter test experiments were conducted in a filter test rig with an airstream at a constant flow rate of 0.25 m/s and an aerosol particle concentration of about 6000 particles/cm^3. For each microfiber-nanofiber composite composition, three individual samples were prepared and subjected to the filter test. The deviations of the filtration efficiencies of the individual composites are below ± 10 % proving that the composite preparation is highly reproducible (see supporting information, **Figure S3**). The averaged filtration efficiencies for a particle range of 200 - 1000 nm of the microfiber-nanofiber composites and of the untreated nonwoven are shown in **Figure 5**. As expected, the filtration efficiency of the nonwoven is poor and in the investigated range the efficiency is around 5% to 6% with a differential pressure of 9 Pa. For the microfiber-nanofiber composite **A** with only 2.8 wt% of nanofibers, the filtration efficiency is more than doubled. The filters are capable of retaining 12% of 0.2 µm particles and 15% of 1 µm particles. The differential pressure is only slightly increased to 13 Pa. The filtration efficiency is further improved for the microfiber-nanofiber composite **B** with 4.4 wt% of nanofibers. A slightly better performance for bigger particles is noticeable, namely 21% for 0.2 µm particles and 32% for 1.0 µm particles. The value of differential pressure of 28 Pa is still low. In the case of the composites **C** and **D**, a significant performance improvement is apparent. This large improvement is assigned to a very high coverage with supramolecular nanofibers for both composites (see Figure 1). The nanofiber composite **C** exhibits a filtration efficiency for 0.2 µm particles of 57% and for 1.0 µm particles of 81%. The

nanofiber composite **D** results in a filtration efficiency for 0.2 µm particles of 67% and for 1.0 µm particles of 87%. This difference is attributed to the denser nanofiber web of the composite **D** compared to the composite **C** and is also reflected in the larger increase in differential pressure from 281 Pa for composite **C** to 429 Pa for composite **D**.

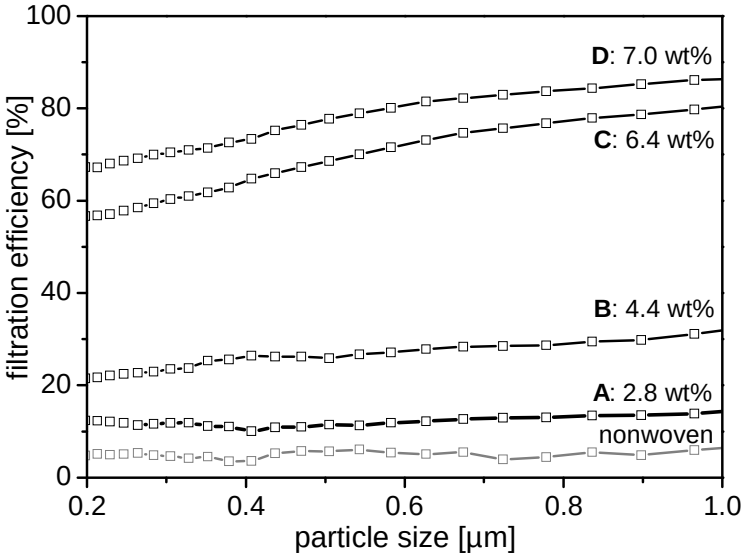

Figure 5. Average filtration efficiencies of microfiber-nanofiber composites with different content of supramolecular nanofibers and of the untreated nonwoven (measuring time: 30 s; flow rate: 0.25 m/s; filtration area: 28.3 cm^2, test aerosol: ISO fine test dust, upstream aerosol concentration: 6000 particles/cm^3).

To conclude, we have demonstrated the successful *in situ* formation of supramolecular nanofiber webs based on a 1,3,5-benzentrisamide inside of nonwoven scaffolds via a solution-based bottom-up approach. It has been revealed that within the investigated BTA concentration range of the immersion solution the influence of the BTA concentration on the morphology of the supramolecular fiber web, nanofiber diameter, and the nanofiber diameter distribution is marginal. Most surprisingly, the supramolecular nanofibers have the tendency to strongly adhere to the polymer microfibers and even wind around the microfiber. This unexpected behavior together with the intrinsic stability of the supramolecular nanofibers contributes to the overall stability of the microfiber-nanofiber composites. These features in combination with the increased surface area make these composite materials suitable as filter media for air filtration. In general, the *in situ* preparation of supramolecular nanofibers via the described bottom-up approach within open porous structures is an appealing, beneficial alternative compared to established top-down processes such as melt-blowing, centrifugal melt spinning, blend melt spinning, and electrospinning.

Experimental Section

Materials:

The synthesis and characterization of the diastereomeric mixture of N,N',N''-Tris(2-ethylhexyl)-1,3,5-benzenetricarboxamide **1** is described in detail in literature.[37] The BTA features a columnar hexagonal plastic phase at room temperature, a columnar hexagonal ordered phase above 241 °C, and becomes optically isotropic at 291 °C.

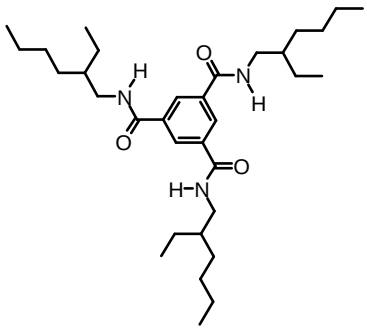

1

2-Butanone (purity: 99.7 %) was purchased from Aldrich and used as received. ISO 12103-1, A2 fine test dust was received from Powder Technology Inc. As scaffold a commercially available viscose/polyester microfiber nonwoven fabric was used (source: AMPri). The fabric has a thickness of 0.15 mm and a basis weight of 32.2 g/m^2. The nonwoven fabrics were cut into squares of 9.5 cm x 9.5 cm.

Preparation of supramolecular nanofiber webs in a nonwoven fabric:

The immersion solutions of **1** in 2-butanone were prepared with concentrations of 0.4, 0.6, 0.8, and 1.0 wt% of **1** by suspending the corresponding amount of BTA in the solvent and heating to 50 °C until a clear solution was obtained. The solution was filled into a custom-made immersion bath, which was placed in a thermostat at a temperature of 50 °C. The cut nonwoven fabric was clamped into a supporting metal frame with an open quadratic area of 8.5 cm x 8.5 cm. The supporting frame with the microfiber fabric was dipped into the immersion solution for 30 s. The soaked fabric was removed and dried in the frame at ambient conditions for 10 min and for 30 min in vacuum.

Scanning electron microscopy (SEM):

For SEM investigations, samples were fixed via a double-sided adhesive conductive carbon tape on a SEM sample holder. Subsequently, the samples were carbon-coated utilizing a MED 010 coating machine from Baltzer. SEM micrographs were recorded using a Zeiss 1530 FESEM equipped with an Inlens detector (acceleration voltage: 5 kV).

Fiber diameter histograms and average nanofiber diameter:
In each analyzed SEM micrograph, fiber diameters of more than 90 self-assembled nanofibers were determined utilizing measureIT software from Olympus. The histograms were prepared in 100 nm steps. The average diameter of nanofibers is calculated for the fraction of nanofibers with diameters below 1 µm and yields for the microfiber-nanofiber composite **A**: 480 nm ± 180 nm (93%), **B**: 470 nm ± 190 nm (95%), **C**: 470 nm ± 180 nm (91%), and **D**: 430 nm ± 170 nm (93%). The fraction of the supramolecular nanofibers with diameters below 1 µm is given in brackets.

Brunauer Emmett Teller Measurements (BET):
All measurements were carried out on a Quantachrome Autosorb 1. Thereby, 0.5 g of the microfiber-nanofiber composite was put in a sample cell (9 mm) with large sphere. All samples were carefully degassed at 25 °C at ultra high vacuum for 12 h. Krypton was used as absorption gas. Seven data points within the range of $0.05 < p/p_0 < 0.3$ were taken to calculate the specific surface area using the BET equation. The BET surface area of each sample was determined at least twice and the average thereof was calculated.

Filter testing procedures:
All measurements were performed utilizing a custom build filter test rig based on the MFP 2000 from PALAS® with a white light-scattering spectrometer Welas ® digital 2100 (particle size detection range: 0.2 µm – 10.0 µm).

Airstream test:
The effective exposed area of the microfiber-nanofiber composite in the filter test rig was reduced from 28.3 cm^2 to 9.4 cm^2 in order to achieve a flow rate of 3.0 m/s. The samples were fixed via a pneumatic sample holder. A continuous air flow without aerosol particles was applied to the filter for a period of 24 h. The differential pressure was recorded every hour and particles or fragments, originating from the microfiber-nanofiber composite, were monitored by means of a particle analyzer.

Filtration test:
As test aerosol ISO fine test dust was used. ISO fine test dust was applied to the filter test rig utilizing a RBG 1000 powder dispenser from PALAS®. The composites were fixed with a pneumatic sample holder in the filter test rig and a particle concentration of 6000 particles/cm^3 was applied at a flow rate of 0.25 m/s to the samples with an effective filtration area of 28.3 cm^2. The measuring time was 30 s. The filtration efficiency was determined by recording the particle concentration without the composite material (upstream concentration) and with the composite material (downstream concentration).

Acknowledgement

We gratefully acknowledge financial support by the Deutsche Forschungsgemeinschaft within the collaborative research centre SFB 840 (Project B8). H.M. acknowledges support by the Elite Study Program - *Macromolecular Science* within the Elite Network of Bavaria. We are indebted to Lena Geiling (Inorganic Chemistry I, University of Bayreuth) for conducting the BET measurements.

References

[1] R. G. Weiss, P. Terech, *Molecular gels: Materials with self-assembled fibrillar networks*, Springer, Dordrecht **2006**.

[2] L. C. Palmer, S. I. Stupp, *Acc. Chem. Res.* **2008**, *41*, 1674.

[3] C. C. Lee, C. Grenier, E. W. Meijer, A. P. H. J. Schenning, *Chem. Soc. Rev.* **2009**, *38*, 671.

[4] Y. Yasuda, E. Iishi, H. Inada, Y. Shirota, *Chem. Lett.* **1996**, 575.

[5] K. Hanabusa, C. Koto, M. Kimura, H. Shirai, A. Kakehi, *Chem. Lett.* **1997**, 429.

[6] J. J. van Gorp, J. A. J. M. Vekemans, E. W. Meijer, *J. Am. Chem. Soc.* **2002**, *124*, 14759.

[7] J. Puigmartí-Luis, Á. Pérez del Pino, E. Laukhina, J. Esquena, V. Laukhin, C. Rovira, J. Vidal-Gancedo, A. G. Kanaras, R. J. Nichols, M. Brust, D. B. Amabilino, *Angew. Chem. Int. Ed.* **2008**, *47*, 1861.

[8] N. E. Shi, H. Dong, G. Yin, Z. Xu, S. H. Li, *Adv. Funct. Mater.* **2007**, *17*, 1837.

[9] Z. Yang, L. Wang, J. Wang, P. Gao, B. Xu, *J. Mater. Chem.* **2010**, *20*, 2128.

[10] A. Bernet, R. Q. Albuquerque, M. Behr, S. T. Hoffmann, H.-W. Schmidt, *Soft Matter* **2011**, *8*, 66.

[11] X. Li, Y. Kuang, H.-C. Lin, Y. Gao, J. Shi, B. Xu, *Angew. Chem. Int. Ed.* **2011**, *50*, 9365.

[12] X. Du, J. Li, Y. Gao, Y. Kuang, B. Xu, *Chem. Commun.* **2012**, *48*, 2098.

[13] A. Raghavanpillai, S. Reinartz, K. W. Hutchenson, *Journal of Fluorine Chemistry* **2009**, *130*, 410.

[14] E. Krieg, H. Weissman, E. Shirman, E. Shimoni, B. Rybtchinski, *Nature Nanotech.* **2011**, *6*, 141.

[15] E. Krieg, B. Rybtchinski, *Chem. Eur. J.* **2011**, *17*, 9016.

[16] Y. Matsunaga, N. Miyajima, Y. Nakayasu, S. Sakai, M. Yonenaga, *Bull. Chem. Soc. Jpn.* **1988**, *61*, 207.

[17] M. P. Lightfoot, F. S. Mair, R. G. Pritchard, J. E. Warren, *Chem. Commun.* **1999**, 1945.

[18] L. Brunsveld, A. Schenning, M. Broeren, H. Janssen, J. Vekemans, E. Meijer, *Chem. Lett.* **2000**, 292.

[19] S. Cantekin, T. F. A. de Greef, A. R. A. Palmans, *Chem. Soc. Rev.* **2012**, DOI: 10.1039/c2cs35156k.

[20] M. Kristiansen, P. Smith, H. Chanzy, C. Baerlocher, V. Gramlich, L. McCusker, T. Weber, P. Pattison, M. Blomenhofer, H.-W. Schmidt, *Crystal Growth & Design* **2009**, *9*, 2556.

[21] M. Blomenhofer, S. Ganzleben, D. Hanft, H.-W. Schmidt, M. Kristiansen, P. Smith, K. Stoll, D. Mäder, K. Hoffmann, *Macromolecules* **2005**, *38*, 3688.

[22] P. M. Kristiansen, A. Gress, P. Smith, D. Hanft, H.-W. Schmidt, *Polymer* **2006**, *47*, 249.

[23] J. Wang, Q. Dou, X. Chen, D. Li, *J. Polym. Sci. B Polym. Phys.* **2008**, *46*, 1067.

[24] F. Abraham, S. Ganzleben, D. Hanft, P. Smith, H.-W. Schmidt, *Macromol. Chem. Phys.* **2010**, *211*, 171.

[25] F. Abraham, H.-W. Schmidt, *Polymer* **2010**, *51*, 913.

[26] H. Nakajima, M. Takahashi, Y. Kimura, *Macromol. Mater. Eng.* **2010**, *295*, 460.

[27] H. Bai, W. Zhang, H. Deng, Q. Zhang, Q. Fu, *Macromolecules* **2011**, *44*, 1233.

[28] P. Song, Z. Wei, J. Liang, G. Chen, W. Zhang, *Polym Eng Sci* **2012**, *52*, 1058.

[29] F. Richter, H.-W. Schmidt, *Macromol. Mater. Eng.* **2012**, DOI: 10.1002/mame.201200034.

[30] N. Mohmeyer, N. Behrendt, X. Zhang, P. Smith, V. Altstädt, G. M. Sessler, H.-W. Schmidt, *Polymer* **2007**, *48*, 1612.

[31] J. Hillenbrand, T. Motz, G. M. Sessler, X. Zhang, N. Behrendt, C. von Salis-Soglio, D. P. Erhard, V. Altstädt, H.-W. Schmidt, *J. Phys. D: Appl. Phys.* **2009**, *42*, 65410.

[32] D. P. Erhard, D. Lovera, C. Salis-Soglio, R. Giesa, V. Altstädt, H.-W. Schmidt, in *Advances in Polymer Science* (Eds.: A. H. E. Müller, H.-W. Schmidt), Springer Berlin Heidelberg. Berlin, Heidelberg **2010**, p. 155.

[33] D. Kluge, F. Abraham, S. Schmidt, H.-W. Schmidt, A. Fery, *Langmuir* **2010**, *26*, 3020.

[34] D. Kluge, J. C. Singer, J. W. Neubauer, F. Abraham, H.-W. Schmidt, A. Fery, *Small* **2012**, DOI: 10.1002/smll.201200259.

[35] S. Agarwal, A. Greiner, J. H. Wendorff, *Adv. Funct. Mater.* **2009**, *19*, 2863.

[36] H.-S. Park, Y. O. Park, *Korean J. Chem. Eng.* **2005**, *22*, 165.

[37] A. Timme, R. Kress, R. Q. Albuquerque, H.-W. Schmidt, *Chem. Eur. J.* **2012**, *18*, 8329.

Supporting Information to

Supramolecular nanofiber webs in nonwoven scaffolds as potential filter media

*Holger Misslitz, Klaus Kreger, and Hans-Werner Schmidt**

Macromolecular Chemistry I
Bayreuther Institut für Makromolekülforschung (BIMF)
Bayreuther Zentrum für Kolloide und Grenzflächen (BZKG)
University of Bayreuth, D-95440 Bayreuth, Germany
E-mail: hans-werner.schmidt@uni-bayreuth.de

Table of contents:

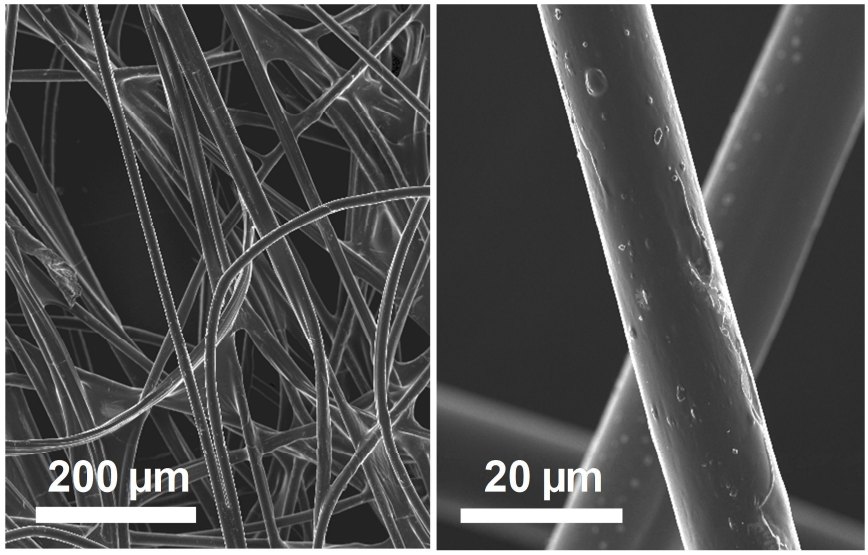

Figure S1. SEM micrographs of the untreated viscose/polyester nonwoven fabric with a uniform fiber diameter of 13 µm.

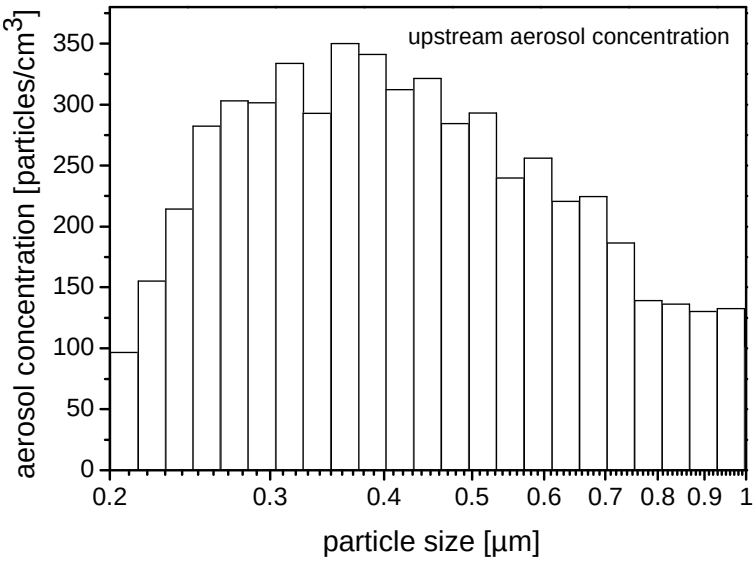

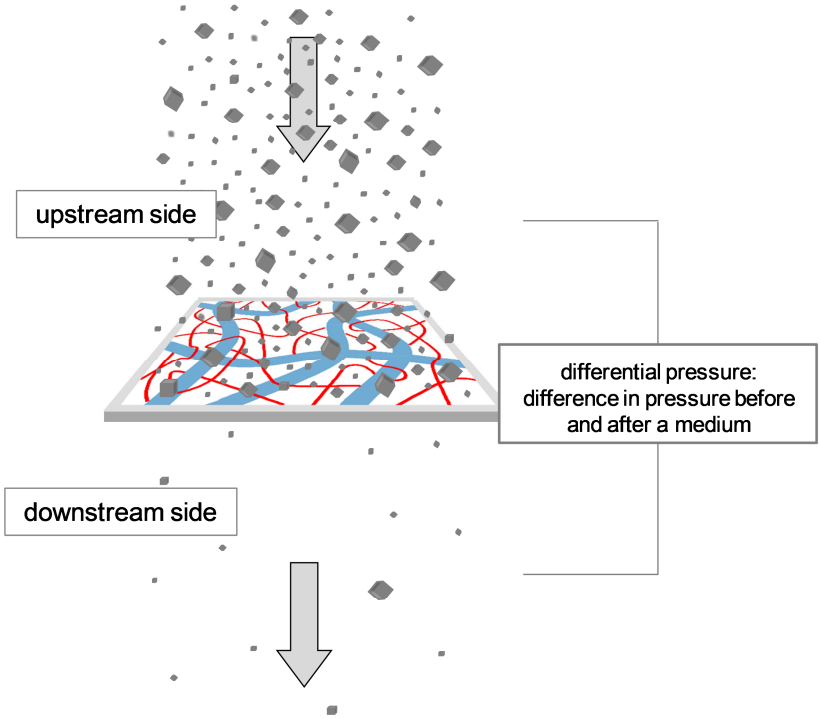

$$\text{filtration efficiency}\ (x) = \left[\,1 - \frac{c_{downstream}(x)}{c_{upstream}(x)}\,\right] \cdot 100\ \ [\%]$$

x: aerosol particle size
$c_{upstream}$ (x): particle concentration of size x (upstream side)
$c_{downstream}$ (x): particle concentration of size x (downstream side)

Figure S2. Top: Particle size distribution of the test aerosol ISO fine test dust (upstream aerosol concentration) Middle: Schematic representation of the filtration process with microfiber-nanofiber composites. Bottom: Calculation of filtration efficiency.

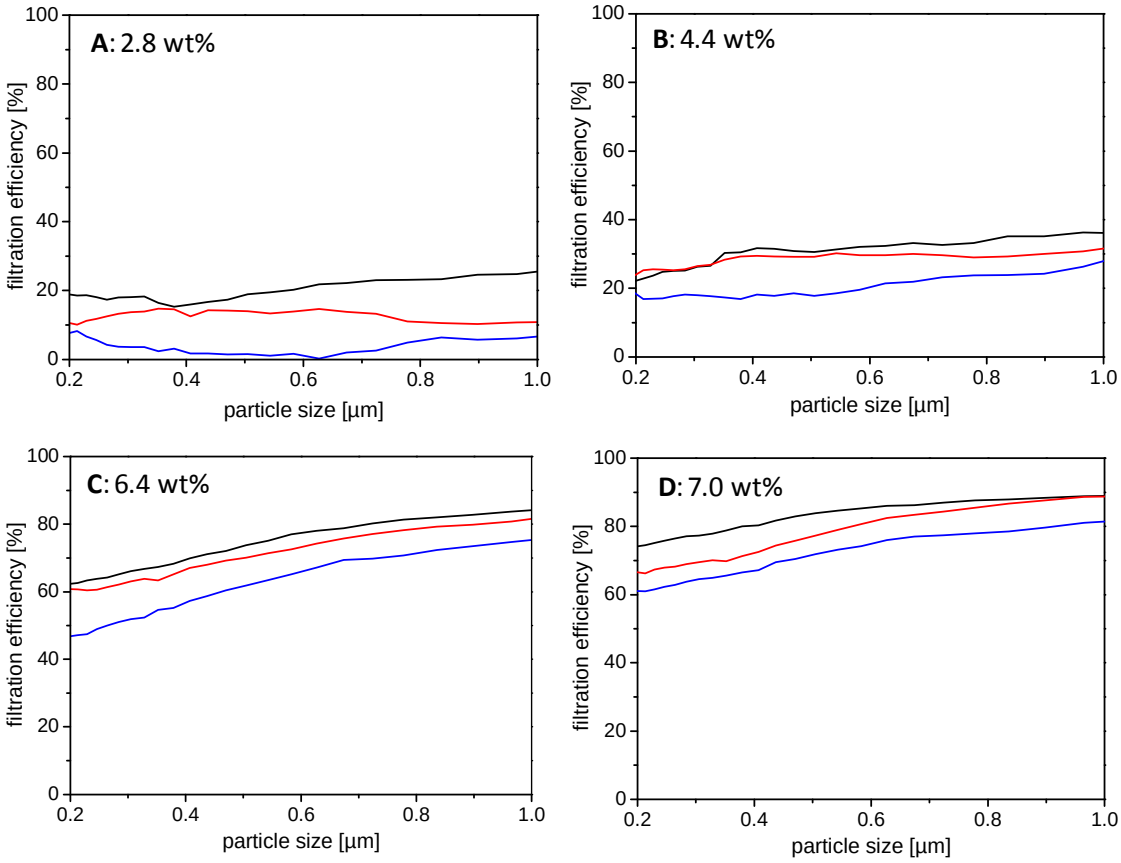

Figure S3. Filtration efficiencies vs. particle size utilizing microfiber-nanofiber composites (content of nanofibers: **A**: 2.8 wt%, **B**: 4.4 wt%, **C**: 6.4 wt%, and **D**: 7.0 wt%). In each plot the filtration efficiencies of three individually prepared microfiber-nanofiber composites are shown.

3.5 Structure-property relations of supramolecular nanofibers in nonwoven scaffolds as media for air filtration applications

*Holger Misslitz, Klaus Kreger, and Hans-Werner Schmidt**

Macromolecular Chemistry I, Bayreuther Institut für Makromolekülforschung (BIMF), Bayreuther Zentrum für Kolloide und Grenzflächen (BZKG), University of Bayreuth, 95440 Bayreuth, Germany

INTENDED FOR SUBMISSION TO **JOURNAL OF MATERIALS CHEMISTRY**

Abstract:
Filtration, separation, and isolation of contaminants are omnipresent in all areas of our lives. A lot of efforts have been made and will become even more important to efficiently diminish respirable dust in the atmosphere by filtration processes. However, there are still enormous requirements for more efficient filter devices. In this work, we report on the in situ formation of supramolecular nanofiber webs based on 1,3,5-benzenetricarboxamides (BTAs) in nonwoven scaffolds. The focus hereby is set on structure property relations in order to control the nanofiber morphology in view of the optimization of the filtration efficiency. Parameters such as the chemical structure of the BTA, the concentration, as well as the solvent used in the immersion process influence the nanofiber web morphology and therefore the filtration efficiency. In addition, the overall filter performance strongly varies with diverging filter setups, thus the quality of the filters can be adjusted as required by certain applications. By using triple-layer filters, the filtration efficiency can be improved while the differential pressure is decreased compared to single-layer filters. Thereby, the performance of supramolecular modified filters almost reaches HEPA standards. The presented results bear important information how to optimize microfiber-nanofiber composites for different kinds of air filtration applications.

Keywords: supramolecular chemistry • self-assembly • nanofibers • filter • structure-property relations

Introduction

Nowadays air filters can be found in manifold fields, for instance in the automotive and building industry, for personal protection in ABC warfare, in the medical and pharmaceutical industry, in the machining and metal working sector, and in the food industry.[1] Their applications reach form standard filters e.g. ventilating and air-conditioning systems to highly specialized filters for applications which are extremely sensitive towards air pollution. The requirements of a top-quality filter are high filtration efficiency and low differential pressure to realize high throughputs. Standard filters possess large porosity and are typically fabricated out of fibers with diameters in the micrometer scale. These filters separate particles in the micrometer dimensions and the low nanometer range with high efficiency. However, there is a size range existing, where aerosol particles are filtered out insufficiently. This aerosol particle size range is defined as most penetrating particle size (MPPS) and in most filters this minimum in filtration efficiency is located at particle sizes of 100 nm to 500 nm.[2] The best approach until now to enhance the filter performance in the MPPS is the utilization of nanofibers. The term nanofiber generally refers to fibers with diameters below one micrometer.[3] The high surface area to volume ratio of nanofibers enhances the probability to capture aerosol particles at the fiber surface leading to improved filtration efficiencies accompanied by a decrease in differential pressure.[4] Thus, in nanofiber modified filters higher throughputs can be obtained. However, polymer nanofibers can not be used without a nonwoven support due to stability reasons.[5] Thereby, nanofibers are typically deposited on top of a support by top-down approaches, such as melt-blowing and electrospinning. Melt-blown fibers generally possess diameters in the high nanometer to the low micrometer range,[6] while electrospun fibers feature diameters down to 40 nm.[7] But the production rates of electrospinning are exceedingly slow and thus electrospinning emerge just as niche process in filtration industry.

A completely different route to prepare microfiber-nanofiber composite filters can be realized by bottom-up approaches, such as self-assembly of low molecular weight compounds. In literature very little is known in the field of supramolecular modified systems suitable for filter applications. Recently, Krieg et al. reported on a deposited supramolecular membrane on top of a supporting syringe filter, which is suitable to separate gold nanoparticles of different size from solution.[8] The big advantage of bottom-up approaches (compared to top-down strategies) is the possibility to form supramolecular nanofibers inside a supporting scaffold. This is exploited by Raghavanpillai et al. who investigated the formation of supramolecular nanofiber webs with organogelators in combination with a porous support, but no data regarding filter experiments are reported.[9]

One of the simplest and well-investigated structural motifs in supramolecular chemistry is based on 1,3,5-benzenetricarboxamides (BTAs). The amide groups form intermolecular hydrogen bonds, which are the driving force of the BTAs to self-assemble in highly defined, one-dimensional aggregates.[10] It is known that the majority of BTAs assemble in a columnar hexagonal fashion.[11] However, a broad variety of morphologies are known depending on the molecular structure, the nature of solvent, concentration and processing conditions.[12] As consequence of this complexity, the class of BTAs finds applications in far-reaching processes. Due to the formation of supramolecular networks a variety of organic solvents can be gelled.[13] In addition, BTAs are used as polymer additives for nucleation and clarification of thermoplastic semi-crystalline polymers[14] and to improve the electret performance of polypropylene.[15] Furthermore, we have shown by atomic force microscopy (AFM) force mapping methodology that single self-assembled BTA nanofibers feature a remarkable mechanical stability with Young's moduli in the low GPa range, demonstrating that supramolecular nanofibers can withstand certain mechanical stress.[16] Based on this, we published a simple but powerful immersion process for the in situ formation of supramolecular BTA nanofiber webs in nonwoven scaffolds, resulting in polymer-microfiber/supramolecular-nanofiber composites (**Scheme 1**).[17]

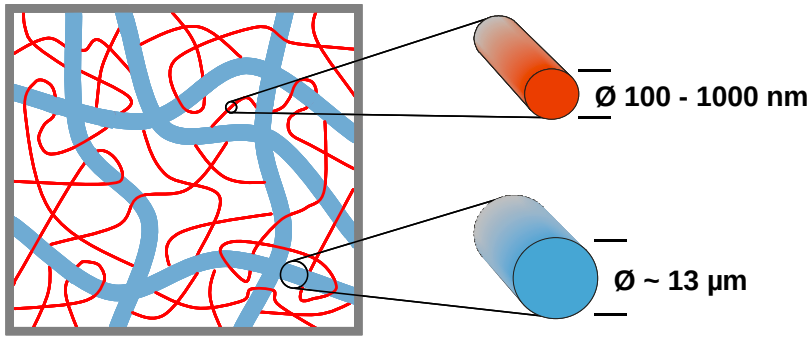

Scheme 1. Schematic representation of polymer microfiber/supramolecular nanofiber composites.

In our previous studies, the overall mechanical stability of the nanofiber webs as well as the principle use of the microfiber-nanofiber composites in air filtration was already demonstrated.

Building on these results, the present paper was designed to optimize the filtration ability of the composite materials by establishing structure property relations with respect to influences of different concentrations, chemical structures, solvents, and different filter setups affecting the nanofiber web morphology, the filtration quality as well as the temperature stability.

Results and Discussion

Preparation of microfiber-nanofiber composites

Our concept to provide polymer microfiber/supramolecular nanofiber composites for air filtration applications contains a solution-based immersion process for the in-situ formation of supramolecular nanofibers in nonwoven scaffolds. The custom made immersion setup is shown in the Supporting Information (**Figure S1**) while its schematic process is already presented.[17] At this process, a commercially available viscose/polyester blended fabric with a thickness of 0.15 mm is dipped into a BTA immersion solution at elevated temperatures. Subsequently, the fabric is removed after an appropriate immersion time leading to cooling effects and solvent evaporation which in turn induces the self-assembly of the BTA building blocks into supramolecular nanofibers in the nonwoven scaffold. After a final drying step, the microfiber-nanofiber composite is obtained (Scheme 1). During the immersion step the nonwoven fabric loses about 7 % of its weight, which may be explained by the dissolution of processing additives as well as oligomeric units of the polymer fabric. The exact amount of weight-loss is dependent on the immersion solvent. However, this weight loss neither influences the nonwoven fabric itself nor the self-assembly process of the BTAs (see Supporting Information, **Figure S2**) and thus we decided that an additional purification step of the scaffolds before the immersion process is not necessary.

Based on exemplary microfiber-nanofiber composites several structure property relations are demonstrated in the following, influencing the nanofiber web, the thermal properties and the filtration efficiency.

In order to find the optimum BTA-system we evaluated several BTAs in screening experiments. Depending on the alkyl rests of the BTAs, they possess diverse behaviors in terms of solubility, self-assembly behavior, as well as thermal properties. BTAs with short alkyl substituents are too insoluble in the used solvents such as butanone, isopropanol, and ethanol. In contrast, BTAs with octyl substituents or longer ones are too soluble which leads to the fact that these BTAs do not self-assemble anymore. Therefore, we utilized BTAs **1-3** (**Figure 1**) whose solubilities are large enough and whose self-assemblies result in well-defined nanofibers in the microfiber scaffold.

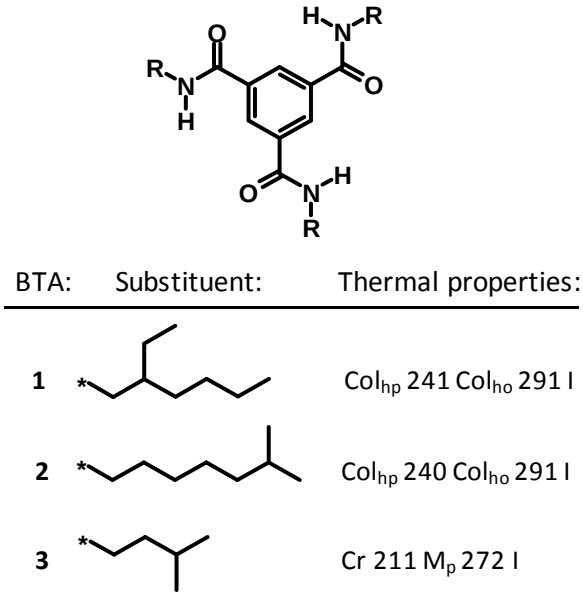

Figure 1. Chemical structures of BTAs **1-3** including thermal properties.

In our previous studies, microfiber-nanofiber composites which were prepared in immersion solutions with a concentration of 1.0 wt% turned out to be suitable for filtration applications.[17] Therefore, in the present work this concentration is taken for the 2-butanone solutions, to investigate the influences of the chemical structure of the BTAs **1-3** on the supramolecular morphology, the thermal properties of the assemblies, and the filtration efficiency. Even though each nonwoven fabric was immersed into a 1.0 wt% concentrated BTA butanone solution the resulting weight percentages of supramolecular nanofibers in the dried filters differ (7.0 wt% for BTA **1**, 7.6 wt% for BTA **2**, and 7.0 wt% for BTA **3**).

The structure property relation between the chemical structure and the supramolecular morphology is shown in **Figure 2**. In the overview SEM micrographs on the left from top to bottom it can be seen that in each case, the supramolecular nanofiber webs assemble within the microfiber openings. Depending on the utilized BTA, a few macro voids remain unfilled, while in the case of BTA **2**, the most homogeneous filling of the openings was observed. In the middle column of Figure 2 micrographs with higher magnification show the nanofiber webs in detail as well as their tendency to adhere to the microfibers, providing the required stability in view of air filtration applications. On the first moment, the microfiber-nanofiber composites are very similar. However, at a closer look the web of BTA **2** seems to be the densest one, followed by the one of BTA **1**. The nanofiber webs of BTA **3** are slightly more coarse-meshed exhibiting larger pores.

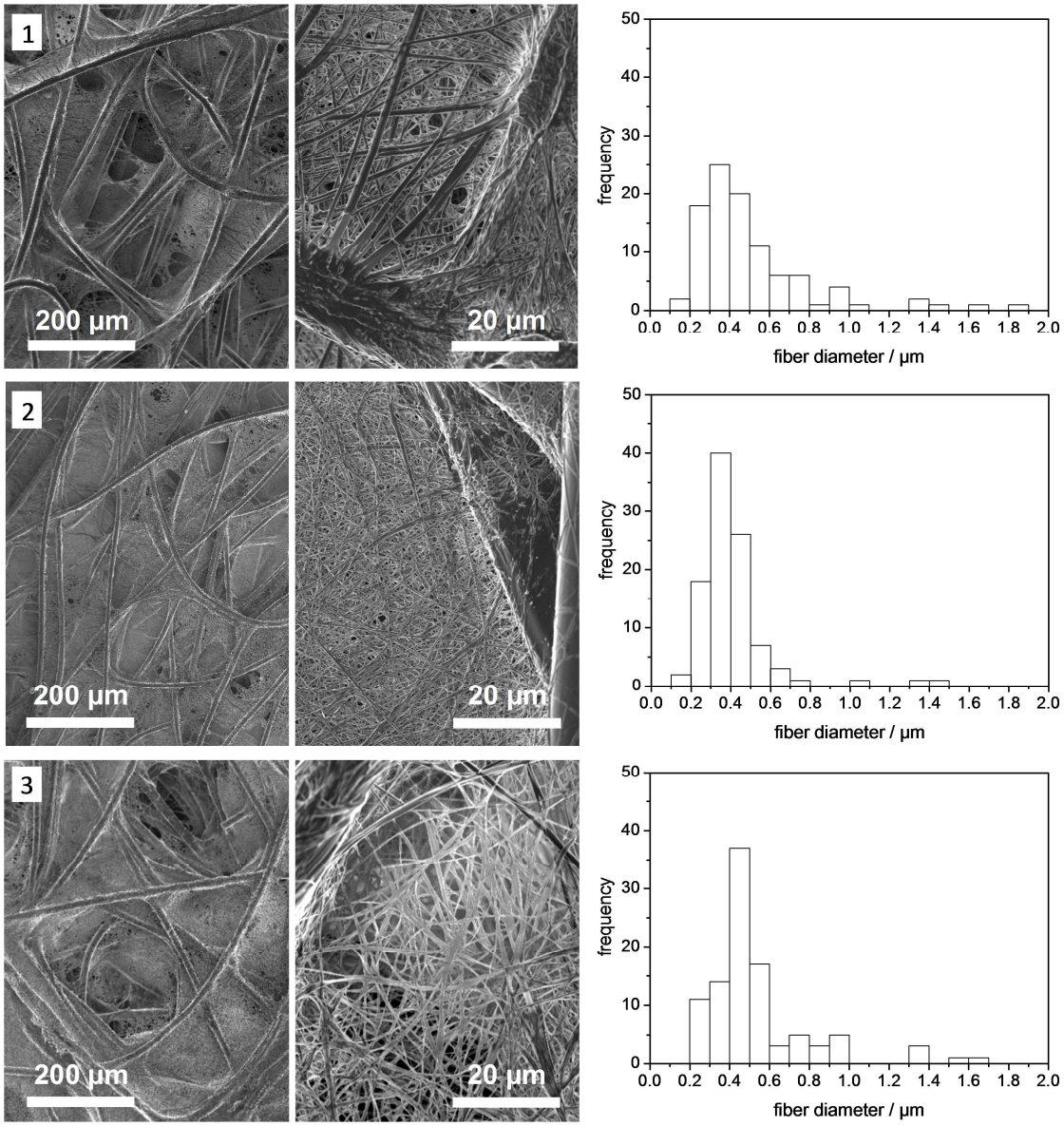

Figure 2. SEM micrographs of the microfiber-nanofiber composites with different BTA's **1**-**3** prepared from butanone immersion solutions with concentrations of 1.0 wt%. The corresponding histograms (100 nm intervals) of the nanofiber diameters on the basis of 100 fibers are shown on the right.

In the right column of Figure 2 the corresponding fiber diameter histograms with 100 nm intervals are shown. The maximum of the fiber diameter distributions of the three BTAs are similar, featuring values of about 400 nm. Also the average fiber diameters are just slightly different; 0.39 µm for BTA **2** and 0.52 µm and 0.53 µm for BTA **1** and **3**, respectively.

These results indicate that the influences of the chemical structure of the BTA on the nanofiber web and the nanofiber diameter are marginal.

Besides the already discussed structure property relation between the molecular structure and the supramolecular morphology, also the thermal properties of these molecules are an important factor with respect to the thermal stability of the

composites in possible filtration applications. Due to the fact that frictional heat can be caused in these processes, the thermal stability of the prepared microfiber-nanofiber composites also has to be ensured. At these investigations, the microfiber-nanofiber composites were subsequently annealed at 100 °C, 120 °C, and 140 °C for one hour. After each annealing step, the samples were investigated by SEM. The maximum temperature of 140 °C was chosen due to the long-term usage temperature of polyester of 120-140 °C. Supramolecular nanofiber degradation of BTA **1** and **2** is observed at 120 °C in both cases, even though BTA **1** and **2** possess columnar hexagonal plastic phases from room temperature up to 241 °C (BTA **1**) and 240 °C (BTA **2**).[18] This can be explained by a decrease in viscosity of both plastic mesophases. In **Figure 3**,A the results of the thermal stability investigations are exemplarily shown for BTA **2**. At this point, however, we want to emphasize, that the majority of air filtration applications are operated below 120 °C. Therefore, we do not see an important restriction for possible industrial filter applications for BTAs possessing columnar hexagonal plastic phases with phase transitions in these temperature regions. In contrast, the nanofibers of BTA **3** are stable up to the maximum of the tested temperature range (Figure 3,B). At room temperature, the aggregates of BTA **3** are crystalline, a mesophase is observed not until 211 °C. According to this thermal behavior, it has to be assumed that nanofibers of BTA **3** would be stable at even higher temperatures than the tested ones.

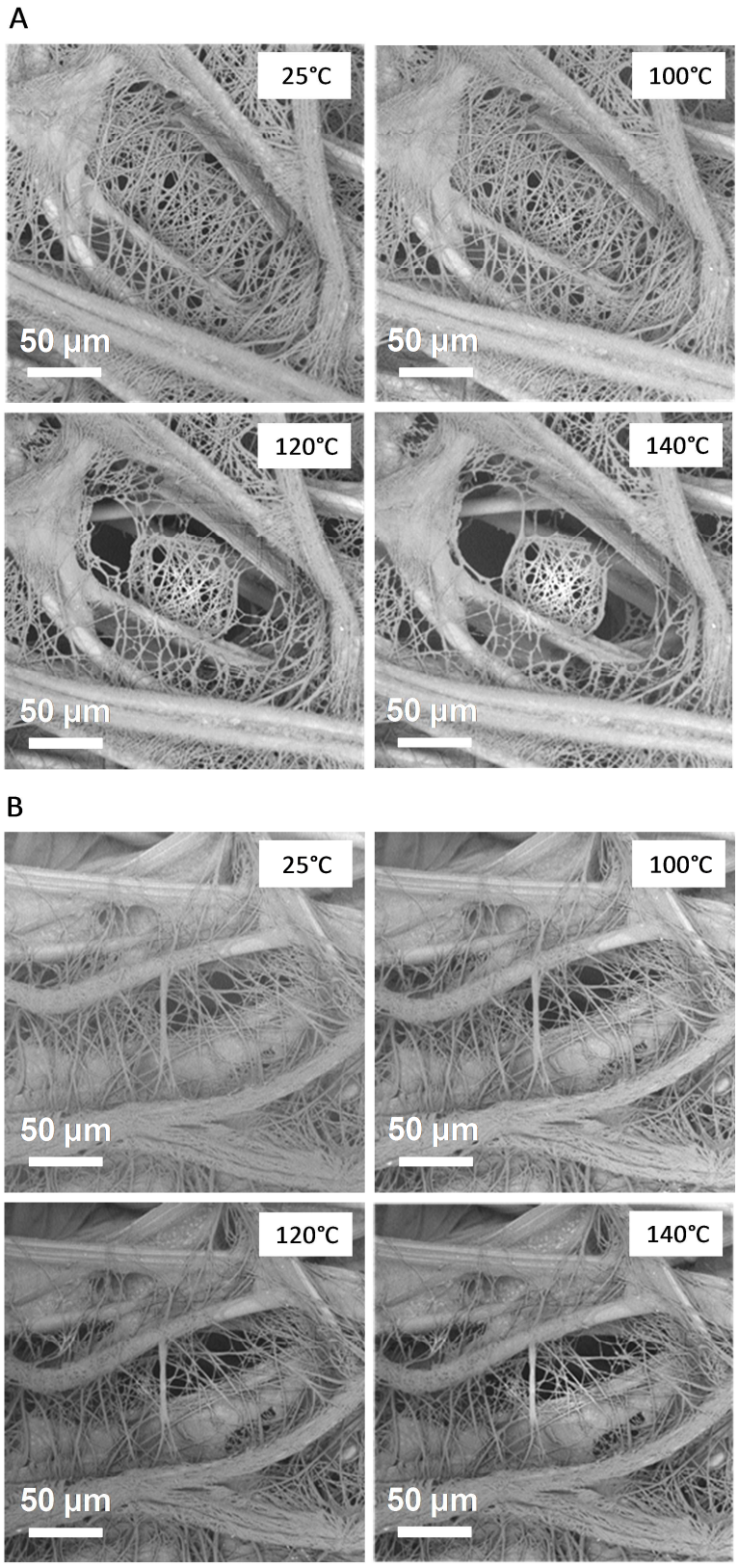

Figure 3. SEM micrographs of the microfiber-nanofiber composite filters with supramolecular nanofibers of BTA **2** (A) and BTA **3** (B) during thermal filter stability tests at 25 °C, 100 °C, 120 °C, and 140 °C. The microfiber-nanofiber composites were prepared in butanone solutions with concentrations of 1.0 wt%, resulting in supramolecular nanofiber contents of 7.6 wt% (BTA **2**) and 7.0 wt% (BTA **3**).

In addition, also the structure property relation between the chemical structure and the filtration efficiency is investigated. Hereby, three individual samples were prepared for each microfiber-nanofiber composite, whose filtration efficiency and differential pressure were determined according to standard filtration procedures at a filter test rig. As reference, the filter performance of the blank polymer nonwoven fabric was measured.

The filtration efficiency is defined as percentage of the removed particles by the filter whereby the size of the separated particles is typically indicated, because aerosol particles of different sizes are separated with distinct quality. Therefore, the filtration efficiency of one filter varies for different aerosol particle sizes. By means of the ratio of the aerosol particle concentration of the upstream side of the filter ("dirty" airstream before the filter) and of the downstream side of the filter ("clean" airstream after the filter), the filtration efficiency can be determined in a specific particle size range. The differential pressure is defined as the pressure difference between the upstream side and the downstream side of the filter. It originates from the air resistance of the filter, and is dependent on the flow velocity.

The average filtration efficiencies of the composites which were modified with supramolecular nanofibers of different BTAs and the one of the reference are shown in **Figure 4**. The blank scaffold separates about 5 – 10 % of the aerosol particles in the size range of 0.2 – 2.0 µm and features a differential pressure of 9 Pa. The corresponding SEM micrographs of the nonwoven fabric prior and after the filter test are shown in the Supporting Information **Figure S3**. As can be seen in Figure 4, the average filtration efficiencies of the different microfiber-nanofiber composites are highly dependent on the used BTA. The composite with nanofibers of BTA **1** separates 70 % of the aerosol particles with a size of 0.2 µm and even 90 % of all aerosol particles with a diameter of 2.0 µm. In comparison, the filtration efficiency of the composite prepared with BTA **2** is slightly reduced, filtering aerosol particles with a size of 0.2 µm to 50 % and aerosol particles with a diameter of 2.0 µm to 80 %. The filtration efficiency of the composite of BTA **3** is even more reduced. Aerosol particles of 0.2 µm size are filtered to a content of 40 % and particles of 2.0 µm are separated to 65 %. The immense divergence in the filtration efficiencies of the composites prepared with different BTA nanofibers can be explained by variations in the resulting nanofiber webs. While the supramolecular nanofibers of BTA **1** and **2** form dense, fine-pored networks, the ones of BTA **3** assembles in more wide-meshed webs.

Besides the variations in the filtration efficiencies of the composites, also the differential pressure varies in the tested samples. The better the filtration efficiencies, the higher are the differential pressures of the tested composites. The microfiber-nanofiber composite with the lowest filtration efficiency (filter with nanofibers of BTA **3**) has a differential pressure of 67 Pa, while the composite with the highest

filtration efficiency (filter with nanofibers of BTA **1**) reveals a differential pressure of 429 Pa.

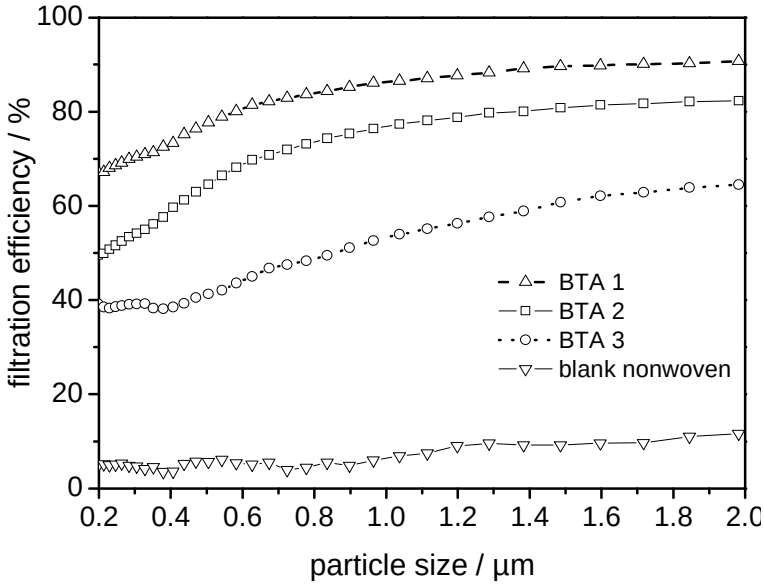

Figure 4. Average filtration efficiencies of the blank nonwoven scaffold as well as the microfiber-nanofiber composites with nanofibers of BTAs **1**-**3** which were prepared from a 1.0 wt% butanone solution, respectively. Test parameters: Filter area: 28.3 cm^2; flow velocity: 25 cm/s; test aerosol: ISO fine dust (upstream aerosol concentration: about 6000 P/cm^3); testing time: 30 s. The differential pressures of the tested composites are 429 Pa for the composite with BTA **1**, 288 Pa with BTA **2**, 67 Pa with BTA **3**, and 9 Pa for the blank nonwoven.

In order to validate the overall filter quality of these composites, both the filtration efficiency and the differential pressure have to be taken into account. The composite prepared with nanofibers of BTA **1** possesses the highest average filtration efficiency of the tested ones. But, the relatively high differential pressure reduces the overall filter quality. In comparison, the filtration efficiency of the composite with nanofibers of BTA **2** is only slightly decreased, while the differential pressure is reduced by 30 % from 429 Pa (BTA **1**) to 288 Pa (BTA **2**). Therefore, the following investigations were focused on composites which were modified with supramolecular nanofibers of BTA **2**.

<u>Influence of concentration on the morphology of the microfiber-nanofiber composite and the filtration efficiency</u>

The structure property relation between the concentration of the immersion solution and the morphology of the microfiber-nanofiber composites as well as their filtration efficiency was investigated by 2-butanone solutions of BTA **2** with different concentrations of 0.6 wt%, 0.8 wt%, and 1.0 wt%. Not surprisingly, we found an increase in the nanofiber content from 4.4 wt% to 7.6 wt% in the microfiber-nanofiber composites correlating with the BTA concentrations in the used immersion solutions. The SEM micrographs of the microfiber-nanofiber composites and the corresponding

fiber diameter histograms are shown in the Supporting Information **Figure S4**. At the lowest nanofiber concentration, the nanofibers assemble unevenly in the openings of the nonwoven fabric, while the nonwoven with the highest concentration is extensively permeated with supramolecular nanofibers. In the Supporting Information, **Figure S5**, **Figure S6**, and **Figure S7**, the corresponding filtration efficiencies and pressure drops of the composites with different nanofiber contents are shown for BTA **2**, BTA **1**, and BTA **3**, respectively. The higher the concentration of the immersion solution at the composite preparation, the better is the filtration efficiency of the filters. These investigations verify our previously published results and confirm their reproducibility.[17] Summarizing, the concentration of the immersion solution just slightly influences the nanofiber morphology but strongly influences the fraction of filled openings in the nonwoven scaffold as well as influences the filtration efficiency to a high extend.

Influence of solvent on the morphology of the microfiber-nanofiber composite and the filtration efficiency

Besides the molecular structure and the concentration, also different solvents used in the immersion process influence the supramolecular nanofiber webs and the filtration performance. In order to reveal these structure property relations, the nonwoven fabrics were exemplarily immersed into solutions of BTA **2** with concentrations of 1.0 wt% in 2-butanone, isopropanol, and ethanol, respectively. Depending in the used solvent, not only the weight loss of the fabric at the immersion process, but also the content of supramolecular nanofibers in the filter differs. The dried composite prepared with ethanol feature a nanofiber content of 6.9 wt%, the one prepared with butanone has a nanofiber content of 7.6 wt%, while the filter prepared with isopropanol possess a nanofiber content of 10.0 wt%. A complete listing of the weight percentages of supramolecular nanofibers in the prepared filters is shown in the Supporting Information (**Table S1**). The resulting microfiber-nanofiber composites were visualized by means of SEM (**Figure 5**). In the left micrographs it can be clearly observed, that in the case of butanone, all macro voids are filled with nanofibers, while in the case of isopropanol and ethanol, some openings remain unfilled. In the detailed view (middle column of Figure 5) one can see that the density of the nanofiber webs decreases when using isopropanol and ethanol instead of butanone in the immersion process. In addition, the diameters of the supramolecular fibers increase from butanone to isopropanol and further to ethanol. The corresponding histograms (right column of Figure 5) reveal fiber diameter distributions with average diameters of 0.39 µm for butanone, 0.56 µm for isopropanol, and 1.44 µm for ethanol. Furthermore, the widths of the diameter distributions of the supramolecular fibers

vary. While fibers prepared in butanone and isopropanol possess narrow diameter distributions, fibers processed from ethanol feature a broad distribution.

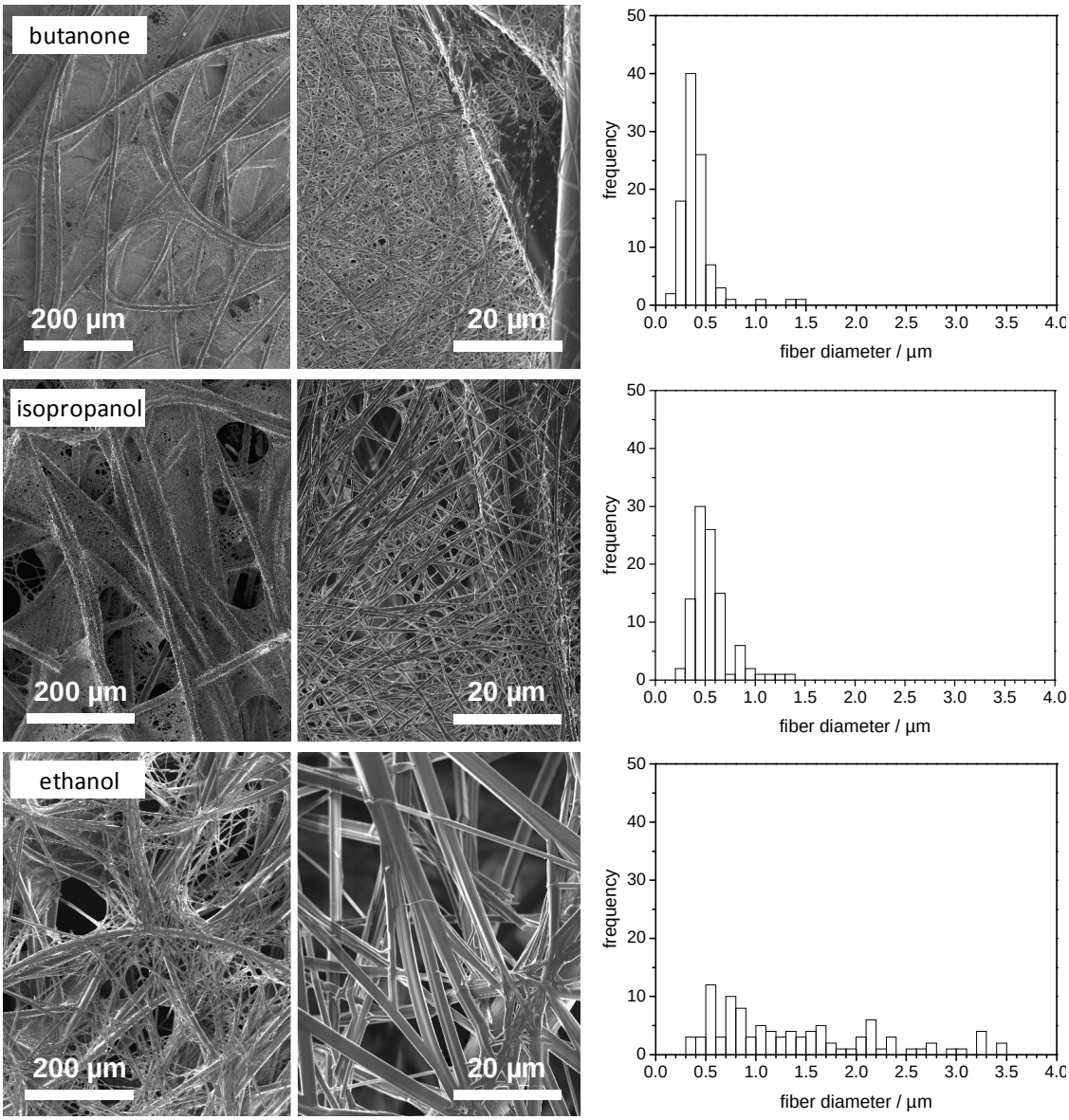

Figure 5. SEM micrographs of the microfiber-nanofiber composites of BTA **2** prepared from immersion solutions with concentrations of 1.0 wt% in butanone, isopropanol, and ethanol. The corresponding histograms (100 nm intervals) of the nanofiber diameters on the basis of 100 fibers are shown on the right.

Furthermore, the solvent in the immersion process also influence the filtration efficiency of the prepared composites. This structure property relation is exemplarily displayed in **Figure 6** for composites with nanofibers of BTA **2** which were prepared from 1.0 wt% concentrated butanone, isopropanol, and ethanol solutions, respectively. The filtration efficiencies decrease from the composite prepared in butanone, to isopropanol, and further to ethanol. The composite prepared in butanone separates 50 % of 0.2 µm sized aerosol particles and even 80 % of the

aerosol particles with a size of 2.0 µm. Even though the resulting nanofiber content in the composite prepared in isopropanol features a value of 10.0 wt%, its average filtration efficiency to separate aerosol particles with 0.2 µm size do not exceed 25 %. In comparison, the composite prepared from ethanol possesses slightly lower filtration efficiency, in particular 20 % for 0.2 µm sized aerosol particles. Not surprisingly, the composite prepared in butanone possesses the highest differential pressure (288 Pa), while those prepared from isopropanol and ethanol, exhibit differential pressures of 21 Pa and 25 Pa, respectively. These results can be explained by the different densities and porosities of the supramolecular nanofiber webs in the composites as well as by the varying fiber diameters discussed before.

To sum up, the solvent used in the preparation of microfiber-nanofiber composites do not only influence the nanofiber morphology, but also influences the filtration efficiency to a high extend.

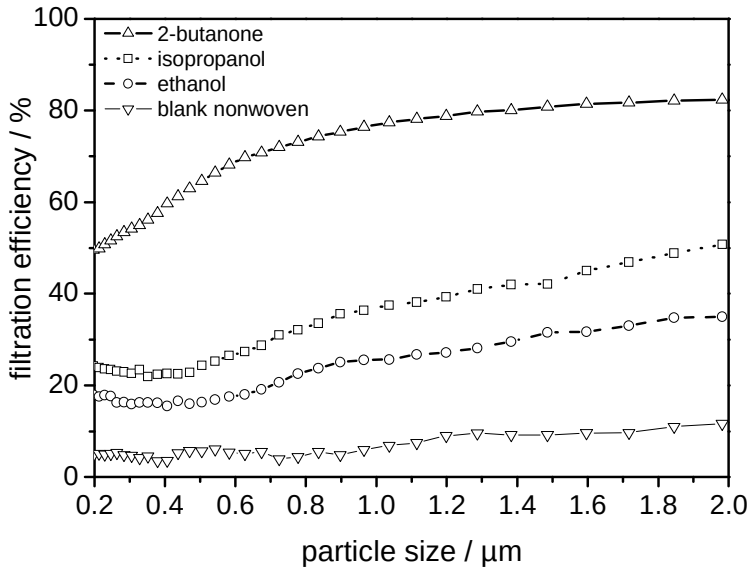

Figure 6. Average fractional efficiencies of the blank nonwoven scaffold as well as of the microfiber-nanofiber composites with nanofibers of BTA **2** prepared from 1.0 wt% concentrated solutions of different solvents. Test parameters: Filter area: 28.3 cm^2; flow velocity: 25 cm/s; test aerosol: ISO fine dust (upstream aerosol concentration: about 6000 P/cm^3); testing time: 30 s. The differential pressures of the tested composites are 288 Pa for butanone, 21 Pa for isopropanol, and 25 Pa for ethanol, and 9 Pa for the blank nonwoven.

Influence of different aerosols on the filtration efficiency

In filtration applications it is often the case that filters have to separate a range of different aerosol dusts, which possess distinct particle sizes, charges, and physical conditions. In a factory for instance particulate fine dust (charged or non-charged) emerge in combination with oil mist originating from the machines, thus the utilized filters have to separate each dust most effectively. Therefore, the behavior of the filtration performance of the prepared composites by utilizing different aerosol dusts at the filter tests is also an important knowledge. In order to investigate the structure property relation between the aerosol dust and the filtration efficiency and to study the versatility of the herein prepared composites, the filter tests were conducted with several test dusts. In this work, ISO fine dust, DEHS (Bis(2-ethylhexyl) sebacate) and KCl were utilized as aerosols, which represent commonly occurring dusts with a broad range of properties. While ISO fine test dust represent a particulate fine dust (desert sand), KCl symbolizes charged particles and DEHS represent dusts in form of oil droplets. The filtration efficiency results conducted with these test dusts are exemplarily displayed in **Figure 7** for a composite featuring a weight percentage of supramolecular nanofibers of BTA **2** of 7.6 wt%. ISO fine dust is captured most efficiently at small particle sizes (0.2 µm) among the used aerosols. At this aerosol particle size, KCl and DEHS is filtered 20 % and 30 % worse. However, compared to ISO fine dust, DEHS droplets were separated more efficiently at aerosol particle sizes above 1.4 µm. After the filter test, the ISO fine dust- and KCl-loaded composites were analyzed by SEM (Figure 7, bottom). DEHS droplets can not be visualized, due to its fast evaporation. As can be seen in the micrographs, particles of both aerosols were separated to high extends onto the surface of the supramolecular nanofibers. ISO fine dust particles possess an undefined, rough shape, while KCl forms spherical particles with a smooth surface. Thus, variations in the filtration efficiencies may also originate from different shapes of the dust particles.

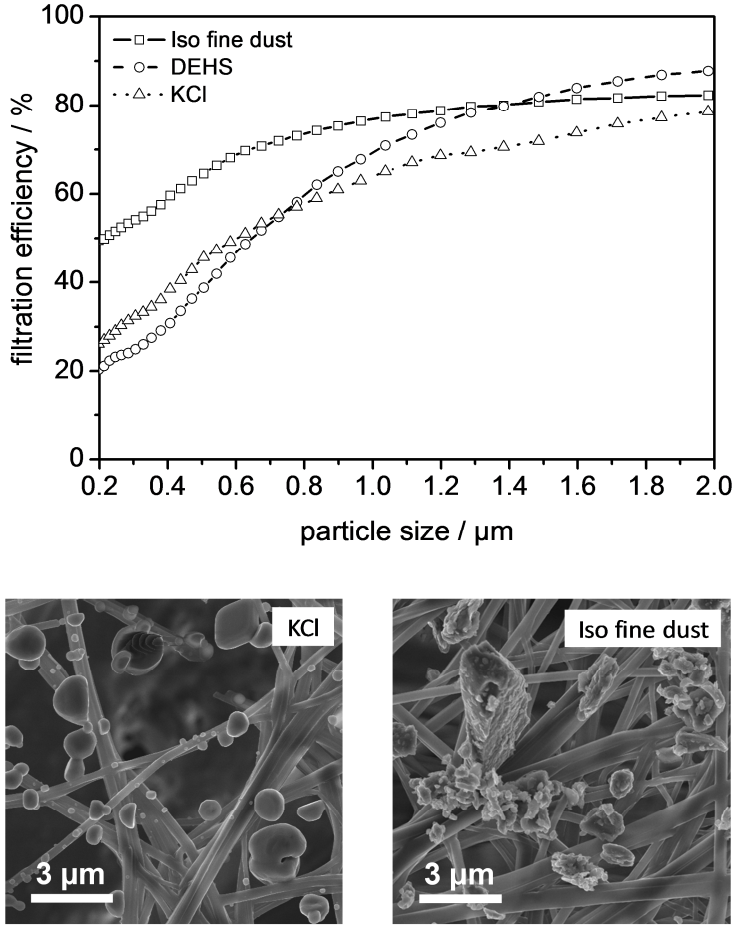

Figure 7. Top: Average filtration efficiencies of the microfiber-nanofiber composites with 7.6 wt% nanofibers of BTA **2** (prepared in butanone, 1.0 wt%) tested with different aerosols. Test parameters: Filter area: 28.3 cm^2; flow velocity: 25 cm/s; test aerosol: ISO fine dust, DEHS or KCl (upstream aerosol concentration in each case: about 6000 P/cm^3); testing time: 30 s. The differential pressures of the tested composites are 288 Pa for ISO fine dust, 201 Pa for DEHS, and 201 Pa for KCl. Bottom: SEM micrographs of the ISO fine dust- and KCl-loaded composites after the filtration tests.

Influence of filter setup on the filtration efficiency

Further structure property relations between filter setups and the filtration performance are revealed in this section of the present paper. The filtration efficiencies presented so far are all based on supramolecular modified single-layer viscose/polyester microfiber fabrics which possess a thickness of 0.15 mm. In view of this slight thickness, the obtained filtration efficiencies of the prepared microfiber-nanofiber composites are even more remarkable. However, in order to find the optimal compromise between high filtration efficiency and low differential pressure multi-layer composites of BTA **2** were designed comprised of two or three single composites stacked upon each other.

The top image of **Figure 8** displays the comparison of the average filtration efficiencies of a single-, a double-, and a triple-layer composite. Each layer of the three samples

exhibits a weight percentage of supramolecular nanofibers of BTA **2** of 4.4 wt%. We found, that the filtration efficiency is increasing with the thickness of the composites. At the aerosol particle size of 0.2 µm, the single-layer composite possesses the poorest filtration efficiency with 20 %, the filtration efficiency of the double-layer composite is already increased to 40 %, and the triple-layer composite possesses a filtration efficiency of 65 %. Also the corresponding differential pressures rise with increasing filter thickness. The single layer composite features a differential pressure of 56 Pa. This is raised to 76 Pa at the douple-layer composite and further to 102 Pa at the triple-layer composite. While the filtration efficiency of the triple-layer composite is enhanced threefold compared to the single-layer composite, the corresponding differential pressure is increased less than twofold. Hence, with increasing thickness of the composite the filtration efficiency is increasing faster than the differential pressure which results in a higher overall filtration performance of the multi-layer composites. As references, the filtration efficiencies and differential pressures of the single-, the double-, and the triple-layer blank nonwoven scaffolds are presented in the Supporting Information **Figure S8**.

Furthermore, this effect is elucidated in the comparison of the single-layer composite with 7.6 wt% nanofibers and the triple-layer composite which possesses 4.4 wt% nanofibers in each layer (Figure 8, Center). The filtration efficiencies of both samples are comparable. However, the single-layer composite has a differential pressure of 288 Pa, while the triple-layer composite features a differential pressure of only 102 Pa, even though twice the overall amount of supramolecular nanofibers is incorporated in the triple-layer composite. Hence, triple-layer composites possess superior quality compared to single-layer composites and thus higher throughputs can be acquired.

To further improve the filtration efficiency triple-layer composites with higher contents of supramolecular nanofibers were investigated (Figure 8, Bottom). Thereby, the weight percentage of supramolecular nanofibers in each layer is successively enhanced from 4.4 wt% to 5.8 wt% and further to 7.6 wt%. Not unexpected, this increase leads to improved filtration efficiencies. The triple-layer composite containing 5.8 wt% nanofibers in each layer already features a filtration efficiency of 75 % for 0.2 µm sized aerosol particles, and for particles with 1.0 µm even 95 %. Regardless, the triple-layer composite with 7.6 wt% nanofibers in each layer features enormous filtration efficiencies for supramolecular modified filters; in particular over 90 % for 0.2 µm sized aerosol particles, 97 % for 0.5 µm particles, and even 99.4 % for 1.0 µm sized aerosol particles. The corresponding differential pressures also increase from 102 Pa for the sample with 4.4 wt% nanofibers in each layer to 406 Pa for 5.8 wt% nanofibers, and further to 894 Pa for 7.6 wt% nanofibers.

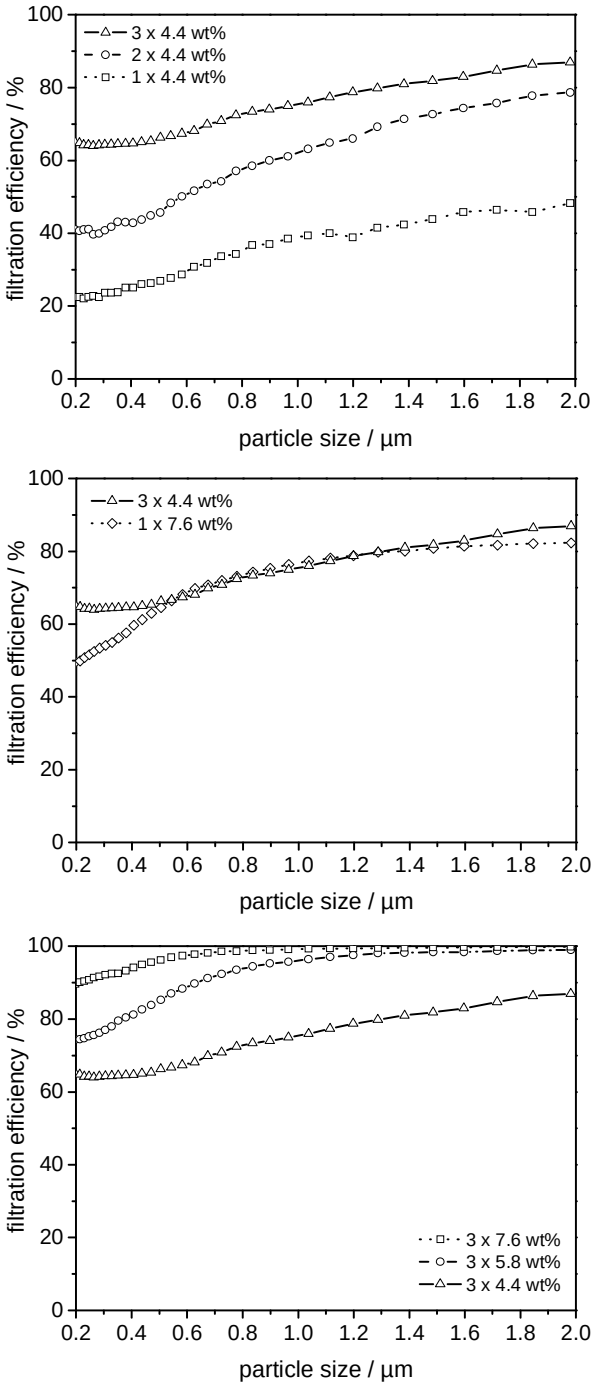

Figure 8. Top: Average filtration efficiencies of a single-, a double-, and a triple-layer composite with weight percentages of supramolecular nanofibers of BTA **2** of 4.4 wt% in each layer. The differential pressures of the tested samples are 56 Pa for the single-layer composite, 76 Pa for the double-layer composite, and 102 Pa for the triple-layer composite. Center: Average filtration efficiencies of a single-layer composite with a weight percentage of supramolecular nanofibers of BTA **2** of 7.6 wt% and a triple-layer composite with weight percentages of supramolecular nanofibers of BTA **2** of 4.4 wt% in each layer. The differential pressures of the tested samples are 288 Pa for the single-layer composite and 102 Pa for the triple-layer composite. Bottom: Average filtration efficiencies of three triple-layer composites with weight percentages of 4.4 wt%, 5.8 wt%, and 7.6 wt% of supramolecular nanofibers of BTA **2** in each layer, respectively. The differential pressures of the tested samples are 102 Pa for 3 x 4.4 wt%, 406 Pa for 3 x 5.8 wt%, and 894 Pa for 3 x 7.6 wt% nanofibers. Test parameters in each case: Filter area: 28.3 cm^2; flow velocity: 25 cm/s; test aerosol: ISO fine dust (upstream aerosol concentration: about 6000 P/cm^3); testing time: 30 s.

After the filter tests, the aerosol particle-loaded triple-layer composite containing 7.6 wt% nanofibers in each layer is investigated by SEM (**Figure 9**). As can be seen in the micrographs, the top-layer of the composite fulfills the task of a coarse filter by separating mainly large aerosol particles. At the center- and the bottom-layer of the triple-layer composite, only small aerosol particles were found. Consequently large particles have to be filtered to 100 % at the top-layer.

These investigations pave the way to future optimizations of the herein presented supramolecular modified specimens to obtain overall powerful filters. By utilization of multi-layer composites with more than three layers the filtration efficiencies of the microfiber-nanofiber composites could be further optimized, possibly leading to even more powerful filters than HEPA (High-Efficiency Particulate Air) filters.

Conclusion

In conclusion, we have demonstrated a simple fabrication of polymer-microfiber/supramolecular-nanofiber composites suitable for air filtration. Based on exemplary composite samples, we revealed several structure property relations influencing the nanofiber web morphology, the thermal properties, and the filtration efficiency:

The chemical structure of the BTAs used in the immersion process just slightly influences the nanofiber web. However, these marginal changes in the morphology are sufficient to affect the filtration efficiency remarkably. In addition, also the thermal properties of the supramolecular nanofibers vary by using different BTAs.

The influence of the concentration of the immersion solution on the nanofiber morphology is marginal but it strongly influences the fraction of filled openings in the nonwoven scaffold as well as affects the filtration efficiency to a high extend.

The solvent used in the preparation of the microfiber-nanofiber composites do not only extremely influence the nanofiber morphology, but also has a huge impact on the filtration efficiency.

Depending on the aerosols utilized in the filter tests, the filtration efficiency of the microfiber-nanofiber composites vary. Herein we have shown versatile composites filtering a range of different aerosol dusts.

Furthermore, the filter setup strongly influences the filtration performance of the composites. Triple-layer composites with just 7.6 wt% supramolecular nanofibers in each layer feature excellent filtration efficiencies for supramolecular modified filters reaching 99.4 % for 1.0 µm sized aerosol particles.

This study clearly points out that the filter performance of polymer-microfiber/supramolecular-nanofiber composites can be optimized by many adjusting screws leading to very adaptive filter systems suitable for each kind of air filtration application.

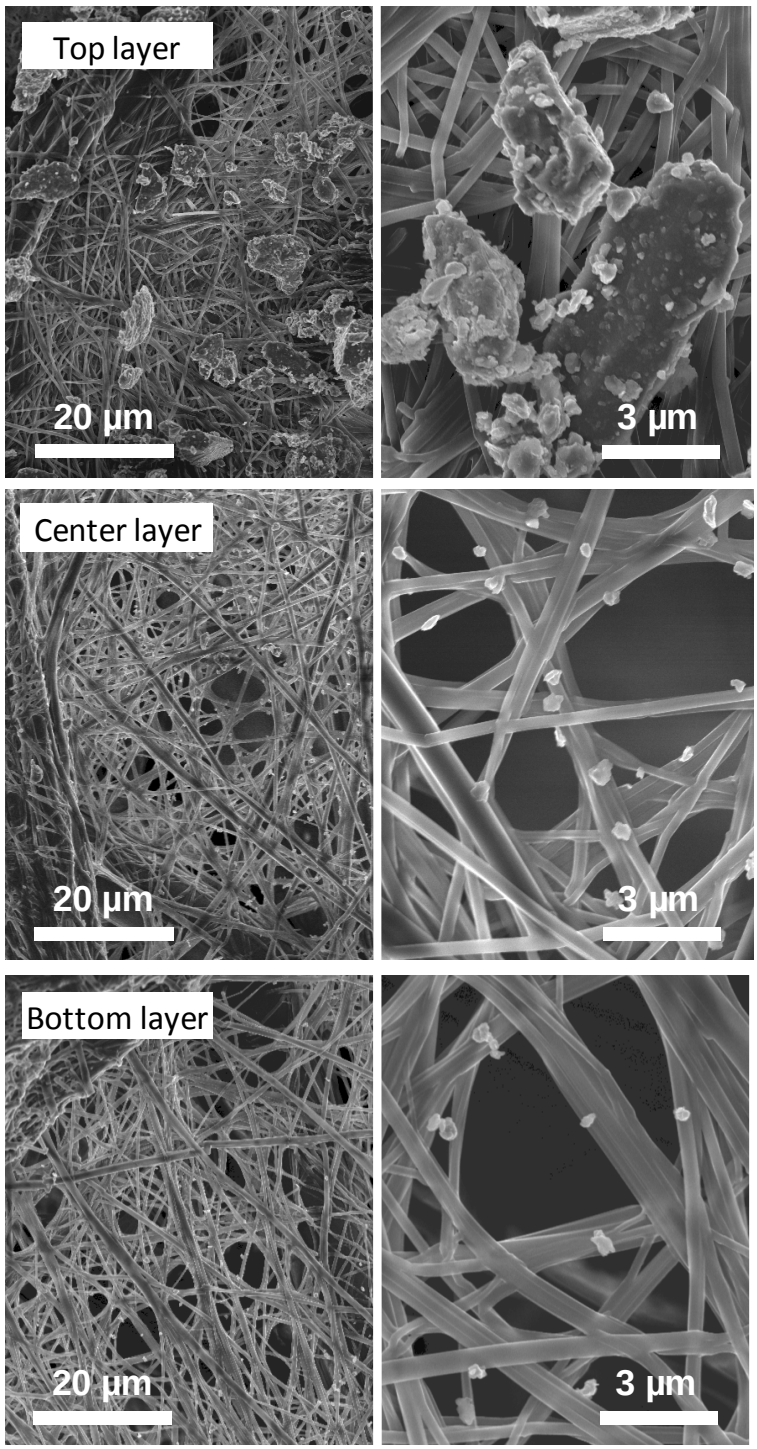

Figure 9. SEM micrographs of the top surface of each layer of the triple-layer composite after the filter test. Each layer of the composite contains a weight percentage of 7.6 wt% of supramolecular nanofibers of BTA **2** (prepared from a butanone immersion solution).

Acknowledgements

We gratefully acknowledge financial support by the Deutsche Forschungsgemeinschaft within the collaborative research centre SFB 840 (Project B8). H.M. acknowledges support by the Elite Study Program - Macromolecular Science (Elite Network of Bavaria). We thank J. Failner and S. Ganzleben providing the compounds in sufficient quantities.

Experimental section

Materials:

The synthesis and characterization of the 1,3,5-benzenetricarboxamides **1-3** is described in detail in reference [18].

As scaffold a commercially available viscose/polyester microfiber nonwoven fabric was used (AMPri). The fabric has a thickness of 0.15 mm and a basis weight of 32.2 g/m^2. The nonwoven fabrics were cut into pieces of 9.5 cm x 9.5 cm (fabric area: 90.25 cm^2). ISO 12103-1, A2 fine test dust and DEHS were received from Powder Technology Inc. and Palas, respectively. KCl and all solvents were purchased from Aldrich and used as received.

Preparation of supramolecular nanofibers in a nonwoven fabric:

The immersion solutions were prepared with concentrations of 0.4, 0.6, 0.8, and 1.0 wt% by suspending the corresponding amount of BTA in 2-butanone, isopropanol, and ethanol, respectively. Subsequent heating to 50 °C leads to a clear solution, which was filled into a custom-made immersion bath placed in a thermostat at a temperature of 50 °C. The nonwoven fabric (9.5 cm x 9.5 cm) was clamped into a supporting frame, which reduces the effective area to 72.25 cm^2 (8.5 cm x 8.5 cm). To equip the nonwoven scaffold with supramolecular nanofibers, the supporting frame with the microfiber fabric was dipped into the immersion bath for 30 s. The soaked fabric was removed from the immersion solution and dried in the frame at ambient conditions for 10 min and subsequently in vacuum for 30 min.

Evalution of weight percentage of supramolecular nanofibers in the nonwovens:

Prior to the estimation of the weight percentage of the supramolecular nanofibers in the model nowoven, the received fabric was dipped into pure 2-butanone, removed and dried carefully. Weighing the model nonwoven before and after the dipping into the solvent allows the determination of the soluble amount of organic compounds from the fabric. In order to determine the nanofiber content, a new nonwoven fabric was dipped into an immersion solution (concentrations: 0.4, 0.6, 0.8, and 1.0 wt%)

carefully dried and weighed before and after this immersion process. The values of the effective area and the soluble amount from the nonwoven were considered while calculating the weight percentage. The values of these calculations represent the averages of ten individual samples.

Scanning electron microscopy (SEM):
For SEM investigations, samples were fixed via a double-sided adhesive conductive carbon tape on a SEM sample holder. Subsequently, the samples were carbon-coated utilizing a MED 010 coating machine from Baltzer. SEM micrographs were recorded using a Zeiss 1530 FESEM equipped with an Inlens detector (acceleration voltage: of 5 kV).

Fiber diameter histograms:
In each analysed SEM micrograph, fiber diameters of 100 self-assembled nanofibers were determined utilizing measureIT software from Olympus. The histograms were prepared with intervals of 100 nm steps.

Thermal stability test:
The samples were fixed via a double-sided adhesive conductive carbon tape on a SEM sample holder. The devices were put into a drying oven at 80 °C, 100 °C, 120 °C and 140 °C successively for 1 h, respectively. After each annealing step, the specimens were investigated by means of a desktop SEM (Phenom G1 from FEI).

Filter testing procedures:
All Measurements were performed utilizing a custom build filter test rig based on the MFP 2000 from PALAS® with a white light-scattering spectrometer Welas® digital 2100 (particle size detection range: 0.2 µm – 10.0 µm).
Airstream test:
The samples (sample area: 9.4 cm^2) were fixed via a pneumatic sample holder. Subsequently a continuous clean air flow (without aerosol particles) was applied to the filter. The flow velocity was set to 3.0 m/s for 24 h and the differential pressure as well as possible particles, originating from the microfiber-nanofiber composite, were recorded.
Filtration test:
As aerosol generator an RBG 1000 from PALAS® was utilized (rotation speed of brush: 1200 r/min, volumetric flow rate of generator: 15 L/min). In addition, an AGK 2000 (concentration of KCl solution: 1.0 wt%) and a PLG-HEPA generator (both from PALAS®) were used for KCl and DEHS measurements, respectively. In the measurements, the flow velocity was set to 0.25 m/s and the measuring time to 30 s. As test aerosol ISO

fine dust, DEHS, and KCl was used, respectively. The samples were fixed with a pneumatic sample holder and a continuous air flow loaded with a particle concentration of 6000 particles/cm^3 was applied to the samples with an effective filtration area of 28.3 cm^2. The filtration efficiency was determined by recording the particle concentration without the composite material (upstream concentration) and with the composite material (downstream concentration). Additionally, the differential pressure was recorded.

References

[1] I. M. Hutten, Elsevier, Oxford; Burlington, MA **2007**.

[2] a) W.C. Hinds, WILEY-VCH Verlag, New York **1999**. b) A. Podgórski, A. Bałazy, L. Gradoń, *Chemical Engineering Science* **2006**, *61*, 6804.

[3] K. Graham, M. Ouyang, T. Raether, T. Grafe, B. McDonald, P. Knauf, Fifteenth Annual Technical Conference & Expo of the American Filtration & Separation Society **2002**

[4] a) H.-S. Park, Y. O. Park, *Korean J. Chem. Eng.* **2005**, *22*, 165. b) Z.-M. Huang, Y.-Z. Zhang, M. Kotaki, S. Ramakrishna, *Composites Science and Technology* **2003**, *63*, 2223.

[5] S. Agarwal, A. Greiner, J. H. Wendorff, *Adv. Funct. Mater.* **2009**, *19*, 2863.

[6] a) C. J. Ellison, A. Phatak, D. W. Giles, C. W. Macosko, F. S. Bates, *Polymer* **2007**, *48*, 3306. b) Y. Lee, L. C. Wadsworth, *Polymer Engineering & Science* **1990**, *30*, 1413-1419.

[7] K. Kosmider, J. Scott, *Filtration & Separation* **2002**, *39*, 20.

[8] E. Krieg, H. Weissman, E. Shirman, E. Shimoni, B. Rybtchinski, *Nature Nanotech.* **2011**, *6*, 141.

[9] a) A. Raghavanpillai, S. Reinartz, K. W. Hutchenson, *Journal of Fluorine Chemistry* **2009**, *130*, 410. b) E. J. Acosta, A. Raghavanpillai, S. Peng, S. Reinartz, S. Moudgil, US20080113573A1, **2008**. c) J. Ding, Y.-L. Hsiao, C. P. Lenges, Y. Niu, S. Reinartz, C. M. Stancik, G. J. J. Van, US20070125700A1, **2007**.

[10] a) P. J. M. Stals, J. F. Haveman, R. Martin-Rapun, C. F. C. Fitie, A. R. A. Palmans, E. W. Meijer, *J. Mater. Chem.* **2009**, *19*, 124. b) P. J. M. Stals, M. M. J. Smulders, R. Martín-Rapún, A. R. A. Palmans, E. W. Meijer, *Chem. Eur. J.* **2009**, *15*, 2071. c) L. Brunsveld, A. Schenning, M. Broeren, H. Janssen, J. Vekemans, E. Meijer, *Chem. Lett.* **2000**, 292.

[11] M. P. Lightfoot, F. S. Mair, R. G. Pritchard, J. E. Warren, *Chem. Commun.* **1999**, 1945.

[12] M. Kristiansen, P. Smith, H. Chanzy, C. Baerlocher, V. Gramlich, L. McCusker, T. Weber, P. Pattison, M. Blomenhofer, H.-W. Schmidt, *Crystal Growth & Design* **2009**, *9*, 2556.

[13] a) K. Hanabusa, C. Koto, M. Kimura, H. Shirai, A. Kakehi, *Chem. Lett.* **1997**, 429. b) A. Sakamoto, D. Ogata, T. Shikata, O. Urakawa, K. Hanabusa, *Polymer* **2006**, *47*, 956. c) Y. Yasuda, E. Iishi, H. Inada, Y. Shirota, *Chem. Lett.* **1996**, 575.

[14] a) M. Blomenhofer, S. Ganzleben, D. Hanft, H.-W. Schmidt, M. Kristiansen, P. Smith, K. Stoll, D. Mäder, K. Hoffmann, *Macromolecules* **2005**, *38*, 3688. b) F. Abraham, H.-W. Schmidt, *Polymer* **2010**, *51*, 913. c) F. Abraham, R. Kress, P. Smith, H.-W. Schmidt, *Macromolecular Chemistry and Physics* **2013**, *214*, 17-24.

[15] a) N. Mohmeyer, N. Behrendt, X. Zhang, P. Smith, V. Altstädt, G. M. Sessler, H.-W. Schmidt, *Polymer* **2007**, *48*, 1612. b) D. P. Erhard, D. Lovera, C. Salis-Soglio, R. Giesa, V. Altstädt, H.-W. Schmidt (Eds.: A. H. E. Müller, H.-W. Schmidt), Springer Berlin Heidelberg. Berlin, Heidelberg **2010**, 155.

[16] D. Kluge, F. Abraham, S. Schmidt, H.-W. Schmidt, A. Fery, *Langmuir* **2010**, *26*, 3020.

[17] H. Misslitz, K. Kreger, H.-W. Schmidt, *Small* **2012**, DOI: 10.1002/smll.201202334.

[18] A. Timme, R. Kress, R. Q. Albuquerque, H.-W. Schmidt, *Chem. Eur. J.* **2012**, *18*, 8329.

Supporting Information to

Structure-property relations of supramolecular nanofibers in nonwoven scaffolds as media for air filtration applications

*Holger Misslitz, Klaus Kreger and Hans-Werner Schmidt**

Macromolecular Chemistry I,
Bayreuther Institut für Makromolekülforschung (BIMF),
Bayreuther Zentrum für Kolloide und Grenzflächen (BZKG),
University of Bayreuth, D-95440 Bayreuth, Germany.
E-mail: hans-werner.schmidt@uni-bayreuth.de

Table of contents:

I. Custom-made immersion setup

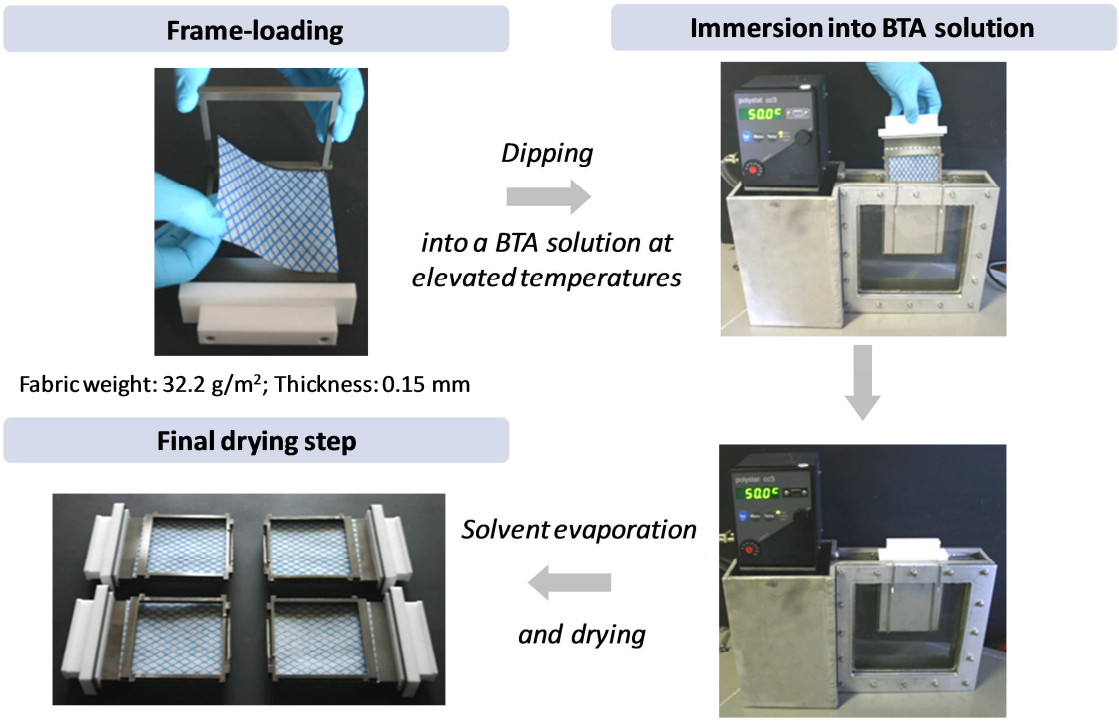

Figure S1. Immersion process in the custom-made immersion bath for the *in-situ* formation of supramolecular nanofibers in nonwoven scaffolds. Polymer nonwoven scaffolds are clamped into a supporting frame, dipped into the immersion bath (which is filled with the BTA solution), removed out of the immersion solution, and finally dried to obtain microfiber-nanofiber composites.

II. Reference experiments on the nonwoven fabric

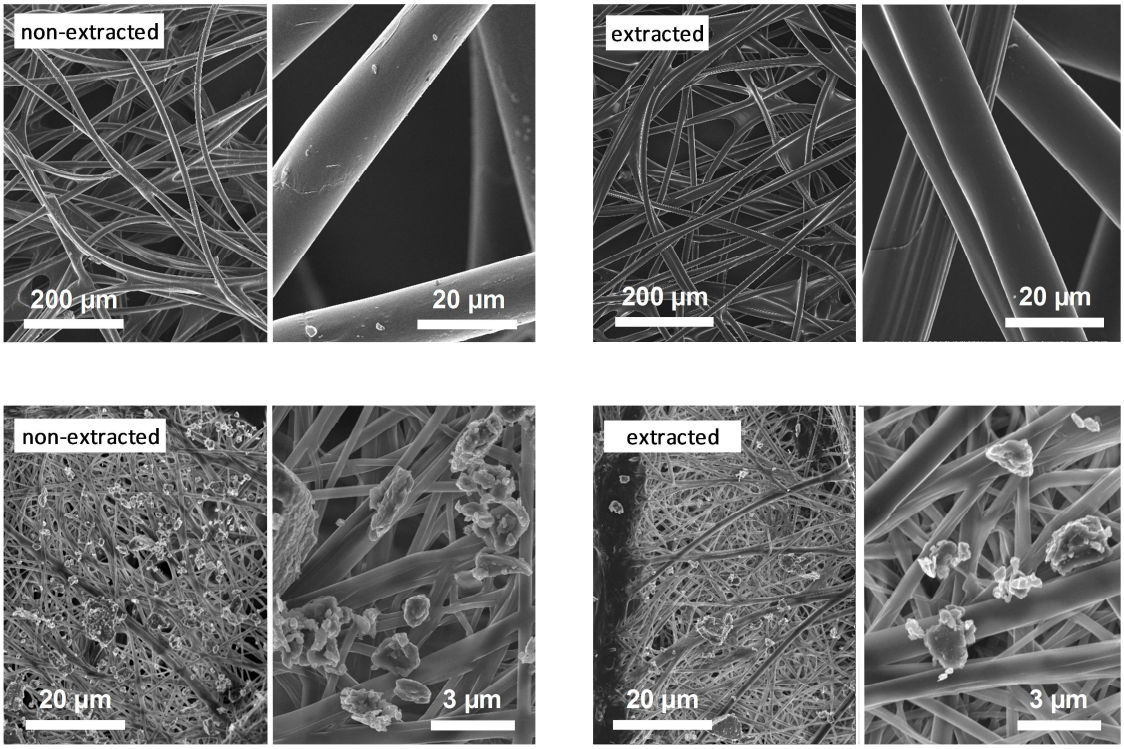

Figure S2. Top: Non-extracted and extracted polymer nonwoven fabric without supramolecular nanofibers. Bottom: Aerosol (ISO fine dust) particle-loaded polymer nonwoven fabric incorporated with BTA **2** nanofibers (immersed in butanone, 1.0 wt%). The nonwoven fabric in the left micrograph was used as received for the immersion process; the nonwoven fabric in the right micrograph was extracted in butanone for 5 days prior use.

III. SEM micrographs of the blank nonwoven fabric prior and after the filter test

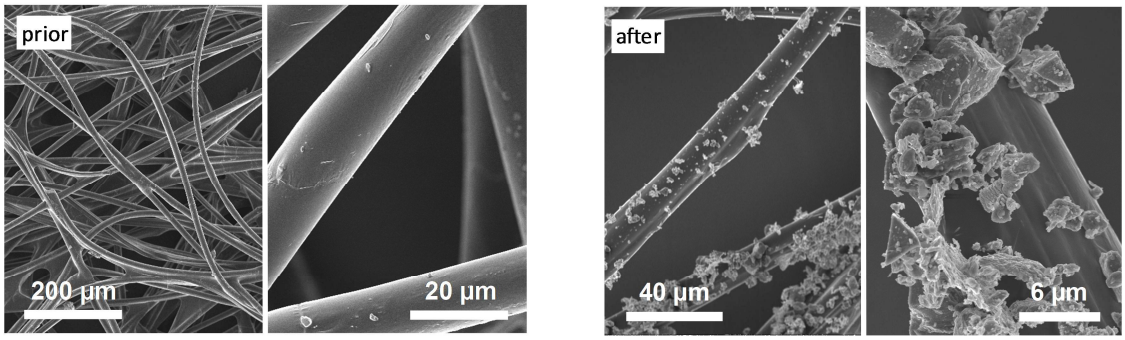

Figure S3. SEM micrographs of the blank nonwoven fabric (left) and an ISO fine dust-loaded nonwoven fabric after the filter test (right).

IV. Influence of concentration on the morphology of the microfiber-nanofiber composite and the filtration efficiency

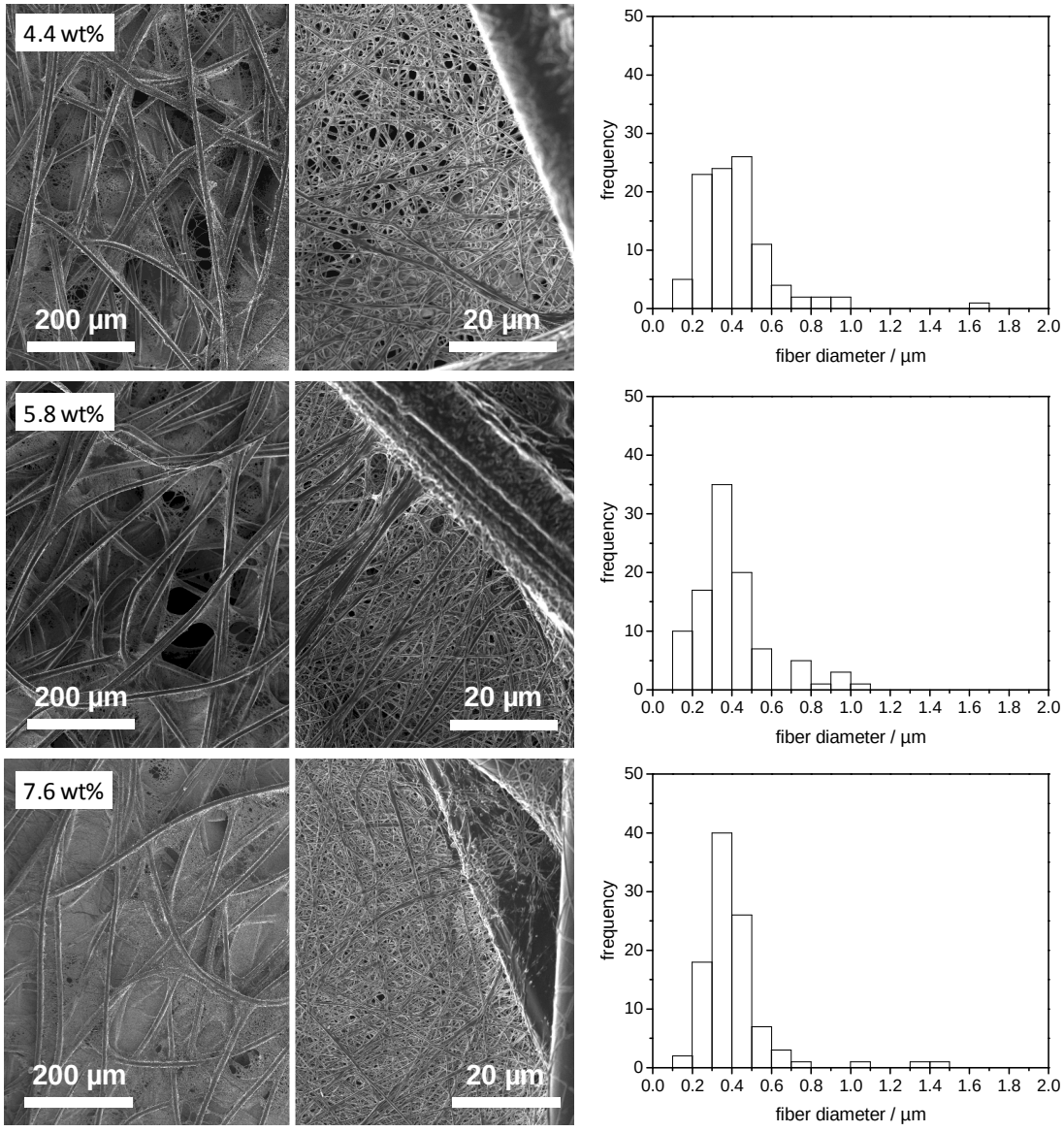

Figure S4. SEM micrographs of the microfiber-nanofiber composites with increasing amount of nanofibers (4.4 wt%, 5.8 wt%, and 7.6 wt%) prepared from three immersion solutions with different concentrations of BTA **2** (0.6 wt%, 0.8 wt%, and 1.0 wt%). The corresponding histograms (100 nm intervals) of the nanofiber diameters on the basis of 100 fibers are shown on the right.

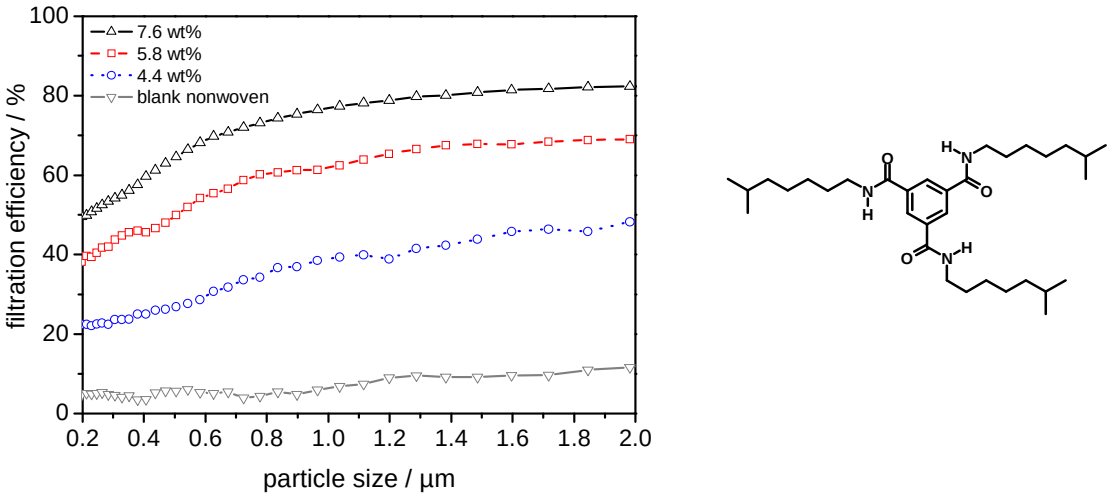

Figure S5. Average filtration efficiencies of the blank nonwoven scaffold as well as the microfiber-nanofiber composites with different weight percentages of supramolecular nanofibers of BTA **2** prepared from butanone solutions. Test parameters: Filter area: 28.3 cm^2; flow velocity: 25 cm/s; test aerosol: ISO fine dust (upstream aerosol concentration: about 6000 P/cm^3); testing time: 30 s. The differential pressures of the tested composites are 288 Pa for 7.6 wt% nanofibers, 199 Pa for 5.8 wt%, and 56 Pa for 4.4 wt%, and 9 Pa for the blank nonwoven.

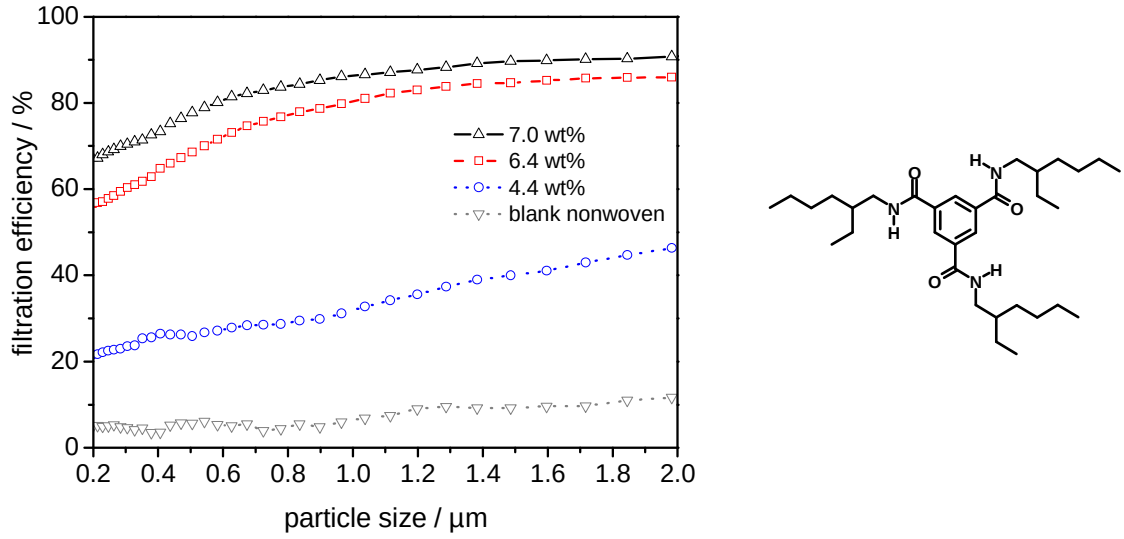

Figure S6. Average filtration efficiencies of the blank nonwoven scaffold as well as the microfiber-nanofiber composites with different weight percentages of supramolecular nanofibers of BTA **1** prepared from butanone solutions. Test parameters: Filter area: 28.3 cm^2; flow velocity: 25 cm/s; test aerosol: ISO fine dust (upstream aerosol concentration: about 6000 P/cm^3); testing time: 30 s. The differential pressures of the tested composites are 429 Pa for 7.0 wt% nanofibers, 281 Pa for 6.4 wt%, and 28 Pa for 4.4 wt%, and 9 Pa for the blank nonwoven.

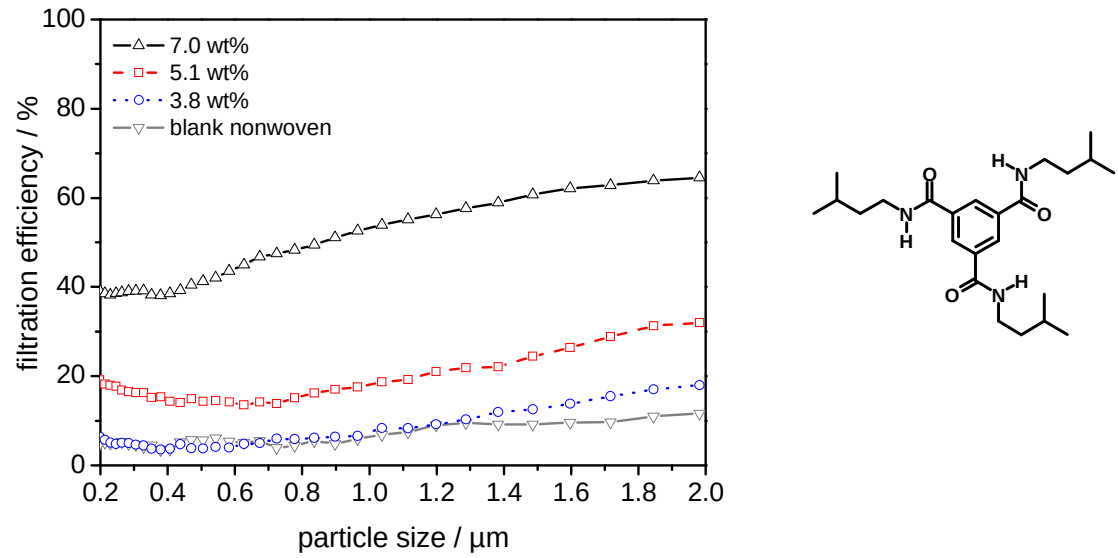

Figure S7. Average filtration efficiencies of the blank nonwoven scaffold as well as the microfiber-nanofiber composites with different weight percentages of supramolecular nanofibers of BTA **3** prepared from butanone solutions. Test parameters: Filter area: 28.3 cm^2; flow velocity: 25 cm/s; test aerosol: ISO fine dust (upstream aerosol concentration: about 6000 P/cm^3); testing time: 30 s. The differential pressures of the tested composites are 67 Pa for 7.0 wt% nanofibers, 16 Pa for 5.1 wt%, and 10 Pa for 3.8 wt%, and 9 Pa for the blank nonwoven.

V. Investigated composites prepared with different BTAs, solvents and concentrations

Table S1. Listing of weight percentages of supramolecular nanofibers in the composites which were prepared with BTAs **1-3**, in three different solvents (2-butanone, isopropanol, and ethanol) with various immersion solution concentrations, respectively.

BTA	solvent	weight percentage of supramolecular nanofibers [wt%] in the composite prepared from 0.6 wt% solution	weight percentage of supramolecular nanofibers [wt%] in the composite prepared from 0.8 wt% solution	weight percentage of supramolecular nanofibers [wt%] in the composite prepared from 1.0 wt% solution
1	butanone	4.4	6.4	7.0
	isopropanol	6.0	7.4	8.5
	ethanol	2.7	4.4	5.5
2	butanone	4.4	5.8	7.6
	isopropanol	7.1	8.8	10.0
	ethanol	4.1	4.5	6.9
3	butanone	3.8	5.1	7.0
	isopropanol	6.2	6.8	8.4
	ethanol	2.5	3.7	4.2

VI. Filtration efficiency of the single-, the double-, and the triple-layer reference filter composed of the blank nonwoven scaffold

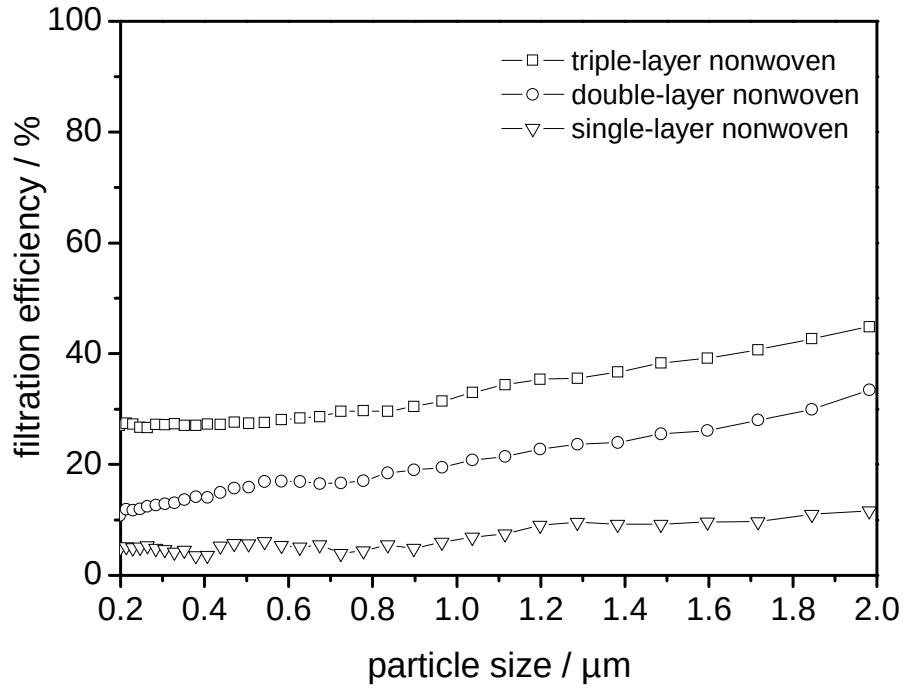

Figure S8. Average filtration efficiencies of the single-, the double-, and the triple-layer blank nonwoven scaffolds used as references. Test parameters: Filter area: 28.3 cm^2; flow velocity: 25 cm/s; test aerosol: ISO fine dust (upstream aerosol concentration: about 6000 P/cm^3); testing time: 30 s. The differential pressures of the tested reference filters are 9 Pa for the single-layer filter, 15 Pa for the double-layer filter and 25 Pa for the triple-layer nonwoven filter.

4. APPENDIX

Filter test rig MFP 2000 from PALAS

Within the scope of this thesis, the *modularly built filter test rig MFP 2000* from Palas® including the characteristic equipment had to be acquired. Thereby, the filter test rig had to be adapted, fitting to our specific research purposes. Within this process, the filter area and the adjustability of the volumetric flow rate were tailored in view of our required test conditions, yielding to a custom build filter test rig from Palas®. Furthermore in this work, the corresponding measuring procedures (for instance stability tests, pressure drop measurements, and filtration efficiency tests) had to be established as well as optimized with respect to our specimens.

The filter test rig MFP 2000 with its setup is shown in Figure 1. At the test rig, the overall *flow velocity* (velocity of airstream [m/s]) at the filter can be continuously adjusted by two different volumetric flow rates (volume of airstream [L/min]), namely *generator volumetric flow rate* and *mixed air volumetric flow rate* which can be accessed separately by means of mass flow controllers. The air from the *generator volumetric flow rate* streams into the aerosol generator. In our laboratory, three different generator types can be utilized at the modularly built test rig. These are an oil droplet, a salt particle, and a dust generator. Each of them is able to produce a constant aerosol amount in a specific time interval. The *mixed air volumetric flow rate* is needed to dilute the particle-enriched airstream flowing out of the generator to obtain the desired flow velocity as well as the requested upstream aerosol concentration, which is applied to a filter. At the filter, some aerosol particles are separated, but others are penetrating through and are directed into the sensor. The sensor works with the principle of white light scattering combined with a light barrier. Thus the aerosol concentration as well as the aerosol particle size can be determined. The resulting signal is transferred to the detector and recorded by a computer.

The filter test rig can be operated with a maximal volumetric flow rate of 170 L/min, which is related to a maximal flow velocity of 1.0 m/s at the filter surface of 28.3 cm^2. Because the filter surface influences the flow velocity, this value can be improved to 3.0 m/s by the reduction to one third of the original filter surface at unchanged volumetric flow rate. In commercial applications the flow velocities differ extremely. While in filters for clean rooms (0.01-0.05 m/s), cabin air filters (0.05-0.20 m/s), and customary vacuum cleaners (0.15-0.35 m/s) a flow velocity of 0.4 m/s is not exceeded, coarse filters for instance in tools such as chain saws, power packs, and lawn mowers are exposed to flow velocities of 1-3 m/s. Because of economic factors for instance

huge differential pressures, flow velocities of 0.40-1.00 m/s are rarely realized in industrial applications.

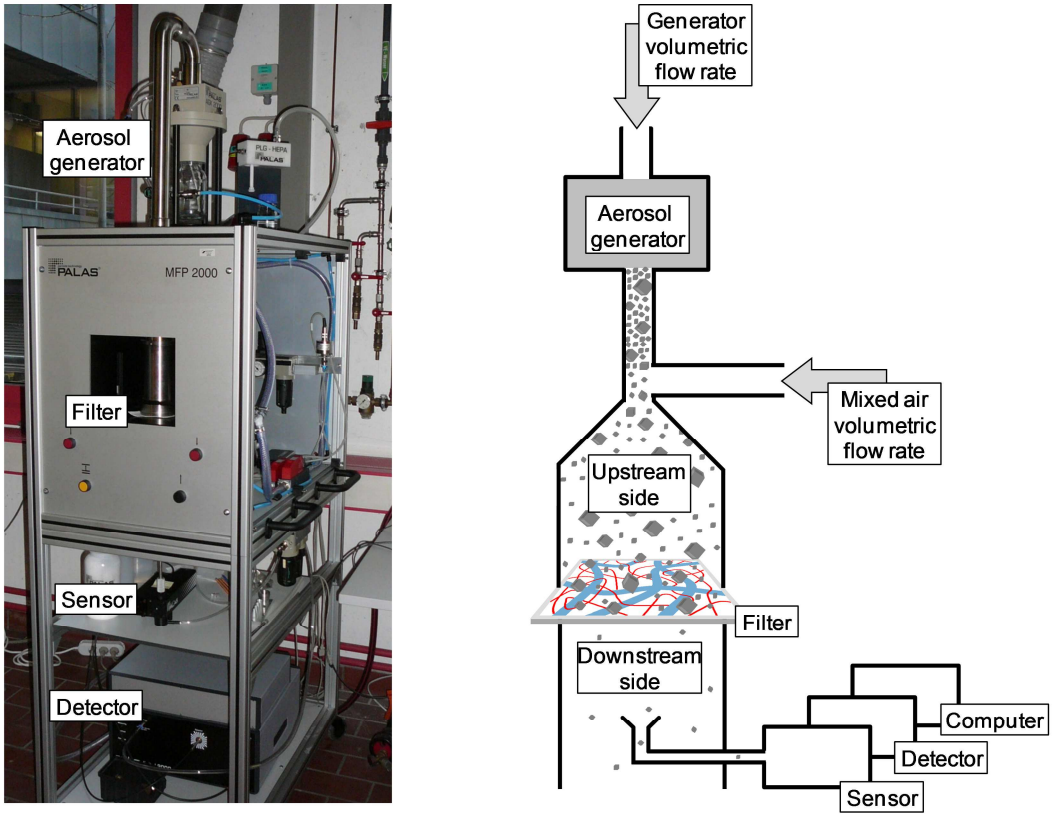

Figure 1. Picture of filter test rig MFP 2000 and schematic representation of its setup.

Various filter tests can be realized at the MFP 2000. In this work *filter stability tests* are conducted to detect the stability of the supramolecular nanofiber modified samples at strong airstreams. For these tests, the aerosol generator has to be removed, so that a clean airstream without any aerosols is applied to the filter. If the supramolecular fibers in the filter would be destroyed by the adjusted airstream, fiber pieces as well as network fragments would be broken out of the filter and would be detected. These tests are performed to a maximal flow velocity of 3.0 m/s.

The second test method is the *determination of the differential pressure*. This test is also realized without any generator. Thereby, the flow velocity is successively increased and the differential pressure between the upstream side and the downstream side of the filter is detected continuously.

At the *determination of the filtration efficiency* an aerosol generator is required. This test is divided into two experimental sections. As reference, the upstream aerosol concentration is measured initially without filter element. Thereby, 100 % of the generated particles can be detected by the sensor. At the second measuring step, the filter is inserted and the resulting downstream particle distribution (penetrating

particles which are not separated at the filter) is quantified. Both particle distributions, at the upstream and the downstream side are shown in Figure 2 exemplarily.
From the ratio of the downstream aerosol concentration and the upstream aerosol concentration the filtration efficiency can be calculated. At the determination of the initial filtration efficiency of an unloaded filter the upstream aerosol concentration which is applied to the filter has to be chosen carefully because of the relatively low dust holding capacity of the plane filter. If the aerosol concentration is adjusted too high, the filter will be "overloaded". As result a filter cake is established and the filtration efficiency of a loaded filter is detected. This value is generally higher compared to the initial filtration efficiency because the filter cake also acts as a filter. At these tests, also the differential pressure is detected at the beginning as well as at the end of the testing time. Due to the fact, that the differential pressure is increasing during measurement when a filter cake is developed, this value gives good control if the filtration efficiency belongs to a virgin filter or to a dust loaded filter including filter cake.

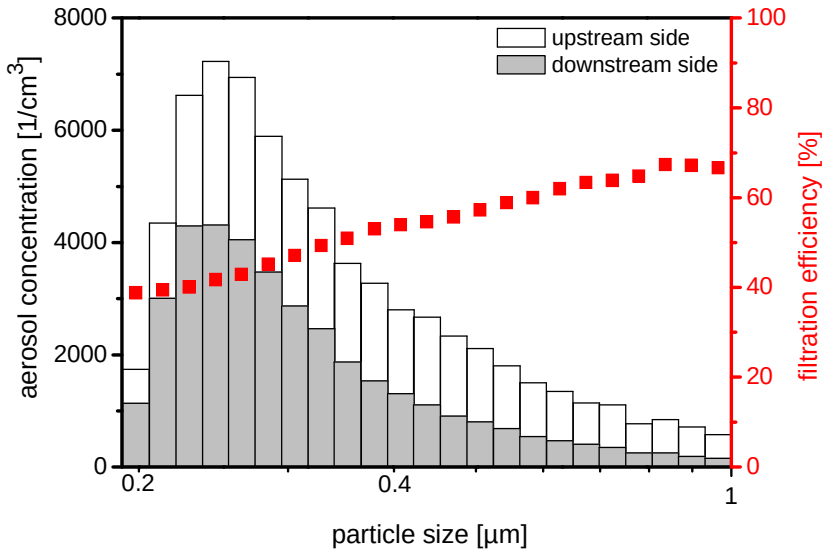

Figure 2. Upstsream and downstream aerosol particle distribution (KCl particles) with the corresponding filtration efficiency of a randomly selected filter.

The filtration efficiency tests can be performed with various aerosols. In this work, oil droplets (DEHS (Di-2-ethylhexyl-sebacate)), salt particles (KCl), and dust aerosols (Iso fine dust) is used. Each kind of aerosol has to be prepared by a different generator and features distinct particle size distributions (Figure 3). To adjust the quantity of the aerosol particles in the measuring process, various parameters at the generators as well as at the test rig can be changed.

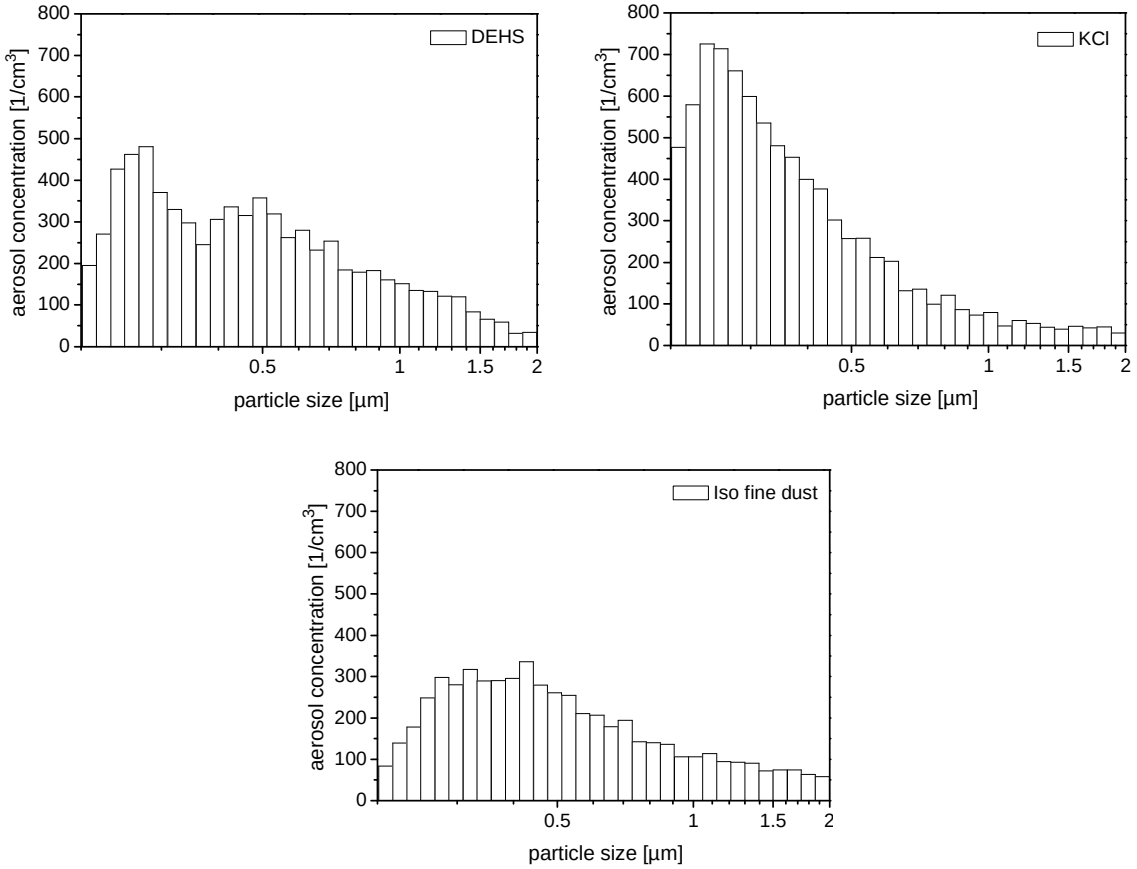

Figure 3. Particle size distributions of the generated test aerosols DEHS, KCl, and Iso fine dust (flow velocity: 25 cm/s).

DEHS generator PLG HEPA

The PLG HEPA generator works on the operating principle of dispersing DEHS-oil by an airstream. In order to ensure consistency of the upstream aerosol concentration of the measurements, the generator has to be operated with a minimal generator volumetric flow rate of 1.40 L/min. The larger the applied generator volumetric flow rate, the more aerosol particles are created (Figure 4). Furthermore, the overall flow velocity also affects the aerosol concentration. At consistent generator volumetric flow rate the produced aerosol particle amount is decreasing in quantity with larger flow velocity. This can be explained by the fact that the mixed air volumetric flow rate has to be enhanced when higher flow velocities are desired while the generator volumetric flow rate is not changed. Thus, the mixed air volumetric flow rate dilutes the aerosol loaded airstream of the generator. As a result of this, the ratio of generator volumetric flow rate and mixed air volumetric flow rate has to be adjusted carefully, when a specific oil droplet concentration at a given overall flow velocity is requested.

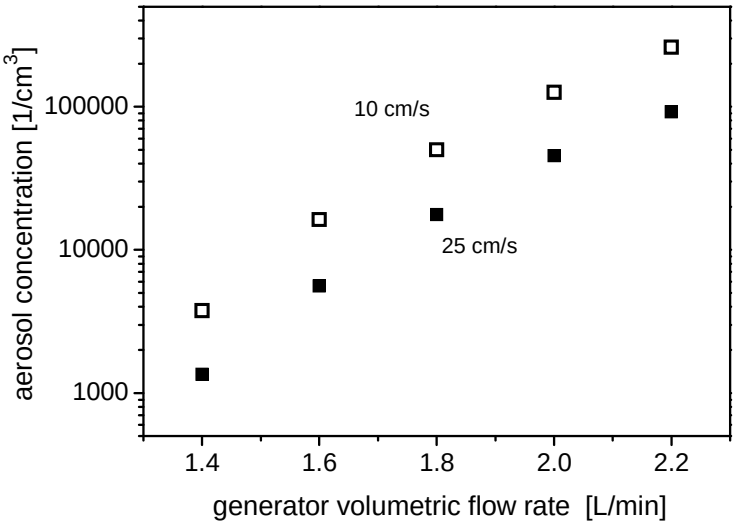

Figure 4. Influence of generator volumetric flow rate on the aerosol concentration at different overall flow velocities (flow velocities: 10 cm/s and 25 cm/s, filtration area: 28.3 cm^3).

Salt generator AGK 2000

In this generator type, different salt aerosols such as KCl and NaCl can be produced. Thereby, the airstream entrains water droplets from an aqueous salt solution into a drying system. Consequently, the water of the droplets evaporates and the dried salt particles remain as test aerosol particles. In this generator, the aerosol concentration can be adjusted by the chosen salt concentration of the solution, by the value of generator volumetric flow rate, and by the overall flow velocity (Figure 5). This generator requires a minimal generator volumetric flow rate of 7.5 L/min for a constant aerosol concentration.

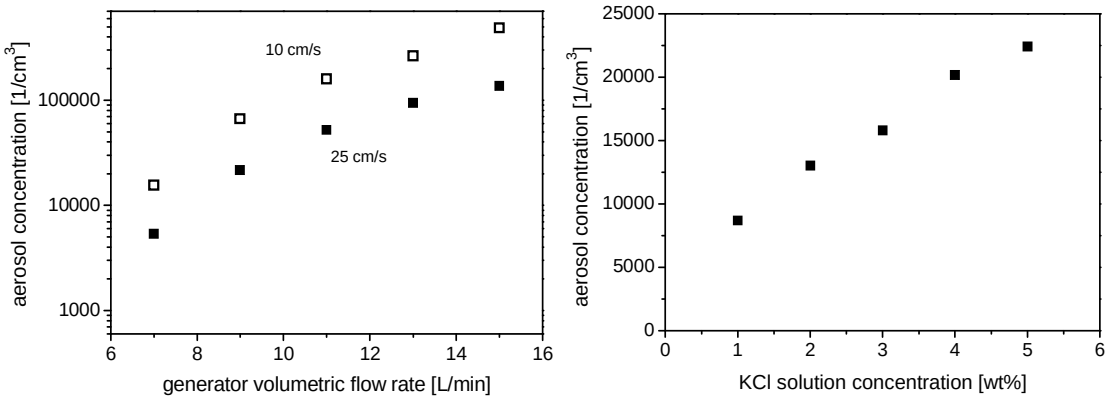

Figure 5. Left: Influence of generator volumetric flow rate on the aerosol concentration at different overall flow velocities (KCl solution concentration: 1.0 wt%). Right: Influence of the concentration of the salt solution utilized in the generator on the aerosol concentration at a constant generator volumetric flow rate (7.5 L/min) and a constant overall flow velocity (25 cm/s). Filtration area for both experiments: 28.3 cm^3.

Dust generator RBG 1000

Contrary to both generators described previously, the RBG 1000 can only ensure consistency in aerosol particle concentration above a minimal generator volumetric flow rate of 15 L/min. Therefore, a minimal overall flow velocity of about 20 m/s is required. The dust generator can be operated with all non-agglomerating dusts. Iso fine dust is one of many examples, which is used in this work. Amongst the three generators described here, this is the most versatile one. In the RBG 1000 the test dust is located in a reservoir tube and pressed towards a rotary brush by a feed piston with a distinct feed rate. By the rotation of the brush, the dust is dispersed into the test aerosol particles of various sizes. The aerosol particle concentration in the air flow at the upstream side of the filter is dependent on the packing density of the dust in the reservoir tube, the feed rate, the rotation speed of the brush, the generator volumetric flow rate, and the overall flow velocity. Figure 6 shows the influence of the feed rate in the reservoir tube, the influence of the rotation speed of the brush, and the influence of the generator volumetric flow rate on the aerosol concentration. By increasing one of the three parameters, the aerosol particle quantity is enhanced in each case.

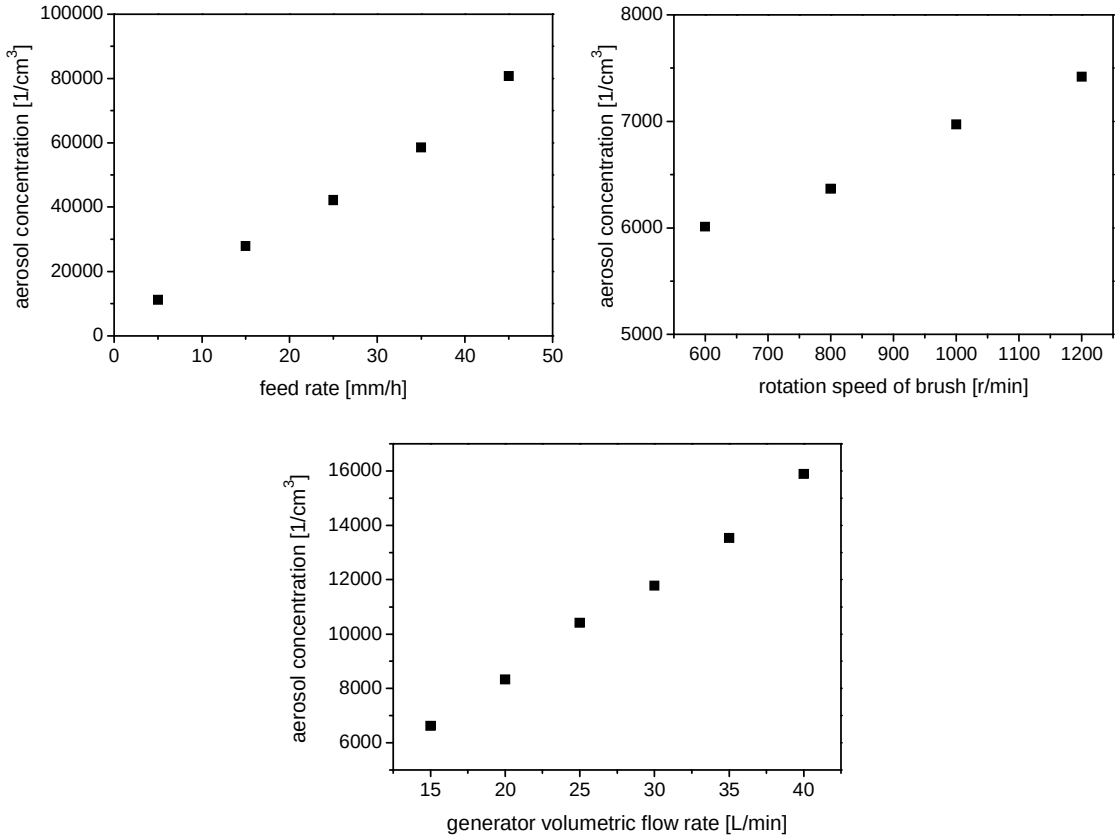

Figure 6. Influences on the aerosol concentration (Iso fine dust). Top left: influence of feed rate (flow velocity: 25 cm/s, generator volumetric flow rate: 15 L/min, rotation speed of brush: 1200 r/min, feed piston: 7 mm, filtration area: 28.3 cm^3). Top right: influence of rotation speed of brush (flow velocity: 25 cm/s, generator volumetric flow rate: 15 L/min, feed piston: 7 mm, feed rate: 5 mm/h, filtration area: 28.3 cm^3). Bottom left: influence of generator volumetric flow rate (flow velocity: 25 cm/s, rotation speed of brush: 1200 r/min, feed piston: 7 mm, feed rate: 5 mm/h, filtration area: 28.3 cm^3).

Danksagung

Die vorliegende Arbeit wäre ohne die Finanzierung der Deutschen Forschungsgemeinschaft durch den Sonderforschungsbereich 840, Teilprojekt B8 und dem Graduiertenkolleg 1640 nicht möglich gewesen.

Ich bedanke mich bei allen, die zum Gelingen dieser Arbeit beigetragen haben sowie beim ganzen Team des Lehrstuhls Makromolekulare Chemie I.

Allen voran bedanke ich mich bei meinem Betreuer Herrn Prof. Dr. Hans-Werner Schmidt, der mich unter seiner Leitung auf einem sehr interessanten Themengebiet vollkommen eigenständig forschen ließ. Besonders seinen fachlichen Anregungen sowie den gemeinsamen wissenschaftlichen Diskussionen gebührt großer Dank. Darüber hinaus bedanke ich mich für das von ihm entgegengebrachte Vertrauen, das es mir ermöglichte, die Filter-Messmethoden am Lehrstuhl Makromolekulare Chemie I zu etablieren und somit die Grundsteine des Filter-Projektes zu legen.

Mein besonderer Dank gilt Dr. Klaus Kreger und Andreas Haedler, die mir durch gute Zusammenarbeit und durch konstruktive Diskussionen besonders in den letzten Zügen meiner Promotion sehr geholfen haben.

Ich danke zudem meinen Kooperationskollegen Christian Bühlmeyer und Prof. Dr. Anna Köhler (Lehrstuhl Experimental Physik II) sowie Prof. Dr. Rodrigo Q. Albuquerque (Lehrstuhl Experimental Physik IV), die mir gezeigt haben welche Mehrwerte fächerübergreifende Kooperationen für jeden Einzelnen aufweisen können.

Großer Dank gebührt den Technikern Jutta Failner, Sandra Ganzleben, Doris Hanft und Irene Bauer für Ihre Hilfe bei der Synthese der Verbindungen. Werner Reichstein danke ich für die Einweisung ins Rasterelektronenmikroskop, welches eine wichtige Rolle bei der Charakterisierung der supramolekularen Strukturen spielte. Zusätzlich danke ich Lena Geiling (Anorganische Chemie I) für die BET Messungen.

Besonders bedanke ich mich bei Petra Weiss für die Erledigung vieler bürokratischer Angelegenheiten.

Vielen Dank an all diejenigen Mitarbeiter am Lehrstuhl MC I bzw. an anderen Lehrstühlen der Universität Bayreuth, die für meine Arbeit relevante Messgeräte betreuten. Zusätzlich danke ich Andreas Timme für die Röntgenmessungen.

Insbesondere bedanke ich mich bei meinen Kollegen aus den Laboren 598 und 570 für ihre stete Diskussionsbereitschaft, ihre konstruktive Kritik, ihren Humor und für viele nette Gespräche. Die angenehme Arbeitsatmosphäre in beiden Laboren wusste ich sehr zu schätzen. Des Weiteren bedanke ich mich bei Dr. Andreas Bernet und Marina Behr für das Korrekturlesen der Arbeit bzw. der einzelnen Manuskripte.

Vielen herzlichen Dank meinen lieben Eltern, die mich in jeder Lebenslage unterstützten und mir vor allem während des Studiums und meiner Doktorarbeit den nötigen Rückhalt gegeben haben.

Der größte Dank geht wohl an meine bezaubernde Frau Iris: Vielen Dank, dass du immer zu mir gestanden und ermutigende Worte gefunden hast. Ich danke dir von ganzem Herzen für die Kraft, die du mir während dieser Zeit gegeben hast.

Erklärung

Hiermit erkläre ich, dass ich die vorliegende Arbeit selbständig verfasst und keine weiteren als die von mir angegebenen Quellen und Hilfsmittel benutzt habe.
Ferner erkläre ich, dass ich weder anderweitig mit oder ohne Erfolg versucht habe eine Dissertation einzureichen noch mich einer Doktorprüfung zu unterziehen.

Bayreuth, Februar 2013

Holger Misslitz